Imperial College London

Organic and Hybrid Semiconductors for Photovoltaic Application — Control of Energetics and Interfacial Properties

Yi-Chun Chin

Department of Physics, Imperial College London

Submitted for the degree of Doctor of Philosophy
June 2023

Abstract

Both organic photovoltaics (OPVs) and perovskite solar cells (PSCs) are gaining attention due to their fast-growing power conversion efficiency (PCE) and potential for indoor or aerospace applications. However, this success is based on semi-empirical choice of specific molecules and interfacial optimization, where performance origin is still partially unknown. Especially, systematic understanding of molecular-structure-dependent energetics and energy-level alignment in organic/hybrid interfaces is highly needed. In this thesis, fine-tuned packing in different organic molecules and interfacial energetic alignment in perovskite/hole transport layer (HTL) interface is extensively studied, combining ambient photoemission spectroscopy, surface photovoltage, and computational simulations.

Firstly, in OPV materials, various molecular structures and packing motifs are investigated, analyzing the correlation with their energetics and trap distribution. For high-performance non-fullerene acceptors (NFAs), molecular rigidity originated from side-chain design is shown to determine energetic disorder and trap formation. Besides, due to strong electric quadrupole moments, NFA energetics is tuned by packing-orientation control in thin films. The impact of packing-dependent energetic shift is further shown to govern recombination loss and device open-circuit voltage (V_{OC}). This energetic analysis is also extended to bulk heterojunctions, as demonstrated in polymer:fullerene blends, where blending-induced energetic shifts are identified for different polymer structures. These findings provide important structure-property-performance relationships and guidance for organic molecular designs for high-efficiency OPVs.

Secondly, in PSC HTLs, interfacial energetic alignment is studied by sequential PEDOT:PSS dedoping. Beneficial band-bending is found for dedoped PEDOT:PSS, reducing non-radiative recombination and leading to higher V_{OC} and PCE.

Finally, the impact of two-dimensional (2D) perovskite interlayer is investigated by tuning

cation concentrations. Here, an extraction barrier is observed in phenethylammonium-based 2D layers, but surface-defect suppression reduces recombination loss and increases V_{OC}. Moreover, significant HTL energetic shift is found, correlated to HTL-to-perovskite dopant diffusion. The study reveals the potential of 2D perovskites to improve PSC performance by reducing this phenomenon.

Acknowledgments

I am very grateful for the physical and mental support that I have received throughout my 5 years of PhD study in Imperial College London. Without it, I would not be able to achieve this PhD. Although I am trying my best knowledge to list everyone here, I acknowledge that there must be some more people I unintentionally miss. Please accept my deepest apology.

I would like to firstly dedicate this thesis to my family which has unconditionally supported me all the way since the beginning of this journey. Despite the significant 7 hours to 8 hours time difference, their warm and powerful cares were still able to reach my heart and provided me immeasurable energy to push forward and take in more challenges.

In this PhD, so much challenging science and complicated collaborations are involved. I am really thankful to have all my colleagues to guide and grow together in the most frontier research. I must particularly thank Matyas who lead me into this challenging perovskite solar cell field and taught me all his precious experience in device fabrication. I also like to thank Saurav, Katie, Ella, Chiara, Katia, Chieh-Ting, Weidong and Joel for their valuable suggestions and discussion time which triggered many inspiring experiments and directions. Although not having long overlap time, partially due to COVID, I really enjoyed all the training, experiments and brainstorming time with Emily, Charlie, Yixin and Lei. I am sure with all your brilliant minds, there will be nothing impossible for you to conquer. Lastly, I would like to thank Gihan for his incessant assistance with all the instruments, which enable all the invaluable measurements.

Statement of Originality

Except where specific reference is made to the work of others, the work contained in this thesis is original and has not been submitted either wholly or in part to satisfy any degree requirement at this or any other university. Where the thesis is written in the first person plural, that is for readability and in recognition that I have not worked in isolation, but the work was carried out by me personally unless otherwise stated.

Yi-Chun Chin, June 2023

Copyright Declaration

The copyright of this thesis rests with the author. Unless otherwise indicated, its contents are licensed under a Creative Commons Attribution-Non Commercial 4.0 International License (CC BY-NC).

Under this license, you may copy and redistribute the material in any medium or format. You may also create and distribute modified versions of the work. This is on the condition that: you credit the author and do not use it, or any derivative works, for a commercial purpose.

When reusing or sharing this work, ensure you make the license terms clear to others by naming the license and linking to the license text. Where a work has been adapted, you should indicate that the work has been changed and describe those changes.

Please seek permission from the copyright holder for uses of this work that are not included in this license or permitted under UK Copyright Law.

"Put down your roots in the soil
Live together with the wind
Pass the winter with the seeds
Sing in the spring with the birds"

Laputa: Castle in the Sky 1986

Contents

Abstract **2**

Acknowledgments **4**

Statement of Originality **5**

Copyright Declaration **6**

Contents **8**

List of Figures **11**

List of Tables **14**

Frequently Used Abbreviation **15**

1 Introduction **17**

1.1 Motivations 17

1.2 Aims 18

References 22

2 Background Theory **23**

2.1 Organic Semiconductors in Photovoltaic Applications 23

2.1.1 Background 23

2.1.2 Organic Transport Layer 29

2.1.3 Organic Photovoltaics: specificity and challenges 30

2.2 Hybrid Perovskites in Photovoltaic Applications 35

2.2.1 Background 35

2.2.2 Ruddlesden-Popper Phase/2D Perovskite 37

2.2.3 Perovskite Solar Cells: specificity and challenges 38

References 42

3 Experimental Methods **54**

3.1 Device and Sample Fabrication 54

3.2 Density Functional Theory 55

3.3 Optical Characterizations . . . 56
3.3.1 UV-Visible Spectroscopy . . . 56
3.3.2 Photoluminescence Spectroscopy . . . 56
3.3.3 Raman Spectroscopy . . . 56
3.4 Energetic Characterizations . . . 57
3.4.1 Fermi Level . . . 57
3.4.2 Ambient Photoemission Spectroscopy . . . 59
3.4.3 Density of States . . . 63
3.5 Morphological and Structural Characterizations . . . 67
3.5.1 Atomic Force Microscopy . . . 67
3.5.2 Thickness Measurements . . . 68
3.5.3 X-Ray Diffraction . . . 68
3.5.4 Grazing-Incidence Wide-Angle X-Ray Scattering . . . 68
3.6 Electronic and Photoelectronic Characterizations . . . 68
3.6.1 Electrical Conductivity . . . 68
3.6.2 Solar Cell Characterizations . . . 69
3.6.3 Surface Photovoltage . . . 69
References . . . 72

4 Organic Photovoltaic Materials – Impact of Molecular Structure and Packing on Electrostatic Potential and Trap States 75
4.1 Introduction . . . 76
4.2 Molecular Structure Induced Traps in Small Molecule Non-Fullerene Acceptors . 77
4.3 Orientation-Dependent Energetic Shifts in Vacuum-processed Organic Small-Molecules . . . 82
4.4 Orientation-Dependent Energetic Shifts in Solution-processed Non-Fullerene Acceptors and Their Impact on OPV Performance . . . 87
4.5 Blending Induced Packing Structure Changes and Trap States formation in Polymer:Fullerene BHJ . . . 96
4.6 Conclusion . . . 101
References . . . 104

5 Hole Transport Materials – Suppressing PEDOT:PSS Doping-Induced Interfacial Recombination Loss in Perovskite Solar Cells 109
5.1 Introduction . . . 110
5.2 Doping Level and Thickness Control on PEDOT:PSS . . . 111
5.3 Characterizations of Dedoped PEDOT:PSS HTL in Perovskite Devices . . . 113
5.4 Reduced Interfacial Recombination Loss in Perovskite Solar Cells . . . 116
5.5 Conclusion . . . 120
5.6 Experimental Methods . . . 122
References . . . 123

6 Perovskite Photovoltaic Materials – Reduced Recombination Loss and Spiro-OMeTAD Dopant Leakage by Phenethylammonium-Based Low-Dimensional Perovskite Passivation **125**
6.1 Introduction . . . 126
6.2 Surface Passivation Induced Energetic Shifts in Perovskite . . . 127
6.3 Reduced Recombination and Improved Charge Extraction with Low-Dimensional Passivation Layer . . . 133
6.4 Suppressed Dopant Leakage by Surface Passivation with Low-Dimensional Perovskite . . . 137
6.5 Conclusion . . . 141
6.6 Experimental Methods . . . 142
References . . . 144

7 Conclusion and Future Work **147**
7.1 Conclusion . . . 147
7.2 Future Work . . . 150
References . . . 152

A List of Publications **153**

B Molecular Abbreviations **155**

C Python code of APS module **158**

D Visualization of Quadrupole Moment and Multipole Expansion **171**

List of Figures

2.1 Energy band diagram of semiconductor 25
2.2 The effect of conjugation extension and Peierls transition in conjugated organic semiconductors 26
2.3 Energy diagrams of neutral, positive/negative polaron and exciton 28
2.4 Optoelectronic processes: charge generation and recombination 29
2.5 An example of photovoltaic architecture and current density-voltage curve . . . 32
2.6 A schematic illustration of methylammonium lead iodide (MAPI) perovskite . . 36
2.7 A schematic illustration of Ruddlesden-Popper phase 2D perovskite with $n = 1, 2, \infty$ 37

3.1 Schematic energy diagram of a semiconductor sample measured by a Kelvin probe tip 58
3.2 Schematic diagram and plots for off-null Kelvin probe measurements 59
3.3 A schematic diagram of ambient photoemission system 60
3.4 Demonstration plots of ambient photoemission spectroscopy spectrum with perovskite and the influence function of baseline 62
3.5 Statistics and fitting of the intrinsic density of states from ambient photoemission spectroscopy and an example DOS plot before and after smoothing 65
3.6 Series of experimental examples of density of states converted from APS spectra with similar chemical structures 67
3.7 Example surface photovoltage and alternating surface photovoltage curves of a perovskite sample with their schematic diagrams 70

4.1 Tail states and energetic shifts of high performance OPV blends and neat NFAs 78
4.2 Potential energy scans as a function of dihedral angle of Y6, ITIC and IDTBRs NFAs with their structures, calculated using DFT calculation 80
4.3 Baseline background corrected and normalized in situ resonant Raman spectra at 633 nm excitation of a neat Y6 film, at 514 nm excitation of a neat ITIC film, at 457 nm excitation of a neat O-IDTBR film 81
4.4 Homojunction organic photovoltaics based on α-6T and various buffer layers . . 83
4.5 Morphological characterization for the orientation of α-6T thin films 84
4.6 Energetic landscape and surface photovoltage response in different morphological α-6T 85

4.7 Orientation-dependent Y6 neat film energetics and charge generation 89
4.8 Density functional theory simulated molecular quadrupole moments perpendicular to π-conjugated backbone (Q_π) and electrostatic potential (ESP) of α-6T, Y6 and other organic semiconductors 90
4.9 Energetics of Y6/PM6 planar heterojunction 91
4.10 Device performance of Y6/PM6 bilayer OPVs 92
4.11 Surface photovoltage measurements of 30 nm or 5 nm PM6 on Y6 CF and Y6 CB with the schematic diagram 93
4.12 Orientation-dependent energetics and device performance of PM6:Y6 BHJ . . . 94
4.13 Electrostatic effect on HOMO level shift of polymer donors upon blending with different NFAs 95
4.14 Molecule structures of Si-PCPDTBT, PDTSiTTz, PCBM, ICMA, ICBA and ICTA 97
4.15 Energetics of PDTSiTTz and Si-PCPDTBT and their blends with PCBM, ICMA, ICBA, and ICTA 98
4.16 DOS comparison and fitting for PDTSiTTz and Si-PCPDTBT blends 99

5.1 Optical and electrical properties of neat and dedoped PEDOT:PSS with 4.5, 20, and 50 % volume fractions of 1 M NaOH 112
5.2 AFM image of PEDOT:PSS with different NaOH blend ratio in vol% 113
5.3 NaOH-dedoped device structure and reverse current density-voltage scans 114
5.4 Fermi level of different thickness 20 vol% NaOH dedoped PEDOT:PSS 115
5.5 Box plots of open-circuit voltage, fill factor, power conversion efficiency, short-circuit current density and shunt resistance of NaOH-dedoped devices 116
5.6 MAPI or PCBM on top of PEDOT:PSS with different NaOH blend ratio in vol% 117
5.7 Thickness-dependent optical and optoelectronic measurements of NaOH-dedoped PEDOT:PSS HTL with MAPI on top 118
5.8 Thickness-dependent optical and optoelectronic measurements of NaOH de-doped PEDOT:PSS with MAPI and PCBM on top 119
5.9 Energetics of MAPI and PCBM 120
5.10 Schematic diagrams of surface photovoltage for neat and dedoped PEDOT:PSS with MAPI on top in three different stages 121

6.1 The effect of phenethylammonium iodide passivation on $Cs_{0.03}FA_{0.82}MA_{0.15}PbBr_{0.44}I_{2.56}$ with different concentrations 128
6.2 Energetics, photoluminescence (PL) and surface topography of PEA_2PbI_4 and/or PEA_2PbBr_4 130
6.3 Atomic force microscopy images of 3D perovskite, PEAI 5, PEAI 10 and PEAI 15 with their pinhole coverage 131
6.4 Charge dynamics of PEAI passivated 3D perovskite on top of TiO_2 132

6.5 The ambient photoemission spectroscopy (APS) spectra with the DOS inset and the energetic diagram of Spiro-OMeTAD (Spiro) on top of the passivated perovskite 134
6.6 The open-circuit voltage, short-circuit current, fill factor and power conversion efficiency statistics of PEAI passivated devices 134
6.7 The absorbance of PEAI passivated perovskite solar cells 135
6.8 The photoluminescence (PL), transient PL, surface photovoltage, alternating surface photovoltage measurements of PEAI passivated perovskite with Spiro-OMeTAD on top 136
6.9 Schematic diagram for 3D case, PEAI 5 and the other passivated devices 137
6.10 Energetics of Spiro-OMeTAD blended with or on top of different materials . . . 139
6.11 Optical characterizations of Spiro-OMeTAD in different doping conditions . . . 140
6.12 Atmoic force microscopy images of Spiro-OMeTAD on 3D, PEAI 5, PEAI 10, PEAI 15, PEABr 5 and their pinhole area percentage 141

List of Tables

B.1 Molecular abbreviations and full names repeatedly used 155

Frequently Used Abbreviation

Abbreviation	Description
AFM	atomic force microscopy
APS	ambient photoemission spectroscopy
BHJ	bulk heterojunction
CT	charge transfer
DFT	density functional theory
DMF	dimethylformamide
DMSO	dimethyl sulfoxide
DOS	density of states
E_F	Fermi level
E_g	band gap
E_{vac}	local vacuum energy level
EQE	external quantum efficiency
ESP	electrostatic potential
ETL	electron transport layer
FF	fill factor
FTO	fluorine-doped tin oxide
GIWAXS	Grazing-incidence wide-angle X-ray scattering
HOMO	highest occupied molecular orbital
ITO	indium tin oxide
J_{SC}	short-circuit current density
MAPI	methylammonium lead iodide
NFA	non-fullerene acceptor
OSC	organic semiconductor
PHJ	planar heterojunction
Q_π	quadrupole moment perpendicular to conjugation backbone
$\mathrm{R_s}$	series resistance
$\mathrm{R_{sh}}$	shunt resistance
UV-Vis	ultraviolet-visible
VBE	valence band edge
V_{OC}	open-circuit voltage

continued on next page

Abbreviation	Description
XRD	X-ray diffraction

Chapter 1

Introduction

1.1 Motivations

In the past centuries, globalization and modern technologies emerge with better convenience and higher efficiency. Aside from those benefits, it leads to a monotonic increase in energy demand and an expectation of continuous growth in the future.[1,2] The main approach to the demand is almost solely depends on primary energy or non-renewable energy, such as petroleum, coal or natural gas. These energies all emit CO_2 under operation and have already caused a significant impact in the environment and climate.[3] Also, these energies rely on limited resources which will eventually be depleted in the near future. Therefore, the search for renewable and green energy sources is urgent and crucial issue for the current century.

Among the renewable energies, solar energy or photovoltaic energy is one of the most promising renewable energy with multiple advantages. One of the advantages is its low levelized cost making it one of the fastest growing source of renewable energy.[4,5] Also, the globally available solar energy is higher than the energy consumption even with the consideration of the practicality such as geographical limitation and the power conversion efficiency (PCE).[6] However, factors like production, maintenance, recycling and PCE are still challenging the application of photovoltaic energy.[7] In order to acquire the potential of solar energy and reduce the barrier of the energy transition, it is necessary to improve the current photovoltaic technology further.

Currently, the silicon based photovoltaic technology dominates the market due to its mature supply chain and the low difficulty in fabrication. However, its brittle, high cost and heavy

nature make it difficult to be applied to wider applications. Therefore, novel photovoltaic materials are vastly explored in order to overcome these issues. One of the novel materials is organic semiconductors which is flexible, light-weight and chemically tunable. These properties make the organic photovoltaics (OPVs) an ideal device in living environment such as indoor or mobile condition. Despite its sharply increasing PCE (∼18 %), OPVs still lag behind in the competition for efficiency.[8] Therefore, a systematic guideline in the molecular design rule for high PCE is necessary to push forward the current limit. An answer to this will enable OPVs to fill up the gap of the silicon photovoltaic markets.

Another promising photovoltaic system is the organic-inorganic hybrid perovskite solar cells (PSCs). Benefiting from low material and synthetic cost, printing compatible fabrication and well-matching bandgap, PSCs have a good potential to provide record-high PCE with a competitive cost. Moreover, its tunable bandgap makes it suitable to be combined with silicon based solar cells for a further boost in PCE. Although PSCs have already achieved a comparable PCE to the commercialized silicon based solar cells, their PCE and stability still require further improvements to complete the final step of commercialization.[9,10] An investigation over the existing materials and the loss mechanism with them is necessary here.

1.2 Aims

In this thesis, the aim is to investigate the energetics of perovskite and organic photovoltaic semiconductors and their impact on interfacial properties in devices. The study aims to pinpoint the key molecular design rules and interfacial energetic engineering conditions to enable high performance or targeted PSCs or OPVs.

OPVs have embraced a sharp performance improvement in recent years, but the approach was mainly based on trial and error. In this thesis, I aim to investigate a selection of critical OSCs and their OPV systems by advanced photoemission measurements. A novel density of state (DOS) conversion relationship is applied to accurately identify the energetic changes from photoemission spectroscopy measurements, and it is coupled to density functional theory (DFT) simulations to highlight the critical functional groups behind the high performance.

Interfacial passivation is widely applied in PSCs to increase device performance. However, some of the mechanisms are not yet fully understood or investigated. To unveil this, I

aim to explore two passivation techniques, namely dedoping transport layer and controlling dimensionality, with systematically changing the passivation levels. The mechanism is then identified by surface photovoltage (SPV) measurements and transient photoluminescence to unveil detailed charge distribution and their kinetics.

Chapter 2 shows the relevant fundamental theories of both perovskite and OSCs as well as their devices. It begins with the basic energetic properties in semiconductors, and the interfacial band bending between semiconductors. Then, OSC related opto-electronic properties, such as packing and charge generation, are reviewed with the latest development of high performance OPVs. For PSCs, an overview of the structural development and the challenge on the interfacial defects are presented with various existing surface engineering techniques.

Chapter 3 lists the methodology and operational information of the common experimental methods shared across chapters. Theoretical background and experimental proves of the DOS conversion from ambient photoemission spectroscopy (APS) is detailed with equation derivations.

Chapter 4 circles the key energetic properties of OSCs influenced by chemical structure, packing condition and blending. In the first section, the charge extraction measurement and APS show the low tail state density in Y6 which contributes to its high PCE and low V_{OC} loss. The unique low tail state character is then further correlated to the conformational rigidity of Y6 by DFT simulations, suggesting the molecule design guideline. Turning to the impact of packing structure, the energetics of sexithiophene show a significant dependence with the packing structure which provides the necessary energy offset for charge separation without the requirement of donor-acceptor blends. The understanding is then extended to solution-processed Y6 where a significant energetic shift is also observed. Its impact on device performance is shown by both planar heterojunction and bulk heterojunction devices. The molecular origin to the orientation-dependent energetic shift is correlated to the quadrupole moment by DFT simulations. Lastly, the recombination mechanisms in different polymer:fullerene blends are investigated and traced back to the change in density of state distribution upon blending. This chapter provides a deeper understanding in the correlation of molecular structures to their energetics and guidelines to harness this towards higher OPV performance.

Chapter 5 focuses on suppressing doping-induced interfacial recombination loss in p-i-n type PSCs by dedoping the highly doped PEDOT:PSS. The PEDOT:PSS is systematically dedoped up to 500 meV with aqueous NaOH, and then its thickness is optimized to compensate the reduced conductivity. A significant reduction of recombination losses at the dedoped PEDOT:PSS/perovskite interface is evidenced by a longer photoluminescence (PL) lifetime and higher magnitude of SPV, leading to an increased open-circuit voltage (V_{OC}), fill factor (FF), and PCE. The result provides a facile approach to improve cost-effective PEDOT:PSS based PSCs while giving insights into the relationship between doping level of hole transport layers (HTLs) and interfacial charge carrier recombination losses.

Chapter 6 explores the energetics of different n-number Ruddlesden-Popper phase (2D perovskite) and its impact on the perovskite/Spiro interface by tuning the passivation concentration. The low concentration passivation leads to pure $n = 1$ 2D perovskite while the high concentration solution also forms quasi-2D perovskite. In general, an extraction barrier from the deeper valence band edge (VBE) of all the 2D perovskite is identified in addition to the reduction in PbI_2 defect states. As a result, the SPV response gets smaller in the low concentration sample due to the inhibited ionic movement and the extraction barrier. However, the Spiro-OMeTAD on top has a higher doping level with the 2D perovskite blocking the dopant leaking, and as a result leading to higher V_{OC} and PCE. For the high concentration samples, the thick quasi-2D perovskite provides hole traps with its intermediate VBE between pure 2D and 3D perovskite and uneven topography, leading to unfavorable device performance with wider distribution. In short, the results unveil the SPV dynamics of passivated perovskite and suggest that a thin and pure $n = 1$ 2D perovskite layer between the 3D perovskite and HTL is critical for improving the device performance. Besides, the details of dopant blocking ability in 2D perovskite, such as what type of dopant is blocked and how the dopants are distributed, would worth further investigations in order to understand its long term impact in device performance.

Chapter 7 summarizes this thesis while showing a rigorous future work that could extend the research further.

Other relevant materials such as publication list (Appendix A), table of chemical abbreviation (Appendix B) and data analysis program (Appendix C) can be found in the

appendix.

References

[1]Z. M. Chen and G. Q. Chen, "An overview of energy consumption of the globalized world economy", Energy Policy, Sustainability of Biofuels **39**, 5920–5928 (2011).

[2]C. S. Mattick, E. Williams, and B. R. Allenby, "Energy and civilization: A history of energy production and consumption in a global cultural, technological and economic context", in 2009 IEEE International Symposium on Sustainable Systems and Technology (May 2009), pp. 1–6.

[3]S. Bilgen, "Structure and environmental impact of global energy consumption", Renewable and Sustainable Energy Reviews **38**, 890–902 (2014).

[4]S. Chu and A. Majumdar, "Opportunities and challenges for a sustainable energy future", Nature **488**, 294–303 (2012).

[5]K. Branker, M. J. M. Pathak, and J. M. Pearce, "A review of solar photovoltaic levelized cost of electricity", Renewable and Sustainable Energy Reviews **15**, 4470–4482 (2011).

[6]E. Dupont, R. Koppelaar, and H. Jeanmart, "Global available solar energy under physical and energy return on investment constraints", Applied Energy **257**, 113968 (2020).

[7]R. York and S. E. Bell, "Energy transitions or additions?: Why a transition from fossil fuels requires more than the growth of renewable energy", Energy Research & Social Science **51**, 40–43 (2019).

[8]*Best research cell efficiency chart. NREL.* (2023) `https://www.nrel.gov/pv/cell-efficiency.html`.

[9]F. Huang, M. Li, P. Siffalovic, G. Cao, and J. Tian, "From scalable solution fabrication of perovskite films towards commercialization of solar cells", Energy & Environmental Science **12**, 518–549 (2019).

[10]P. Wang, Y. Wu, B. Cai, Q. Ma, X. Zheng, and W.-H. Zhang, "Solution-Processable Perovskite Solar Cells toward Commercialization: Progress and Challenges", Advanced Functional Materials **29**, 1807661 (2019).

Chapter 2

Background Theory

In this chapter, a selection of the fundamental theories and current progresses are shown to assist the understanding of this work. It begins with the background of organic semiconductors (OSCs) and organic-inorganic hybrid perovskites. The organic part will cover the material development and few critical energetic points that are related to the organic photovoltaic (OPV) applications and organic transport layers. For the perovskite parts, a brief review of the material properties, including energetics, chemical components, crystal structures and dimensionality, are given. Then, the working principle of perovskite solar cells (PSCs) is shown together with current challenges and approaches.

2.1 Organic Semiconductors in Photovoltaic Applications

2.1.1 Background

Organic semiconductors (OSCs) are a class of semiconducting materials that exploit the delocalized conjugated π bonds to facilitate their semiconducting properties. In general, OSCs can be categorized into two groups, polymers and small molecules, based on their molecular weight. Following from the concept of extending the conjugation backbone, polymer type OSCs facilitates the long conjugation backbone by repeating their sub-units to achieve semiconducting properties. According to the types of the sub-units, polymer OSCs can be either homopolymer (one repeating unit) or copolymer (more than one repeating unit). The sub-units of the copolymer OSCs are usually categorized into donor or acceptor units based

on their electron deficiency. With the large degree of freedom from the backbone, polymer OSCs can adopt into various morphology or crystal structure, and thus the morphology is usually amorphous with weak inter-molecular interaction. As a result, they are ideal to be solution-processed.[1,2] In the other hand, small molecular OSCs are usually composed of conjugated rings to facilitate the semiconducting properties. Different from polymer OSCs, the small molecular OSCs have the advantage of precision in chemical structure and are more reproducible with monodisperse nature.[3] Furthermore, their small molecular weight allows them to be evaporated with fine-tuned packing structures.[4,5] The complementary nature of polymer and small molecular OSCs makes them indispensable in photovoltaic applications.

Electronic Structures and Charge Carriers

As one of the semiconductors, the energetic structure of the OSCs shares the fundamental properties of semiconductors and can be described by band theory. In band theory, the accumulated energy levels of the material form electronic bands which may be filled by the electrons. For semiconductors, the bands are not continuous across the energy spectrum, but leaving an empty energy range without bands, also known as electronic band gap E_g, in the energy spectrum. By definition, the energy band that lies in the deep energy range is typically filled by electrons and is named as valence band while the shallower energy band has no electrons and is named as the conduction band. The two energy states that are the closest to the band gap are deterministic for the electronic properties and are usually named as either valence band edge (VBE) or conduction band edge (CBE). For organic materials, where the fundamental energetic unit is approximately a molecule, ignoring intermolecular interactions or regarding intermolecular interactions to be weak, and thus another widespread model based on frontier orbitals are applied to describe the energetic landscape instead of band theory.[6] Here, the most relevant energy levels become the highest occupied molecular orbital (HOMO) and the lowest unoccupied molecular orbital (LUMO), which can be related to VBE and CBE respectively when forming solid state films. In this thesis, both HOMO and LUMO are used for OSCs as interchangeable synonyms of VBE and CBE respectively. In practice, there is a chance to have defects in materials, such as crystal defects in inorganics, packing disorder, chemical impurities in organics etc., that may form a small amount of electronic states inside

the E_g. Depending on their energy level, the defect states can further be categorized as shallow traps (near electronic bands) or deep traps (middle of the E_g). In summary, an energy band diagram of semiconductor is shown in Fig. 2.1.

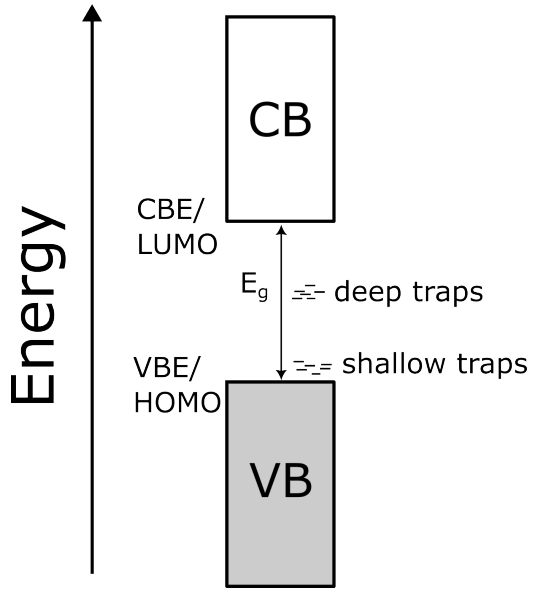


Figure 2.1: Energy band diagram of semiconductor with a band gap (E_g). The valence band is denoted as VB while the conduction band is denoted as CB. The closest energy states near the E_g are the valence band edge/highest occupied molecular orbital (VBE/HOMO) and the conduction band edge/lowest unoccupied molecular orbital (CBE/LUMO). Both shallow traps and deep traps are illustrated by the black bars.

For OSCs, the electronic states around the E_g are dominated by the delocalized π bonds. These bonds are formed by the overlapping unhybridized p_z atomic orbitals from the sp^2 hybridized atoms, typically atoms from group 15, 16 and 17.[7] The overlapping of p_z atomic orbitals lead to two molecular orbitals (MOs), a filled bonding π orbital and an unfilled antibonding orbital, and thus the energy difference between the two MOs defines the E_g. By extending the conjugation length, for example extending ethylene into 1,3-butadiene (Fig. 2.2a), more p_z orbitals are involved, and thus the E_g will reduce. Intuitively, for polymer OSCs, this phenomenon would continue with more and more conjugated atoms involved until the E_g reduces to zero, and the material eventually becomes metallic with a continuous energy spectrum. However, in real situation, the linear delocalized system would not have perfectly uniformed conjugated bond length but rather forms an alternating single-double-bond system.[8] This phenomenon is known as Peierls transition or Peierls distortion where the system reaches a lower energy state by a distorted periodic system (Fig. 2.2b). In general, the E_g is typically around 1 eV to 4 eV for OSCs.[9]

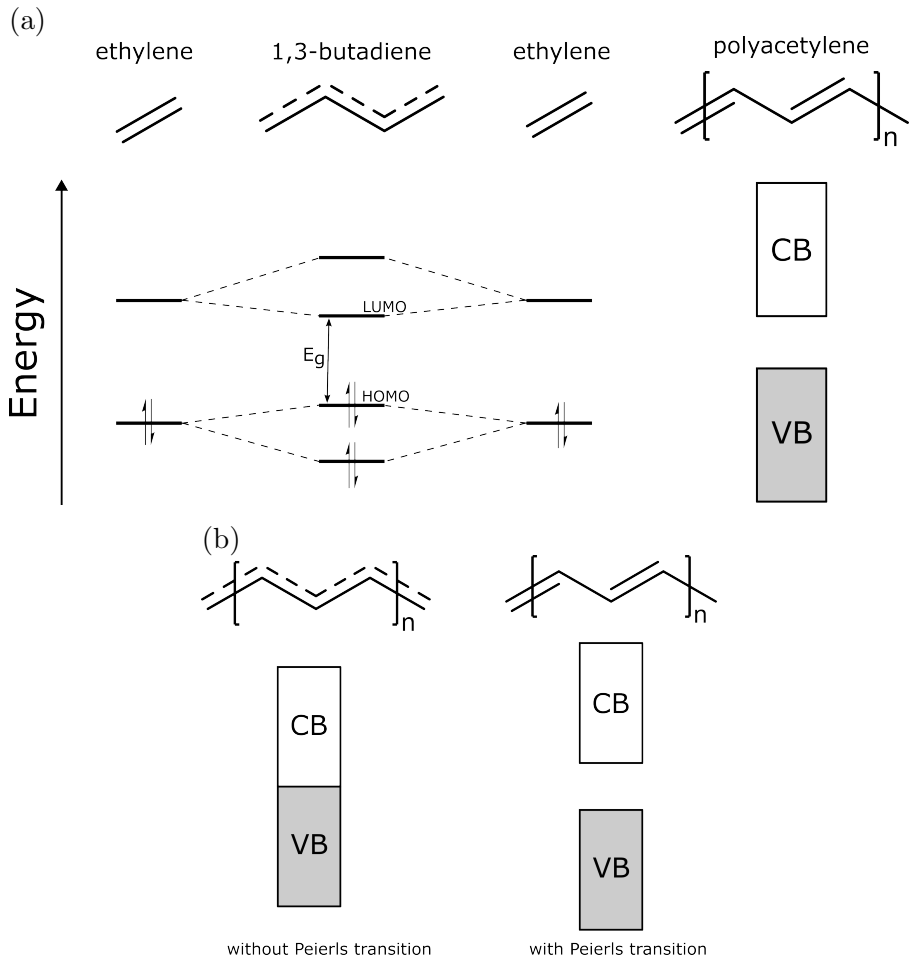


Figure 2.2: The effect of conjugation extension and Peierls transition in conjugated organic semiconductors (OSCs). (a) A conjugation extension example of two ethylene combined into 1,3−butadiene with the highest occupied molecular orbital (HOMO), the lowest unoccupied molecular orbital (LUMO) and the band gap (E_g). The right most panel shows the conduction band (CB) and valence band (VB) of polyacetylene. (b) The band structure of OSCs without Peierls transition (left) and with Peierls transition (right).

Since electrons are Fermions, the electron distribution can be described by Fermi-Dirac statistic. The average electron occupation n can be described by the Fermi function:

$$n(E) = \frac{1}{e^{(E-E_F)/k_BT} + 1}, \tag{2.1}$$

where E is the energy of the state, E_F is the Fermi energy, k_B is the Boltzmann constant and T is the absolute temperature. The distribution function monotonically decays from unity to zero when E increases, following Pauli exclusion principle. Therefore, the average number of electron per unit energy N can be expressed as

$$N = n(E) \times DOS(E), \tag{2.2}$$

where $DOS(E)$ is the quasi-continuum electron density of state (DOS) or MOs for OSCs. Note that E_F is a characteristic point where the average occupation is exactly 0.5 independent from T, making it a useful conceptual reference point. For an ideal OSC, the electrons have exactly the number to fill up to the HOMO level, and therefore the E_F should be located exactly in the middle of the E_g. In this case, the material is considered intrinsic as it does not have excess holes or electrons. Typically, intrinsic semiconductors have very low amount of free charge carriers with the sharp decay from the Fermi function (Eq. (2.1)), resulting in low conductivity.[10] When E_F lies closer to either the HOMO level or the LUMO level, the material would be considered as p-type or n-type semiconductors respectively based on the type of major charge carrier. With more available charge carriers, the conductivity of both p-type and n-type semiconductors is higher than the same material in intrinsic electronic condition.

To modulate the electronic or optoelectronic properties, doping in semiconductors is typically used to shift the E_F.[10–12] It is typically done by adding dopants to extract or give electrons into the system. For OSCs, there are a range of n-type or p-type dopants, such as F4TCNQ and LiTFSi (see Appendix B for full chemical names).[13,14] The doped OSCs are either positively or negatively charged with excess holes or electrons on the conjugation bonds. Due to the spin of unpaired electron, the relevant MOs, either HOMO or LUMO, will split into singly occupied/unoccupied MOs (SOMOs/SUMOs) to minimize the overall energy and reduce the E_g (Fig. 2.3).[15] Furthermore, the electric field of the charges will distort the molecules to screen the electric field by forming polarons leading to an energy minimization.[16,17] Due to the low dielectric constants and weak inter-molecular interactions, the polarons in the OSCs are not able to move freely but rather by hopping between molecules.[18–20] Thus, the conductivity of the OSCs are typically in orders of magnitude lower than inorganic semiconductors.

Optoelectronic Processes

When OSCs are illuminated by photons with sufficient energy, electrons reside in the VB will be promoted into the CB. As seen in Fig. 2.1, the photon energy, E_{photon}, for the photoexcitation intuitively should be no less than the band gap in neutral state ($E_{photon} \geq E_g$). However, due to the low dielectric constant, the photoexcited electron and hole pairs in OSCs are tightly bound by the Coulomb interaction and form excitons with a smaller band gap (Fig. 2.3).[21,22] Thus, the

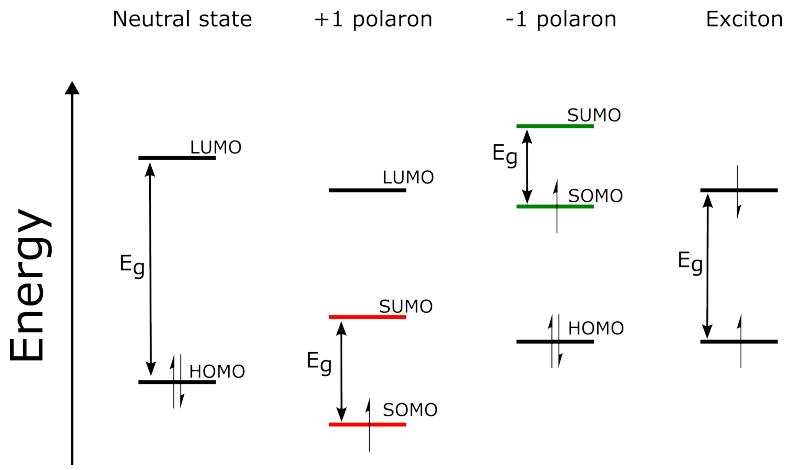


Figure 2.3: Energy diagrams of neutral, positive/negative polaron and exciton. For positive polaron state, the HOMO splits into singly occupied molecular orbital (SOMO) and singly unoccupied molecular orbital (SUMO) colored in red and vice versa for the negative polaron states colored in green. For both polaron and exciton states, the band gap (E_g) becomes smaller than in the neutral state.

optical band gap is about 0.2 eV to 1.4 eV smaller than the electronic band gap.[23] The tightly bound excitons in OSCs are much more localized and regarded as Frenkel excitons compared to Wannier-Mott excitons in inorganic semiconductors.[24,25] This type of excitons also has a much shorter exciton diffusion length (5 nm to 10 nm) due to the strong binding energy, making them harder to be utilized.[26,27] With sufficient driving force, such as energy offset between the HOMO/LUMO levels of molecules or thermal energy, these excitons may undergo partial charge separation into intermediate charge-transfer (CT) state, which is still locally bound by Coulomb interactions.[28] Further dissociation of CT states leads to full charge separation into polarons where the charge is only coupled with lattice distortion without Coulomb interactions.[29] The process from photon absorption to charge separation is shown in Fig. 2.4.

After photoexcitation, the photoexcited species may be recombined depending on their types (Fig. 2.4). The exciton decay may happen even before the charges are separated.[21,30] This process is typically within the time scale of femtoseconds by the proximity and strong binding energy. When excitons partially dissociated into CT states, geminate recombination may happen within the time scale of picoseconds.[31,32] This is a common recombination loss mechanism on the material interfaces where the holes and electrons are partially separated by the energy offset. Even though free charge species are formed, they may still reach each other and recombine during the process of charge extraction. This type of recombination is called non-geminate recombination and is correlated to the dielectric constant of the material.[33,34]

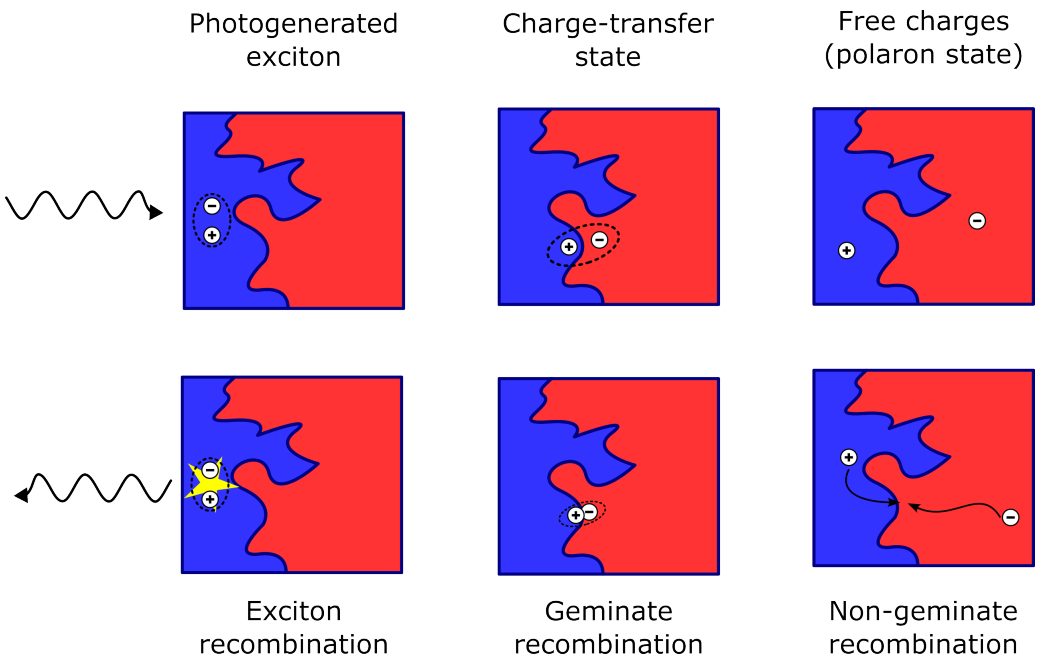


Figure 2.4: Optoelectronic processes: charge generation and recombination. Top panels are charge generation processes: exciton state (left), charge-transfer (CT) state (middle) and polaron state (right). Bottom panels are recombination processes: exciton recombination (left), geminate recombination (middle) and non-geminate recombination (right). The Coulombic binding is shown by the dash circles, and the photons are shown by the wiggly lines.

For OSCs, their polaron diffusion length is much shorter than the Coulomb capture radius, making the polarons nearly always recombine when they meat.[35] In this situation, the non-geminate recombination can be described by Langevin recombination model, and it is one of the crucial loss mechanism in OPVs.[36,37] There are few example systems exhibiting non-Langevin recombination which makes them usually performing better with lower recombination rate.[38] The origin of non-Langevin recombination in PDTSiTTz is shown in Section 4.5. Lastly, the trap states within the E_g can serve as recombination sites where the free charge carriers may be trapped and recombined.[39,40] Therefore, understanding and controlling the trap or defect states are the keys to high performance devices.

2.1.2 Organic Transport Layer

Photovoltaic systems usually are composed of two major parts: the photoactive layer where the photons are converted into free charges and the transport layer or blocking layer which assist the free charges to be extracted (see an example device structure in Fig. 2.5). The advantages of OSCs in versatile chemical design freedom, tunable energetics, flexable nature, and solution-processes enable them to be applied into both functions. Here, the essential properties related

to these specific functions are detailed below.

The various advantages of OSCs enable it to be charge transport layer in different types of photovoltaic systems, such as PSCs and OPVs.[41–44] As a transport layer, the OSCs are tailored to have a matching energy level for efficient and low energy loss extraction process.[21] When interfaces of semiconductors form, the electrons from the shallower E_F semiconductor will flow into the deeper one until their E_F aligns and reaches equilibrium. This phenomenon is known as Fermi level alignment or Fermi level pinning. This leaves a space charge region on the interface where the charge carriers are depleted. Within the depletion region, the imbalanced charges lead to an electric field which bends the band structure on the interface. According to the bending direction, charges may experience the electric field which interfere the extraction process. In some cases, it is shown that the band bending is shown to play an important role in assisting charge extraction process.[45,46] Besides band bending, the low conductivity as mentioned in Section 2.1.1 can lead to charge accumulation on the interface where the free charges may be lost through interfacial recombination.[47] This is a significant issue when the organic hole transport layer (HTL) is applied into PSCs as perovskite has at least three to four orders of magnitude larger hole mobility ($1\,\mathrm{cm^2V^{-1}s^{-1}}$ to $5\,\mathrm{cm^2V^{-1}s^{-1}}$).[48,49]

In order to increase the conductivity, dopants are used to increasing the number of charge carriers. For example, the organic hole transport layers (HTLs) in PSCs are commonly doped by LiTFSi, 4TBP or F4TCNQ to have a deeper HOMO level or E_F matching the photoactive perovskite layer.[50–52] Nonetheless, dopants can lead to problems such as interfacial traps, morphological change, material degradation and dopant segregation, leading to short or long term issues.[53–56] An investigation on the interfacial recombination loss of PSCs with highly doped PEDOT:PSS is discussed in Chapter 5.

2.1.3 Organic Photovoltaics: specificity and challenges

In OPVs, OSCs are used as the main photoactive layer, where the photons are converted into free charges. As mentioned in Section 2.1.1, the absorbed photon will generate tightly bound electron and hole pairs, known as excitons. Therefore, single component OPVs were predicted to have very low power conversion efficiency (PCE).[57] In order to separate excitons into free charges, an energy offset would be necessary to proceed the separation process.[58,59]

This is typically achieved by blending an electron donor and an acceptor which have an energy difference between their HOMO levels and LUMO levels. Typically, donors have shallower LUMO levels while acceptors have deeper HOMO levels, so that the charge carriers may be separated on the interface. Apart from the charge separation issue, OPVs also suffer from its slow charge mobility which limits the charge extraction process while increases the probability of charge recombination. In order to shorten the extraction route and increase the donor-acceptor interface, the photoactive layer is usually made into a bulk heterojunction (BHJ) where the donor and acceptor are finely mixed.[60] In the last few years, the PCE of OPVs have been dramatically improved to over 18 %.[61,62] This is based on the non-fullerene accpetors (NFAs) which has various advantages in improving the loss mechanisms, such as efficient charge separation and complimentary absorption.[63,64]

Electrical properties of Photovoltaics

To characterize the performance of a solar cell, current density-voltage (J-V) measurements are typically carried out. In dark, the photovoltaic device exhibits diodic behavior with a preferential injection direction governed by the transport layers.[65] Under illumination, usually the standard is 1 sun or AM 1.5, photovoltaic devices will generate free charges and result in a J-V curve as shown in Fig. 2.5. The current density J can be expressed as

$$J = J_0 \left(e^{\frac{qV}{nk_BT}} - 1 \right) - J_{ph}, \tag{2.3}$$

where J_ph is the photocurrent density under illumination, J_0 is the reverse saturation current density, q is the unit charge, V is the voltage, n is the ideality factor, k_B is the Boltzmann constant and T is the temperature. Usually, the ideality factor of photovoltaics is larger than 1 and is correlated to the recombination process inside.

There are few indicative parameters that are useful to convey the device performance. When the device is operated under a short-circuit condition without applying voltage, the photogenerated charges are all extracted and recombined in the circuit. The current density at this point is named as the short-circuit current density (J_{SC}). When the photovoltaic device has some defects, such as pin-holes or leakage from the transport layer, some of the charges may recombine within the solar cell system instead of being extracted and recombined in the

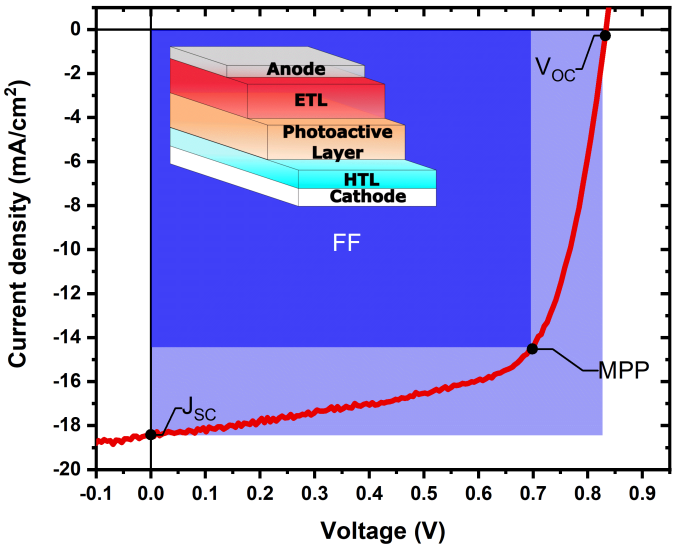


Figure 2.5: An example of photovoltaic architecture and current density-voltage (J-V) curve. The notations are short-circuit current (J_{SC}), open-circuit voltage (V_{OC}), maximum power point (MPP), fill factor (FF), electron transport layer (ETL) and hole transport layer (HTL). The FF is the area ratio between the light purple area to the deep blue area.

circuit. As a result, the J-V curve around the J_{SC} point will have a linear voltage dependency, and the inverse of the slope is a good approximation to its shunt resistance (R_{sh}).[66,67] As its name, the R_{sh} is to describe the parasitic short circuit within the system, and therefore ideal photovoltaics should have a nearly infinite R_{sh}. When the device is operated in an open-circuit condition, the separated free charges will build up in the system until the charge generation rate equals to the recombination rate. Therefore, the open-circuit voltage (V_{OC}) is related to charge recombination, and the V_{OC} loss, difference between theoretical limit to experimental value, can be used to understand the recombination loss.[68,69] The inverse slope near V_{OC} point is used to approximate the series resistance (R_s) which describes the resistance of current passing through the system. In idea solar cells, R_s should be close to zero.[70] The output energy density of a solar cell is the multiplication of the voltage and the current density. Therefore, the maximum power point (MPP) is located between the V_{OC} and the J_{SC} with the largest rectangular area to both x-axis and y -axis. To describe the overall non-ideal behavior, fill factor (FF) is introduced as

$$FF = \frac{V_{OC} J_{SC}}{V_{MPP} J_{MPP}}, \tag{2.4}$$

where the V_{MPP} and J_{MPP} are the voltage and current density at the MPP point. Lastly, the

power conversion efficiency (PCE) can be expressed as

$$PCE = \frac{P_{max}}{P_{in}} = \frac{V_{\mathrm{OC}} J_{\mathrm{SC}} FF}{P_{in}}, \tag{2.5}$$

where P_{max} is the maximum output energy density, P_{in} is the input photon energy density.

Loss Mechanisms in OPVs

There are many loss mechanisms in OPVs that are challenging the advancement of their PCE. As indicated in Section 2.1.1, many types of recombination mechanisms can happen before the extraction of free charges. Firstly, the short lifetime of Frankel excitons limits their probability to diffuse to the donor/acceptor interface where charge transfer could happen. To tackle this, finely mixed BHJ architecture is applied for OPVs to maximize the donor/acceptor interface despite it may also introduce to non-percolated domains.[71] Once the charge transfer occurs, radiative or non-radiative geminate recombination can still quench the CT state. This will reduce the efficiency of charge generation and thus lower the J_{SC}. Usually, by increasing the energy offset between donor and acceptor, the efficient transition from CT state into polarons would reduce this recombination loss.[72,73] Lastly, the free charges may still undergo non-geminate recombination or Langevin recombination. The morphology highly determines this type of recombination, and there are studies showing that BHJ architecture could reduce the recombination rate.[74]

Apart from direct recombinations between charges residing in frontier molecular orbitals, trap-assisted recombination loss may happen. The traps are typically classified as two types: the deep traps, orginated from impurities, dopants, crystal defects or degradation species, and the shallow traps or tail states, the protruding energy states close to the HOMO or LUMO levels.[39,75] For deep traps, free charges may be localized inside them with a preferential energy reduction. These trapped charges would require more energy to be reactivated while they may also recombine with other free charges through Shockley-Read-Hall recombination.[76] OPVs are prone to shallow traps based on their soft and disordered nature from solution processing.[77] These states slow down the charge extraction and result in increased recombination losses.[78,79] In particular, the DOS distribution at the band edge of NFAs and its origin have been demonstrated as a crucial factor to control recombination mechanisms, as a broader DOS

results in voltage loss by carrier relaxation at the energy minima.[80] A clear example of this is illustrated in Section 4.2, where structural rigidity reducing energetic disorder in Y6 enhancing its OPV performance.

Besides the recombination loss, the energy loss from the energy offset between donor and acceptor is one of the critical point. Based on some theoretical models and measurements, the necessary energy offset for charge transfer is found to be at least >0.3 eV.[59,81] However, the recent year NFA development has shown highly efficient charge dissociation with a much smaller energy offset (∼0.15 eV).[82] Although the origin is still under debate, there are few proposed possibilities, such as long exciton lifetime, low non-radiative recombination or exciton-CT hybridization.[29,83,84] These characters may be related to their acceptor-donor-acceptor (A-D-A) structure with linear or flat two-dimensional backbone and high quadrupole moment, such that the energetics depends on the relative molecular orientation (see Section 4.4).[85–87]

Molecular Packing and Morphology

The soft nature of OSCs allows them to be adapted into different packing structure or orientations depend on the preparation procedures, and it leads to morphological or energetic changes that has a strong impact in device performance. For π conjugated aromatic rings in OSCs, the molecules commonly exhibit a preference in a face-to-face stacking structure, and is usually referred as π-π stacking.[88] Despite its controversial origin, this packing structure allows the molecule to have not only strong inter-molecular MO overlapping, which delocalizes the electronic states in highly crystalline domains, but also shifting the energetic environment by the build up electrostatic field.[89,90] One of the main ways to control the packing structure is by evaporating small molecules under different evaporation speed, temperature or bottom substrates.[91] By exploiting this technique, Duhm et al. showed that a significant energy level shift by 0.4 eV between standing and lying oriented crystalline α-6T.[92] Theoretical simulations show that this is possibly due to the large quadrupole moment along the π-π stacking direction which creates an electric field around the grain boundaries.[93] Such a dramatic shift would be important for the charge separation which highly depends on the interfacial energetics. An investigation on utilizing the packing structure and free charge generation is shown in Section 4.3.

Besides finely controlled evaporation deposition, solution-processed small molecules can also be influenced in their orientation and degree of π-π stacking. In particular, this has been demonstrated by utilizing different solvents and additives as well as by post-deposition annealing.[94,95] This morphology control is crucial to optimize exciton diffusion and charge transport and minimize loss pathways,[96] while molecular arrangement at NFA/donor interface plays an important role in CT-state separation. As will be illustrated in details in Section 4.4, the orientation and packing morphology of NFAs has also a strong effect of energy levels of materials. Here, the strong electrostatic field from the A-D-A or A-D-A'-D-A structures plays an important role, determining different energetics for face-on versus edge-on orientations.

2.2 Hybrid Perovskites in Photovoltaic Applications

2.2.1 Background

Perovskite crystals are a group of minerals which share the same crystal structure of calcium titanium oxide ($CaTiO_3$) or perovskite.[97] Although the phrase perovskite was specifically assigned to $CaTiO_3$, now the term "perovskite" is generalized and used for other perovskite crystals as well. A general formula of perovskite is ABX_3, where A, B are cations and X is an anion. By substituting the composition, perovskites can incorporate organic cations (e.g. methylammonium cation (MA^+), formamidinium cation (FA^+)) at A-side, metal ions (e.g. Pb^{2+}, Sn^{2+}) at B-site and halide anion (e.g. $I-$,Br^-) at X-cite to form organic-inorganic hybrid perovskite. A methylammonium lead iodide (MAPI) example of hybrid perovskite is shown in Fig. 2.6 with four octahedrons composed of ${PbI_6}^{4-}$ circling the MA^+.

Hybrid perovskites have many unique optoelectronic properties making them promising materials for optoelectronic applications, such as light emitting diodes, photovoltaics or photodetectors.[99–101] As hybrid perovskites have many choices of ions to substitute with, their band gap is adaptable by compositional engineering. For example, by varying the ratio of iodide and bromide anions at the X-site, the optical band gap can be tuned from 1.6 eV to 2.3 eV.[102] This allows perovskites to be finely tailored for the optimal absorption to match specific applications. Besides, perovskites have high absorption coefficients ($10^4\,cm^{-1}$ to $10^5\,cm^{-1}$) with direct band gap transition that enable thin films to perform efficiently.[103] Unlike

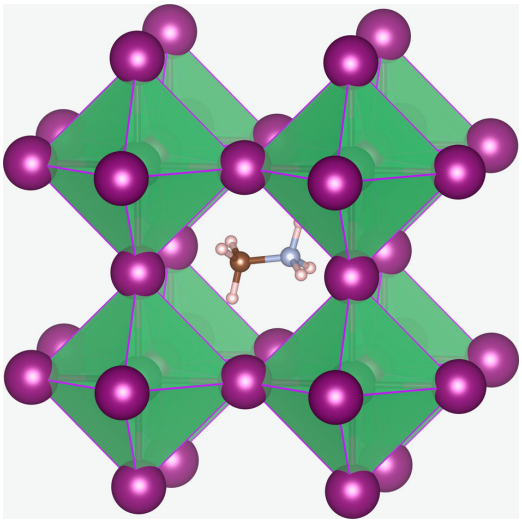


Figure 2.6: A schematic illustration of methylammonium lead iodide (MAPI) perovskite (adapted from Eames et al. [98]). There are four green octahedrons, composed of one Pb^{2+} core and six I^-, surrounding the methylammonium cation (MA^+).

OSCs, perovskite has a low exciton binding energy. For iodide based perovskite, the binding energy is only about $\sim$10 meV at room temperature.[104,105] Therefore, photoexcited charge pairs are intrinsically free and do not require an extra driving force for separation. Lastly, perovskites have an ambipolar character with high mobility ($1\,cm^2V^{-1}s^{-1}$ to $50\,cm^2V^{-1}s^{-1}$) for both electrons and holes.[106] As a result, the charges are able to be efficiently extracted or injected with low recombination losses.

Apart from the optoelectronic properties, perovskites also benefits from vastly improved solution processing. One of the most successful preparation procedure is achieved by coating the stoichiometric solution precursor with antisolvent treatment during the crystallization process.[107] As the antisolvent does not dissolve the solutes, such as PbI_2, it reduces the solubility and forces a fast and uniform crystallization to take place. This procedure improves the quality of solution-processed perovskite and was accounted as a major breakthrough for PSCs.[108] The realization of solution processing also relies on the defect tolerance of perovskite under vacancies.[109] The tolerance allows the existence of some crystal vacancies without altering its electronic properties. Also, the high formation energy in deep traps minimizes trap related loss mechanisms.[110] These advantages make perovskites one of the most studied optoelectronic materials.

2.2.2 Ruddlesden-Popper Phase/2D Perovskite

Ruddlesden-Popper phase is a (quasi-)two-dimensional perovskite like crystal with a chemical composition of $A_{n-1}A'_2B_nX_{3n+1}$ where A' is a bulky cation located between each perovskite layer and n is the number of octahedral layers (Fig. 2.7). When $n = 1$, the 2D perovskite is effectively one layer perovskite thin separated by the A' bulky cation. Therefore, it is also known as the pure 2D perovskite. As the n number increases ($n > 1$), the crystal turns into quasi-2D perovskite and approaches to 3D perovskite (unless specified the phrase "perovskite" reserves for 3D perovskite described in Section 2.2.1) once $n \to \infty$. As its structure similar to perovskite, Ruddlesden-Popper phase is sometimes addressed as 2D perovskite for convenience.[111] In optoelectronic applications, the A' cation is typically larger organic cations, such as phenethylammonium or n-butylammonium cations, while keeping the other ions the same in 3D perovskite.[112,113]

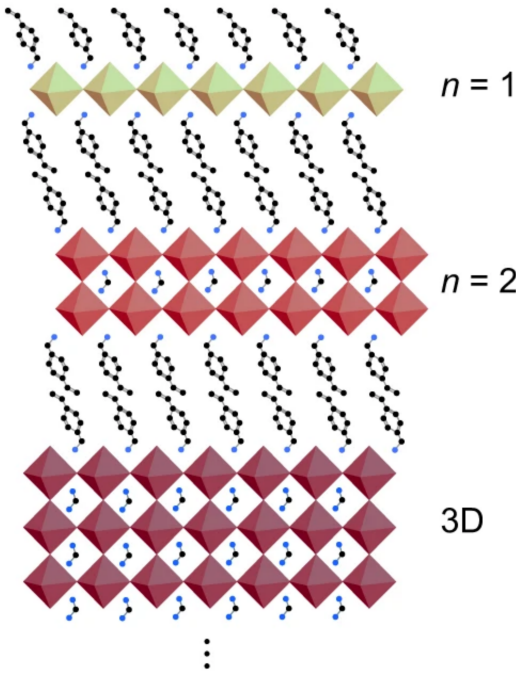


Figure 2.7: A schematic illustration of Ruddlesden-Popper phase 2D perovskite with $n = 1, 2, \infty$ (adapted from Proppe et al. [114]).

Although 2D perovskites have similar advantages as perovskites do, such as facile solution processing and tunable E_g, the low-dimensional structure results in some unique optoelectronic properties.[115,116] 2D perovskites have its E_g depending on the n number. Due to quantum confinement, the E_g of 2D perovskites increases with decreasing n number.[117] Also, the physical constrain reduces the free space for charge species to be separated, and thus the exciton binding

energy is much larger than perovskite (200 meV to 400 meV).[118] In addition to these advantages, its better stability makes it desirable for optoelectronic applications.[119] Unlike 3D perovskites, 2D perovskites are known to be much more inert to moisture, strong light and heat, making it a good candidate to strengthen the device durability.[120] This is due to the fact that 2D perovskites exhibit higher formation energy by the reduction of n number.[121] Therefore, 2D perovskite is widely applied into PSCs as an additive to passivate grain boundaries or as a surface treatment to introduce a buffer layer beteween the photoactive layer and the charge transport layer.[122] However, the morphology, energetic alignment and dimensionality of 2D perovskite in PSCs are not yet fully investigated. The impact of interfacial phenethylammonium-based 2D perovskite and dimensionality is investigated in Chapter 6.

2.2.3 Perovskite Solar Cells: specificity and challenges

In the past decades, PSCs have become one of the most-promising next-generation solar cell technologies with sharply increasing PCE of up to 25.7 % together with improved operational lifetimes (∼1000 h).[62,123] These advancements are attributed to improvements in compositional engineering, deposition technique, device architecture and development of transport materials.[41,124] The state-of-the-art PSCs are made of mixed ion perovskites in planar structure similar to typical planar solar cell structure illustrated in Section 2.1.3.[125,126] Thus, they share similar working principle; the photoactive layer generates free charges which are transported out through both ETLs and HTLs accordingly. By convention, PSCs can be categorized into two types: p-i-n (cathode/HTL/photoactive layer/ETL/anode also known as inverted structure) or n-i-p (also known as conventional structure). For inverted structure, the HTLs are typically polymeric OSCs, such as PEDOT:PSS or poly(triarylamine), and the ETLs are fullerene based acceptors, such as PCBM or fullerne.[127] On the other hand, conventional structure PSCs usually uses inorganic materials (eg. TiO_2, SnO) as the ETLs while using OSCs for the HTLs (eg. Spiro-OMeTAD, poly(triarylamine)).[128]

PSCs are still having few challenges in either performance or commercialization. Although perovskites have the unique deep trap tolerance character as mentioned in Section 2.2.1, shallow traps and surface deep traps still exist and contributes to significant non-radiative recombination losses and V_{OC} loss.[129] Studies showed that the trap states are predominantly

located on the interface between transport layers, particularly the HTLs.[130] Therefore, it is indispensable to tackle the trap states on the interface in order to achieve high performance PSCs. Two major approaches include tuning the energetics of the organic HTL for better alignment as well as charge mobility, and interfacial passivation.[131,132] The background of these two approaches will be detailed in Section 2.2.3. This is also applied in the main research in Chapter 5, showing the effect of tuning HTL energetics for better energetic alignment to the photoactive perovskite layer.

In addition to interfacial traps, hybrid perovskites are highly sensitive to moisture, oxygen, heat and light.[133–135] These factors trigger the degradation process of perovskites and dramatically reduce the stability and durability. Some of these factors such as moisture and oxygens are typically coming from the adjacent transport layers which typically composed of hygroscopic dopants (eg. LiTFSi).[136] Few approaches are demonstrated to effectively extend the device stability, including using mixed ion perovskites, 2D perovskites or dopant free charge transport materials.[137,138] Mixed ion perovskites and 2D perovskites are more resistance to degradation processes due to their larger formation energy. 2D perovskites are also used as a thin interlayer to remove the direct contact with charge transport materials.[139] The role of 2D perovskite in Spiro-OMeTAD based PSCs will be illustrated in Chapter 6.

Organic Hole Transport Layers

As elucidated above, charge transport layers and their development play an important role in PSCs, as they govern charge extraction and can contribute toward device degradation.[41,140–142] Particularly, organic HTLs have been shown to be critical in determining both the PCE and the lifetime of PSCs.[140,143] Since organic HTLs have lower hole mobilities compared to the photoactive perovskites, this mobility mismatch in most cases results in charge accumulation at the interface between perovskite and HTL, eventually leading to undesired recombination losses.[45,144,145]

One of the most common strategy is to add p-type dopants (eg. LiTFSi, F4TCNQ or FK209) to the HTL.[125,132] These dopants deepen the E_F of the HTL and, therefore, can create a favorable interfacial energetic alignment, which reduces the energy loss at the interface between the perovskite and HTL.[146–148] Importantly, p-type dopants increase the conductivity

of the HTL, which can improve the fill factor (FF) of the devices via more-efficient charge extraction.[149–152] Despite the success of utilizing dopants in the HTL, some undesirable effects are also introduced with doping. One of the issues is the device instability caused by dopant dissociation and the hygroscopic nature of some dopants such as LiTFSi.[153,154] Another significant effect of doping the HTL is stronger recombination loss at the interface. T. Du et al. has shown that the high density of holes in the highly p-doped PEDOT:PSS can non-radiatively recombine with the photoexcited electrons in the perovskite layer.[45] Therefore, many studies are focusing on developing organic HTLs with better matching energetics and faster hole mobility without the requirement of dopants.[138] However, these materials are generally complicate and expensive, and thus not ideal for commercialization. On the other hand, dedoping the existing HTLs still remain unclear, and it can provide a wider potential to the existing HTLs. Here, a systematic non-radiative recombination study on dedoping the originally highly doped PEDOT:PSS is shown in Chapter 5.

Surface Passivation

The presence of trap states is another key issue to achieve high performance PSCs since they can significantly reduce device performance, namely V_{OC}, by acting as recombination sites. Although trap states can exist both in the bulk or on the interface, many studies have shown that the major trap related recombination happens on the interface between perovskites and charge transport layers.[155,156] In order to minimize the interfacial trap states, surface passivation is one of the most studied approaches to this issue. In general, surface passivation exploits either coordinate chemicals (eg. Lewis acid or Lewis base) or ionic bonding materials (eg. phenethylammonium iodide (PEAI) or n-butylammonium iodide) to pair with the non-stoichiometic perovskite precursors.[131] In addition, surface passivation also reduces the ionic movement in perovskite which is accounted for the notorious hysteresis and degradation.[157,158] These benefits make surface passivation one of the indispensable technique in high performance PSCs.

Among different passivation materials, a group of bulky organic cations, such as phenethylammonium ions and n-butylammonium ions, are heavily studied due to their excellent performance in improving the V_{OC} loss from trap related recombination.[122] When

these bulky cations are used in surface passivation, they do not only passivate the trap states but also converts the existing 3D perovskites into 2D perovskites. As 2D perovskites have a much more stable chemical nature, this approach also gives the advantage of excellent device stability with the higher formation energy.[159,160] Moreover, the long hydrophobic organic chain in passivating ions can act as a protecting layer repelling oxygen and moisture to have direct contact with the underneath photoactive 3D perovskite.[161] Passivating 2D perovskite on the interface also exhibits a more prominent PL intensity and longer PL lifetime due to a reduction in non-radiative recombination between grain boundaries.[162] As 2D perovskite typically has a wider E_g, it forms a type-I band alignment which is beneficial in reducing interfacial recombination.[162] However, type-I alignment will also create an extraction barrier with a shallower CBE and deeper VBE. Although this issue can be tuned by the dimensionality of 2D perovskites to minimize the extraction barrier on the interface, studies on tuning the dimensionality on the interface is still not fully understood. Also, by introducing 2D perovskite as an interlayer, 3D perovskite no longer has the direct contact with the charge transport layer which was well established to be efficient for charge generation by energetic alignment. The relationship between 2D perovskite and the charge transport layer is crucial to be understood and optimized for maximum performance. Here, an investigation in the dimensionality of 2D perovskite heterostructure PSCs is shown in Chapter 6.

References

[1]X. Guo, A. Facchetti, and T. J. Marks, "Imide- and Amide-Functionalized Polymer Semiconductors", Chemical Reviews **114**, 8943–9021 (2014).

[2]A. Pron and P. Rannou, "Processible conjugated polymers: from organic semiconductors to organic metals and superconductors", Progress in Polymer Science **27**, 135–190 (2002).

[3]A. Mishra and P. Bäuerle, "Small Molecule Organic Semiconductors on the Move: Promises for Future Solar Energy Technology", Angewandte Chemie International Edition **51**, 2020–2067 (2012).

[4]T. Takahashi, S. Tamura, Y. Akiyama, T. Kadoya, T. Kawamoto, and T. Mori, "Organic Field-Effect Transistors Based on Small-Molecule Organic Semiconductors Evaporated under Low Vacuum", Applied Physics Express **5**, 061601 (2012).

[5]Z. Zhou, Q. Wu, R. Cheng, H. Zhang, S. Wang, M. Chen, M. Xie, P. K. L. Chan, M. Grätzel, and S.-P. Feng, "Orientation-Engineered Small-Molecule Semiconductors as Dopant-Free Hole Transporting Materials for Efficient and Stable Perovskite Solar Cells", Advanced Functional Materials **31**, 2011270 (2021).

[6]L. Alcácer, "Orbitals and bands in organic semiconductors", Electronic Structure of Organic Semiconductors: Polymers and small molecules, `10.1088/2053-2571/aaddd8ch5` (2018).

[7]G. Malliaras and R. Friend, "An Organic Electronics Primer", Physics Today **58**, 53–58 (2005).

[8]D. Jacquemin, A. Femenias, H. Chermette, I. Ciofini, C. Adamo, J.-M. André, and E. A. Perpète, "Assessment of Several Hybrid DFT Functionals for the Evaluation of Bond Length Alternation of Increasingly Long Oligomers", The Journal of Physical Chemistry A **110**, 5952–5959 (2006).

[9]P. N. Rivers, *Leading Edge Research in Solar Energy*, UK ed. edition (Nova Science Publishers Inc, New York, Nov. 5, 2007), 283 pp.

[10]B. Lüssem, M. Riede, and K. Leo, "Doping of organic semiconductors", physica status solidi (a) **210**, 9–43 (2013).

[11]I. E. Jacobs and A. J. Moulé, "Controlling Molecular Doping in Organic Semiconductors", Advanced Materials **29**, 1703063 (2017).

[12]A. D. Scaccabarozzi, A. Basu, F. Aniés, J. Liu, O. Zapata-Arteaga, R. Warren, Y. Firdaus, M. I. Nugraha, Y. Lin, M. Campoy-Quiles, N. Koch, C. Müller, L. Tsetseris, M. Heeney, and T. D. Anthopoulos, "Doping Approaches for Organic Semiconductors", Chemical Reviews **122**, 4420–4492 (2022).

[13]Z. Bin, Z. Liu, Y. Qiu, and L. Duan, "Efficient n-Dopants and Their Roles in Organic Electronics", Advanced Optical Materials **6**, 1800536 (2018).

[14]N. Sakai, R. Warren, F. Zhang, S. Nayak, J. Liu, S. V. Kesava, Y.-H. Lin, H. S. Biswal, X. Lin, C. Grovenor, T. Malinauskas, A. Basu, T. D. Anthopoulos, V. Getautis, A. Kahn, M. Riede, P. K. Nayak, and H. J. Snaith, "Adduct-based p-doping of organic semiconductors", Nature Materials **20**, 1248–1254 (2021).

[15]I. Salzmann, G. Heimel, M. Oehzelt, S. Winkler, and N. Koch, "Molecular Electrical Doping of Organic Semiconductors: Fundamental Mechanisms and Emerging Dopant Design Rules", Accounts of Chemical Research **49**, 370–378 (2016).

[16]S.-S. Sun and N. S. Sariciftci, eds., *Organic Photovoltaics: Mechanisms, Materials, and Devices* (CRC Press, Boca Raton, Jan. 31, 2017), 666 pp.

[17]M. L. P. Junior, R. T. d. S. Júnior, G. M. e Silva, and L. A. R. Júnior, "Stationary polaron properties in organic crystalline semiconductors", Physical Chemistry Chemical Physics **21**, 2727–2733 (2019).

[18]J. Nelson, J. J. Kwiatkowski, J. Kirkpatrick, and J. M. Frost, "Modeling Charge Transport in Organic Photovoltaic Materials", Accounts of Chemical Research **42**, 1768–1778 (2009).

[19]N. Lu, L. Li, D. Geng, and M. Liu, "A review for polaron dependent charge transport in organic semiconductor", Organic Electronics **61**, 223–234 (2018).

[20]H. Yang, F. Gajdos, and J. Blumberger, "Intermolecular Charge Transfer Parameters, Electron–Phonon Couplings, and the Validity of Polaron Hopping Models in Organic Semiconducting Crystals: Rubrene, Pentacene, and C60", The Journal of Physical Chemistry C **121**, 7689–7696 (2017).

[21]N. Zarrabi, *Optoelectronic Properties of Organic Semiconductors: Charge Generation and Recombination in Next-Generation Photovoltaic Devices*, SpringerBriefs in Materials (Springer International Publishing, Cham, 2022).

[22]J. C. S. Costa, R. J. S. Taveira, C. F. R. A. C. Lima, A. Mendes, and L. M. N. B. F. Santos, "Optical band gaps of organic semiconductor materials", Optical Materials **58**, 51–60 (2016).

[23]M. Knupfer, "Exciton binding energies in organic semiconductors", Applied Physics A **77**, 623–626 (2003).

[24]R. Schuster, M. Knupfer, and H. Berger, "Exciton Band Structure of Pentacene Molecular Solids: Breakdown of the Frenkel Exciton Model", Physical Review Letters **98**, 037402 (2007).

[25]S. Blumstengel, S. Sadofev, C. Xu, J. Puls, and F. Henneberger, "Converting Wannier into Frenkel Excitons in an Inorganic/Organic Hybrid Semiconductor Nanostructure", Physical Review Letters **97**, 237401 (2006).

[26]O. V. Mikhnenko, P. W. M. Blom, and T.-Q. Nguyen, "Exciton diffusion in organic semiconductors", Energy & Environmental Science **8**, 1867–1888 (2015).

[27]T. M. Clarke and J. R. Durrant, "Charge Photogeneration in Organic Solar Cells", Chemical Reviews **110**, 6736–6767 (2010).

[28]X.-Y. Zhu, Q. Yang, and M. Muntwiler, "Charge-Transfer Excitons at Organic Semiconductor Surfaces and Interfaces", Accounts of Chemical Research **42**, 1779–1787 (2009).

[29]F. D. Eisner, M. Azzouzi, Z. Fei, X. Hou, T. D. Anthopoulos, T. J. S. Dennis, M. Heeney, and J. Nelson, "Hybridization of Local Exciton and Charge-Transfer States Reduces Nonradiative Voltage Losses in Organic Solar Cells", Journal of the American Chemical Society **141**, 6362–6374 (2019).

[30]J. Kurpiers, T. Ferron, S. Roland, M. Jakoby, T. Thiede, F. Jaiser, S. Albrecht, S. Janietz, B. A. Collins, I. A. Howard, and D. Neher, "Probing the pathways of free charge generation in organic bulk heterojunction solar cells", Nature Communications **9**, 2038 (2018).

[31]F. Deschler, M. Price, S. Pathak, L. E. Klintberg, D. D. Jarausch, R. Higler, S. Hüttner, T. Leijtens, S. D. Stranks, H. J. Snaith, M. Atatüre, R. T. Phillips, and R. H. Friend, "High photoluminescence efficiency and optically pumped lasing in solution-processed mixed halide perovskite semiconductors", Journal of Physical Chemistry Letters **5**, 1421–1426 (2014).

[32]M. Stolterfoht, A. Armin, S. Shoaee, I. Kassal, P. Burn, and P. Meredith, "Slower carriers limit charge generation in organic semiconductor light-harvesting systems", Nature Communications **7**, 11944 (2016).

[33]N. Cho, C. W. Schlenker, K. M. Knesting, P. Koelsch, H.-L. Yip, D. S. Ginger, and A. K.-Y. Jen, "High-Dielectric Constant Side-Chain Polymers Show Reduced Non-Geminate Recombination in Heterojunction Solar Cells", Advanced Energy Materials **4**, 1301857 (2014).

[34]C. Göhler, A. Wagenpfahl, and C. Deibel, "Nongeminate Recombination in Organic Solar Cells", Advanced Electronic Materials **4**, 1700505 (2018).

[35]C. M. Proctor, M. Kuik, and T.-Q. Nguyen, "Charge carrier recombination in organic solar cells", Progress in Polymer Science, Topical Issue on Conductive Polymers **38**, 1941–1960 (2013).

[36]A. Pivrikas, H. Neugebauer, and N. S. Sariciftci, "Charge Carrier Lifetime and Recombination in Bulk Heterojunction Solar Cells", IEEE Journal of Selected Topics in Quantum Electronics **16**, 1746–1758 (2010).

[37]J. Marin-Beloqui, G. Zhang, J. Guo, J. Shaikh, T. Wohrer, S. M. Hosseini, B. Sun, J. Shipp, A. J. Auty, D. Chekulaev, J. Ye, Y.-C. Chin, M. B. Sullivan, A. J. Mozer, J.-S. Kim, S. Shoaee, and T. M. Clarke, "Insight into the Origin of Trapping in Polymer/Fullerene Blends with a Systematic Alteration of the Fullerene to Higher Adducts", The Journal of Physical Chemistry C **126**, 2708–2719 (2022).

[38]F. C. Krebs, "Fabrication and processing of polymer solar cells: A review of printing and coating techniques", Solar Energy Materials and Solar Cells, Processing and Preparation of Polymer and Organic Solar Cells **93**, 394–412 (2009).

[39]J. Wu, J. Luke, H. K. H. Lee, P. Shakya Tuladhar, H. Cha, S. Y. Jang, W. C. Tsoi, M. Heeney, H. Kang, K. Lee, T. Kirchartz, J. S. Kim, and J. R. Durrant, "Tail state limited photocurrent collection of thick photoactive layers in organic solar cells", Nature Communications **10**, 1–10 (2019).

[40]S. Zeiske, O. J. Sandberg, N. Zarrabi, W. Li, P. Meredith, and A. Armin, "Direct observation of trap-assisted recombination in organic photovoltaic devices", Nature Communications **12**, 3603 (2021).

[41]Z. Shariatinia, "Recent progress in development of diverse kinds of hole transport materials for the perovskite solar cells: A review", Renewable and Sustainable Energy Reviews **119**, 109608 (2020).

[42]A. A. Said, J. Xie, and Q. Zhang, "Recent Progress in Organic Electron Transport Materials in Inverted Perovskite Solar Cells", Small **15**, 1900854 (2019).

[43]S. S. Reddy, K. Gunasekar, J. H. Heo, S. H. Im, C. S. Kim, D.-H. Kim, J. H. Moon, J. Y. Lee, M. Song, and S.-H. Jin, "Highly Efficient Organic Hole Transporting Materials for Perovskite and Organic Solar Cells with Long-Term Stability", Advanced Materials **28**, 686–693 (2016).

[44]O. Malinkiewicz, A. Yella, Y. H. Lee, G. M. Espallargas, M. Graetzel, M. K. Nazeeruddin, and H. J. Bolink, "Perovskite solar cells employing organic charge-transport layers", Nature Photonics **8**, 128–132 (2014).

[45]T. Du, W. Xu, M. Daboczi, J. Kim, S. Xu, C.-T. Lin, H. Kang, K. Lee, M. J. Heeney, J.-S. Kim, J. R. Durrant, and M. A. McLachlan, "P-Doping of organic hole transport layers in p–i–n perovskite solar cells: correlating open-circuit voltage and photoluminescence quenching", Journal of Materials Chemistry A **7**, 18971–18979 (2019).

[46]M.-C. Shih, S.-S. Li, C.-H. Hsieh, Y.-C. Wang, H.-D. Yang, Y.-P. Chiu, C.-S. Chang, and C.-W. Chen, "Spatially Resolved Imaging on Photocarrier Generations and Band Alignments at Perovskite/PbI2 Heterointerfaces of Perovskite Solar Cells by Light-Modulated Scanning Tunneling Microscopy", Nano Letters **17**, 1154–1160 (2017).

[47]M. Daboczi, I. Hamilton, S. Xu, J. Luke, S. Limbu, J. Lee, M. A. McLachlan, K. Lee, J. R. Durrant, I. D. Baikie, and J. S. Kim, "Origin of Open-Circuit Voltage Losses in Perovskite Solar Cells Investigated by Surface Photovoltage Measurement", ACS Applied Materials and Interfaces **11**, 46808–46817 (2019).

[48]C. Motta, F. El-Mellouhi, and S. Sanvito, "Charge carrier mobility in hybrid halide perovskites", Scientific Reports **5**, 12746 (2015).

[49]J. Niu, D. Yang, X. Ren, Z. Yang, Y. Liu, X. Zhu, W. Zhao, and S. (Liu, "Graphene-oxide doped PEDOT:PSS as a superior hole transport material for high-efficiency perovskite solar cell", Organic Electronics **48**, 165–171 (2017).

[50]A. Abate, T. Leijtens, S. Pathak, J. Teuscher, R. Avolio, M. E. Errico, J. Kirkpatrik, J. M. Ball, P. Docampo, I. McPherson, and H. J. Snaith, "Lithium salts as "redox active" p-type dopants for organic semiconductors and their impact in solid-state dye-sensitized solar cells", Physical Chemistry Chemical Physics **15**, 2572–2579 (2013).

[51]H. J. Snaith and M. Grätzel, "Enhanced charge mobility in a molecular hole transporter via addition of redox inactive ionic dopant: Implication to dye-sensitized solar cells", Applied Physics Letters **89**, 262114 (2006).

[52]J. Krüger, R. Plass, L. Cevey, M. Piccirelli, M. Grätzel, and U. Bach, "High efficiency solid-state photovoltaic device due to inhibition of interface charge recombination", Applied Physics Letters **79**, 2085–2087 (2001).

[53]Y. Yue, N. Salim, Y. Wu, X. Yang, A. Islam, W. Chen, J. Liu, E. Bi, F. Xie, M. Cai, and L. Han, "Enhanced Stability of Perovskite Solar Cells through Corrosion-Free Pyridine Derivatives in Hole-Transporting Materials", Advanced Materials (Deerfield Beach, Fla.) **28**, 10738–10743 (2016).

[54]D. Liu, Y. Wang, H. Zheng, J. Wu, L. Ji, P. Zhang, W. Ahmad, H. Chen, Z. Chen, and S. Li, "Improved stability of perovskite solar cells with enhanced moisture-resistant hole transport layers", Electrochimica Acta **296**, 508–516 (2019).

[55]B. Ecker, J. C. Nolasco, J. Pallarés, L. F. Marsal, J. Posdorfer, J. Parisi, and E. von Hauff, "Degradation Effects Related to the Hole Transport Layer in Organic Solar Cells", Advanced Functional Materials **21**, 2705–2711 (2011).

[56]Y. Ren, M. Ren, X. Xie, J. Wang, Y. Cai, Y. Yuan, J. Zhang, and P. Wang, "A spiro-OMeTAD based semiconductor composite with over 100 °C glass transition temperature for durable perovskite solar cells", Nano Energy **81**, 105655 (2021).

[57]P. J. Reucroft, K. Takahashi, and H. Ullal, "Theoretical efficiency in an organic photovoltaic energy conversion system", Applied Physics Letters **25**, 664–666 (1974).

[58]G. Yu, J. Gao, J. C. Hummelen, F. Wudl, and A. J. Heeger, "Polymer photovoltaic cells: Enhanced efficiencies via a network of internal donor-acceptor heterojunctions", Science **270**, 1789 (1995).

[59]R. A. J. Janssen and J. Nelson, "Factors Limiting Device Efficiency in Organic Photovoltaics", Advanced Materials **25**, 1847–1858 (2013).

[60]G. Dennler, M. C. Scharber, and C. J. Brabec, "Polymer-Fullerene Bulk-Heterojunction Solar Cells", Advanced Materials **21**, 1323–1338 (2009).

[61]Q. Liu, Y. Jiang, K. Jin, J. Qin, J. Xu, W. Li, J. Xiong, J. Liu, Z. Xiao, K. Sun, S. Yang, X. Zhang, and L. Ding, "18% Efficiency organic solar cells", Science Bulletin **65**, 272–275 (2020).

[62]*Best research cell efficiency chart. NREL.* (2023) `https://www.nrel.gov/pv/cell-efficiency.html`.

[63]Y. Tamai, "Delocalization boosts charge separation in organic solar cells", Polymer Journal **52**, 691–700 (2020).

[64]V. A., S.-W. Liu, and K.-T. Wong, "Organic polymeric and small molecular electron acceptors for organic solar cells", Materials Science and Engineering: R: Reports **124**, 1–57 (2018).

[65]J. Nelson, *The Physics of Solar Cells* (PUBLISHED BY IMPERIAL COLLEGE PRESS AND DISTRIBUTED BY WORLD SCIENTIFIC PUBLISHING CO., May 2003).

[66]W. M. Saslow, "Chapter 7 - Ohm's Law: Electric Current Is Driven by Emf, and Limited by Electrical Resistance", in *Electricity, Magnetism, and Light*, edited by W. M. Saslow (Academic Press, San Diego, Jan. 1, 2002), pp. 281–335.

[67]C. M. Proctor and T.-Q. Nguyen, "Effect of leakage current and shunt resistance on the light intensity dependence of organic solar cells", Applied Physics Letters **106**, 083301 (2015).

[68]X. Liu, X. Du, J. Wang, C. Duan, X. Tang, T. Heumueller, G. Liu, Y. Li, Z. Wang, J. Wang, F. Liu, N. Li, C. J. Brabec, F. Huang, and Y. Cao, "Efficient Organic Solar Cells with Extremely High Open-Circuit Voltages and Low Voltage Losses by Suppressing Nonradiative Recombination Losses", Advanced Energy Materials **8**, 1801699 (2018).

[69]D. Ompong, K. S. Ram, D. D. Y. Setsoafia, H. Mehdizadeh Rad, and J. Singh, "Saturation of Open-Circuit Voltage at Higher Light Intensity Caused by Interfacial Defects and Nonradiative Recombination Losses in Perovskite Solar Cells", Advanced Materials Interfaces **10**, 2201578 (2023).

[70]K. Ramalingam and C. Indulkar, "Chapter 3 - Solar Energy and Photovoltaic Technology", in *Distributed Generation Systems*, edited by G. B. Gharehpetian and S. M. Mousavi Agah (Butterworth-Heinemann, Jan. 1, 2017), pp. 69–147.

[71]A. J. Heeger, "25th Anniversary Article: Bulk Heterojunction Solar Cells: Understanding the Mechanism of Operation", Advanced Materials **26**, 10–28 (2014).

[72]H. Ohkita, S. Cook, Y. Astuti, W. Duffy, S. Tierney, W. Zhang, M. Heeney, I. McCulloch, J. Nelson, D. D. C. Bradley, and J. R. Durrant, "Charge Carrier Formation in Polythiophene/Fullerene Blend Films Studied by Transient Absorption Spectroscopy", Journal of the American Chemical Society **130**, 3030–3042 (2008).

[73]A. A. Bakulin, S. D. Dimitrov, A. Rao, P. C. Y. Chow, C. B. Nielsen, B. C. Schroeder, I. McCulloch, H. J. Bakker, J. R. Durrant, and R. H. Friend, "Charge-Transfer State Dynamics Following Hole and Electron Transfer in Organic Photovoltaic Devices", The Journal of Physical Chemistry Letters **4**, 209–215 (2013).

[74]L. J. A. Koster, O. Stenzel, S. D. Oosterhout, M. M. Wienk, V. Schmidt, and R. A. J. Janssen, "Morphology and Efficiency: The Case of Polymer/ZnO Solar Cells", Advanced Energy Materials **3**, 615–621 (2013).

[75]H. F. Haneef, A. M. Zeidell, and O. D. Jurchescu, "Charge carrier traps in organic semiconductors: a review on the underlying physics and impact on electronic devices", Journal of Materials Chemistry C **8**, 759–787 (2020).

[76]W. Shockley and W. T. Read, "Statistics of the Recombinations of Holes and Electrons", Physical Review **87**, 835–842 (1952).

[77]J. M. Frost, M. A. Faist, and J. Nelson, "Energetic Disorder in Higher Fullerene Adducts: A Quantum Chemical and Voltammetric Study", Advanced Materials **22**, 4881–4884 (2010).

[78]H. Cha, J. Wu, A. Wadsworth, J. Nagitta, S. Limbu, S. Pont, Z. Li, J. Searle, M. F. Wyatt, D. Baran, J.-S. Kim, I. McCulloch, and J. R. Durrant, "An Efficient, "Burn in" Free Organic Solar Cell Employing a Nonfullerene Electron Acceptor", Advanced Materials **29**, 1701156 (2017).

[79]H. K. H. Lee, A. M. Telford, J. A. Röhr, M. F. Wyatt, B. Rice, J. Wu, A. d. C. Maciel, S. M. Tuladhar, E. Speller, J. McGettrick, J. R. Searle, S. Pont, T. Watson, T. Kirchartz, J. R. Durrant, W. C. Tsoi, J. Nelson, and Z. Li, "The role of fullerenes in the environmental stability of polymer:fullerene solar cells", Energy & Environmental Science **11**, 417–428 (2018).

[80]J. Wu, J. Lee, Y.-C. Chin, H. Yao, H. Cha, J. Luke, J. Hou, J. S. Kim, and J. R. Durrant, "Exceptionally low charge trapping enables highly efficient organic bulk heterojunction solar cells", Energy and Environmental Science **13**, 2422–2430 (2020).

[81]K. H. Hendriks, A. S. G. Wijpkema, J. J. van Franeker, M. M. Wienk, and R. A. J. Janssen, "Dichotomous Role of Exciting the Donor or the Acceptor on Charge Generation in Organic Solar Cells", Journal of the American Chemical Society **138**, 10026–10031 (2016).

[82]A. Karki, J. Vollbrecht, A. J. Gillett, P. Selter, J. Lee, Z. Peng, N. Schopp, A. L. Dixon, M. Schrock, V. Nádaždy, F. Schauer, H. Ade, B. F. Chmelka, G. C. Bazan, R. H. Friend, and T.-Q. Nguyen, "Unifying Charge Generation, Recombination, and Extraction in Low-Offset Non-Fullerene Acceptor Organic Solar Cells", Advanced Energy Materials **10**, 2001203 (2020).

[83]T. Umeyama, K. Igarashi, Y. Tamai, T. Wada, T. Takeyama, D. Sasada, K. Ishida, T. Koganezawa, S. Ohtani, K. Tanaka, H. Ohkita, and H. Imahori, "Prolongation of the singlet exciton lifetime of nonfullerene acceptor films by the replacement of the central benzene core with naphthalene", Sustainable Energy & Fuels **5**, 2028–2035 (2021).

[84]P. Bi, S. Zhang, Z. Chen, Y. Xu, Y. Cui, T. Zhang, J. Ren, J. Qin, L. Hong, X. Hao, and J. Hou, "Reduced non-radiative charge recombination enables organic photovoltaic cell approaching 19% efficiency", Joule **5**, 2408–2419 (2021).

[85]S. Holliday, R. S. Ashraf, C. B. Nielsen, M. Kirkus, J. A. Röhr, C.-H. Tan, E. Collado-Fregoso, A.-C. Knall, J. R. Durrant, J. Nelson, and I. McCulloch, "A Rhodanine Flanked Nonfullerene Acceptor for Solution-Processed Organic Photovoltaics", Journal of the American Chemical Society **137**, 898–904 (2015).

[86]W. Zhao, D. Qian, S. Zhang, S. Li, O. Inganäs, F. Gao, and J. Hou, "Fullerene-Free Polymer Solar Cells with over 11% Efficiency and Excellent Thermal Stability", Advanced Materials **28**, 4734–4739 (2016).

[87]J. Yuan, Y. Zhang, L. Zhou, G. Zhang, H.-L. Yip, T.-K. Lau, X. Lu, C. Zhu, H. Peng, P. A. Johnson, M. Leclerc, Y. Cao, J. Ulanski, Y. Li, and Y. Zou, "Single-Junction Organic Solar Cell with over 15% Efficiency Using Fused-Ring Acceptor with Electron-Deficient Core", Joule **3**, 1140–1151 (2019).

[88]C. A. Hunter and J. K. M. Sanders, "The nature of .pi.-.pi. interactions", Journal of the American Chemical Society **112**, 5525–5534 (1990).

[89]L. Benatto, C. F. N. Marchiori, C. Moyses Araujo, and M. Koehler, "Molecular origin of efficient hole transfer from non-fullerene acceptors: insights from first-principles calculations", Journal of Materials Chemistry C **7**, 12180–12193 (2019).

[90]G. D'Avino, L. Muccioli, F. Castet, C. Poelking, D. Andrienko, Z. G. Soos, J. Cornil, and D. Beljonne, "Electrostatic phenomena in organic semiconductors: fundamentals and implications for photovoltaics", Journal of Physics: Condensed Matter **28**, 433002 (2016).

[91]T. Taima, M. Shahiduzzaman, T. Ishizeki, K. Yamamoto, M. Karakawa, T. Kuwabara, and K. Takahashi, "Sexithiophene-Based Photovoltaic Cells with High Light Absorption Coefficient via Crystalline Polymorph Control", The Journal of Physical Chemistry C **121**, 19699–19704 (2017).

[92]S. Duhm, G. Heimel, I. Salzmann, H. Glowatzki, R. L. Johnson, A. Vollmer, J. P. Rabe, and N. Koch, "Orientation-dependent ionization energies and interface dipoles in ordered molecular assemblies", Nature Materials **7**, 326–332 (2008).

[93]M. Schwarze, K. S. Schellhammer, K. Ortstein, J. Benduhn, C. Gaul, A. Hinderhofer, L. Perdigón Toro, R. Scholz, J. Kublitski, S. Roland, M. Lau, C. Poelking, D. Andrienko, G. Cuniberti, F. Schreiber, D. Neher, K. Vandewal, F. Ortmann, and K. Leo, "Impact of molecular quadrupole moments on the energy levels at organic heterojunctions", Nature Communications **10**, 2466 (2019).

[94]L. Zhu, M. Zhang, G. Zhou, T. Hao, J. Xu, J. Wang, C. Qiu, N. Prine, J. Ali, W. Feng, X. Gu, Z. Ma, Z. Tang, H. Zhu, L. Ying, Y. Zhang, and F. Liu, "Efficient Organic Solar Cell with 16.88% Efficiency Enabled by Refined Acceptor Crystallization and Morphology with Improved Charge Transfer and Transport Properties", Advanced Energy Materials **10**, 1904234 (2020).

[95]Y. Xiao, J. Yuan, G. Zhou, K. Chak Ngan, X. Xia, J. Zhu, Y. Zou, N. Zhao, X. Zhan, and X. Lu, "Unveiling the crystalline packing of Y6 in thin films by thermally induced "backbone-on" orientation", Journal of Materials Chemistry A **9**, 17030–17038 (2021).

[96]C. B. Nielsen, S. Holliday, H.-Y. Chen, S. J. Cryer, and I. McCulloch, "Non-Fullerene Electron Acceptors for Use in Organic Solar Cells", Accounts of Chemical Research **48**, 2803–2812 (2015).

[97]H.-R. Wenk and A. Bulakh, *Minerals: Their Constitution and Origin* (Cambridge University Press, Apr. 2004), 616 pp.

[98]C. Eames, J. M. Frost, P. R. F. Barnes, B. C. O'Regan, A. Walsh, and M. S. Islam, "Ionic transport in hybrid lead iodide perovskite solar cells", Nature Communications **6**, 7497 (2015).

[99]N.-G. Park, "High Efficiency Perovskite Solar Cells: Materials and Devices Engineering", Transactions on Electrical and Electronic Materials **21**, 1–15 (2020).

[100]A. Fakharuddin, M. K. Gangishetty, M. Abdi-Jalebi, S.-H. Chin, A. R. bin Mohd Yusoff, D. N. Congreve, W. Tress, F. Deschler, M. Vasilopoulou, and H. J. Bolink, "Perovskite light-emitting diodes", Nature Electronics **5**, 203–216 (2022).

[101]F. Wang, X. Zou, M. Xu, H. Wang, H. Wang, H. Guo, J. Guo, P. Wang, M. Peng, Z. Wang, Y. Wang, J. Miao, F. Chen, J. Wang, X. Chen, A. Pan, C. Shan, L. Liao, and W. Hu, "Recent Progress on Electrical and Optical Manipulations of Perovskite Photodetectors", Advanced Science **8**, 2100569 (2021).

[102]M. Daboczi, S. R. Ratnasingham, L. Mohan, C. Pu, I. Hamilton, Y.-C. Chin, M. A. McLachlan, and J.-S. Kim, "Optimal Interfacial Band Bending Achieved by Fine Energy Level Tuning in Mixed-Halide Perovskite Solar Cells", ACS Energy Letters **6**, 3970–3981 (2021).

[103]F. Brivio, K. T. Butler, A. Walsh, and M. van Schilfgaarde, "Relativistic quasiparticle self-consistent electronic structure of hybrid halide perovskite photovoltaic absorbers", Physical Review B **89**, 155204 (2014).

[104]V. D'Innocenzo, G. Grancini, M. J. P. Alcocer, A. R. S. Kandada, S. D. Stranks, M. M. Lee, G. Lanzani, H. J. Snaith, and A. Petrozza, "Excitons versus free charges in organo-lead tri-halide perovskites", Nature Communications **5**, 3586 (2014).

[105]A. Miyata, A. Mitioglu, P. Plochocka, O. Portugall, J. T.-W. Wang, S. D. Stranks, H. J. Snaith, and R. J. Nicholas, "Direct measurement of the exciton binding energy and effective masses for charge carriers in organic–inorganic tri-halide perovskites", Nature Physics **11**, 582–587 (2015).

[106]L. M. Herz, "Charge-Carrier Mobilities in Metal Halide Perovskites: Fundamental Mechanisms and Limits", ACS Energy Letters **2**, 1539–1548 (2017).

[107]S. Ghosh, S. Mishra, and T. Singh, "Antisolvents in Perovskite Solar Cells: Importance, Issues, and Alternatives", Advanced Materials Interfaces **7**, 2000950 (2020).

[108]M. Xiao, F. Huang, W. Huang, Y. Dkhissi, Y. Zhu, J. Etheridge, A. Gray-Weale, U. Bach, Y.-B. Cheng, and L. Spiccia, "A Fast Deposition-Crystallization Procedure for Highly Efficient Lead Iodide Perovskite Thin-Film Solar Cells", Angewandte Chemie International Edition **53**, 9898–9903 (2014).

[109]K. X. Steirer, P. Schulz, G. Teeter, V. Stevanovic, M. Yang, K. Zhu, and J. J. Berry, "Defect Tolerance in Methylammonium Lead Triiodide Perovskite", ACS Energy Letters **1**, 360–366 (2016).

[110]W.-J. Yin, T. Shi, and Y. Yan, "Unusual defect physics in CH3NH3PbI3 perovskite solar cell absorber", Applied Physics Letters **104**, 063903 (2014).

[111]C. C. Stoumpos, D. H. Cao, D. J. Clark, J. Young, J. M. Rondinelli, J. I. Jang, J. T. Hupp, and M. G. Kanatzidis, "Ruddlesden–Popper Hybrid Lead Iodide Perovskite 2D Homologous Semiconductors", Chemistry of Materials **28**, 2852–2867 (2016).

[112]S. Heo, G. Seo, K. T. Cho, Y. Lee, S. Paek, S. Kim, M. Seol, S. H. Kim, D.-J. Yun, K. Kim, J. Park, J. Lee, L. Lechner, T. Rodgers, J. W. Chung, J.-S. Kim, D. Lee, S.-H. Choi, and M. K. Nazeeruddin, "Dimensionally Engineered Perovskite Heterostructure for Photovoltaic and Optoelectronic Applications", Advanced Energy Materials **9**, 1902470 (2019).

[113]S. Gharibzadeh, B. Abdollahi Nejand, M. Jakoby, T. Abzieher, D. Hauschild, S. Moghadamzadeh, J. A. Schwenzer, P. Brenner, R. Schmager, A. A. Haghighirad, L. Weinhardt, U. Lemmer, B. S. Richards, I. A. Howard, and U. W. Paetzold, "Record Open-Circuit Voltage Wide-Bandgap Perovskite Solar Cells Utilizing 2D/3D Perovskite Heterostructure", Advanced Energy Materials **9**, 1803699 (2019).

[114]A. H. Proppe, A. Johnston, S. Teale, A. Mahata, R. Quintero-Bermudez, E. H. Jung, L. Grater, T. Cui, T. Filleter, C.-Y. Kim, S. O. Kelley, F. De Angelis, and E. H. Sargent, "Multication perovskite 2D/3D interfaces form via progressive dimensional reduction", Nature Communications **12**, 3472 (2021).

[115]C. Zuo, A. D. Scully, and M. Gao, "Drop-Casting Method to Screen Ruddlesden–Popper Perovskite Formulations for Use in Solar Cells", ACS Applied Materials & Interfaces **13**, 56217–56225 (2021).

[116]M. P. Hautzinger, D. Pan, A. K. Pigg, Y. Fu, D. J. Morrow, M. Leng, M.-Y. Kuo, N. Spitha, D. P. I. Lafayette, D. D. Kohler, J. C. Wright, and S. Jin, "Band Edge Tuning of Two-Dimensional Ruddlesden–Popper Perovskites by A Cation Size Revealed through Nanoplates", ACS Energy Letters **5**, 1430–1437 (2020).

[117]Y. Chen, Y. Sun, J. Peng, J. Tang, K. Zheng, and Z. Liang, "2D Ruddlesden–Popper Perovskites for Optoelectronics", Advanced Materials **30**, 1703487 (2018).

[118]Q. Wang, X.-D. Liu, Y.-H. Qiu, K. Chen, L. Zhou, and Q.-Q. Wang, "Quantum confinement effect and exciton binding energy of layered perovskite nanoplatelets", AIP Advances **8**, 025108 (2018).

[119]F. A. Roghabadi, M. Alidaei, S. Maryam Mousavi, T. Ashjari, A. Shokrolahzadeh Tehrani, V. Ahmadi, and S. Mojtaba Sadrameli, "Stability progress of perovskite solar cells dependent on the crystalline structure: From 3D ABX 3 to 2D Ruddlesden–Popper perovskite absorbers", Journal of Materials Chemistry A **7**, 5898–5933 (2019).

[120]H. Xu, G. Liu, X. Xu, S. Xu, L. Zhang, X. Chen, H. Zheng, and X. Pan, "Hydrophobic 2D Perovskite-Modified Layer with Polyfunctional Groups for Enhanced Performance and High Moisture Stability of Perovskite Solar Cells", Solar RRL **4**, 2000647 (2020).

[121]L. N. Quan, M. Yuan, R. Comin, O. Voznyy, E. M. Beauregard, S. Hoogland, A. Buin, A. R. Kirmani, K. Zhao, A. Amassian, D. H. Kim, and E. H. Sargent, "Ligand-Stabilized Reduced-Dimensionality Perovskites", Journal of the American Chemical Society **138**, 2649–2655 (2016).

[122]S. Gharibzadeh, P. Fassl, I. M. Hossain, P. Rohrbeck, M. Frericks, M. Schmidt, T. Duong, M. R. Khan, T. Abzieher, B. A. Nejand, F. Schackmar, O. Almora, T. Feeney, R. Singh, D. Fuchs, U. Lemmer, J. P. Hofmann, S. A. L. Weber, and U. W. Paetzold, "Two birds with one stone: dual grain-boundary and interface passivation enables >22% efficient inverted methylammonium-free perovskite solar cells", Energy & Environmental Science **14**, 5875–5893 (2021).

[123]S. Ma, Y. Bai, H. Wang, H. Zai, J. Wu, L. Li, S. Xiang, N. Liu, L. Liu, C. Zhu, G. Liu, X. Niu, H. Chen, H. Zhou, Y. Li, and Q. Chen, "1000 h Operational Lifetime Perovskite Solar Cells by Ambient Melting Encapsulation", Advanced Energy Materials **10**, 1902472 (2020).

[124]J. Y. Kim, J.-W. Lee, H. S. Jung, H. Shin, and N.-G. Park, "High-Efficiency Perovskite Solar Cells", Chemical Reviews **120**, 7867–7918 (2020).

[125]M. Saliba, J. P. Correa-Baena, C. M. Wolff, M. Stolterfoht, N. Phung, S. Albrecht, D. Neher, and A. Abate, "How to Make over 20% Efficient Perovskite Solar Cells in Regular (n-i-p) and Inverted (p-i-n) Architectures", Chemistry of Materials **30**, 4193–4201 (2018).

[126]G.-H. Kim and D. S. Kim, "Development of perovskite solar cells with >25% conversion efficiency", Joule **5**, 1033–1035 (2021).

[127]X. Lin, D. Cui, X. Luo, C. Zhang, Q. Han, Y. Wang, and L. Han, "Efficiency progress of inverted perovskite solar cells", Energy & Environmental Science **13**, 3823–3847 (2020).

[128]N. Suresh Kumar and K. Chandra Babu Naidu, "A review on perovskite solar cells (PSCs), materials and applications", Journal of Materiomics **7**, 940–956 (2021).

[129]D. Luo, R. Su, W. Zhang, Q. Gong, and R. Zhu, "Minimizing non-radiative recombination losses in perovskite solar cells", Nature Reviews Materials **5**, 44–60 (2020).

[130]Z. Ni, C. Bao, Y. Liu, Q. Jiang, W.-Q. Wu, S. Chen, X. Dai, B. Chen, B. Hartweg, Z. Yu, Z. Holman, and J. Huang, "Resolving spatial and energetic distributions of trap states in metal halide perovskite solar cells", Science **367**, 1352–1358 (2020).

[131]B. Chen, P. N. Rudd, S. Yang, Y. Yuan, and J. Huang, "Imperfections and their passivation in halide perovskite solar cells", Chemical Society Reviews **48**, 3842–3867 (2019).

[132]T. H. Schloemer, J. A. Christians, J. M. Luther, and A. Sellinger, "Doping strategies for small molecule organic hole-transport materials: impacts on perovskite solar cell performance and stability", Chemical Science **10**, 1904–1935 (2019).

[133]L. Lanzetta, T. Webb, N. Zibouche, X. Liang, D. Ding, G. Min, R. J. E. Westbrook, B. Gaggio, T. J. Macdonald, M. S. Islam, and S. A. Haque, "Degradation mechanism of hybrid tin-based perovskite solar cells and the critical role of tin (IV) iodide", Nature Communications **12**, 2853 (2021).

[134]L. Lanzetta, N. Aristidou, and S. A. Haque, "Stability of Lead and Tin Halide Perovskites: The Link between Defects and Degradation", The Journal of Physical Chemistry Letters **11**, 574–585 (2020).

[135]N. Aristidou, C. Eames, I. Sanchez-Molina, X. Bu, J. Kosco, M. S. Islam, and S. A. Haque, "Fast oxygen diffusion and iodide defects mediate oxygen-induced degradation of perovskite solar cells", Nature Communications **8**, 15218 (2017).

[136]S. Wang, Z. Huang, X. Wang, Y. Li, M. Gü, S. Valenzuela, P. Parikh, A. Cabreros, W. Xiong, and Y. S. Meng, "Unveiling the Role of tBP-LiTFSI Complexes in Perovskite Solar Cells", `10.1021/jacs.8b09809` (2018).

[137]J. Hieulle, X. Wang, C. Stecker, D.-Y. Son, L. Qiu, R. Ohmann, L. K. Ono, A. Mugarza, Y. Yan, and Y. Qi, "Unraveling the Impact of Halide Mixing on Perovskite Stability", Journal of the American Chemical Society **141**, 3515–3523 (2019).

[138]X. Yin, Z. Song, Z. Li, and W. Tang, "Toward ideal hole transport materials: a review on recent progress in dopant-free hole transport materials for fabricating efficient and stable perovskite solar cells", Energy & Environmental Science **13**, 4057–4086 (2020).

[139]G. Wu, R. Liang, M. Ge, G. Sun, Y. Zhang, and G. Xing, "Surface Passivation Using 2D Perovskites toward Efficient and Stable Perovskite Solar Cells", Advanced Materials **34**, 2105635 (2022).

[140]G.-W. Kim, H. Choi, M. Kim, J. Lee, S. Y. Son, and T. Park, "Hole Transport Materials in Conventional Structural (n–i–p) Perovskite Solar Cells: From Past to the Future", Advanced Energy Materials **10**, 1903403 (2020).

[141]S. Pitchaiya, M. Natarajan, A. Santhanam, V. Asokan, A. Yuvapragasam, V. Madurai Ramakrishnan, S. E. Palanisamy, S. Sundaram, and D. Velauthapillai, "A review on the classification of organic/inorganic/carbonaceous hole transporting materials for perovskite solar cell application", Arabian Journal of Chemistry **13**, 2526–2557 (2020).

[142]L. Lin, T. W. Jones, T. C.-J. Yang, N. W. Duffy, J. Li, L. Zhao, B. Chi, X. Wang, and G. J. Wilson, "Inorganic Electron Transport Materials in Perovskite Solar Cells", Advanced Functional Materials **31**, 2008300 (2021).

[143]X. Ding, H. Wang, C. Chen, H. Li, Y. Tian, Q. Li, C. Wu, L. Ding, X. Yang, and M. Cheng, "Passivation functionalized phenothiazine-based hole transport material for highly efficient perovskite solar cell with efficiency exceeding 22%", Chemical Engineering Journal **410**, 128328 (2021).

[144]L. Dongxue and Y. Liu, "Recent progress of dopant-free organic hole-transporting materials in perovskite solar cells", Journal of Semiconductors **38**, 011005 (2017).

[145]A. Krishna and A. C. Grimsdale, "Hole transporting materials for mesoscopic perovskite solar cells – towards a rational design?", Journal of Materials Chemistry A **5**, 16446–16466 (2017).

[146]Y. Wu, J. Wang, X. Qiu, R. Yang, H. Lou, X. Bao, and Y. Li, "Highly Efficient Inverted Perovskite Solar Cells with Sulfonated Lignin Doped PEDOT as Hole Extract Layer", ACS Applied Materials and Interfaces **8**, 12377–12383 (2016).

[147]D. Liu, Y. Li, J. Yuan, Q. Hong, G. Shi, D. Yuan, J. Wei, C. Huang, J. Tang, and M. K. Fung, "Improved performance of inverted planar perovskite solar cells with F4-TCNQ doped PEDOT:PSS hole transport layers", Journal of Materials Chemistry A **5**, 5701–5708 (2017).

[148]Q. Wang, C. C. Chueh, M. Eslamian, and A. K. Jen, "Modulation of PEDOT:PSS pH for efficient inverted perovskite solar cells with reduced potential loss and enhanced stability", ACS Applied Materials and Interfaces **8**, 32068–32076 (2016).

[149]S. Wang, W. Yuan, and Y. S. Meng, "Spectrum-Dependent Spiro-OMeTAD Oxidization Mechanism in Perovskite Solar Cells", ACS Applied Materials & Interfaces **7**, 24791–24798 (2015).

[150]Q. Wang, C. Bi, and J. Huang, "Doped hole transport layer for efficiency enhancement in planar heterojunction organolead trihalide perovskite solar cells", Nano Energy **15**, 275–280 (2015).

[151]H. M. Alishah, F. P. G. Choi, F. Kuruoglu, A. Erol, and S. Gunes, "Improvement of fill factor by the utilization of Zn-doped PEDOT:PSS hole-transport layers for p-i-n planar type of perovskite solar cells", Electrochimica Acta **388**, 138658 (2021).

[152]H. Kwon, J. Won Lim, J. Han, L. Na Quan, D. Kim, E.-S. Shin, E. Kim, D.-W. Kim, Y.-Y. Noh, I. Chung, and D. Ha Kim, "Towards efficient and stable perovskite solar cells employing non-hygroscopic F4-TCNQ doped TFB as the hole-transporting material", Nanoscale **11**, 19586–19594 (2019).

[153]T. A. Berhe, W.-N. Su, C.-H. Chen, C.-J. Pan, J.-H. Cheng, H.-M. Chen, M.-C. Tsai, L.-Y. Chen, A. A. Dubale, and B.-J. Hwang, "Organometal halide perovskite solar cells: degradation and stability", Energy & Environmental Science **9**, 323–356 (2016).

[154]N. H. Tiep, Z. Ku, and H. J. Fan, "Recent Advances in Improving the Stability of Perovskite Solar Cells", Advanced Energy Materials **6**, 1501420 (2016).

[155]C. T. Lin, J. Lee, J. Kim, T. J. Macdonald, J. Ngiam, B. Xu, M. Daboczi, W. Xu, S. Pont, B. Park, H. Kang, J. S. Kim, D. J. Payne, K. Lee, J. R. Durrant, and M. A. McLachlan, "Origin of Open-Circuit Voltage Enhancements in Planar Perovskite Solar Cells Induced by Addition of Bulky Organic Cations", Advanced Functional Materials **30**, 1906763 (2020).

[156]M. Stolterfoht, C. M. Wolff, J. A. Márquez, S. Zhang, C. J. Hages, D. Rothhardt, S. Albrecht, P. L. Burn, P. Meredith, T. Unold, and D. Neher, "Visualization and suppression of interfacial recombination for high-efficiency large-area pin perovskite solar cells", Nature Energy **3**, 847–854 (2018).

[157]W. Tress, N. Marinova, T. Moehl, S. M. Zakeeruddin, M. K. Nazeeruddin, and M. Grätzel, "Understanding the rate-dependent J–V hysteresis, slow time component, and aging in CH3NH3PbI3 perovskite solar cells: the role of a compensated electric field", Energy & Environmental Science **8**, 995–1004 (2015).

[158]K. Domanski, B. Roose, T. Matsui, M. Saliba, S.-H. Turren-Cruz, J.-P. Correa-Baena, C. R. Carmona, G. Richardson, J. M. Foster, F. D. Angelis, J. M. Ball, A. Petrozza, N. Mine, M. K. Nazeeruddin, W. Tress, M. Grätzel, U. Steiner, A. Hagfeldt, and A. Abate, "Migration of cations induces reversible performance losses over day/night cycling in perovskite solar cells", Energy & Environmental Science **10**, 604–613 (2017).

[159]Y. Du, Q. Tian, S. Wang, T. Yang, L. Yin, H. Zhang, W. Cai, Y. Wu, W. Huang, L. Zhang, K. Zhao, and S. (Liu, "Manipulating the Formation of 2D/3D Heterostructure in Stable High-Performance Printable CsPbI3 Perovskite Solar Cells", Advanced Materials **35**, 2206451 (2023).

[160]D. Zhao, D. Gao, X. Wu, B. Li, S. Zhang, Z. Li, Q. Wang, Z. Wu, C. Zhang, W. C. H. Choy, X. Zhong, Q. He, and Z. Zhu, "Efficient and Stable 3D/2D Perovskite Solar Cells through Vertical Heterostructures with (BA)4AgBiBr8 Nanosheets", Advanced Materials **34**, 2204661 (2022).

[161]M. Jung, T. J. Shin, J. Seo, G. Kim, and S. I. Seok, "Structural features and their functions in surfactant-armoured methylammonium lead iodide perovskites for highly efficient and stable solar cells", Energy & Environmental Science **11**, 2188–2197 (2018).

[162]Z. Wang, Q. Lin, F. P. Chmiel, N. Sakai, L. M. Herz, and H. J. Snaith, "Efficient ambient-air-stable solar cells with 2D–3D heterostructured butylammonium-caesium-formamidinium lead halide perovskites", Nature Energy **2**, 1–10 (2017).

Chapter 3

Experimental Methods

In this chapter, only common experimental methods are covered. For specific details in each experiment, such as material providers and fabrication specifications, refer to the experimental methods in each chapter.

3.1 Device and Sample Fabrication

Substrates were chosen according to the type of measurements. For solar cell devices or electrical characterizations, either indium tin oxide (ITO) substrates or fluorine doped tin oxide (FTO) substrates were used. For optical measurements, quartz substrates were used in order to reduce interference or substrate absorption. Then, substrates were cleaned in an ultrasonic bath in 2 % (%v/v) Hellmanex III solution, deionized water, acetone, and isopropanol, consecutively. Between each solvent, substrates were washed and rinsed with the next solvent to minimize the residuals. Immediately before thin film deposition, 15 minutes of 100 W oxygen plasma or 20 minutes ultraviolet-ozone (UV-ozone) treatment was performed.

Most of the materials, except perovskite layers, MoO_3 and top metal contacts, were deposited by static spin-coating in ∼30 µL for ITO and quartz, or with ∼60 µL for FTO. For perovskite thin films, a modified two-step deposition method was used with an anti-solvent dripping step during spinning.[1] Details of spin rate, concentrations and solvents for each material, refer to the experimental sections of each chapters.

The MoO_3 transport layer for organic photovoltaics and top metal contacts were vacuum evaporated in physics department under 10^{-6} mbar to 10^{-7} mbar. For perovskite devices,

80 nm – 100 nm of top metal contacts were made by vacuum evaporation of either silver (inverted devices, p-i-n) or gold (conventional devices, n-i-p) with a deposition rate lower than 1 Å s^{-1}. For organic photovoltaic devices, a 10 nm of MoO_3 hole transport layer was deposited first followed by a 80 nm – 100 nm of Ag.

In order to minimize environmental contamination, samples were prepared either in cleanroom or inside nitrogen glovebox. In Chapter 5, PEDOT:PSS layers were deposited in the clearnroom in physics department, and then immediately transferred to the glovebox in material department for the other layers. In Chapter 6, all the layers were prepared in the cleanroom and the glovebox in physics department.

3.2 Density Functional Theory

Density functional theory (DFT) simulations were carried out to show quantum chemical properties of organic molecules by software Gaussian 16 on Imperial High Performance Computing service.[2] Molecules were all simulated as in gas phase in B3LYP theory model with 6-311G(d,p) basis set.[3–7] Alkyl side chains of the simulated molecules were mostly included without omission. However, in some calculations (indicated together with the data), the alkyl side chains were simplified as a methyl group to reduce the computational complexity. In polymer cases, simulations were done to at least trimer level for a sufficient conjugation length. For conventions, z-direction was chosen to be perpendicular to the conjugated backbone.

Ground states were simulated by converging to an energy minimum with multiple starting points in order to minimize initial condition bias. Energy levels of molecular orbitals, electrostatic potential (ESP) maps, dipole moments and quadrupole moments were extracted from ground state optimizations. ESP maps were presented by mapping to isotropic electron density surface to show electron distribution. The reported quadrupole moments were derived from the traceless quadrupole moments in the output file.

Frequency calculations were used to find Raman modes in both neutral ground states and polaronic ground states. A scaling factor of 0.97 was used for the frequency of vibration.[8] Software Gaussview 6.1 was used to simulate spectra as well as assign peaks.

In conformational scans, a specific dihedral angle was scanned while optimizing the other geometric parameters. Scan steps of 18° for a full 360° rotation were carried out to show a

potential curve under dihedral rotations.

3.3 Optical Characterizations

3.3.1 UV-Visible Spectroscopy

Absorbance spectra were measured with a Shimadzu UV-2600 UV-visible (UV-vis) spectrophotometer. The absorbance ($A_s(\lambda)$) of the sample was converted by the definition of absorbance:

$$A_s(\lambda) = \ln\left(\frac{I_{sub}(\lambda)}{I_s(\lambda)}\right) \quad = \ln\left(\frac{T_{sub}(\lambda)}{T_s(\lambda)}\right) \tag{3.1}$$

where $I(\lambda)$ is the light intensity passing through and $T(\lambda)$ is the transmittance with the footnote s for sample and sub for substrate.

3.3.2 Photoluminescence Spectroscopy

Photoluminescence (PL) were carried out with an FLS1000 PL spectrometer from Edinburgh Instruments. Samples were excited with appropriate incident light frequency from a 450 W xenon lamp. The excitation light was filtered by a short-pass filter before the sample to reduce the background noise. The emitted light was filtered by a long-pass filter to eliminate interference from the incident light. The PL emission was scanned with dwell time of 0.2 s and spectral resolution of 1 nm. For specific excitation wavelength, refer to the experimental section at the end of each chapter.

Transient PL was done under the same filter setup with a laser incident light probing at the peak PL position. The PL intensity was set to the same counts per second to provide a similar initial condition between samples. The instrument response function was measured and provided with the transient curve. Results were fitted with FAST software to indicate the decay rate constant.

3.3.3 Raman Spectroscopy

Raman spectra were measured by a Renishaw inVia Raman microscope in a backscattering configuration with a 50 × objective and holographic notch filters to remove Rayleigh scattered

light. A diffraction grating with 2400 line/mm or 1200 line/mm was used for 514 nm or 633 nm laser. Averaging was implemented over different spots on the sample to improve the signal-to-noise ratio, and a polynomial background subtraction was carried out. To reduce degradation, samples were placed in a Linkam stage under a constant nitrogen flow. Laser power, exposure time, and measurement accumulation number were optimized and kept consistent for the same experiments.

3.4 Energetic Characterizations

For all the energetic characterizations, an APS04 system from KP Technology Ltd was used. Density of states (DOS) was converted from the spectra of ambient photoemission spectroscopy (APS) by a Python program included in Appendix C. Further discussion on the conversion principles are discussed in Section 3.4.3.

3.4.1 Fermi Level

To determine the Fermi level (E_F) of a material, a non-contact Kelvin probe measurement is applied. Testing samples are grounded while being linked to the Kelvin probe, forming a close electric circuit. Due to the E_F difference, free charges flow between the testing sample and the tip, creating a capacitor system. The redistributed charges produces a contact potential difference (CPD), which balances out the E_F difference (Fig. 3.1). By applying a backing voltage (V_b) to nullify the build-up potential difference, the CPD can be measured and then be converted to the absolute E_F of the testing material as shown in Fig. 3.1c. This method was firstly used by Lord Kelvin, after whom the probe is named, in 1861.[9]

Despite the simplicity, this measurement is highly sensitive and is easily influenced by the environmental background noise. In order to improve the signal-to-noise ratio, a common approach in modern Kelvin probe measurements utilizes the probe-to-sample distance to enable an off-null measurement as shown in Fig. 3.2c.[10,11] In this approach, the reference tip is oscillating sinusoidally above the sample and the distance $d(t)$ can be described as

$$d(t) = \Delta d \sin(\omega t) + d_0 \tag{3.2}$$

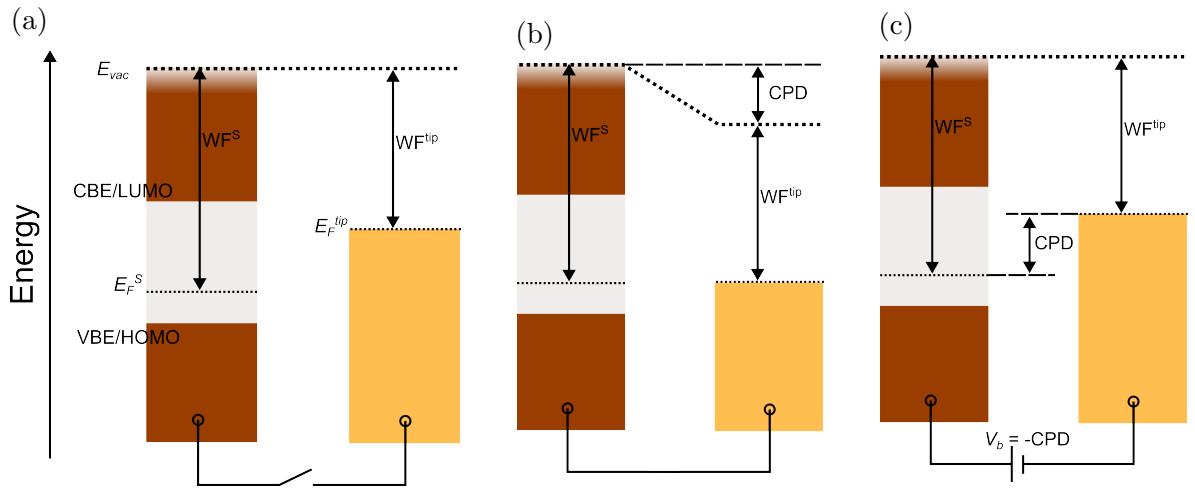


Figure 3.1: Schematic energy diagram of a semiconductor sample measured by a Kelvin probe tip in (a) before contact (in isolation), (b) after electrical contact and (c) applied with backing voltage V_b = CPD. The Fermi levels and work functions are labeled as E_F and WF with superscript tip or S for sample. The local vacuum energy level, valence band edge/highest occupied molecular orbital and conduction band edge/lowest unoccupied molecular orbital are labeled as E_{vac}, VBE/HOMO and CBE/LUMO.

with t as time, Δd as half of the oscillating magnitude, ω as frequency and d_0 as average distance. With the approximation of the capacitance $C(t)$ across the tip and the sample as a simple parallel-plate capacitor, the time dependent surface charge $Q(t)$ on the tip can be described as

$$\begin{aligned} Q(t) &= C(t)V \\ &= \frac{\epsilon A}{d(t)}V \\ &= \frac{\epsilon A}{\Delta d \sin(\omega t) + d_0}(V_b + V_{CPD}) \end{aligned} \tag{3.3}$$

with C as capacitance, V as voltage, ϵ as electric permittivity, A as area of capacitance, V_b as backing potential and V_{CPD} as CPD. The output voltage V_{output} from the system can then be further expressed as

$$\begin{aligned} V_{output} &= IR \\ &= \frac{dQ}{dt}R \\ &= \frac{-\epsilon A R\,\Delta d}{\omega} \times \frac{\cos(\omega t)}{(\Delta d \sin(\omega t) + d_0)^2}(V_b + V_{CPD}) \end{aligned} \tag{3.4}$$

with R as the effective system resistance. A demonstrative plot of $Q(t)$ and V_{output} is shown in Fig. 3.2. Despite the complex time dependency of V_{output}, Eq. (3.4) shows that the peak-to-peak

output voltage V_{ptp} is linearly proportional to $V_b + V_{CPD}$. Therefore, V_{CPD} can be obtained by measuring V_{ptp} with various non-zero V_b (off-null measurement). Since off-null method applies a significant V_b compared to the background noise, this method improves the accuracy of CPD measurements.

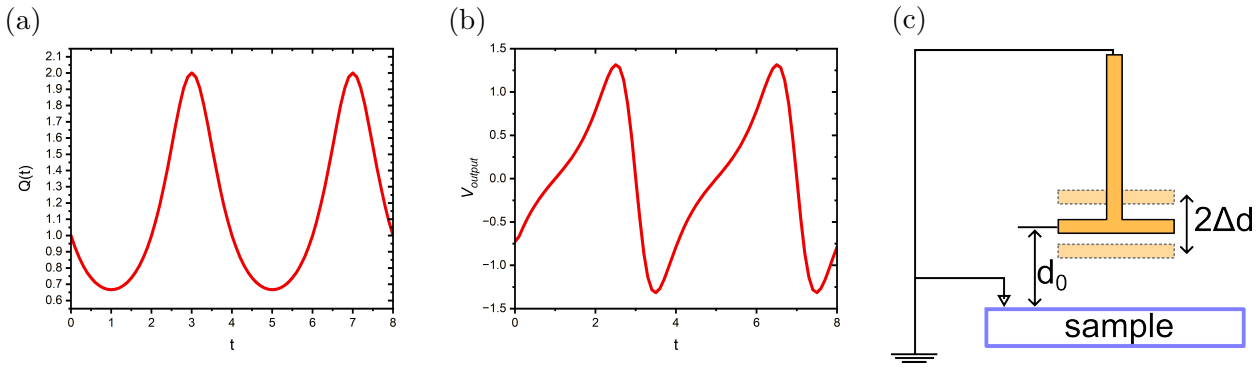


Figure 3.2: Schematic diagram and plots for off-null Kelvin probe measurement. (a) Surface charge $Q(t)$ on tip and (b) output voltage V_{output} with ω set as $1/2\pi$, Δd set as 0.5; ϵ, A, d_0 and $(V_b + V_{CPD})$ set as 1. (c) A diagram of off-null Kelvin probe setup with the average distance d_0 and oscillation magnitude $2\Delta d$.

In order to obtain absolute E_F of samples, the tip was calibrated in a daily basis to guarantee the high accuracy across measurements. Firstly, the CPD of the tip with respect to a silver reference was measured. The work function of the silver reference was, then, determined by APS to calibrate the absolute work function/E_F of the tip with respect to the vacuum level.

In this report, the tip was oscillating in ∼81 Hz with V_b swapping between −7 V and 7 V. The samples were grounded through ITO or FTO substrates for an unbiased electrical background. Kelvin probe measurements were kept in dark for at least 200 s or longer in order to reach dark equilibrium. The measured CPD was then further converted to E_F by the calibrated E_F of the tip.

3.4.2 Ambient Photoemission Spectroscopy

Ambient photoemission spectroscopy (APS) is used to determine the energy levels of valence band edge (VBE) for inorganic semiconductors, highest occupied molecular orbital (HOMO) for organic semiconductors or Fermi level (E_F) for conductors. In APS measurement, ultraviolet (UV) light is generated by a deuterium lamp, and then the UV light is selected by a monochromator with photon energy range from 3.5 eV to 6.8 eV. The monochromatic UV light pumps out the electrons from sample surface within ∼10 nm. The photogenerated free

electrons react with air and generate ions and radicals such as N_2^- and O_2^-. These charge species are then collected by a positively biased tip (10 V) and recorded. A schematic diagram of APS is shown in Fig. 3.3.

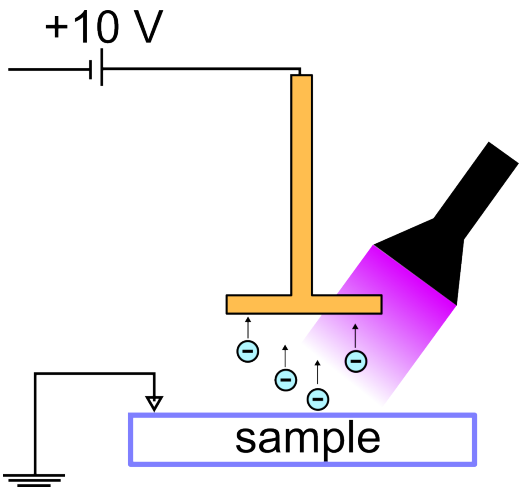


Figure 3.3: A schematic diagram of ambient photoemission system. The tip is positively biased in 10 V while the monochromatic ultraviolet (UV) light source exiting the sample. The negative spheres are representing the negatively charged atmospheric radicals/ions.

Unlike ultraviolet photoelectron spectroscopy, APS signal was found to be either square-root or cube-root related to excitation energy according to Fowler's theory.[11–13] To understand the power relationship between photoemission and UV excitation energy, an estimation on the number of UV accessible electrons, which have high enough energy to be extracted from the sample, is crucial. To begin with, the electron distribution in metallic samples should follow the Fermi-Dirac statistics:

$$N = \iiint 2\left(\frac{m}{h}\right)^3 \frac{dv_x\, dv_y\, dv_z}{e^{\left[\frac{1}{2}m({v_x}^2+{v_y}^2+{v_z}^2)-\epsilon\right]/kT}+1} \tag{3.5}$$

where N is total number of electrons, m is electron mass, h is Planck constant, ϵ is total chemical potential, k is Boltzmann constant, T is temperature and v_n is electron's velocity on n-direction. To an acceptable first approximation, ϵ is an isotropic constant equal to the highest energy level where the electrons reside at 0 K.

According to Fowler's theory, only electrons with sufficient energy normal to the surface (z-direction) are to be considered accessible by APS measurement. Therefore, by integrating

over the horizontal directions, the number of APS accessible electrons N_{APS} is

$$\begin{aligned} N_{APS} &= 2\left(\frac{m}{h}\right)^3 \int\int_0^\infty \int_0^{2\pi} \frac{\rho\, dv_z\, d\rho\, d\theta}{e^{\left[\frac{1}{2}m({v_z}^2+\rho^2)-\epsilon\right]/kT}+1} \\ &= \frac{4\pi kT}{m}\left(\frac{m}{h}\right)^3 \int \ln\left[1+e^{(\epsilon-\frac{1}{2}m{v_z}^2)/kT}\right] dv_z. \end{aligned}$$

With ψ_0 as extraction energy barrier and $\psi = \psi_0 - \epsilon$ be work function, the N_{APS} is now

$$\begin{aligned} N_{APS} &= \frac{4\pi kT}{m}\left(\frac{m}{h}\right)^3 \int_{\frac{1}{2}m{v_z}^2=\psi_0-h\nu}^\infty \ln\left[1+e^{(\epsilon-\frac{1}{2}m{v_z}^2)/kT}\right] dv_z \\ &= \frac{2\sqrt{2}\pi(mkT)^{3/2}}{h^3}\int_0^\infty \frac{\ln\left[1+e^{-\xi+(h\nu-\psi)/kT}\right]}{\left[\xi+(\psi_0-h\nu)/kT\right]^{1/2}}\, d\xi \end{aligned} \tag{3.6}$$

where $h\nu$ is the photon energy and $\xi = \left[\frac{1}{2}m{v_z}^2 - (\psi_0 - h\nu)\right]/kT$.

Since APS is only focusing on the photon energy close to the onset of photoemission ($h\nu \approx \psi$), the denominator of Eq. (3.6) can be approximated as $\left[(\psi_0 - h\nu)/kT\right]^{1/2}$, so

$$N_{APS} = \frac{2\sqrt{2}\pi m^{3/2}}{h^3}\frac{k^2T^2}{(\psi_0-h\nu)^{1/2}}\int_0^\infty \ln\left[1+e^{-\xi+(h\nu-\psi)/kT}\right] d\xi. \tag{3.7}$$

The logarithmic numerator in Eq. (3.7) can further be expanded with respect to $\mu = (h\nu - \psi)/kT$ and be separated into two cases:

$$N_{APS} = \begin{cases} \frac{2\sqrt{2}\pi m^{3/2}}{h^3}\frac{k^2T^2}{(\psi_0-h\nu)^{1/2}}\left[e^\mu - \frac{e^{2\mu}}{2^2} + \frac{e^{3\mu}}{3^2} - \dots\right] & (\mu \le 0) \\ \frac{2\sqrt{2}\pi m^{3/2}}{h^3}\frac{k^2T^2}{(\psi_0-h\nu)^{1/2}}\left[\frac{\pi^2}{6} + \frac{\mu^2}{2} - \left(e^{-\mu} - \frac{e^{-2\mu}}{2^2} + \frac{e^{-3\mu}}{3^2} - \dots\right)\right] & (\mu \ge 0). \end{cases} \tag{3.8}$$

When $T \to 0$, the two cases become

$$N_{APS} \propto \begin{cases} (h\nu-\psi)^2 & (h\nu > \psi) \\ 0 & (h\nu < \psi). \end{cases} \tag{3.9}$$

Eq. (3.9) shows that the square-root of N_{APS} will be linear proportional to the photon energy of UV light while the linear cutoff with respect to the baseline determines the energy of the highest electron state.

Based on the success in metallic materials, Baikie et al. extended the theory to semiconducting materials by experiments and found that the power of N_{APS} should be

cube root for semiconductors in 2014.[11,13] An example APS spectrum is shown in Fig. 3.4a. Typically, there are some weak APS signals shallower than the linear fitting line (red shaded area in Fig. 3.4a). These signals was shown to be related to tail states (shallow traps), and the integration of the area between APS signal and the fitting line could qualitatively show the amount of tail states.[14,15]

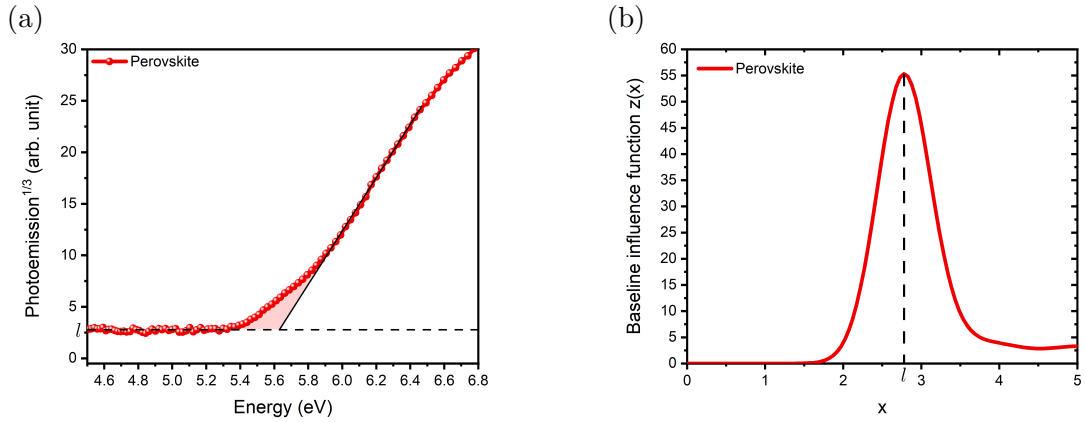


Figure 3.4: Demonstration plots of ambient photoemission spectroscopy spectrum (APS) with perovskite and the baseline influence function. (a) An example APS spectrum of perovskite with black dash line for the baseline at l and the solid black line for the linear fit. The intersect of the baseline and the linear fit determines the energy level of valence band edge (VBE) of this perovskite sample. The red shaded area shows the area of tail states. (b) The baseline influence function converted from the APS spetrum with its maximum located at l for the baseline.

To improve the consistency and the speed of processing APS spectra, a systematic algorithm (Appendix C) is introduced. For searching the baseline, normalized Gaussian function is used as a weighting function for each data point to calculate the baseline influence function z:

$$z(x) = \sum_i \frac{1}{\sqrt{(2\pi)}c} e^{\frac{-(x-y_i)^2}{2c^2}} \tag{3.10}$$

with y_i as the cube-root (square-root) photoemission of i-th data point and weighting window $c = 0.3$ (0.3 is tested to be the best weighting window for APS04) as shown in Fig. 3.4b. Therefore, the value l for the baseline, where z is maximized, can be easily determined by $z'(l) = 0$. For the energy level of VBE/HOMO, a linear regression is applied to find the most linear region of the curve together with the fitting error. The intrinsic system error of APS04 is about 50 meV, so the errors indicated in this thesis is the larger one out of the fitting error and the intrinsic system error. For some special cases in which a specific band of electron states are studied, the fitting will be limited to the energy range of interest. The final output data in

this thesis will be subtracted from the baseline for a better visual presentation.

3.4.3 Density of States

Ambient photoemission spectroscopy (APS) has multiple advantages in its convenience of use, resembling real operation conditions and less degradation on the sample. However, unlike ultraviolet photoelectron spectroscopy (UPS) which has an established conversion correlation to electron density of states (DOS), the correlation between APS signal to DOS was still remained unclear. In order to link APS signal to DOS, a comparison of the methodology behind APS and UPS is provided here. The theoretical as well as experimental studies reveal the high accuracy of APS technique for DOS measurement and this has never been applied or reported in the literature. The theoretical derivation here shows the conversion relationship for metals and the empirical correlation (cube root relation) for the semiconducting materials. Further comparison to UPS may enrich the findings and allow it to be complete for publication.

In Eq. (3.6), Fowler's theory indicate that only electrons with sufficient velocity normal to the sample surface (v_z) are able to be extracted, and it has been further supported by experiments. This could be related to that, in ambient environment, electrons with misaligned kinetic movement may not be able to leave the surface easily and also the charge species formed by these electrons will be more likely reabsorbed by the material. However, this constrain is not applicable to UPS where the measurement is done in high vacuum environment. By releasing this constrain, the number of accessible electrons N_{UPS} for UPS can be described as:

$$\begin{aligned} N_{UPS} &= 2\left(\frac{m}{h}\right)^3 \int_{\frac{1}{2}mr^2=\psi_0-h\nu}^{\infty} \int_0^{\pi} \int_0^{2\pi} \frac{r^2 \sin\theta \, dr \, d\theta \, d\phi}{e^{(\frac{1}{2}mr^2-\epsilon)/kT}+1} \\ &= 8\pi\left(\frac{m}{h}\right)^3 \int_{\frac{1}{2}mr^2=\psi_0-h\nu}^{\infty} \frac{r^2}{e^{(\frac{1}{2}mr^2-\epsilon)/kT}+1} \, dr \\ &= \frac{16\pi kT}{m}\left(\frac{m}{h}\right)^3 \int_0^{\infty} \frac{\xi+(\psi_0-h\nu)/kT}{e^{\xi+(\psi-h\nu)/kT}+1} \, d\xi \end{aligned} \tag{3.11}$$

with m as mass of electron, h as plank constant, ψ_0 as extraction energy barrier, ϵ as total chemical potential, k as Boltazmann constant, T as temperature, ν as UV light frequency, $\psi = \psi_0 - \epsilon$ as work function and $\xi = (\frac{1}{2}mr^2 - \psi_0 + h\nu)/kT$.

Following the same approximation that $h\nu \approx \psi$, the numerator of Eq. (3.11) can be

approximated as $(\psi_0 - h\nu)/kT$. This leads to an analytical solution:

$$N_{UPS} = \frac{16\pi(\psi_0 - h\nu)}{m}\left(\frac{m}{h}\right)^3 \ln\left[e^{(h\nu-\psi)/kT} + 1\right]. \tag{3.12}$$

When $T \to 0$,

$$N_{UPS} \propto \begin{cases} (\psi_0 - h\nu)(h\nu - \psi) \approx h\nu - \psi & (h\nu > \psi) \\ 0 & (h\nu < \psi). \end{cases} \tag{3.13}$$

The results show that N_{UPS} will be linearly proportional to the excitation photon energy which is consistent to the usual interpretation for UPS.[16] By comparing Eq. (3.9) and Eq. (3.13), a conversion between APS signal to UPS signal should be

$$N_{UPS} \propto (h\nu - \psi) \propto \begin{cases} {N_{APS}}^{1/2} & \text{(for conductors)} \\ {N_{APS}}^{1/3}. & \text{(for semiconductors)} \end{cases} \tag{3.14}$$

Since the DOS of interest should be the intrinsic state distribution without orientation bias, DOS should be the first derivative of N_{UPS} to energy E as DOS $= \frac{d}{dE}N_{UPS}$. Therefore, the conversion relationship of N_{APS} to DOS should be

$$\text{DOS} = \frac{d}{dE}N_{UPS} = \begin{cases} \frac{d}{dE}{N_{APS}}^{1/2} & \text{(for conductors)} \\ \frac{d}{dE}{N_{APS}}^{1/3}. & \text{(for semiconductors)} \end{cases} \tag{3.15}$$

Despite the simplicity of DOS conversion, the sharp noises in regions of APS baseline are confusing the real DOS signal of the material as shown in Fig. 3.5a. A clear transition from large standard deviation to merely no deviation is shown around 4.9 eV. Since the APS signal around baseline is merely just the noise of the equipment, it is not surprising to have nearly random or scattered distribution for this region. However, the surprisingly low errors for the signal region, where APS signal is above baseline, demonstrates the high reproducibility of this method.

In order to find the intrinsic error behavior of DOS from APS, a large collection (20 types of neat or blend materials) of DOS and its error is studied (Fig. 3.5b). Since each material has its own unique HOMO/VBE level, a systematic adjustment on the energy is crucial to remove

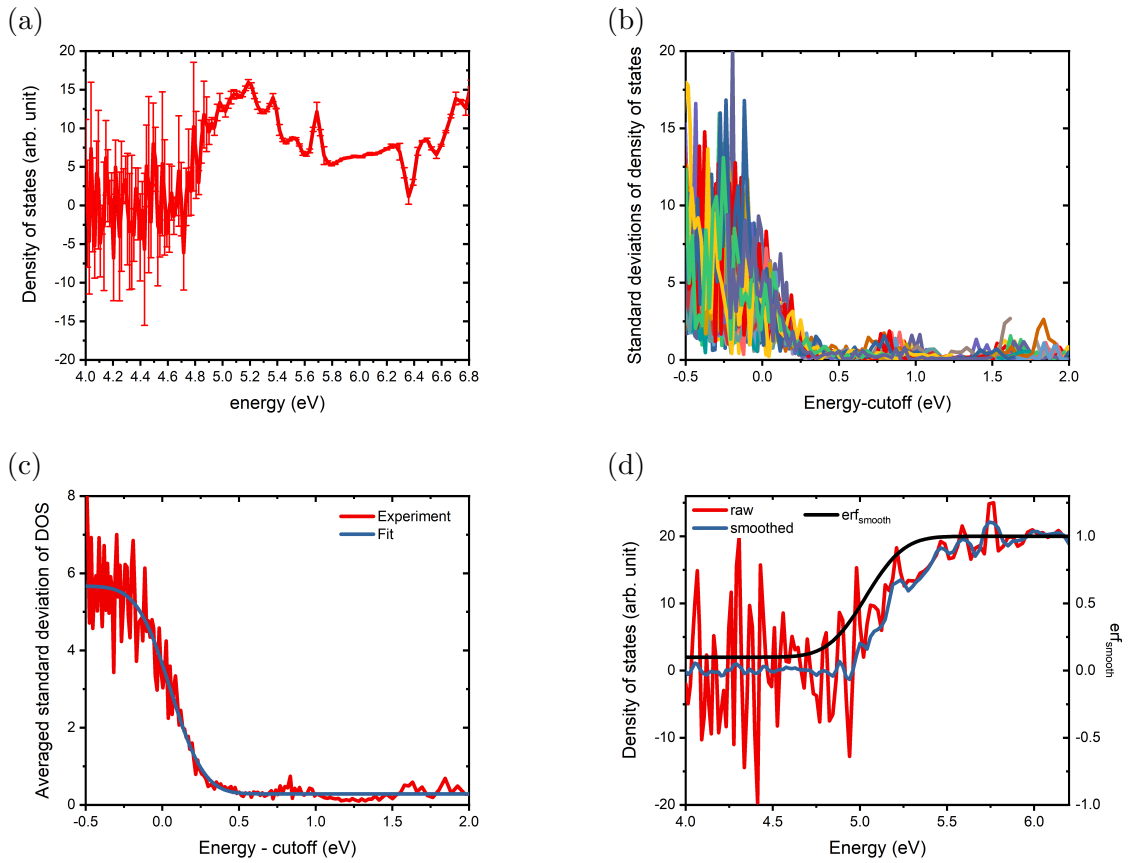


Figure 3.5: Statistics and fitting of the intrinsic density of states (DOS) from ambient photoemission spectroscopy (APS) and an example DOS plot before and after smoothing. (a) An example of DOS with its standard deviation (error bars). (b) Overlaying 20 different materials' DOS standard deviation against the energy offset from their own cutoff energy. The cutoff energy is defined as the highest energy point at which APS signal intersects with its baseline for each material. (c) The averaged standard deviation of DOS from experiment (red) is fitted with a flipped error function (see Eq. (3.16)). (d) An example of the raw DOS (red) and the smoothed DOS (blue) by applying Savitzky-Golay filter as well as an erf_{smooth} filter (Eq. (3.17)).

the influence. Here, the energy axis is adjusted by the cutoff energy of each material, the highest energy point at which APS signal intersects with its baseline, to create a standardized measure. The plot demonstrates that the standard deviation tails off after the cutoff energy and is independent from materials. The average of intrinsic standard deviation trend is then further analyzed by fitting it to a flipped error function $erf_{DOS}(E)$:

$$erf_{DOS}(E) = \frac{\delta_1 - \delta_0}{\sqrt{\pi}} \int_0^{-c(E-\Delta E)} e^{-t^2}\, dt + \frac{\delta_1 + \delta_0}{2} \tag{3.16}$$

where δ_1 is the average standard deviation before cutoff energy, δ_0 is the average standard deviation after cutoff energy, c is the scaling factor for transition between cutoff energy and

ΔE is the center position of transition. The fitting result is shown in Fig. 3.5c where the fit value is $c = 4.123$, $\Delta E = 0.0535$, $\delta_1 = 5.67$ and $\delta_0 = 0.284$. The drastic difference between δ_1 and δ_0 clearly indicates that DOS after cutoff energy is highly accurate and not subject to materials. It is worth noticing that ΔE is roughly about 0.0535 eV which is about the same value to the resolution of APS. This demonstrates that the area shallower than the linear fit, despite being close to cutoff energy, is still with a high level of confidence for revealing the amount of tail states. Also, it shows the high resolution as well as reproducibility of the converted DOS from APS signals.

To improve the clarity without the loss of meaningful data, a specially tailored filter is used for the DOS presentation (Fig. 3.5d). Succeeding from the fitting result, a modified error function with the same scaling factor $c = 4.123$ and shift $\Delta E = 0.0535$ is applied on the raw DOS data:

$$erf_{smooth}(E) = \frac{1 - f_0}{\sqrt{\pi}} \int_0^{c(E-\Delta E)} e^{-t^2}\, dt + \frac{f_0 + 1}{2} \tag{3.17}$$

with f_0 as the multiplication factor for background noise. A Savitzky-Golay filter is then applied to remove the high frequency noises. Though the smooth filter erf_{smooth} will have a small impact on the tail states region, it improves the details below HOMO/VBE levels and consistency across different measurements.

Despite having a robust theory behind the DOS conversion, demonstrations of the applicability in experiment would be essential to strengthen the conversion methodology. Therefore, three series of molecules (see Fig. 3.6d were checked to further prove the validity in real practice. In each series, the organic molecules are having the same dominating donor units with either different alkyl side chains, different acceptor units or different halogenations. Firstly, in Fig. 3.6a, ITICs with different alkyl side chains show the same DOS distribution. This agrees with the report and the common understanding that alkyl side chain does not influence the conjugated backbone.[17] On the other hand, by changing the accepting units in the small molecules (Fig. 3.6b), different levels of molecular orbital interaction would be expected. This will result in a shift to the density distribution, yet maintaining the distribution shape across energy.[18–20] Lastly, through comparing different halogenations on PBDB-T molecule, a significant down shift on DOS distribution is seen. It is coherent with the understanding of electron withdrawing effect deepening the HOMO levels.[21] These results prove the applicability

of photoemission-to-DOS conversion experimentally which widens the range of information which can be extracted by APS analysis on energetics.

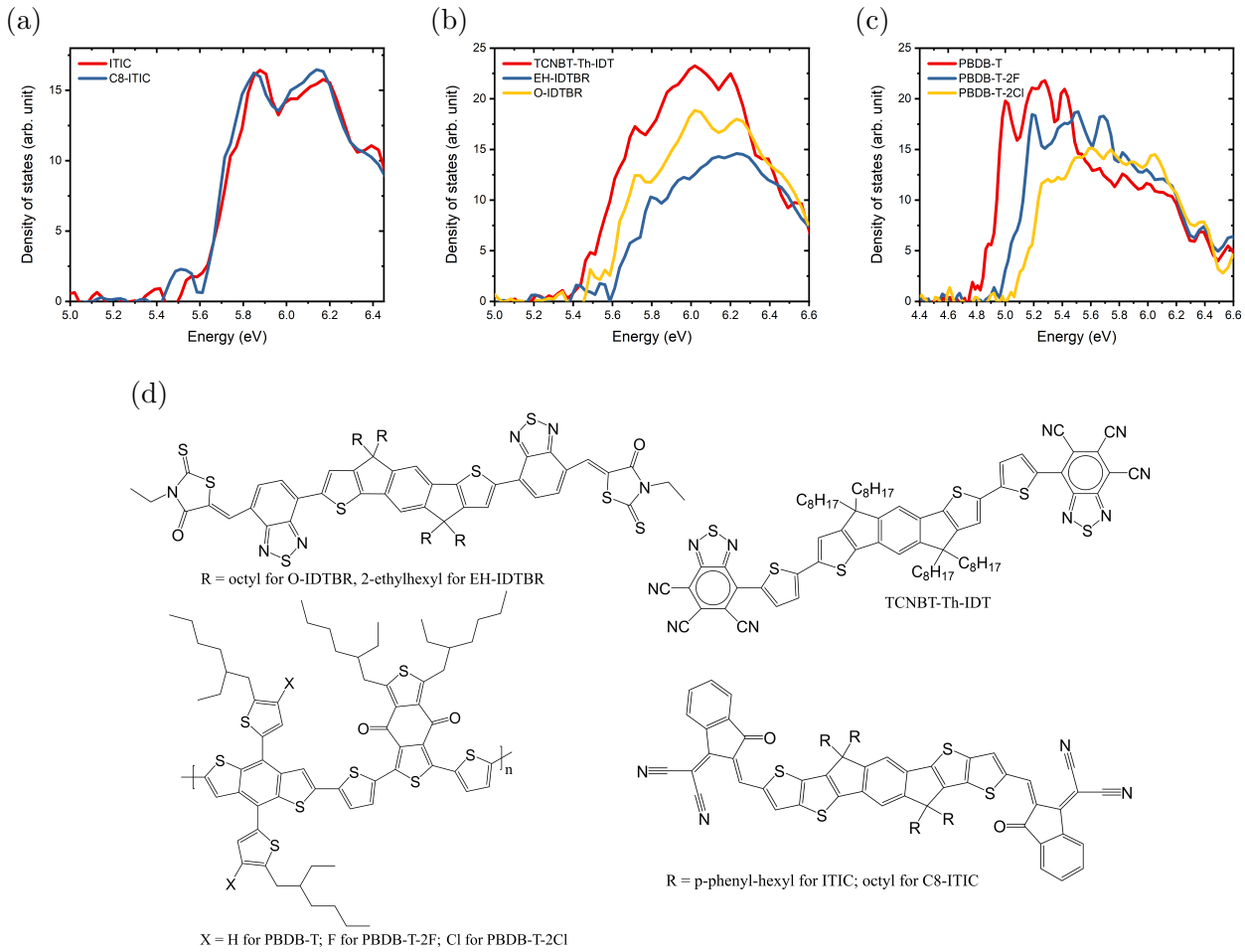


Figure 3.6: Series of experimental examples of density of states (DOS) converted from APS spectra with similar chemical structures. Small organic molecules with (a) different types of side chain, (b) different accepting units and (c) different halogenations. The structure of the molecules are drawn in (d) for reference.

To facilitate efficient DOS conversion as well as smoothing, DOS analysis is also done with a program as attached in Appendix C.

3.5 Morphological and Structural Characterizations

3.5.1 Atomic Force Microscopy

Atomic force microscopy (AFM) is measured by a Park NX10 with a PPP-NCHR type tip under non-contact mode. The images of $5\,\mu m \times 5\,\mu m$ are taken in a resolution of $96\,dpi \times 96\,dpi$ with scan rate of $0.5\,s^{-1}$ to $1\,s^{-1}$. Three different locations are measured for each film in

order to minimize the bias of choice. The images are leveled, scar corrected and polynomial background corrected with Gwyddion. The root mean square (RMS) of the surface height is used to represent the surface roughness.

3.5.2 Thickness Measurements

Film thicknesses are measured by a Brüker Dektak profilometer. Most of the samples are scratched by a metal needle in different locations and orientations to find the average thickness across the film. For hard inorganic layers such as titanium oxide, samples are spin-coated with a protection cover to create the height differences for thickness measurements.

3.5.3 X-Ray Diffraction

X-ray diffraction (XRD) with Cu Ka (1.54 Å) is applied to analyze perovskite crystal structure. The diffraction pattern is scanned over the angle 2θ from 5° to 45° with a step of 0.029 83°. The method is used to identify PbI_2 defect states which has a characteristic peak at 12.67° and low dimensional perovskite (Ruddlesden-Popper phase).

3.5.4 Grazing-Incidence Wide-Angle X-Ray Scattering

Grazing-Incidence Wide-Angle X-Ray Scattering (GIWAXS) is a great tool to study the packing structure of soft material, e.g. organic molecules.[22,23] The measurement is operated at the XRD1 beamline with the beam energy at 12.4 keV. A small incident angle (0.13°) is used to generate the diffraction pattern close to total reflection. Finally, the pattern is recorded with PILATUS 2M area detector, 35 cm behind the samples.

3.6 Electronic and Photoelectronic Characterizations

3.6.1 Electrical Conductivity

Conductivity is measured using the transmission line method on organic field effect transistors with Fraunhofer prefabricated substrates.[24] The conductance is extracted from output curves measured in four different channel lengths 2.5 µm, 5 µm, 10 µm and 20 µm, and the conductivity is derived from the slope of linear fitting.

3.6.2 Solar Cell Characterizations

Solar cell characterizations are mainly current density-voltage (J-V) scans, device stability test and external quantum efficiency (EQE) measurements. In these measurements, samples were kept in a sample chamber of either one slot or six slots which was sealed inside glovebox for inert nitrogen environment. Photomasks with a circular area of $0.045\,\mathrm{cm}^2$ were used to improve the precision on illumination area as well as reduce potential crosstalk between pixels.

J-V scans were obtained using a solar simulator with AM1.5G filters (Oriel Instruments) and a Keithley 2400 Source Measure Unit. The solar simulator was warmed up for at least 30 min and the intensity was calibrated to $100\,\mathrm{mW\,cm^{-2}}$ with a silicon photodiode (Osram BPW21) prior to devices. Both reversed and forward scans were carried out with reverse scans first. The voltage was ranged from 1.2 V to −0.4 V for PEDOT:PSS work in Chapter 5 and 1.6 V to −0.4 V for low dimensional work in Chapter 6 at a rate of $0.1\,\mathrm{V\,s^{-1}}$. For dark scans, lower scan rate of about $0.05\,\mathrm{V\,s^{-1}}$ was used for a higher accuracy in low currents. The scan rates are tuned by adjusting the number of power line cycles (NPLC) factors in Keithley 2400.

A QEX10 system from PV Measurements inc. was used for EQE measurements. The system was also warmed up for at least 30 min and was calibrated with a silicon reference.

3.6.3 Surface Photovoltage

Surface photovoltage (SPV) dynamic is defined as the change of surface electric potential between cycles of dark and illumination.[25,26] An operational schematic diagram and an example SPV curve can be seen in Fig. 3.7. During the measurement, the tip is vibrating in a similar way to the Kelvin probe measurement. The SPV signal is defined as the change of surface potential with a positive sign for electron accumulation and vice versa. Before the measurement, the sample is left in dark to reach equilibrium. When illumination kicks in, charge species such as free charges or ions are either generated or redistributed across the layers of sample by the internal electric field originated from different Fermi levels (E_F) across materials. As SPV signal comes from the potential difference between the tip vibration cycle, it can also record the decay dynamics after the illumination is finished. Since SPV is measured under an open-circuit condition similar to devices operating at open-circuit voltage (V_{OC}), SPV dynamic reveals the kinetic balance between charge generation and recombination. Despite the similarity between

SPV signal and V_{OC}, SPV does not require a complete device setup, so it is able to focus on the recombination or charge separation on specific interfaces by adding in or removing the layers of interests. Here, SPV signals are facilitated by a Kelvin probe as described in Section 3.4.1 by operating with the same vibration frequency and backing voltage.

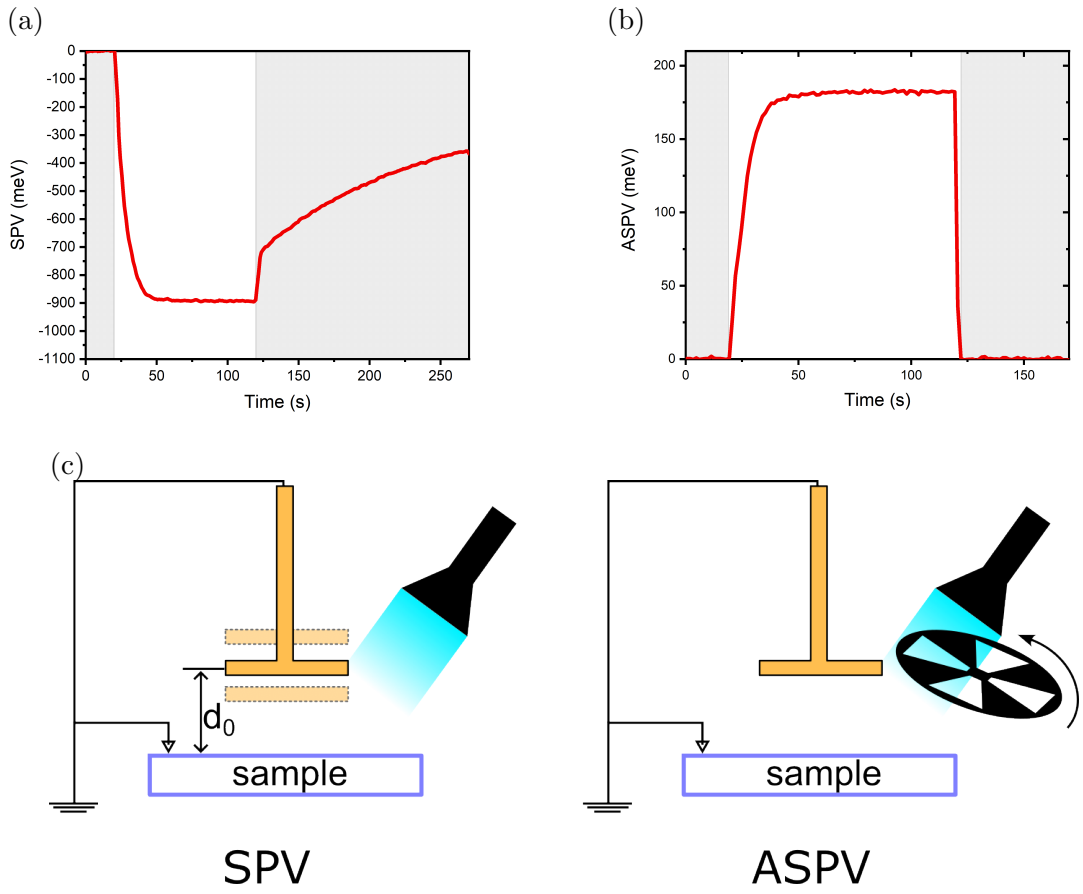


Figure 3.7: Example (a) surface photovoltage (SPV) and (b) alternating surface photovoltage (ASPV) curves of a perovskite sample with (c) their schematic diagrams. The gray background area indicates the light off period. The negative sign of SPV signal indicates hole accumulation and vice versa while the ASPV signal is by definition always positive.

SPV measurements in this work was operated with APS04 from KP Technology. Before measuring SPV, the E_F of test samples were monitored in dark condition for long hours to guarantee a good equilibrium condition was reached. Then, the sample was illuminated with white light generated from a quartz tungsten halogen light source (Dolan-Jenner) at $\sim$20 mW cm^{-2} intensity. The illumination cycle was 100 s followed by the dark decay of 150 s. To compare the signal across different samples, the average of the first 20 s dark equilibrium signal was subtracted as the reference point. Analysis were carried by a Python software for efficiency as copied in Appendix C.

Alternating Surface Photovoltage

As indicated in Section 3.6.3, SPV signal is derived from the change of surface electric potential which does not distinguish what charge species are contributing to the signal. Some materials such as perovskites have significant ionic movements which also contribute to a large build-up potential shift under illumination.[27,28] In order to distinguish signals from different charge species, a high-frequency alternating illumination (or chopped illumination) is applied in alternating surface photovoltage (ASPV).[29,30] As shown in Fig. 3.7c, ASPV measurements does not depend on the tip vibration cycle but on the oscillating illumination cycle governed by an optical chopper. By tuning the alternating illumination frequency, slow moving charge species, such as ions, will not be able to redistribute and generate a potential change, leaving the potential shift from fast moving species only, typically free charges. This makes ASPV suitable for detecting the free charge generation and recombination in perovskite. In ASPV, the signal is defined as the peak-to-peak electric potential difference within the chopped illumination which is different from SPV signal, the change of potential between dark and constant illumination. Beware that, by definition, ASPV does not have signals in the dark period of illumination cycles since there is no peak-to-peak potential changes under constant dark environment.

To screen out the ionic contribution, high frequency (300 Hz) chopped white light at $20\,\mathrm{mW\,cm^{-2}}$ intensity was used on perovskite samples. The illumination cycle was composed of repeating 100 s illumination and 20 s dark, similar to SPV measurements. The dark period in ASPV measurement was shorter than in SPV measurement since ASPV does not have signal without illumination by definition.

References

[1]J.-H. Im, H.-S. Kim, and N.-G. Park, "Morphology-photovoltaic property correlation in perovskite solar cells: One-step versus two-step deposition of $CH_3NH_3PbI_3$", APL Materials **2**, 081510 (2014).

[2]M. J. Frisch, G. W. Trucks, H. B. Schlegel, G. E. Scuseria, M. A. Robb, J. R. Cheeseman, G. Scalmani, V. Barone, G. A. Petersson, H. Nakatsuji, X. Li, M. Caricato, A. V. Marenich, J. Bloino, B. G. Janesko, R. Gomperts, B. Mennucci, H. P. Hratchian, J. V. Ortiz, Izmaylov, J. L. Sonnenberg, D. Williams-Young, F. Ding, F. Lipparini, F. Egidi, J. Goings, B. Peng, A. Petrone, T. Henderson, D. Ranasinghe, V. G. Zakrzewski, J. Gao, N. Rega, G. Zheng, W. Liang, M. Hada, M. Ehara, K. Toyota, R. Fukuda, J. Hasegawa, M. Ishida, J. Nakajima, Y. Honda, O. Kitao, H. Nakai, T. Vreven, K. Throssell, J. A. Montgomery Jr., J. E. Peralta, F. Ogliaro, M. J. Bearpark, J. J. Heyd, E. N. Brothers, K. N. Kudin, V. N. Staroverov, T. A. Keith, R. Kobayashi, J. Normand, K. Raghavachari, A. P. Rendell, J. C. Burant, S. S. Iyengar, J. Tomasi, M. Cossi, J. M. Millam, M. Klene, C. Adamo, R. Cammi, J. W. Ochterski, R. L. Martin, K. Morokuma, O. Farkas, J. B. Foresman, and D. J. Fox, *Gaussian 16 Revision C.01*, Wallingford CT: Gaussian, Inc., 2016.

[3]A. D. McLean and G. S. Chandler, "Contracted Gaussian basis sets for molecular calculations. I. Second row atoms, Z =11–18", The Journal of Chemical Physics **72**, 5639–5648 (1980).

[4]R. Krishnan, J. S. Binkley, R. Seeger, and J. A. Pople, "Self-consistent molecular orbital methods. XX. A basis set for correlated wave functions", The Journal of Chemical Physics **72**, 650–654 (1980).

[5]R. C. Binning and L. A. Curtiss, "Compact contracted basis sets for third-row atoms: Ga-Kr", Journal of Computational Chemistry **11**, 1206–1216 (1990).

[6]M. P. McGrath and L. Radom, "Extension of Gaussian-1 (G1) theory to bromine-containing molecules", The Journal of Chemical Physics **94**, 511–516 (1991).

[7]L. A. Curtiss, M. P. McGrath, J.-P. Blaudeau, N. E. Davis, R. C. Binning, and L. Radom, "Extension of Gaussian-2 theory to molecules containing third-row atoms Ga–Kr", The Journal of Chemical Physics **103**, 6104–6113 (1995).

[8]M. L. Laury, M. J. Carlson, and A. K. Wilson, "Vibrational frequency scale factors for density functional theory and the polarization consistent basis sets", Journal of Computational Chemistry **33**, 2380–2387 (2012).

[9]L. Kelvin, "V. Contact electricity of metals", The London, Edinburgh, and Dublin Philosophical Magazine and Journal of Science **46**, 82–120 (1898).

[10]I. D. Baikie, S. Mackenzie, P. J. Z. Estrup, and J. A. Meyer, "Noise and the Kelvin method", Review of Scientific Instruments **62**, 1326–1332 (1991).

[11]I. D. Baikie, A. C. Grain, J. Sutherland, and J. Law, "Dual Mode Kelvin Probe: Featuring Ambient Pressure Photoemission Spectroscopy and Contact Potential Difference", Energy Procedia, Advanced Materials and Characterization Techniques for Solar Cells II **60**, 48–56 (2014).

[12]R. H. Fowler, "The analysis of photoelectric sensitivity curves for clean metals at various temperatures", Physical Review **38**, 45–56 (1931).

[13]I. D. Baikie, A. C. Grain, J. Sutherland, and J. Law, "Ambient pressure photoemission spectroscopy of metal surfaces", Applied Surface Science **323**, 45–53 (2014).

[14]S. Lee, D. B. Kim, I. Hamilton, M. Daboczi, Y. S. Nam, B. R. Lee, B. Zhao, C. H. Jang, R. H. Friend, J. S. Kim, and M. H. Song, "Control of Interface Defects for Efficient and Stable Quasi-2D Perovskite Light-Emitting Diodes Using Nickel Oxide Hole Injection Layer", Advanced Science **5**, 1801350 (2018).

[15]C. T. Lin, J. Lee, J. Kim, T. J. Macdonald, J. Ngiam, B. Xu, M. Daboczi, W. Xu, S. Pont, B. Park, H. Kang, J. S. Kim, D. J. Payne, K. Lee, J. R. Durrant, and M. A. McLachlan, "Origin of Open-Circuit Voltage Enhancements in Planar Perovskite Solar Cells Induced by Addition of Bulky Organic Cations", Advanced Functional Materials **30**, 1906763 (2020).

[16]J. H. D. Eland, *Photoelectron Spectroscopy: An Introduction to Ultraviolet Photoelectron Spectroscopy in the Gas Phase* (Elsevier, Oct. 22, 2013), 286 pp.

[17]Z. Fei, F. D. Eisner, X. Jiao, M. Azzouzi, J. A. Röhr, Y. Han, M. Shahid, A. S. R. Chesman, C. D. Easton, C. R. McNeill, T. D. Anthopoulos, J. Nelson, and M. Heeney, "An Alkylated Indacenodithieno[3,2-b]thiophene-Based Nonfullerene Acceptor with High Crystallinity Exhibiting Single Junction Solar Cell Efficiencies Greater than 13% with Low Voltage Losses", Advanced Materials **30**, 1705209 (2018).

[18]H. Cha, J. Wu, A. Wadsworth, J. Nagitta, S. Limbu, S. Pont, Z. Li, J. Searle, M. F. Wyatt, D. Baran, J.-S. Kim, I. McCulloch, and J. R. Durrant, "An Efficient, "Burn in" Free Organic Solar Cell Employing a Nonfullerene Electron Acceptor", Advanced Materials **29**, 1701156 (2017).

[19]J. Luke, E. M. Speller, A. Wadsworth, M. F. Wyatt, S. Dimitrov, H. K. H. Lee, Z. Li, W. C. Tsoi, I. McCulloch, D. Bagnis, J. R. Durrant, and J.-S. Kim, "Twist and Degrade—Impact of Molecular Structure on the Photostability of Nonfullerene Acceptors and Their Photovoltaic Blends", Advanced Energy Materials **9**, 1803755 (2019).

[20]P. Kafourou, M. I. Nugraha, A. Nikitaras, L. Tan, Y. Firdaus, F. Aniés, F. Eisner, B. Ding, J. Wenzel, M. Holicky, L. Tsetseris, T. D. Anthopoulos, and M. Heeney, "Near-IR Absorbing Molecular Semiconductors Incorporating Cyanated Benzothiadiazole Acceptors for High-Performance Semitransparent n-Type Organic Field-Effect Transistors", ACS Materials Letters **4**, 165–174 (2022).

[21]S. Zhang, Y. Qin, J. Zhu, and J. Hou, "Over 14% Efficiency in Polymer Solar Cells Enabled by a Chlorinated Polymer Donor", Advanced Materials **30**, 1800868 (2018).

[22]I. Osaka, R. Zhang, G. Sauvé, D.-M. Smilgies, T. Kowalewski, and R. D. McCullough, "High-Lamellar Ordering and Amorphous-Like π-Network in Short-Chain Thiazolothiazole-Thiophene Copolymers Lead to High Mobilities", Journal of the American Chemical Society **131**, 2521–2529 (2009).

[23]M. L. Chabinyc, M. F. Toney, R. J. Kline, I. McCulloch, and M. Heeney, "X-ray Scattering Study of Thin Films of Poly(2,5-bis(3-alkylthiophen-2-yl)thieno[3,2-b]thiophene)", Journal of the American Chemical Society **129**, 3226–3237 (2007).

[24]S. Luan and G. W. Neudeck, "An experimental study of the source/drain parasitic resistance effects in amorphous silicon thin film transistors", Journal of Applied Physics **72**, 766–772 (1992).

[25]D. K. Schroder, "Surface voltage and surface photovoltage: history, theory and applications", Measurement Science and Technology **12**, R16 (2001).

[26]H. Shimizu and C. Munakata, "Nondestructive diagnostic method using ac surface photovoltage for detecting metallic contaminants in silicon wafers", Journal of Applied Physics **73**, 8336–8339 (1993).

[27]P. Calado, A. M. Telford, D. Bryant, X. Li, J. Nelson, B. C. O'Regan, and P. R. Barnes, "Evidence for ion migration in hybrid perovskite solar cells with minimal hysteresis", Nature Communications **7**, 13831 (2016).

[28]G. Alosaimi, S. J. Shin, R. L. Chin, J. H. Kim, J. S. Yun, and J. Seidel, "Probing Charge Carrier Properties and Ion Migration Dynamics of Indoor Halide Perovskite PV Devices Using Top- and Bottom-Illumination SPM Studies", Advanced Energy Materials **11**, 2101739 (2021).

[29]R. S. Nakhmanson, "Frequency dependence of the photo-EMF of strongly inverted Ge and Si MIS structures—I. Theory", Solid-State Electronics **18**, 617–626 (1975).

[30]R. S. Nakhmanson, Z. S. Ovsyuk, and L. K. Popov, "Frequency dependence of photo-EMF of strongly inverted Ge and Si MIS structures—II experiments", Solid-State Electronics **18**, 627–634 (1975).

Chapter 4

Organic Photovoltaic Materials – Impact of Molecular Structure and Packing on Electrostatic Potential and Trap States

Benefiting from the high chemical design freedom, organic semiconductors (OSCs) have been tailored for organic photovoltaic (OPV) applications to reduce loss mechanisms and improve device performance with few successful breakthroughs. Despite the fast improving power conversion efficiency (PCE) in recent years (>18 %), a clear understanding in the density of state (DOS) distribution, particularly its correlation to the molecular design, packing structures and orientations, are still unclear. Herein, a systematic study is carried out from neat materials to blends showing how chemical structure and packing determine their energetics and furthermore device characters. Firstly, the structural origin of energy disorder is investigated to provide understandings and design rules. Secondly, the orientation dependent energetics and its impact on device performance are studied through vacuum deposition or solution process. The origin is then correlated well to the quadrupole moment. This sheds light on understanding interfacial energetics which governs free charge generation. Lastly, blending induced energetic shift is studied by pinpointing DOS distribution to chemical moieties unveiling the packing origin behinds non-Langevin recombination process.

This chapter is based on four publications, Wu et al. [1], Dong et al. [2] and Marin-Beloqui

et al. [3]. One of the publication is recently accepted in Nature Communications as entitled "Molecular orientation-dependent energetic shifts in solution-processed non-fullerene acceptors and their impact on organic photovoltaic performance". In Section 4.2, devices and thin films were fabricated by Jinho Lee.[1] Accelerated photodegradation for Y6, ITIC and O-IDTBR and dihedral scans for ITIC and O-IDTBR were measured or simulated by Joel Luke. In Section 4.3, Vasileios C. Nikolis fabricated films and tested photovoltaic devices (J-V and EQE measurements).[2] Felix Talnack and Stefan C. B. Mannsfeld performed and analyzed the GIWAXS measurements. Work in Section 4.4 was published in Nature Communications. The orientation controlled Y6 and PM6/Y6 planar heterojunctions were fabricated by Yuang Fu and Tack Ho Lee. Y6 orientation-dependent energetic was simulated by Dr. Daiki Minami. PM6:Y6 BHJ devices were fabricated by Chiara Labanti and Song Yi Park. In Section 4.5, thin films of neat polymers or polymer:fullerene blends were fabricated by Jose Marin-Beloqui.[3]

4.1 Introduction

In recent years, organics semiconductors (OSCs) have drawn a significant amount of attention, particularly in organic photovoltaics (OPVs), due to the sharply rising device performance and promising applications, such as low-light or semi-transparent applications.[4–6] This is owing to few successful chemical designs which have unique energetics boosting charge dissociation and reducing recombination loss, such as ITIC and Y6.[7,8] Although these OSCs have led to huge success with their unique optoelectronic properties, the chemical origin of these properties is still under strong debates. In this chapter, molecular structure, packing and orientation dependent energetics and its impact on OPVs are investigated step by step from neat OSCs to blends, including energy disorder, packing dependent energetics by either evaporation or solution-process.

Firstly, the impact of chemical structure on energetic disorders and tail states distribution in high performance non-fullerene acceptors (NFAs) are investigated in Section 4.2. The amount of tail states are extracted from photoemission spectra, and are correlated to the structural rigidity by density functional theory (DFT) simulations pinpointing out the critical locking moiety providing design guides to reduce chemical disorders and recombination losses. In Section 4.3, the impact of molecular packing structure on energetics is investigated by

fine tuning the packing structure of vacuum evaporated sexithiophene (α-6T), a simple small molecule composed of six thiophenes. The electrostatic effect is shown to determine the energetics of lying and standing packing structure, resulting in a sufficient energetic separation to efficiently generate free charges as in a homojunction device. This shows the importance of controlling packing structure can further manipulate the energetics beyond chemical structures. Extending the control of packing structure from evaporation to solution-processed OSCs, Section 4.4 shows a significant orientation dependent energy shift in Y6 depending on the processing solvent. This is correlated to the strong electrical quadrupole moment perpendicular to the conjugated backbone (Q_π) of Y6, which determines the interfacial band bending and device V_{OC}. Lastly, applying the understanding of packing-to-energetic correlation, two polymer:fullerene blend systems are studied. PDTSiTTz:fullerene blends show a systematic shift in density of states (DOSs) originated from the twisting of the conjugated backbone inside the polymer. These studies demonstrate some of the key factors, such as chemical designs and packing structures, which highly correlate to the energetics and furthermore OPV device performance.

4.2 Molecular Structure Induced Traps in Small Molecule Non-Fullerene Acceptors

To begin with, the degree of energetic disorder and charge trapping of different polymer:NFA blends are studied, namely Y6, ITIC and O-IDTBR, in order to unveil the exceptional OPV performance of PM6:Y6 BHJ. The light-intensity-dependent tail state density is characterized by charge extraction measurements at open circuit. The extracted charge carrier density n, which is normally associated with trapped charge in tail states if the device is operated far below the band edge, can be described as:

$$n \propto exp(\Delta E_f / 2E_{ch}) \tag{4.1}$$

where ΔE_f is the quasi-Fermi level splitting and E_{ch} is characteristic slope of the energy tail states. By approximating V_{OC} to ΔE_f, E_{ch} can be determined by the slope of linear regression between $\ln(n)$ and V_{OC}.[9–13] In an ideal band edge condition, E_{ch} is dominated by the thermal

fluctuation k_BT, which is ∼25 meV around room temperature. E_{ch} >25 meV indicates a non-ideal shallow tail state distribution extending into the band gap (E_g). Here, multiple high performance polymer:NFA OPV blends have their E_{ch} ≥60 meV as shown in Fig. 4.1a, which is similar to other fullerene based OPV blends reported before.[14] These large E_{ch} (about 2 to 2.5 times of ideal band edge condition) demonstrate that almost all OPVs reported before have significant tail state density which contributes to charge recombination and serve as trap states.[15] Nonetheless, the E_{ch} values of PM6:Y6 and PM6:BTP-4Cl blends are nearly ideal at 27 meV and 28 meV respectively. These near-ideal E_{ch} were the lowest value reported so far, and it may be one of the key factors which supports the superior performance in both blends despite the small energetic offset between PM6 and Y6 (or BTP-4Cl).[14]

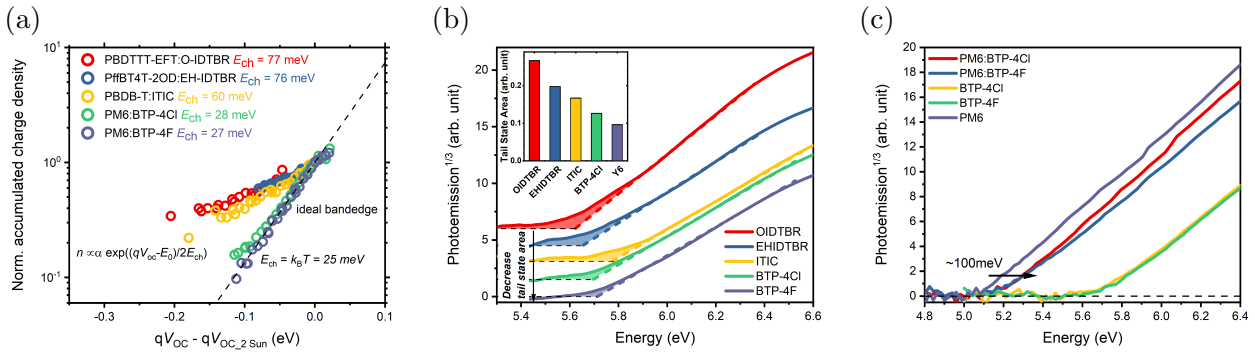


Figure 4.1: Tail states and energetic shifts of high performance OPV blends and neat NFAs. (a) Measurements of the accumulated charge density versus quasi-Fermi level splitting qV_{OC} determined from charge extraction measurements at open circuit as a function of irradiation intensity for a range of polymer:NFA blends. The accumulated charge density is normalized to the charge carrier density at 2 Sun open-circuit condition, and the measured V_{OC} relative to that, (b) The photoemission spectra for selected NFA films, illustrating the extrapolated HOMO level (dashed lines) and the additional sub-gap tail states (the shaded areas)with an insert plot of the integrated tail state areas. (c) PM6:Y6 and PM6:BTP-4Cl blend films compared to PM6, Y6 and BTP-4Cl neat films. ∼100 meV band edge shift on PM6 upon blending with either Y6 or BTP-4Cl.

To unveil the exceptional low tail state density in Y6, the NFAs are investigated for their energetics by APS as shown in Fig. 4.1b. The linear extrapolation (dash lines) indicates the highest occupied molecular orbital (HOMO) energy levels of each NFA.[16] Here, the APS gives the HOMO level of Y6 as 5.70 eV, which is consistent with cyclic voltammetry in literature, 5.65 eV, showing the accuracy of APS measurement.[17] Besides the value of HOMO level, the APS signal below the extrapolation clearly indicates the existence of tail states shallower than the HOMO level. By integrating the tail state area (shaded area in Fig. 4.1b), a relative

comparison of the tail state density between different NFAs could be made. The integrated area of Y6 (and BTP-4Cl) is the smallest among these high performance NFAs, suggesting the low tail state density nature in the BTP based molecules. Moreover, the integrated area of Y6 is nearly 2.5 times of the integrated value of O-IDTBR. This is coherent with the charge extraction results where IDTBRs and ITIC have about 2.5 times and 2 times E_{ch} than the E_{ch} of Y6. Furthermore, these trap states extend into the E_g for about 100 meV, similar to the fitted E_{ch} in Fig. 4.1a. Apart from the low tail states width found in Y6, a noticeable HOMO level deepening by ∼100 meV in PM6 is seen upon blending with Y6 (Fig. 4.1c). This significant deepening may be related to the packing between PM6 and Y6 which may be covered in Section 4.4. The deepening of donor HOMO level may provide an energetic offset between the bulk of donor and the interface between donor and acceptor. Thus, it stabilizes generated free charges by extracting the charges away from the interface. This factor may be a critical key in explaining the high efficiency of PM6:Y6 devices, and further studies such as the origin of such energetic shift will be discussed in Section 4.4.[18]

The previous tail state density measured by APS indicates that Y6 OPV blend has exceptional high performance due to its low tail state density which reduces charge trapping and recombination loss. Furthermore, ideal energetic band edge was accounted for the efficient charge generation in these blends despite the small energy level offset for charge separation.[19] Recently, there were also other reports showing near ideal optical absorption in PM6:Y11 blends (Y11 shares a similar chemical structure with Y6), which has remarkable performance similar to PM6:Y6.[20] These findings indicate the importance of low tail states is a general rule for high performance OPVs, and correlating the origin of this character to the fundamental molecular structure would lead to a deeper knowledge to design relevant molecules for OPV applications. Since tail states are originated from disordered energetic, conformational uniformity and rigidity of the Y6 molecule may explain its exceptional low tail state density. Dihedral energy scans in Fig. 4.2 show the energy barrier of rotating the end group of IDTBR, ITIC and Y6. Here, unlike the other NFAs, Y6 shows a single global energy minimum implying that only the structure at 0° is thermodynamically favored. For the other two linear NFAs (ITIC and IDTBRs), more than one potential energy minima is found within the thermal fluctuation range, k_BT, suggesting the possible existence of different

conformations. Therefore, the co-existing conformations of ITIC and IDTBR result to higher conformational disorder and thus larger energetic disorders.

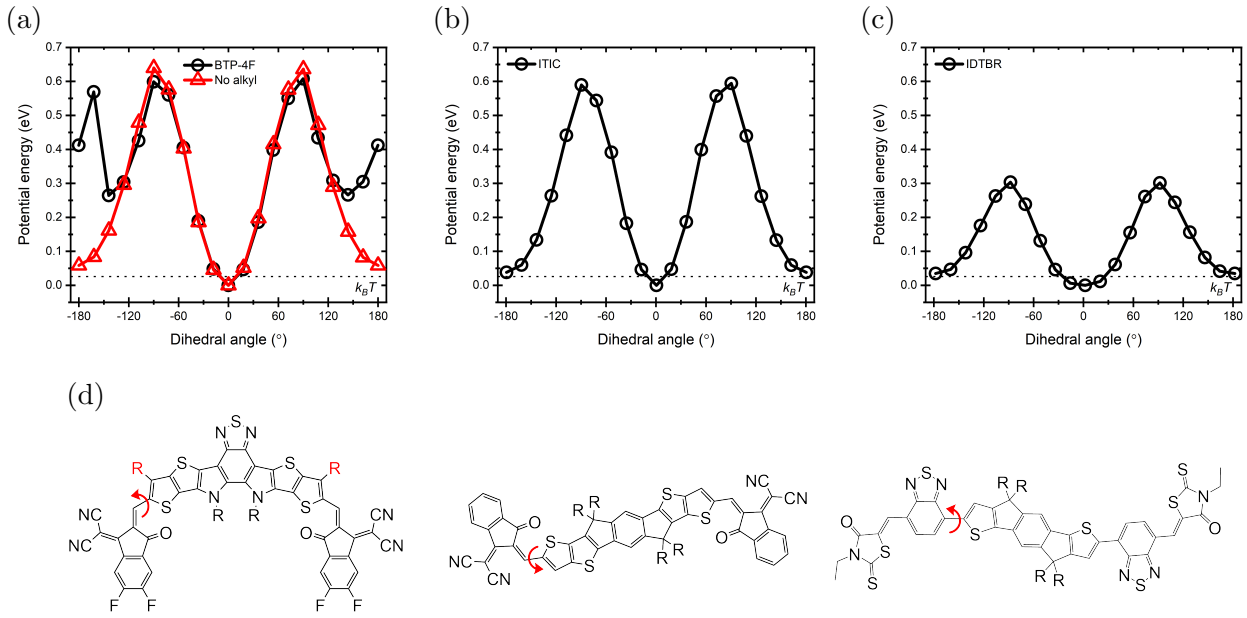


Figure 4.2: Potential energy scans as a function of dihedral angle (red arrows) of (a) Y6, (b) ITIC and (c) IDTBRs NFAs with their structures in (d), calculated using DFT calculation. One global potential energy minimum is observed for Y6 molecule (0°) compared to ITIC and IDTBRs (0° and 180°), suggesting its conformational uniformity and rigidity, potentially leading to the low energetic disorder. R groups are simplified to methyl groups for simulations. The red line in (a) refers to the dihedral scan when the red highlighted R group is replaced with a hydrogen.

For NFA end group twisting, it is well known that the carbonyl oxygen in the end groups and the thiophene sulfur in the donor backbone have non-covalent interaction which is present in both Y6 and ITIC.[21,22] Therefore, this interaction could not be the main cause to multiple conformational energy minima in ITIC and IDTBRs. A critical structural difference between Y6 and ITIC is the long alkyl chain on the outer core thiophene unit in Y6 which may contribute to a steric hindrance to the end group twisting. To highlight the steric effect, a modified Y6 without alkyl side chain on the outer core thiophene units was performed. The profile of potential energy without alkyl side chain leads to a similar shape to ITIC where there are two local energy minima within thermal fluctuation (see the red line in Fig. 4.2a at 0° and 180°). This confirms that the alkyl side chain on the outer donor core of Y6 serves as a conformational locker and is the deterministic design which makes Y6 conformationally rigid and therefore has low energetic disorder. Since the simulation here replaced the long alkyl side chain with only a simple methyl group, the results even further indicates the long side

chain may not be necessary to reproduce the same property of low energetic disorder. In a former publication by J. Luke et al., the photostability of NFAs is directly linked to their own conformational rigidity and their energetic landscape under end-group twisting.[22] To test whether the photostability of Y6 is relatively higher than the other two NFAs, an accelerated in situ photostability test was measured in N_2 (Fig. 4.3). For both O-IDTBR and ITIC, their conformations and vibrational spectra significantly change after laser irradiation, showing the strong photo-instability. Nonetheless, for Y6, its vibrational spectra are strikingly stable with no changes in relative peak intensities nor positions, indicating its exceptional conformational stability. The exceptional characters of Y6, both conformational rigidity and its leading low tail state density, may also explain the low optical Urbach energy observed for Y11.[20]

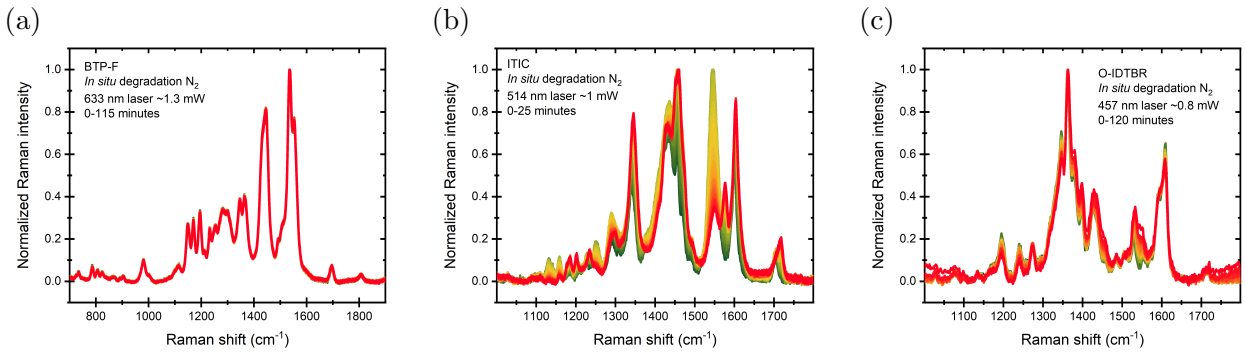


Figure 4.3: Baseline background corrected and normalized in situ resonant Raman spectra (a) at 633 nm excitation of a neat Y6 film, (b) at 514 nm excitation of a neat ITIC film, (c) at 457 nm excitation of a neat O-IDTBR film shown as a function of laser irradiation time starting with green spectra and progressing to red. Different laser wavelengths were used to achieve resonant accelerated excitation of each NFAs. The films are kept under a high nitrogen flow to minimize photo-oxidation.

In this work, the underlying mechanisms by which PM6:Y6 blend can achieve high quantum efficiency in generating high photocurrent and low energy loss comparing to other polymer:NFA blends is investigated. Here, an extremely low tail states is found in Y6 (and BTP-4Cl). This exceptional low energetic disorder is originated from the outer alkyl side chain locking the dihedral rotation of the accepting end-groups creating strong conformational rigid structure. DFT simulations show that only a single energy minimum for Y6 while there are two energy minima for ITIC and IDTBRs within the thermal energy range k_BT. To emphasize the influence of conformational rigidity and low tail states, a further accelerated photostability test on these NFAs indicates a superior neat film stability in Y6 only.

Experimental Methods for Section 4.2

Sample Fabrication

PM6:Y6 OSCs were fabricated with an inverted structure of ITO/ZnO/PM6:Y6/MoO_3/Ag. The sol-gel based ZnO precursor solution was prepared by dissolving 220 mg of zinc acetate dehydrate in 60 µL of ethanolamine and 2 ml of 2-methoxyethanol. The PM6 and Y6 were synthesized according to the methods in the previous work.[8] The ZnO solution was spin-coated at 4000 rpm on the pre-cleaned ITO substrate. Subsequently, the samples were annealed at 150 °C for 20 min in air and then transferred into an N_2 glovebox for spin-coating of the photoactive layers. The PM6:Y6 (1:1.2 %W/W) layers were deposited from 7 mg/mL chlorobenzene/chloronaphthalene (99.5 %V/V) solution by spin-coating at 2000 rpm and then annealed at 100 °C for 10 min.

4.3 Orientation-Dependent Energetic Shifts in Vacuum-processed Organic Small-Molecules

In Section 4.2, the energetic disorder in different neat NFAs is investigated, and it is correlated well to the conformational rigidity originated from the alkyl side chain which eventually influences their blend OPV performance. These findings lead to an idea of whether by controlling microscopic structures may enable the ability to tune energetics and furthermore assist charge generation in OPV devices. α-sexithiophene (α-6T), one of the archetypal OSCs, was commonly applied in OPVs as a donor material and blended with various fullerene or NFAs.[23,24] Its simple chemical structure allows it to be vacuum evaporated into polymorphic or mixed crystal structures by tuning the evaporation conditions.[25] Here, mixed α-6T homojunction OPV (HOPV) is fabricated by fast deposition (1 Å s^{-1}) on unheated substrate with its device structure shown in Fig. 4.4a.[26]

To prevent silver penetration, a thin cathode buffer layer (BL) of BPhen is inserted together with some other common BL materials in OPVs or organic light emitting diodes (Rubrene, C545T, DBzA, TCTA, TPBA, TBPe, TPBI - full names are provided in Appendix B).[27,28] The BLs here are chosen based on their lowest unoccupied molecular orbital (LUMO) energy which should be compatible to that of α-6T in order to assist charge extraction process. Overall, the

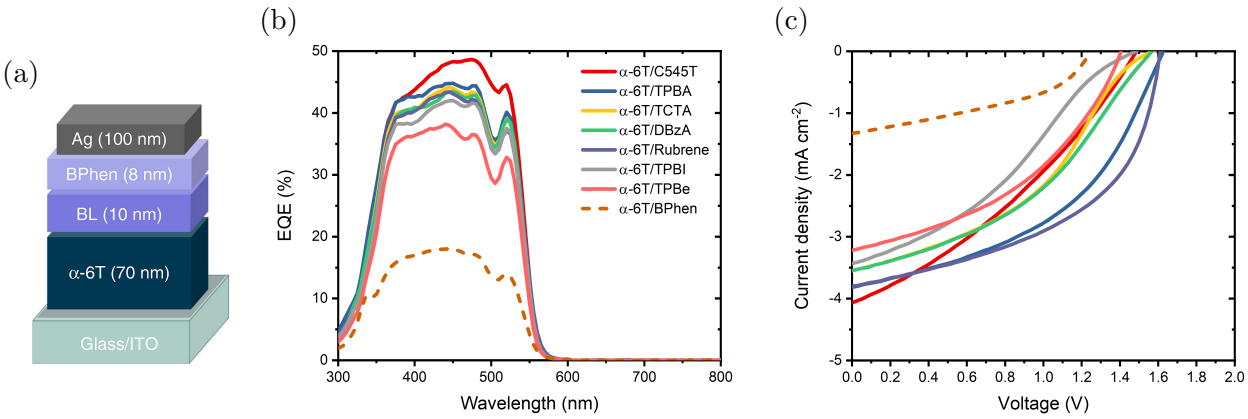


Figure 4.4: Homojunction organic photovoltaics based on α-6T and various buffer layers. (a) The Device architecture of the devices. BPhen and an additional buffer layer (BL) are used between α-6T and the top silver (Ag) contact. The thickness of each layer is denoted in the parentheses. (b) External quantum efficiency (EQE) spectra and (c) current density–voltage curves of the devices with various BL materials.

BLs are only used to improve charge selectivity and device performance.[27,29] The EQE spectra and the current density-voltage curves of the devices with different BLs are shown in Figs. 4.4b–4.4c. These devices demonstrate efficient charge separation with an EQE from 35 % to 50 % (Fig. 4.4b). Since HOPV has no donor-acceptor interface assisting charge generation as in the BHJ devices, the α-6T/BL interface becomes the possible interface where charge generation might occur. Nonetheless, the similar EQE distribution across different BLs suggests that charge generation happens instead of on the interface but within the bulk of the α-6T film. There are more transient absorption evidence showing charge generation in the bulk α-6T rather than the interface in the publication.[2] More evidence from surface photovoltage (SPV) measurements in later paragraphs will show the domination of charge generation inside α-6T instead of the BL interface. Such an efficient charge generation demonstrates that the mixed α-6T may have complex energetic landscape which provides the necessary energy offset to separate excitons and generate free charges even within a single component layer.

To understand how charges are generated inside mixed α-6T, three differently oriented α-6T films, namely standing, lying and mixed, are fabricated by utilizing the evaporation conditions in previous reports (detail fabrication methods see Section 4.3).[26,30,31] Grazing-incidence wide-angle X-ray scattering (GIWAXS) is carried out to detail the packing structures, as shown in Figs. 4.5a–4.5c. Firstly, for α-6T deposited in low evaporation rate (∼0.1 Å s^{-1}) at 100 °C, the resonance peaks in Fig. 4.5a have a clear out-of-plane pattern indicating a standing orientation

on the substrate as illustrated in Fig. 4.5d. To highlight the pattern, the resonance peaks derived from the unit cell are shown in red circles here.[32] On the contrary, for α-6T deposited on top of a thin copper iodide layer (2 nm), the GIWAXS data shows a clear packing direction changing from out-of-plane to in-plane direction (see the blue circles). Here, the thin copper iodide layer serves as a template by the strong π-π interaction leading to the lying oriented α-6T. Finally, the mixed α-6T film has the resonance peaks from both orientations (red and blue circles) indicating that both standing and lying domains are presented (Fig. 4.5b). For all three cases, schematic diagram for each is shown in Figs. 4.5d–4.5f.

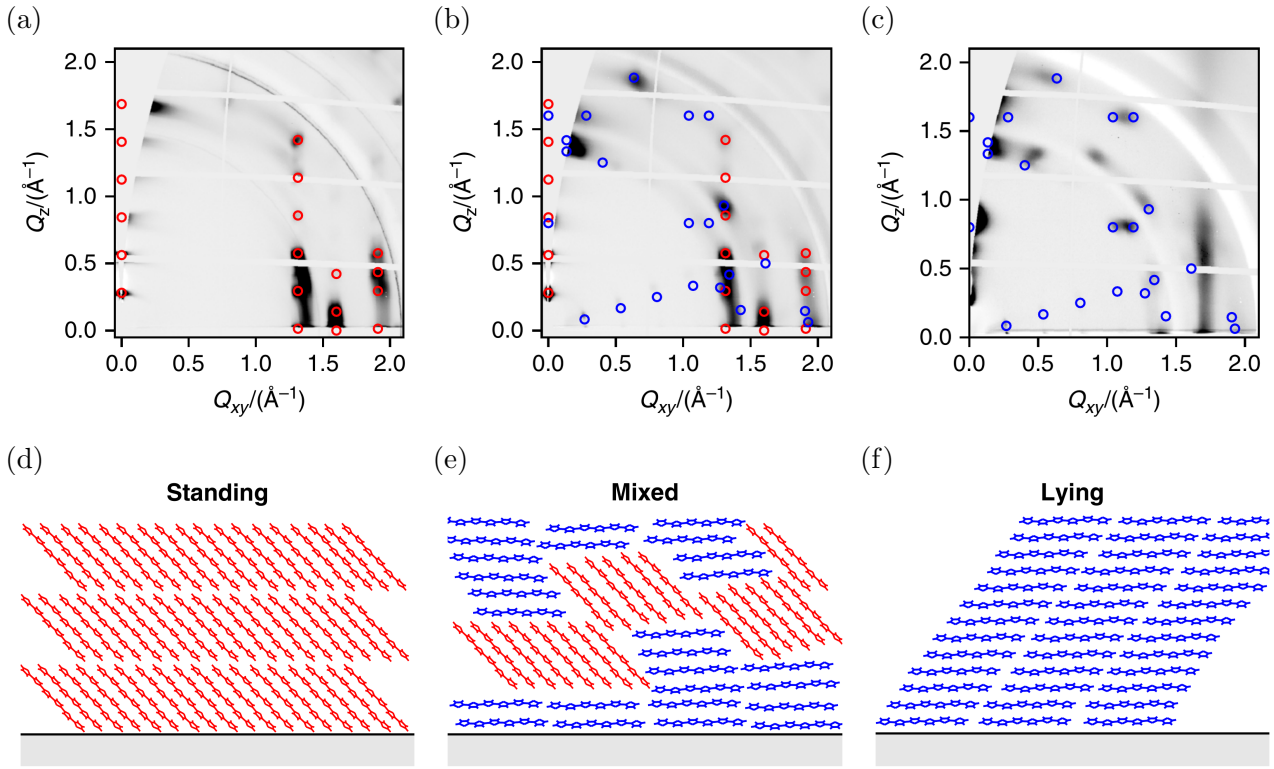


Figure 4.5: Morphological characterization for the orientation of α-6T thin films. (a) – (c) Grazing-incidence wide-angle X-ray scattering (GIWAXS) diffraction images showing three different molecular orientations of α-6T by tuning the evaporation conditions. The resonance peaks of standing (red circles) and lying (blue circles) derived from crystallites are overlaid as a guide to the eye. (d) – (e) Schematic morphology for α-6T thin films with different molecular orientations (standing, mixed, and lying).

In literature, it is known that the energetic of OSCs is strongly correlated to the molecular packing structure.[33] Since mixed α-6T is composed of both standing and lying structure, the driving force for free charge generation may rely in the energetic difference of the two packing structures. Therefore, APS measurement is applied to the three packing structure with two different thickness each to reveal the vertical energetic landscape (Fig. 4.6). The HOMO levels of

both thin and thick standing α-6T are measured to be 4.8 eV while the lying oriented samples have their HOMO level at ∼5.2 eV. This is coherent with a previous report from Duhm et al. that a 0.4 eV difference was recorded between standing and lying packing structures by ultraviolet photoelectron spectroscopy.[34,35] Further molecular dynamic simulations can be found in the publication showing the energetic shift between the two orientations.[2] The electrostatic field building up within different packing structure results to a packing-dependent energy level shift. In contrast to both standing and lying orientation, the mixed samples show a significant HOMO level shift from 4.8 eV for 20 nm to 5.0 eV for 60 nm. It indicates the standing structure is preferential and dominating the crystal structure close to ITO substrate which is coherent with the fact that standing structure does not require any template layer for fabrication. A shallower HOMO level at the bottom ITO contact is beneficial for holes to be extracted with a vertical cascade energetic landscape and thus reduce charge recombination by transporting free charges away.

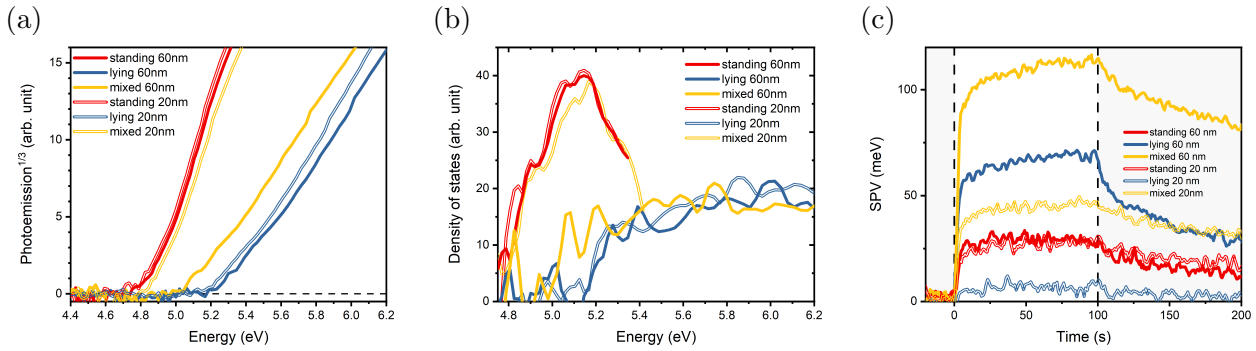


Figure 4.6: Energetic landscape and surface photovoltage response in different morphological α-6T. (a) Ambient photoemission spectroscopy (APS) responses and (b) its converted density of state (DOS) distribution of 20 nm (double line) and 60 nm (solid line) α-6T films with standing orientation (red), lying orientation (blue) and mixed orientation (yellow). DOS distributions of the standing and 20 nm mixed samples are plotted till the saturation point of the equipment. (c) Surface photovoltage (SPV) signals of all samples under 0.2 sun white light illumination. Dashed vertical lines indicate the transitions between light off (gray) and light on (white).

It is interesting that the HOMO level of the 60 nm mixed sample is located well between that of the standing and the lying samples at 5.0 eV (Fig. 4.6a). A direct explanation would be that the mixed sample has an averaged electrostatic effect which results in an averaged HOMO level between standing and lying cases. However, a uniform energetic environment would mean that there is no energy offset driving charge dissociation and thus no free charge generation. To unveil the energetic details beyond the averaged HOMO level, the converted DOS distribution

is shown in Fig. 4.6b. The standing samples, both 20 nm and 60 nm, are having nearly the same DOS distribution with a characteristic double-peak center at 5.05 eV and 5.15 eV showing a well-controlled packing structure across the whole deposition depth. For the lying samples, their DOS distribution is found to be broad and equally distributed across the energy spectra with some small features such as small frontier peak. Despite the similarity, clearer DOS distribution features are measured for the 60 nm lying sample which may be originated from the gradually vanishing template effect when growing thicker and farther away from the CuI template. Turning to the mixed samples, 20 nm mixed α-6T shows a DOS distribution similar to the standing α-6T which is coherent with their similar APS spectra (Fig. 4.6a). It suggests that the standing α-6T dominates the beginning growth in the mixed α-6T. Surprisingly, for 60 nm α-6T (solid yellow line in Fig. 4.6b), both the double-peak feature as well as the broad distribution in deep energy region appear confirming the existing of both standing and lying α-6T as measured in GIWAXS data (Fig. 4.5b). Therefore, the intermediate HOMO level in mixed α-6T is not originated from a uniform electrostatic environment averaged from the two orientations but rather a lower frontier electron density which results in reduced photoemission from the standing oriented α-6T.

With the in-depth detail of the energetics, further SPV measurements are carried out to show that efficient free charge generation is only occurred in mixed α-6T and not related to the BL layers in the HOPV devices. As shown in Fig. 4.6c, 20 nm lying and both 20 nm and 60 nm standing samples have a small SPV response (∼25 meV) indicating a small to almost negligible free charge generation under white light illumination due to lack of energy offset to generate free charges. For 60 nm lying sample, a slightly larger SPV response (∼60 meV) is recorded despite not having differently oriented α-6T. This may be originated from the gradually misaligned α-6T noticed by its DOS distribution since lying structure is built on top of CuI template of which the template effect decays with growing α-6T thickness. The mixed samples, both 20 nm and 60 nm, have large SPV response compared to the other two orientation samples in the same thickness respectively indicating an efficient charge generation only occurred in mixed energetic environment. This corroborates the domination of charge generation in α-6T instead of the BL interface. In summary, through controlling the orientation of α-6T, the energetic landscape may be tuned by the non-zero electric field within the single component α-6T crystal. The different

energetics of standing and lying α-6T thus contribute to the unusual efficient charge generation despite not having typical donor-acceptor pairs.

Experimental Methods for Section 4.3

Sample and Device Fabrication

The α-6T thin film samples were prepared on top of sputtered ITO substrates. Thickness of 20 nm and 60 nm were fabricated for each orientation. Both thicknesses were used for the APS measurements, while GIWAXS and TAS were performed on samples, which had a thickness of 60 nm. For the standing orientation where the long axis is nearly perpendicular to the substrate, α-6T was evaporated at the a low rate of $\sim$0.1 Å s^{-1} on pre-heated substrate at 100 °C. To obtain the lying orientation where the conjugated backbone is parallel to the substrate, a thin (2 nm) CuI layer was evaporated first before evaporating the α-6T layer. The strong π-π interaction between the conjugated backbone of α-6T and the d orbitals of CuI provides a template effect for the lying orientation as reported in the literature.[31] Lastly, the mixed α-6T films where both standing and lying orientation co-exist was evaporated at room temperature but high evaporation rate ($\sim$1 Å s^{-1}).

4.4 Orientation-Dependent Energetic Shifts in Solution-processed Non-Fullerene Acceptors and Their Impact on OPV Performance

In Section 4.3, α-6T proves the importance of molecular packing structures and orientations in energetics, and this, furthermore, leads to efficient free charge generation in α-6T HOPV devices which does not have a typical energetic offset between donors and acceptors as in BHJ devices. However, what the molecular origin of electrostatic effect is in small molecule OSCs and whether the orientation dependent energetic shift can be achieved by solution processing require further investigations. To answer these questions, Y6 in different orientations is manifested by processing in different solvents in order to compare the energetics and moreover the influence in OPV devices.

To begin with, chloroform (CF) and chlorobenzene (CB) are utilized here for Y6 deposition on top of ITO/ZnO in order to achieve two types of orientations (see schematic in Fig. 4.7a) as reported by Zhu et al.[36] For Y6 deposited from CF (denoted as Y6 CF), Y6 molecules forms a face-on orientation where the molecules are parallel to the substrate akin to lying α-6T in Section 4.3. In contrast, Y6 deposited from CB (denoted as Y6 CB) adapts a mixed orientation where both edge-on and face-on orientation exist similar to the mixed α-6T samples. Both Y6 CF and Y6 CB are prepared in similar thickness (∼40 nm) for the convenience to compare. Due to the change of Y6 orientation, the absorption cross section is lower in Y6 CB than in Y6 CF (Fig. 4.7b) despite having similar film thickness. Also, the peak position of Y6 CB is slightly redshifted compared to that of Y6 CF indicating a narrower E_g in Y6 CB. This may be originated from the stronger intermolecular electron delocalization due to the change of aggregation structure and was reported in the literature.[36] Turning to energetic, the HOMO level of Y6 CB is measured to be −5.83 eV which is deeper than that of Y6 CF (−5.62 eV) by 210 meV (Fig. 4.7c). This orientation-dependent HOMO level shift is similar to α-6T and is regarded as the effect of different electrostatic strength originated from the molecular orientations. Since electrostatic field would shift the whole energetic environment,i.e. all the energy levels shifting in the same direction by the same amount, the energy gap, $\Delta = E_F - E_{HOMO}$ where E_{HOMO} is the energy of the HOMO level, of the same material should remain the same across different orientations. Here, the Δ of Y6 CF and Y6 CB is shown in Fig. 4.7d where it maintains almost the same value (1.13 eV to 1.14 eV), proving the origin relies in electrostatic environment shift.[33,37,38] To elucidate the origin of the energetic shift, DFT simulation combined with molecular dynamics show a significant HOMO and LUMO level shifts as shown in Fig. 4.7f. The simulated HOMO levels concur with the experimental results with 5.59 eV for face-on and 5.85 eV for edge-on.

As free charge generation is observed in mixed α-6T, photoinduced charge generation in Y6 might also occur due to the complex orientation-dependent energetic landscape. To investigate this, SPV of both Y6 CF and Y6 CB on top of ITO/ZnO are measured (Fig. 4.7e).[16] Under 0.2 sun white light illumination (the center white band region), Y6 CB generates a slightly larger SPV response (∼290 meV) than Y6 CF does (∼150 mV). The signal here is slightly larger than the α-6T as the electron transport layer (ZnO) is assisting electrons to be extracted

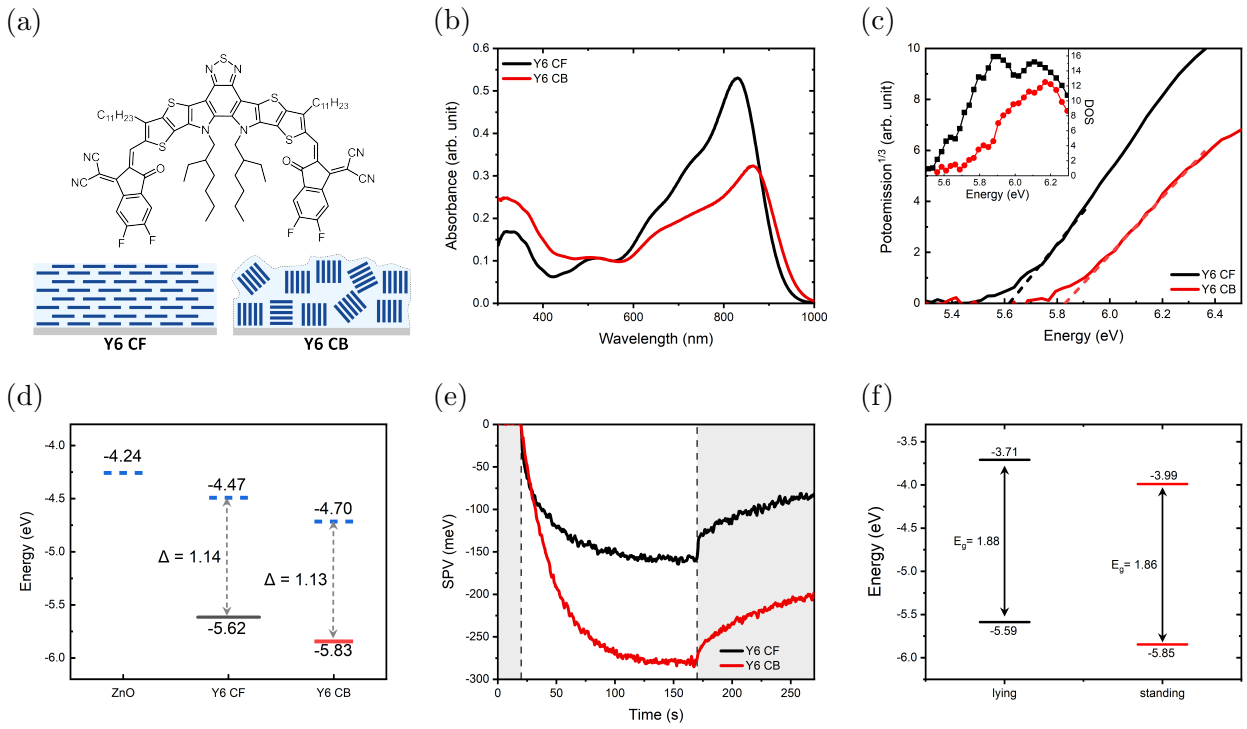


Figure 4.7: Orientation-dependent Y6 neat film energetics and charge generation. (a) Y6 molecule structure and the schematic diagrams for packing structures, (b) absorption spectra and (c) ambient photoemission spectroscopy (APS) spectra with an inset of the density of state (DOS). (d) The energetic diagram of HOMO levels (E_{HOMO}), Fermi levels (E_F) and the energy gap between them ($\Delta = E_F - E_{HOMO}$) for ZnO, Y6 CF and Y6 CB and (e) surface photovoltage (SPV) measurements of Y6 CF and Y6 CB on ITO/ZnO substrates. (f) Simulated HOMO levels, LUMO levels and their gap E_g of face-on and edge-on Y6 with electrostatic effect using molecular dynamics and density functional theory (DFT).

and reducing recombination loss.[39] The negative SPV signal indicates the free hole accumulation on the surface which implies a more efficient charge generation within the bulk of Y6 CB on top of the ZnO interface. This free charge generation may be coming from the energetic offset between different Y6 orientation (Fig. 4.7f) similar to α-6T, and it might play an important role in OPV devices.

Before testing the role of orientation in OPV devices, it is crucial to understand the molecular origin of electrostatic effect and how it determines the energetics of α-6T and Y6 thin films. According to Schwarze et al., electric quadrupole moment dominates the electrostatic effect in OSCs since the dipole moment of OSCs usually cancels out by forming their crystal structures.[37] Furthermore, with the symmetry, high performance NFAs are mostly linear and as a result leaving a relatively small dipole moment. A brief summary and visualization technique of quadrupole moment is shown in Appendix D. To verify this, the quadrupole moment perpendicular to the π-conjugated backbone (Q_π) of α-6T, high performance NFAs

and some other OSCs are simulated by DFT calculations (Fig. 4.8a). Since most of the OSCs have a shorter π-π stacking distance compared to other directions, the Q_π would be the dominating quadrupole component among all the other directions as an indicative value to verify the strength.[40,41] As shown in Fig. 4.8a, Y6 has a positive Q_π at $192\,ea_0^2$ which is the opposite sign to that of α-6T ($-70\,ea_0^2$). The sign of the Q_π correlates well to the direction of HOMO level shift where the negative Q_π of α-6T shifts the energetics deeper from standing to lying and vice versa in Y6 with positive Q_π. Besides that, the value of Q_π among different NFAs is getting larger by adding halogens on the side groups, and the larger electron negativity leads to more positive Q_π value. This could be due to the planar molecular design in NFAs which is typically composed of an A-D-A (acceptor-donor-acceptor) or A-D-A′-D-A structure which introduces a strong push-pull across the conjugated backbone. To elucidate how the molecular structure influences its own Q_π value, an electrostatic potential (ESP) mapping of α-6T and Y6 is carried out (Fig. 4.8b). Here, α-6T has a uniform electron rich core with positive charges circling the core leading to a negative Q_π. On the contrary, Y6 has an electron deficient donor core with strong electron rich side groups particularly the carbonyl, cyano and halogen groups leading to a much larger Q_π than α-6T.[42] Interestingly, these modifications are in line with the trend of high performance NFA development which may be another key factor to explain the performance improvement.[43]

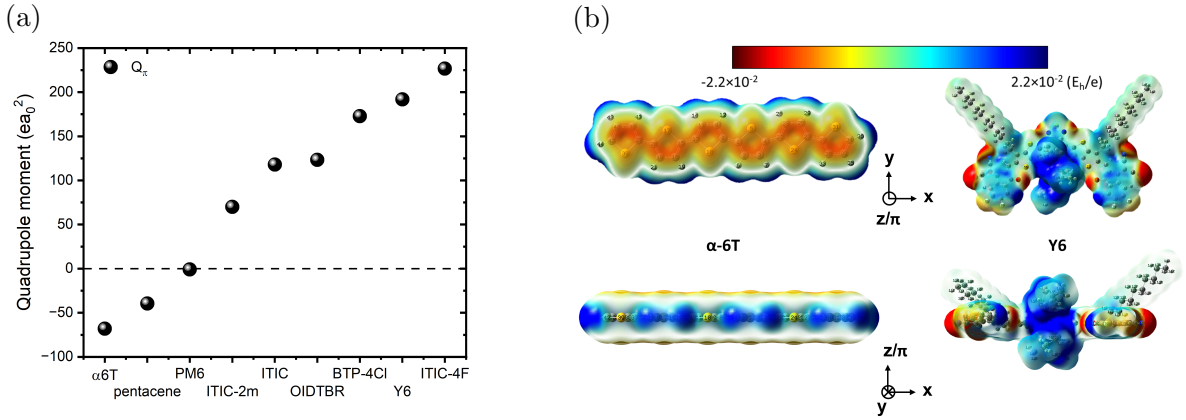


Figure 4.8: Density functional theory (DFT) simulated (a) molecular quadrupole moments perpendicular to π-conjugated backbone (Q_π) with e as elementary charge and a_0 as Bohr radius, and (b) electrostatic potential (ESP) of α-6T, Y6 and other organic semiconductors with E_h as Hartree energy.

Turning to the impact on nearby donor molecules and furthermore on OPV performance, Y6/PM6 planar heterojunction are fabricated by further depositing PM6 layers through water

transfer method (details in Section 4.4).[44,45] With the water transfer method, a clear acceptor-donor interface is acquired and different thickness of PM6 (5 10nm) is exploited to reveal the influence from differently oriented Y6 underlayer. As shown in Fig. 4.9a, thin PM6 (5 nm) on top of both Y6 cases results in a deeper HOMO level which was usually attributed to the crystallinity or packing disruption within BHJ.[46] However, in this case, the deepening should not be coming from the packing disruption as PM6 and Y6 layers are not intermixed here. Interestingly, the deepening in Y6 CF case is about 100 meV which is the same amount in PM6:Y6 BHJ observed in Fig. 4.1c. Furthermore, both the HOMO levels and DOS distributions of 10 nm PM6 are similar to neat PM6 (Fig. 4.9b). This fast distance decay coherent with quadrupole moment as it decays to the power of third by distance ($\propto 1/r^3$, where r is the distance between quadrupole to the test point). Turning to the Y6 CB cases, the PM6 on top shows a nearly unchanged HOMO level as well as DOS distribution. This may be due to the cancellation among the mostly mixed Y6 leading to no consistent electrostatic field from Y6. To summarize, the HOMO levels of PM6 in different environment are shown in Fig. 4.9c. The electrostatic effect not only influences the Y6 film but also its nearby PM6 which would play a significant role in charge generation and OPV performance.

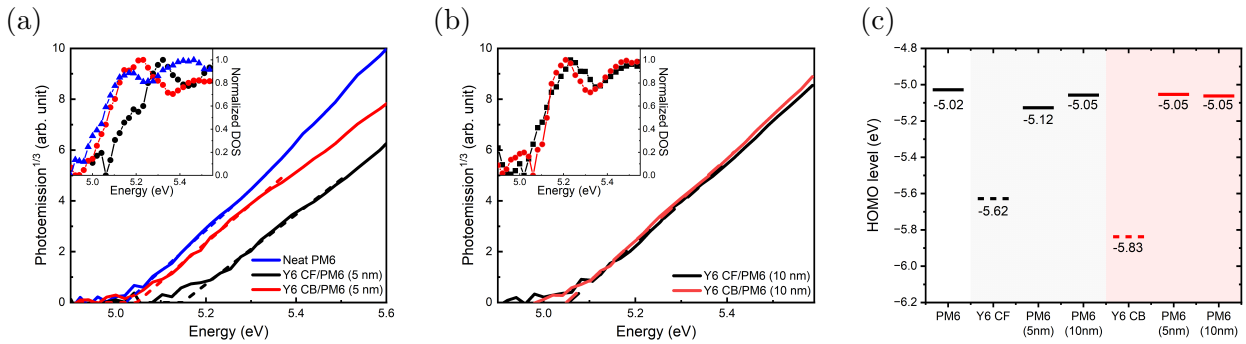


Figure 4.9: Energetics of Y6/PM6 planar heterojunction. APS spectra with normalized DOS insets of (a) neat and 5 nm or (b) 10 nm PM6 in planar heterojunction with Y6 CF or Y6 CB underneath. (c) The HOMO level plot of PM6 in neat (white background), with Y6 CF underlayer (gray background) and with Y6 CB underlayer (red background). The HOMO levels of the underneath Y6 layer (dash lines) are derived from Figs. 4.7c and 4.7d.

Following the PM6 energetics in bilayer structure, bilayer OPV devices (namely CF and CB devices) are fabricated, and their current density-voltage (J-V) curves are shown in Fig. 4.10a. Reflecting the significant energetic shifts, the CF device shows a significantly better photovoltaic performance compared to the CB devices, J_{SC} (6.21 mA cm^{-2} vs. 4.95 mA cm^{-2}),

V_{OC} (0.86 V vs. 0.75 V) and PCE (3.73 % vs. 2.13 %). The difference of J_{SC} between the two devices is unveiled by their external quantum efficiency (EQE) and optical absorbance spectra (Fig. 4.10b). Overall, the CF device has a higher EQE between 350 650nm which is related to PM6 absorption. Since, in both devices, the PM6 layer has the same thickness and absorbance, this higher EQE could be related to a more efficient energy transfer from PM6 to the underneath Y6 layer achieved by the favored Y6 alignment and better overlapped absorption spectra.[47] Interestingly, the EQE above 650 nm is nearly the same between the two devices despite the lower absorbance in CB device. It could be explained by the free charge generation within Y6 CB as shown by the neat Y6 SPV measurement (Fig. 4.7e).[48,49] Turning to V_{OC}, the CF device shows a higher V_{OC} than the CB device by ∼120 mV. This is as expected since Y6 CF has a slightly shallower LUMO as well as HOMO levels (Figs. 4.7b and 4.7d) which leads to a larger effective E_g (the energy gap between Y6 LUMO and PM6 HOMO). Nonetheless, the energetic shift in Y6 CF is ∼200 meV which is larger than the measured V_{OC} increment implying a larger V_{OC} loss happens in the CF device.

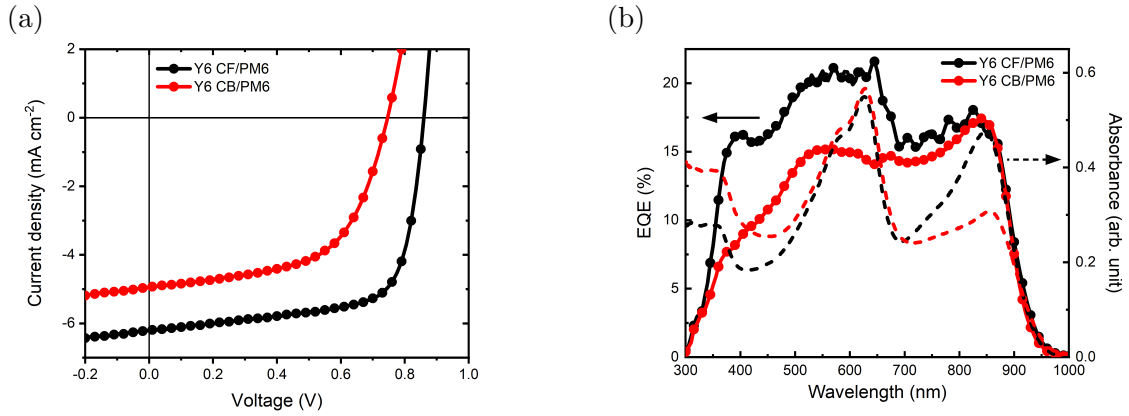


Figure 4.10: Device performance of Y6/PM6 bilayer OPVs. (a) J-V characteristics and (b) external quantum efficiency (EQE) spectra (solid lines) with absorbance spectra (dash lines).

To understand deeper in the V_{OC} loss, further PM6 thickness dependent SPV measurements are carried out in bilayer structure (Fig. 4.11). When the PM6 is in 30 nm (Fig. 4.11a), the same as in bilayer devices, the SPV response concurs with the V_{OC} as −470 meV for the CF sample and −390 meV for the CB sample. However, as the thickness of PM6 layer is reduced to 5 nm (Fig. 4.11b), the relationship swaps as the CB sample has a larger SPV response (−453 meV) than that of the CF sample (−369 mV). Furthermore, the SPV response of CB sample is counter-intuitively higher with thinner PM6 than with thicker PM6. This suggests that the

mechanism behind the swap is not simply due to the reduced PM6 absorption by thickness but rather a change in the recombination rate.[16] With thinner PM6, holes would be more concentrated around the Y6/PM6 interface which then boosts interfacial charge recombination. By considering the positive quadrupole moment of Y6, the energetic on the interface should have a upward band bending as the quadrupole moment increases and saturates inside the bulk. Therefore, the band bending supports the extraction of electrons and leaving less electrons on the interface to recombine. Since Y6 CB has a deeper HOMO level and a rougher interface, the band bending effect is much stronger than the CF sample leaving less electrons on the interface to be recombined. To illustrate it, a schematic diagram is drawn in Fig. 4.11c with the band bending caused by quadrupole moment as Δ^+.

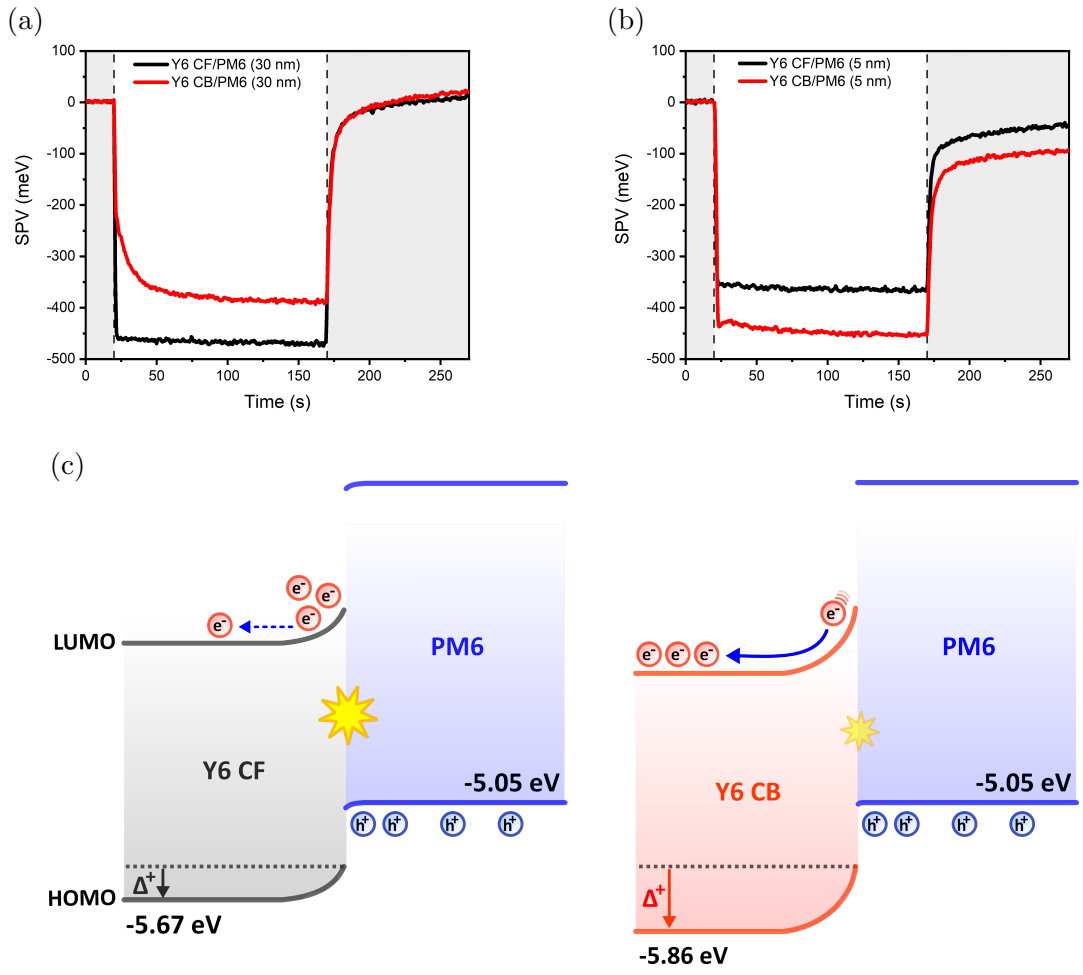


Figure 4.11: Surface photovoltage (SPV) measurements of (a) 30 nm or (b) 5 nm PM6 on Y6 CF and Y6 CB with (c) the schematic diagram. The interfacial band bending by the positive Q_π is indicated as Δ^+.

Despite the clear evidence of how orientation influences energetics in neat films as well as planar OPV device performance, its importance in BHJ devices would be indispensable to make

an impact on high performance OPVs. Thus, PM6:Y6 BHJs ((ITO/ZnO/PM6:Y6/MoO_3/Ag) with CF or CB are fabricated and studied. Firstly, the PM6 HOMO level is deepened by 87 meV when CF is used while there is not much change (<10 meV) for its CB counterpart (Figs. 4.12a and 4.12b) consistent with the bilayer cases. The DOS also confirms that the energetic change is a parallel shift. Although the HOMO level of the Y6 inside could not be probed directly, the Y6 energetic is still expected to be following or similar to their neat films as the packing within the domain is still dominated by the choice of solvent. As a result, the J-V characteristics of both BHJs are similar to the bilayer devices with a higher J_{SC}, V_{OC} and PCE for the CF case (Fig. 4.12c). In the EQE spectra (Fig. 4.12d), the CF BHJ device shows higher EQE as it also has higher absorbance over the whole spectra. Also, the efficient charge generation within Y6 CB is limited here with more fragmented domains and longer extraction distance further reducing its EQE. In summary, the BHJ results are consistent with that of the bilayer devices emphasizing the orientation-dependent electrostatic effect of Y6 in OPV performance.

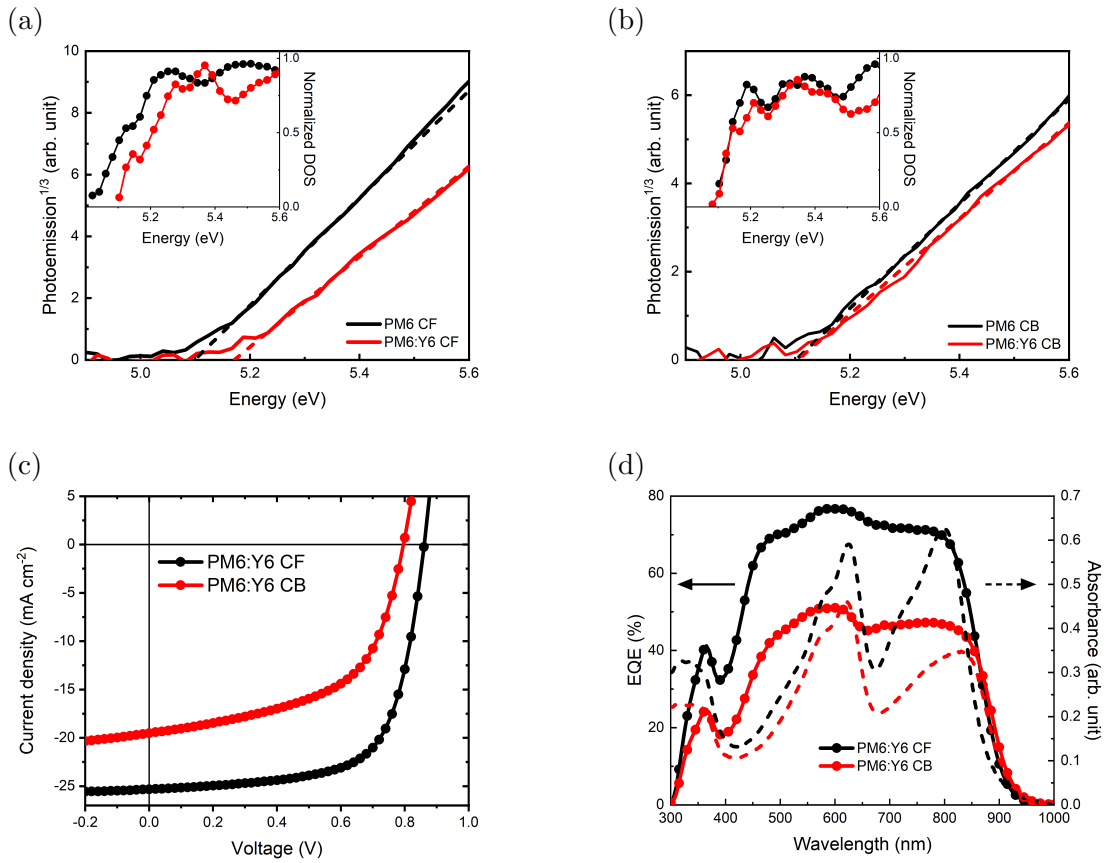


Figure 4.12: Orientation-dependent energetics and device performance of PM6:Y6 BHJ. The APS spectra of neat PM6 and PM6:Y6 blend films processed from (a) CF and (b) CB. Their DOS distributions are shown as insets. (c) Current density-Voltage (J-V) characteristics, (d) EQE spectra (solid line) and absorbance (dash line) of PM6:Y6 BHJ devices.

To verify the wide applicability of electrostatic effect especially its indicative component, Q_π, some commonly used polymers (PBDB-T, PM6) are blended through a range of NFAs (IDIC, ITIC-series, Y6) with different Q_π values (Fig. 4.13). As mentioned above, these NFAs all have a positive Q_π (Fig. 4.13a) which should down shift the HOMO level of the polymers upon blending. As shown in both Figs. 4.13b and 4.13c, a positive correlation is observed between the polymer HOMO level deepening ($|\Delta HOMO|$) and the Q_π of the NFAs. This provides an explanation to the systematic engineering on NFAs examined so far. For example, halogenations on the end groups would increase the Q_π value of the NFA as shown in the ITIC series, and thus deepening more the HOMO level of the polymer. This enlarges the effective E_g of the OPV system and maintains the V_{OC} despite the deepening LUMO level in the NFAs. Although the correlation is not qualitatively applicable across different polymers (may be due to the different mixing conditions), this general trend may still provide some hints to further NFA engineering for high performance OPV systems.

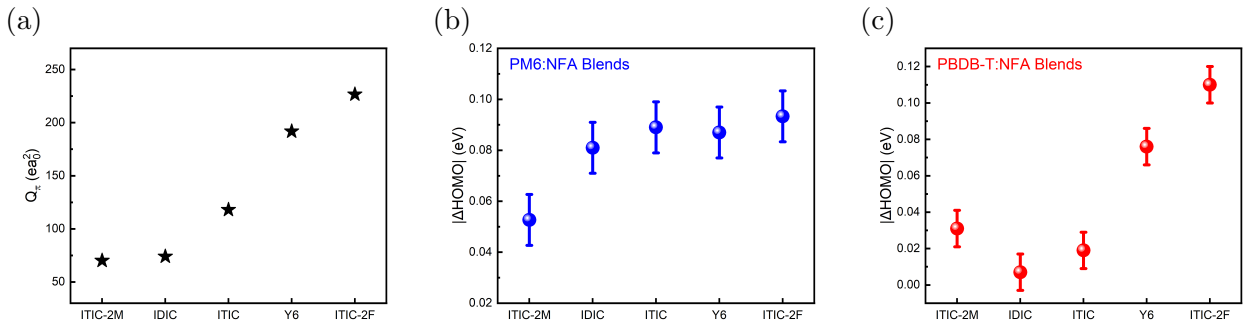


Figure 4.13: Electrostatic effect on HOMO level shift ($|\Delta HOMO|$) of polymer donors upon blending with different NFAs. (a) The quadrupole moments of the NFAs and the magnitude of $|\Delta HOMO|$ of (b) PM6 and (c) PBDB-T.

Experimental Methods for Section 4.4

Sample Fabrication

ZnO layer was prepared by sol-gel method with its precursor zinc acetate dihydrate ($0.11\,g\,mL^{-1}$) in 2-methoxyethanol with an additional 3 vol% ethanolamine and sonicated for >2 hr. After spin-coating, the sample was annealed at 200 °C for 20 min. Y6 from Organtec was dissolved in either chloroform (CF, $8\,mg\,mL^{-1}$) or chlorobenzene (CB, $10\,mg\,mL^{-1}$), and then spin-coated following an annealing at 100 °C for 5 min in a N_2 glovebox. PM6 (Organtec)

was dissolved in CB:1,8-diiodooctane (99 %v/v) with a concentration of 20 mg mL^{-1}. 15 µL of PM6 solution was dropped on deionized water to form pristine films which were then transferred by water transfer method.[44,45] Samples were annealed at 100 °C for 10 min in the N_2 glovebox. For BHJ samples, PM6:Y6 blend solution (1:1.2 W : W , 14 mg mL^{-1} in CF and 0.5 %v 1-chloronaphthalene, or 20 mg mL^{-1} in CB) was spin-coated on the ZnO layer, and then annealed at 100 °C for 10 min. A similar procedure was applied to other polymer:NFA combinations (ITIC, Sigma Aldrich; IDIC, Organtec; ITIC-2M and ITIC-2F, synthesized by collaborators, PM6 and PBDB-T, Organtec) in 1:1 blend ratio and 20 mg mL^{-1}.

Orientation-Dependent Energetic Simulation

For the orientation-dependent energetic simulation (Fig. 4.7f), the face-on and the edge-on packing structures were obtained using Vienna ab initio simulation package (VASP) and then were relaxed with molecular dynamics. The HOMO/LUMO energies of each orientation were calculated by DFT method with basis sets of b3lyp/6-31G**, including the electrostatic environment.

4.5 Blending Induced Packing Structure Changes and Trap States formation in Polymer:Fullerene BHJ

With previous sections focusing on small molecules, it is now important to understand how small molecules influence different polymer donors upon blending, more specifically the energetic of the polymer donors. As seen in Fig. 4.13, small molecules with different molecular structures would significantly alter the mixing conditions and complicate comparisons across different polymers. At this regard, the polymers PDTSiTTz and Si-PCPDTBT are an interesting choice to study since they have very different charge carrier dynamics from each other despite the same donor moiety (see Fig. 4.14). Also, PDTSiTTz has been reported to have unusual non-Langevin recombination dynamics only in neat films or blended with PCBM, while this recombination nature is not shown in the indene-C_{60} adduct blends.[50–52] Herein, these two polymers as well as their fullerene blends are fabricated and studied in order to show how small molecules may alter the polymers upon blending and elucidate the origin of this uncommon non-Langevin

recombination nature of PDTSiTTz.

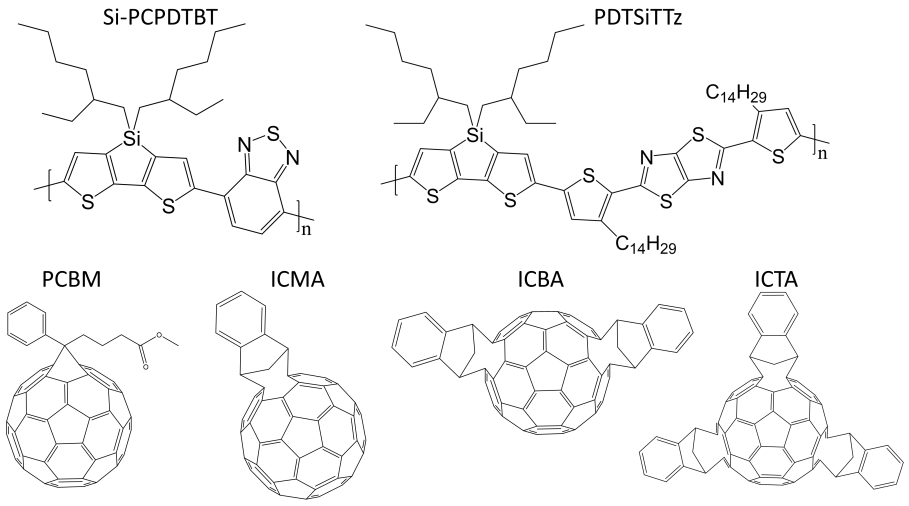


Figure 4.14: Molecule structures of Si-PCPDTBT, PDTSiTTz, PCBM, ICMA, ICBA and ICTA.

The APS measurements of neat PDTSiTTz, Si-PCPDTBT, and their blends are shown in Fig. 4.15. For PDTSiTTz, a clear progressive change in the APS spectra is observed from the PCBM blend to the indene-C_{60} adduct blends (Fig. 4.15a). The HOMO levels shift $\sim$200 eV shallower from neat polymer to the ICMA blend, and reach a saturation at $\sim$4.9 eV for all the indene-C_{60} adduct blends. A shallower HOMO level of a polymer upon blending is unusual as most of the time blending disruption should result in a deeper HOMO level due to decreased conjugation length.[22,46] Here, this unusual shallow shifting may be due to an increasing effective conjugation length or an interruption in inter-chain interaction. Since all PDTSiTTz samples show the same Raman spectra (see Marin-Beloqui et al. [3]), the conjugation length of different blends should be relatively the same. It is therefore most likely to be a disruption in inter-chain interactions to make the frontier orbitals dominated by the donor moieties with clear features, concurring to diminish non-Langevin recombination. In contrast to PDTSiTTz, Si-PCPDTBT has a relatively constant HOMO level at 4.8 eV regardless of blending conditions, as shown in the inset of Fig. 4.15d. Only a very small deepening ($\sim$0.03 eV) occurs which correlates well to the disruption in the conjugation length.

To further unveil whether trap states play a role in determining recombination mechanisms in these different materials, the tail states and their integrated areas are shown in Figs. 4.15b and 4.15e. Interestingly, the tail state areas of both polymers are comparable to each other within 0.05 to 0.1, which is also the typical value of other known polymers.[1,21] Since

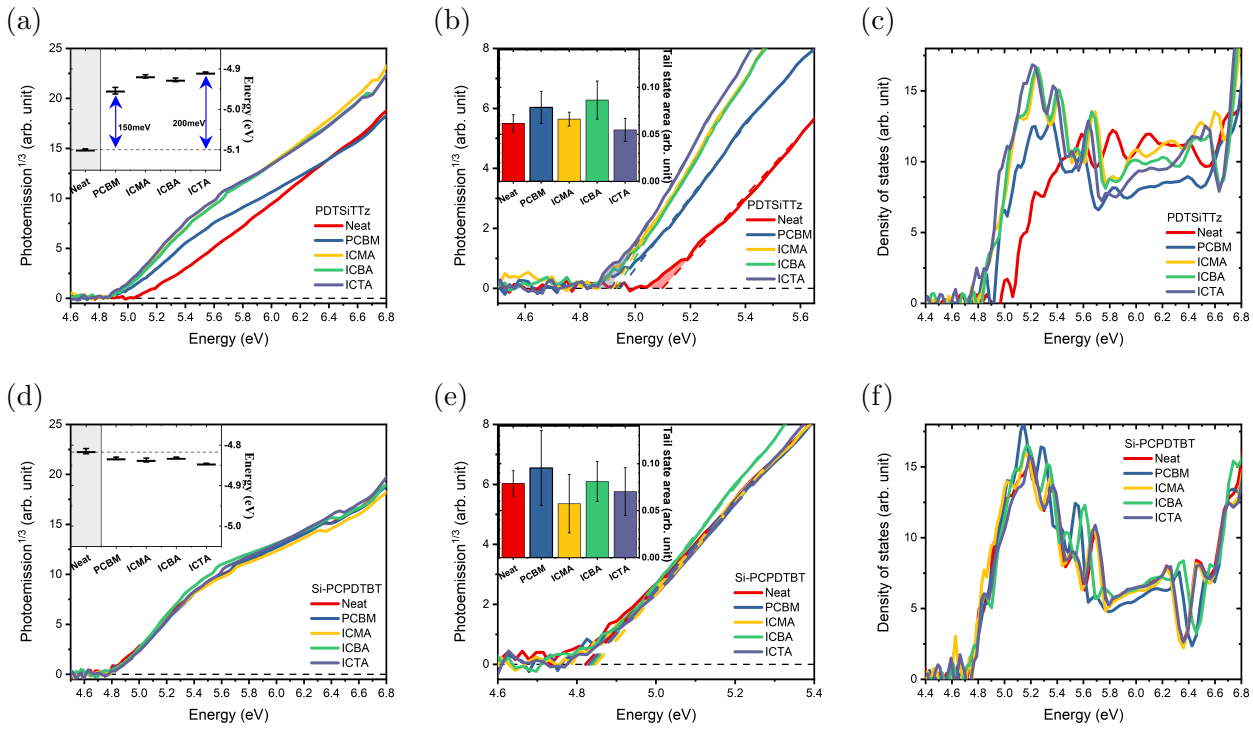


Figure 4.15: Energetics of (a) – (c) PDTSiTTz and (d) – (f) Si-PCPDTBT and their blends with PCBM, ICMA, ICBA, and ICTA. (a), (d) The ambient photoemission spectroscopy (APS) data with the HOMO levels shown in the insets. (b), (e) The enlargement of APS spectra showing the tail states (shaded area) with the integrated tail state area as insets. (c), (f) The converted DOS from (a) and (d) respectively.

recombination is normally understood to be dominated by tail states, the tail state areas observed here indicate that the dramatic change in recombination losses between the two polymers may not be simply explained by the trap states. At this regard, specific energetic distribution in each polymer and its changes upon blending may play a crucial role. Here, by converting the APS spectra, the DOS distribution of all the samples is extracted, as seen in Figs. 4.15c and 4.15f. Coherent to the APS, the DOS distribution of PDTSiTTz changes significantly upon blending (Fig. 4.15c). For the neat PDTSiTTz, the DOS is much broader and featureless across the entire energy range consistently with strong inter-chain interactions. It is interesting to note that the PCBM blend appears to be an intermediate state between the neat and the indene-C_{60} adduct blends with more distinctive peaks at 5.2 eV and 5.4 eV. This transition agrees with what observed from other transient absorption spectroscopy measurements (see Marin-Beloqui et al. [3]), in which the blends show a progressive change in recombination dynamics. As expected from the invariant APS spectra, the DOS distribution of Si-PCPDTBT is the same across different fullerene blends (Fig. 4.15f) showing the most

intrinsic properties of this polymer. There are also clear frontier peaks at 5.1 eV and 5.3 eV indicating a more localized HOMO similar to the PDTSiTTz:fullerene blends. This explains the similar charge dynamics between PDTSiTTz:indene-C_{60} adducts and Si-PCPDTBT blends, with both suffering the same trap-related recombination loss.

Besides the DOS changes within the blend series of the same polymer, a cross polymer comparison on the DOS distribution is shown in Fig. 4.16a. Interestingly, the DOS distribution of PDTSiTTz:ICTA appears to be nearly the same as that of Si-PCPDTBT:ICTA. Since Si-PCPDTBT has a more intrinsic DOS upon blending, this implies that the indene-C_{60} adducts manages to change the packing structure of PDTSiTTz into a more intra-molecular dominating condition, where the two frontier DOS peaks should be originated from their common donor moiety. This proves that the flat DOS distribution of the neat PDTSiTTz is mostly due to the strong intra-chain interaction which is inhibited by the bulky fullerenes spacing out the chain-to-chain distance.

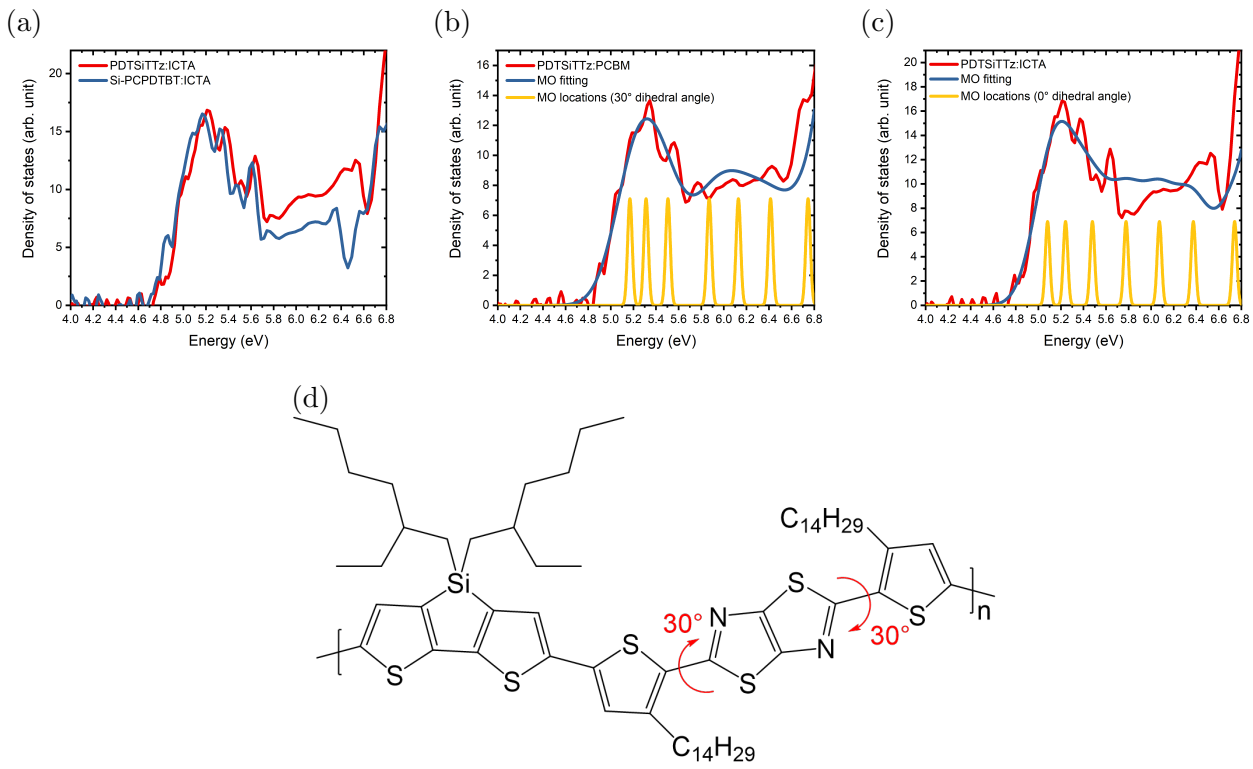


Figure 4.16: DOS comparison and fitting for PDTSiTTz and Si-PCPDTBT blends. (a) The overlay DOS distributions of both polymer:ICTA blends. The DOS fitting (blue lines) from the density functional theory calculated molecular orbitals (MOs, yellow lines) without structural constraints for (b) PDTSiTTz:ICTA and with 30° twisted dihedral angles for (c) PDTSiTTz:PCBM as shown in (d).

To demonstrate that the frontier orbitals are mostly dominated by the donor moiety, a DOS

fitting by the DFT simulated molecular orbitals (MOs) is carried out (Figs. 4.16b and 4.16c). As shown in Fig. 4.16c, the DOS distribution of PDTSiTTz:ICTA is well-fitted by the MO fitting (blue line) with clear frontier orbital peaks from 4.8 eV to 5.8 eV despite some small discrepancy above 5.8 eV, which might be due to the UV-responsivity between different orbitals. This successful fitting corroborates the fact that fullerenes reduce the intra-chain nature of PDTSiTTz. To elucidate where the MOs are located in the energy spectra and how they matches with the features of the DOS, the simulated MOs are presented as narrow gaussian functions (yellow lines) with an arbitrary chosen magnitude and width. With the success in fitting the ICTA blend, a further fitting to the PDTSiTTz:PCBM blend would be able to elucidate the role of fullerenes as it has an intermediate DOS distribution between the neat and the ICTA blend (Fig. 4.15c). Since the PCBM blend has the same frontier DOS, the structural changes should be mostly coming from the accepting moiety. Also, this moiety has a similar structure to which was reported forming fullerene intercalation upon blending.[53] By simulating different dihedral angles between the thiophene and the fused thiazoles in between (Fig. 4.16d), the DOS distribution of PDTSiTTz:PCBM is found to be best fitted with a 30° twisting as shown in Fig. 4.16b. This demonstrates that the fullerenes within the PDTSiTTz blends interact with the accepting moiety by intercalating between polymer chains which results in a reduced intra-chain interaction, and ultimately inhibits the non-Langevin recombination path ways.

Experimental Methods for Section 4.5

Sample Fabrication

15 mg/mL solutions of neat PDTSiTTz, Si-PCPDTBT, and their 9:1 blends with PCBM, ICMA, ICBA, and ICTA were dissolved in 1,2-dichlorobenzene and kept stirring overnight. The solutions were then spin coated at 2000 rpm for 60 s on top of the cleaned ITO substrates.

DOS Fitting

The energy of the molecular orbitals (MOs) were obtained from DFT simulations of short oligomers (trimer or tetramer). Then, a uniform gaussian broadening equation was applied

$$DOS_{fitting} = \sum_i \frac{A}{\sqrt{2\pi}c} e^{\frac{-1}{2c^2}(x-MO_i-\Delta)^2}, \tag{4.2}$$

where A is a scaling factor, c is the broadening factor, Δ is a horizontal shift on the MO energy and MO_i is the i-th MO energy. Beware that factors c and Δ are isotropic for all the MOs as a first order approximation as well as prevent over-parametrizing. The fitting factors were found to be relatively similar to each fitting showing the high confidence that they are intrinsic properties of the APS measurements. To carry out the fitting, algorithms are built into APS module as shown in Appendix C.

4.6 Conclusion

In this chapter, molecular structure, packing and orientation dependent energetics are investigated from neat films to blends in order to clear out the key molecular designs and packing guidelines for OPV applications. In Section 4.2, the energetic disorder, namely the tail states, of different high performance NFAs are measured. A clear trend of tail state reduction is observed from O-IDTBR to Y6 following the advancement of V_{OC} loss reduction in NFA development.[54] From DFT simulations, the significantly low tail state in Y6 is correlated to its high conformational stability originating from the alkyl chain on the donor moiety which locks the dihedral angle between the donor and acceptor moieties. Since this dihedral angle is shown to be involved in NFA degradation, the robust conformation in Y6 also leads to a much higher photostability.[22] The results connects the conformational rigidity to energetic disorder and photostability, which are critical points in developing high performance OPV systems.

In Section 4.3, instead of different chemical structures, a classic thiophene-based oligomer, α-6T, is vacuum evaporated into three different orientations, namely standing, lying and mixed packing structures, to unveil the orientation dependent energetics. The APS spectra indicates a 0.4 eV HOMO level shift between the standing and lying samples, and an intermediate APS onset for the mixed sample. By converting the APS spectra into DOS distribution, the mixed

sample shows both standing and lying oriented α-6T DOS indicating the existence of energy offset despite being a single material thin film. Therefore, mixed α-6T manifests efficient free charge generation with a large SPV signal and an EQE up to ∼50 % despite being a homojunction device. This work demonstrates the importance of packing induced energetic shift and shows the high precision of DOS conversion from APS measurements.

Following the orientation dependent energetics, different Y6 orientations are achieved by CF and CB in Section 4.4. The HOMO level of Y6 CF shows a 0.2 eV shallower HOMO level than Y6 CB while maintaining the same optical band gap. This indicates that the energetic shift is purely an electrostatic effect which pull down or push up the whole energetics. By DFT simulations, this energetic shift is then correlated to the strong quadrupole moment perpendicular to the π-π stacking direction (Q_π). Similar to α-6T, Y6 CB shows a significant SPV signal (280 meV) due to its mixed structure indicating free charge generation under illumination. To understand the effect of Q_π on the neighboring materials, Y6/PM6 bilayer bilayer samples are fabricated. Here, the strong Q_π of Y6 also influences the energetics of PM6 in close proximity (<5 nm) due to the inverse cubic distant dependency. Combining the energetic landscape of CF and CB samples, the CB device shows a lower V_{OC} than the CF device due to a much smaller effective band gap. Lastly, the Q_πs of different NFAs is correlated to the HOMO level shift in high performance BHJ OPVs, which may explain the highly efficient charge dissociation in recent NFA developments. The results demonstrate that orientation dependent energetics is originated from the Q_π and can be tuned through solution processing. Furthermore, it has a strong impact in OPV device performance and charge generation.

In the last section (Section 4.5), the focus shifts to the energetics and packing structures in two polymer:fullerene acceptor blends. For PDTSiTTz, the blends from PCBM to ICTA show a systematic shift in DOS distribution from flat distribution to clear peaks across the energy spectra. On the contrary, PCPDTBT shows a stable DOS distribution with or without fullerene acceptors. Surprisingly, the DOS distributions of PDTSiTTz:fullerene blends are identical to the PCPDTBT indicating a less inter-chain interaction and more twisted conjugated backbone for PDTSiTTz upon blending. This provides a better understanding to the unusual non-Langevin recombination nature in PDTsiTTz and its correlation in DOS distribution.

Based on all the findings in this chapter, a design of higher Q_π and structural rigid NFAs is

recommended for developing higher performance NFAs based OPVs. To fulfill this, functional groups/atoms like fluorine, carbonyl, cyano or other strong electron withdrawing groups should be considered to be added on the accepting end units in order to increase Q_π. The donating core unit can also be extended for a larger distance between the electron negative accepting units and the core leading to higher Q_π. Long alkyl chains or other electron pushing groups are suggested to be attached to the adjacent carbon on the donating unit in order to provide a higher structural rigidity. Moreover, in order to utilize the strong Q_π, solvent engineering or packing engineering is necessary for highly crystalline face-on packing structure.

References

[1]J. Wu, J. Lee, Y.-C. Chin, H. Yao, H. Cha, J. Luke, J. Hou, J. S. Kim, and J. R. Durrant, "Exceptionally low charge trapping enables highly efficient organic bulk heterojunction solar cells", Energy and Environmental Science **13**, 2422–2430 (2020).

[2]Y. Dong, V. C. Nikolis, F. Talnack, Y.-C. Chin, J. Benduhn, G. Londi, J. Kublitski, X. Zheng, S. C. Mannsfeld, D. Spoltore, L. Muccioli, J. Li, X. Blase, D. Beljonne, J. S. Kim, A. A. Bakulin, G. D'Avino, J. R. Durrant, and K. Vandewal, "Orientation dependent molecular electrostatics drives efficient charge generation in homojunction organic solar cells", Nature Communications **11**, 4617 (2020).

[3]J. Marin-Beloqui, G. Zhang, J. Guo, J. Shaikh, T. Wohrer, S. M. Hosseini, B. Sun, J. Shipp, A. J. Auty, D. Chekulaev, J. Ye, Y.-C. Chin, M. B. Sullivan, A. J. Mozer, J.-S. Kim, S. Shoaee, and T. M. Clarke, "Insight into the Origin of Trapping in Polymer/Fullerene Blends with a Systematic Alteration of the Fullerene to Higher Adducts", The Journal of Physical Chemistry C **126**, 2708–2719 (2022).

[4]*Best research cell efficiency chart. NREL.* (2023) `https://www.nrel.gov/pv/cell-efficiency.html`.

[5]J. Luke, L. Corrêa, J. Rodrigues, J. Martins, M. Daboczi, D. Bagnis, and J.-S. Kim, "A Commercial Benchmark: Light-Soaking Free, Fully Scalable, Large-Area Organic Solar Cells for Low-Light Applications", Advanced Energy Materials, 2003405 (2021).

[6]R. Waller, M. Kacira, E. Magadley, M. Teitel, and I. Yehia, "Semi-Transparent Organic Photovoltaics Applied as Greenhouse Shade for Spring and Summer Tomato Production in Arid Climate", Agronomy **11**, 1152 (2021).

[7]W. Zhao, D. Qian, S. Zhang, S. Li, O. Inganäs, F. Gao, and J. Hou, "Fullerene-Free Polymer Solar Cells with over 11% Efficiency and Excellent Thermal Stability", Advanced Materials **28**, 4734–4739 (2016).

[8]J. Yuan, Y. Zhang, L. Zhou, G. Zhang, H.-L. Yip, T.-K. Lau, X. Lu, C. Zhu, H. Peng, P. A. Johnson, M. Leclerc, Y. Cao, J. Ulanski, Y. Li, and Y. Zou, "Single-Junction Organic Solar Cell with over 15% Efficiency Using Fused-Ring Acceptor with Electron-Deficient Core", Joule **3**, 1140–1151 (2019).

[9]A. Maurano, R. Hamilton, C. G. Shuttle, A. M. Ballantyne, J. Nelson, B. O'Regan, W. Zhang, I. McCulloch, H. Azimi, M. Morana, C. J. Brabec, and J. R. Durrant, "Recombination Dynamics as a Key Determinant of Open Circuit Voltage in Organic Bulk Heterojunction Solar Cells: A Comparison of Four Different Donor Polymers", Advanced Materials **22**, 4987–4992 (2010).

[10]C. G. Shuttle, A. Maurano, R. Hamilton, B. O'Regan, J. C. de Mello, and J. R. Durrant, "Charge extraction analysis of charge carrier densities in a polythiophene/fullerene solar cell: Analysis of the origin of the device dark current", Applied Physics Letters **93**, 183501 (2008).

[11]F. Deledalle, P. Shakya Tuladhar, J. Nelson, J. R. Durrant, and T. Kirchartz, "Understanding the Apparent Charge Density Dependence of Mobility and Lifetime in Organic Bulk Heterojunction Solar Cells", The Journal of Physical Chemistry C **118**, 8837–8842 (2014).

[12]S. Wheeler, F. Deledalle, N. Tokmoldin, T. Kirchartz, J. Nelson, and J. R. Durrant, "Influence of Surface Recombination on Charge-Carrier Kinetics in Organic Bulk Heterojunction Solar Cells with Nickel Oxide Interlayers", Physical Review Applied **4**, 024020 (2015).

[13]C. G. Shuttle, B. O'Regan, A. M. Ballantyne, J. Nelson, D. D. C. Bradley, and J. R. Durrant, "Bimolecular recombination losses in polythiophene: Fullerene solar cells", Physical Review B **78**, 113201 (2008).

[14]J. Wu, J. Luke, H. K. H. Lee, P. Shakya Tuladhar, H. Cha, S. Y. Jang, W. C. Tsoi, M. Heeney, H. Kang, K. Lee, T. Kirchartz, J. S. Kim, and J. R. Durrant, "Tail state limited photocurrent collection of thick photoactive layers in organic solar cells", Nature Communications **10**, 1–10 (2019).

[15]R. A. Street, "Localized state distribution and its effect on recombination in organic solar cells", Physical Review B **84**, 075208 (2011).

[16]M. Daboczi, I. Hamilton, S. Xu, J. Luke, S. Limbu, J. Lee, M. A. McLachlan, K. Lee, J. R. Durrant, I. D. Baikie, and J. S. Kim, "Origin of Open-Circuit Voltage Losses in Perovskite Solar Cells Investigated by Surface Photovoltage Measurement", ACS Applied Materials and Interfaces **11**, 46808–46817 (2019).

[17]Y. Cui, H. Yao, J. Zhang, T. Zhang, Y. Wang, L. Hong, K. Xian, B. Xu, S. Zhang, J. Peng, Z. Wei, F. Gao, and J. Hou, "Over 16% efficiency organic photovoltaic cells enabled by a chlorinated acceptor with increased open-circuit voltages", Nature Communications **10**, 2515 (2019).

[18]R. J. Kline and M. D. McGehee, "Morphology and Charge Transport in Conjugated Polymers", Journal of Macromolecular Science, Part C: Polymer Reviews **46**, 27–45 (2006).

[19]S. M. Menke, A. Cheminal, P. Conaghan, N. A. Ran, N. C. Greehnam, G. C. Bazan, T.-Q. Nguyen, A. Rao, and R. H. Friend, "Order enables efficient electron-hole separation at an organic heterojunction with a small energy loss", Nature Communications **9**, 277 (2018).

[20]S. Liu, J. Yuan, W. Deng, M. Luo, Y. Xie, Q. Liang, Y. Zou, Z. He, H. Wu, and Y. Cao, "High-efficiency organic solar cells with low non-radiative recombination loss and low energetic disorder", Nature Photonics **14**, 300–305 (2020).

[21]C. Labanti, M. J. Sung, J. Luke, S. Kwon, R. Kumar, J. Hong, J. Kim, A. A. Bakulin, S.-K. Kwon, Y.-H. Kim, and J.-S. Kim, "Selenium-Substituted Non-Fullerene Acceptors: A Route to Superior Operational Stability for Organic Bulk Heterojunction Solar Cells", ACS Nano **15**, 7700–7712 (2021).

[22]J. Luke, E. M. Speller, A. Wadsworth, M. F. Wyatt, S. Dimitrov, H. K. H. Lee, Z. Li, W. C. Tsoi, I. McCulloch, D. Bagnis, J. R. Durrant, and J.-S. Kim, "Twist and Degrade—Impact of Molecular Structure on the Photostability of Nonfullerene Acceptors and Their Photovoltaic Blends", Advanced Energy Materials **9**, 1803755 (2019).

[23]K. Cnops, B. P. Rand, D. Cheyns, B. Verreet, M. A. Empl, and P. Heremans, "8.4% efficient fullerene-free organic solar cells exploiting long-range exciton energy transfer", Nature Communications **5**, 3406 (2014).

[24]B. Crone, A. Dodabalapur, Y.-Y. Lin, R. W. Filas, Z. Bao, A. LaDuca, R. Sarpeshkar, H. E. Katz, and W. Li, "Large-scale complementary integrated circuits based on organic transistors", Nature **403**, 521–523 (2000).

[25]B. Servet, G. Horowitz, S. Ries, O. Lagorsse, P. Alnot, A. Yassar, F. Deloffre, P. Srivastava, and R. Hajlaoui, "Polymorphism and Charge Transport in Vacuum-Evaporated Sexithiophene Films", Chemistry of Materials **6**, 1809–1815 (1994).

[26]C. Lorch, R. Banerjee, J. Dieterle, A. Hinderhofer, A. Gerlach, J. Drnec, and F. Schreiber, "Templating Effects of α-Sexithiophene in Donor–Acceptor Organic Thin Films", The Journal of Physical Chemistry C **119**, 23211–23220 (2015).

[27]Z. Yin, J. Wei, and Q. Zheng, "Interfacial Materials for Organic Solar Cells: Recent Advances and Perspectives", Advanced Science **3**, 1500362 (2016).

[28]Z. Xu, B. Zhong Tang, Y. Wang, and D. Ma, "Recent advances in high performance blue organic light-emitting diodes based on fluorescence emitters", Journal of Materials Chemistry C **8**, 2614–2642 (2020).

[29]Q. Burlingame, B. Song, L. Ciammaruchi, G. Zanotti, J. Hankett, Z. Chen, E. A. Katz, and S. R. Forrest, "Reliability of Small Molecule Organic Photovoltaics with Electron-Filtering Compound Buffer Layers", Advanced Energy Materials **6**, 1601094 (2016).

[30]U. Hörmann, C. Lorch, A. Hinderhofer, A. Gerlach, M. Gruber, J. Kraus, B. Sykora, S. Grob, T. Linderl, A. Wilke, A. Opitz, R. Hansson, A. S. Anselmo, Y. Ozawa, Y. Nakayama, H. Ishii, N. Koch, E. Moons, F. Schreiber, and W. Brütting, "V_{OC} from a Morphology Point of View: the Influence of Molecular Orientation on the Open Circuit Voltage of Organic Planar Heterojunction Solar Cells", The Journal of Physical Chemistry C **118**, 26462–26470 (2014).

[31]T. Taima, M. Shahiduzzaman, T. Ishizeki, K. Yamamoto, M. Karakawa, T. Kuwabara, and K. Takahashi, "Sexithiophene-Based Photovoltaic Cells with High Light Absorption Coefficient via Crystalline Polymorph Control", The Journal of Physical Chemistry C **121**, 19699–19704 (2017).

[32]G. Horowitz, B. Bachet, A. Yassar, P. Lang, F. Demanze, J.-L. Fave, and F. Garnier, "Growth and Characterization of Sexithiophene Single Crystals", Chemistry of Materials **7**, 1337–1341 (1995).

[33]G. D'Avino, L. Muccioli, F. Castet, C. Poelking, D. Andrienko, Z. G. Soos, J. Cornil, and D. Beljonne, "Electrostatic phenomena in organic semiconductors: fundamentals and implications for photovoltaics", Journal of Physics: Condensed Matter **28**, 433002 (2016).

[34]S. Duhm, G. Heimel, I. Salzmann, H. Glowatzki, R. L. Johnson, A. Vollmer, J. P. Rabe, and N. Koch, "Orientation-dependent ionization energies and interface dipoles in ordered molecular assemblies", Nature Materials **7**, 326–332 (2008).

[35]Y. Li, P. Li, and Z.-H. Lu, "Molecular Orientation and Energy Levels at Organic Interfaces", Advanced Electronic Materials **2**, 1600306 (2016).

[36]L. Zhu, M. Zhang, G. Zhou, T. Hao, J. Xu, J. Wang, C. Qiu, N. Prine, J. Ali, W. Feng, X. Gu, Z. Ma, Z. Tang, H. Zhu, L. Ying, Y. Zhang, and F. Liu, "Efficient Organic Solar Cell with 16.88% Efficiency Enabled by Refined Acceptor Crystallization and Morphology with Improved Charge Transfer and Transport Properties", Advanced Energy Materials **10**, 1904234 (2020).

[37]M. Schwarze, K. S. Schellhammer, K. Ortstein, J. Benduhn, C. Gaul, A. Hinderhofer, L. Perdigón Toro, R. Scholz, J. Kublitski, S. Roland, M. Lau, C. Poelking, D. Andrienko, G. Cuniberti, F. Schreiber, D. Neher, K. Vandewal, F. Ortmann, and K. Leo, "Impact of molecular quadrupole moments on the energy levels at organic heterojunctions", Nature Communications **10**, 2466 (2019).

[38]K. Yamada, S. Yanagisawa, T. Koganezawa, K. Mase, N. Sato, and H. Yoshida, "Impact of the molecular quadrupole moment on ionization energy and electron affinity of organic thin films: Experimental determination of electrostatic potential and electronic polarization energies", Physical Review B **97**, 245206 (2018).

[39]F. Eisner, G. Foot, J. Yan, M. Azzouzi, D. G. Georgiadou, W. Y. Sit, Y. Firdaus, G. Zhang, Y.-H. Lin, H.-L. Yip, T. D. Anthopoulos, and J. Nelson, "Emissive Charge-Transfer States at Hybrid Inorganic/Organic Heterojunctions Enable Low Non-Radiative Recombination and High-Performance Photodetectors", Advanced Materials **34**, 2104654 (2022).

[40]Y. Xiao, J. Yuan, G. Zhou, K. Chak Ngan, X. Xia, J. Zhu, Y. Zou, N. Zhao, X. Zhan, and X. Lu, "Unveiling the crystalline packing of Y6 in thin films by thermally induced "backbone-on" orientation", Journal of Materials Chemistry A **9**, 17030–17038 (2021).

[41]R. Li, W. Hu, Y. Liu, and D. Zhu, "Micro- and Nanocrystals of Organic Semiconductors", Accounts of Chemical Research **43**, 529–540 (2010).

[42]J. Luke, E. J. Yang, Y.-C. Chin, Y. Che, L. Winkler, D. Whatling, C. Labanti, S. Y. Park, and J.-S. Kim, "Strong Intermolecular Interactions Induced by High Quadrupole Moments Enable Excellent Photostability of Non-Fullerene Acceptors for Organic Photovoltaics", Advanced Energy Materials **12**, 2201267 (2022).

[43]D. Luo, W. Jang, D. D. Babu, M. Soo Kim, D. Hwan Wang, and A. K. Ko Kyaw, "Recent progress in organic solar cells based on non-fullerene acceptors: materials to devices", Journal of Materials Chemistry A **10**, 3255–3295 (2022).

[44]J. Noh, S. Jeong, and J.-Y. Lee, "Ultrafast formation of air-processable and high-quality polymer films on an aqueous substrate", Nature Communications **7**, 12374 (2016).

[45]T. H. Lee, W.-W. Park, S. Y. Park, S. Cho, O.-H. Kwon, and J. Y. Kim, "Planar Organic Bilayer Heterojunctions Fabricated on Water with Ultrafast Donor-to-Acceptor Charge Transfer", Solar RRL **5**, 2100326 (2021).

[46]H. Cha, G. Fish, J. Luke, A. Alraddadi, H. H. Lee, W. Zhang, Y. Dong, S. Limbu, A. Wadsworth, I. P. Maria, L. Francàs, H. L. Sou, T. Du, J.-S. Kim, M. A. McLachlan, I. McCulloch, and J. R. Durrant, "Suppression of Recombination Losses in Polymer:Nonfullerene Acceptor Organic Solar Cells due to Aggregation Dependence of Acceptor Electron Affinity", Advanced Energy Materials **9**, 1901254 (2019).

[47]S. Y. Park, S. Chandrabose, M. B. Price, H. S. Ryu, T. H. Lee, Y. S. Shin, Z. Wu, W. Lee, K. Chen, S. Dai, J. Zhu, P. Xue, X. Zhan, H. Y. Woo, J. Y. Kim, and J. M. Hodgkiss, "Photophysical pathways in efficient bilayer organic solar cells: The importance of interlayer energy transfer", Nano Energy **84**, 105924 (2021).

[48]M. B. Price, P. A. Hume, A. Ilina, I. Wagner, R. R. Tamming, K. E. Thorn, W. Jiao, A. Goldingay, P. J. Conaghan, G. Lakhwani, N. J. L. K. Davis, Y. Wang, P. Xue, H. Lu, K. Chen, X. Zhan, and J. M. Hodgkiss, "Free charge photogeneration in a single component high photovoltaic efficiency organic semiconductor", Nature Communications **13**, 2827 (2022).

[49]R. Wang, C. Zhang, Q. Li, Z. Zhang, X. Wang, and M. Xiao, "Charge Separation from an Intra-Moiety Intermediate State in the High-Performance PM6:Y6 Organic Photovoltaic Blend", Journal of the American Chemical Society **142**, 12751–12759 (2020).

[50]J. Peet, L. Wen, P. Byrne, S. Rodman, K. Forberich, Y. Shao, N. Drolet, R. Gaudiana, G. Dennler, and D. Waller, "Bulk heterojunction solar cells with thick active layers and high fill factors enabled by a bithiophene-co-thiazolothiazole push-pull copolymer", Applied Physics Letters **98**, 043301 (2011).

[51]T. M. Clarke, D. B. Rodovsky, A. A. Herzing, J. Peet, G. Dennler, D. DeLongchamp, C. Lungenschmied, and A. J. Mozer, "Significantly Reduced Bimolecular Recombination in a Novel Silole-Based Polymer: Fullerene Blend", Advanced Energy Materials **1**, 1062–1067 (2011).

[52]T. M. Clarke, J. Peet, P. Denk, G. Dennler, C. Lungenschmied, and A. J. Mozer, "Non-Langevin bimolecular recombination in a silole-based polymer:PCBM solar cell measured by time-resolved charge extraction and resistance-dependent time-of-flight techniques", Energy & Environmental Science **5**, 5241–5245 (2012).

[53]J. Wade, S. Wood, E. Collado-Fregoso, M. Heeney, J. Durrant, and J. S. Kim, "Impact of Fullerene Intercalation on Structural and Thermal Properties of Organic Photovoltaic Blends", Journal of Physical Chemistry C **121**, 20976–20985 (2017).

[54]J. Yuan, H. Zhang, R. Zhang, Y. Wang, J. Hou, M. Leclerc, X. Zhan, F. Huang, F. Gao, Y. Zou, and Y. Li, "Reducing Voltage Losses in the A-DA'D-A Acceptor-Based Organic Solar Cells", Chem **6**, 2147–2161 (2020).

Chapter 5

Hole Transport Materials – Suppressing PEDOT:PSS Doping-Induced Interfacial Recombination Loss in Perovskite Solar Cells

PEDOT:PSS is widely used as a hole transport layer (HTL) in perovskite solar cells (PSCs) due to its facile processability, industrial scalability, and commercialization potential. However, PSCs utilizing PEDOT:PSS suffer from strong recombination losses compared to other organic HTLs. This results in lower open-circuit voltage (V_{OC}) and power conversion efficiency (PCE). Most studies focus on doping PEDOT:PSS to improve charge extraction, but it has been suggested that a high doping level can cause strong recombination losses. Herein, systematically dedope PEDOT:PSS with aqueous NaOH, raising its Fermi level by up to 500 meV, is investigated and optimized its layer thickness in p-i-n devices. A significant reduction of recombination losses at the dedoped PEDOT:PSS/perovskite interface is evidenced by a longer photoluminescence lifetime and higher magnitude of surface photovoltage, leading to an increased device V_{OC}, fill factor (FF), and PCE. These results provide insights into the relationship between doping level of HTLs and interfacial charge carrier recombination losses.

This chapter is mainly based on Chin et al. [1] published in ACS Energy Letters. All the works are done by this thesis author with coauthors contributing in discussions.

5.1 Introduction

As described in Section 2.2.3, HTL and its interface between perovskite layer is one of the biggest hurdle to device performance. Therefore, many research focusing on further p-doping HTLs by adding various p-type dopants into the HTL.[2,3] These p-type dopants enable a favorable interfacial energetic alignment and faster hole mobility, and therefore improving the PCE.[4–6] However, highly doped HTL was shown to exhibit a significant interfacial recombination between the doping induced holes and the free electrons on the interface.[7] Thus, a systematic study on dedoping of a highly doped HTL such as PEDOT:PSS can lead to a better understanding of the loss mechanisms and provide a wider strategy to HTL modification.

PEDOT:PSS is one of the most widely studied HTL in perovskite devices because of its facile fabrication and suitable wettability for perovskite formation on top.[8] Also, PEDOT:PSS is well-adopted in industry with a very low price and high quality, which makes it a strong HTL candidate for PSC commercialization. However, its highly doped nature leads to the issues mentioned above (such as strong interfacial recombination) rendering PEDOT:PSS as an HTL with relatively low stability and low performance compared to other HTLs for PSCs.[9,10] Many studies have followed the common approach of further p-doping of PEDOT:PSS in order to match the energetics and to increase conductivity for performance improvements.[4–6,11] In this work, instead of doping PEDOT:PSS, we provide a strategy to investigate and reduce interfacial recombination by dedoping PEDOT:PSS. Since dedoping decreases the conductivity, an efficient charge extraction is maintained by reducing the thickness of dedoped PEDOT:PSS layer. This study provides the clear linkage between the HTL doping level and interfacial recombination loss and paves the way for a new strategy for tailoring HTLs for higher PSC performance.

5.2 Doping Level and Thickness Control on PEDOT:PSS

To prepare dedoped PEDOT:PSS layers, we blend its solution with 4.5 %, 20 % and 50 % (vol %) of 1 M NaOH, which is then spin-coated onto different substrates for optical and electrical characterization as well as for devices.[12] The normalized absorption spectra in Fig. 5.1a show typical bipolaron peaks at wavelengths >1100 nm, which are reduced with an increasing NaOH blend ratio and accompanied by an increase in the polaronic peak at around 800 nm.[13,14] The dedoping of PEDOT:PSS with NaOH is further confirmed by Raman spectroscopy (Fig. 5.1b). The central peak around 1425 cm^{-1}, assigned to the PEDOT intraring double bond oscillation, becomes narrower with a higher NaOH blend ratio.[14–16] This correlates to the resonance of dedoped PEDOT with a 633 nm laser as can be seen from the absorption spectra. A decrease of the intraring single bond peak at 1370 cm^{-1} as well as the emergence of a new peak at 1520 cm^{-1} are consistent with previous reports of biased Raman spectroscopy of PEDOT:PSS.[17] Note that beyond the 20 % blend ratio, there is no significant change in the absorption or Raman spectra, indicating dedoping saturation is reached at the 20 % NaOH blend ratio. The high blend ratio of 50 % simply dilutes the PEDOT:PSS content, therefore reducing the absorbance and decreasing the signal-to-noise ratio.

The Fermi level (E_F) of the blend series is measured by a Kelvin probe with respect to the vacuum level and, therefore, its magnitude is equivalent to the work function. It shows a clear linear trend, decreasing from −5.15 eV to −4.55 eV with an increasing NaOH ratio (Fig. 5.1c). The E_F of the 4.5 % blend (−4.85 eV) lies in between the neat and 20 % blend samples, making it an ideal intermediate dedoping ratio for the study. On the other hand, the E_F of the 50 % blend ratio has a similar E_F to the 20 % blend but with a larger deviation. This could be possibly due to PSS dissociation in strong basic environment, which is in agreement with the lower absorbance and similar normalized Raman spectrum compared to the 20 % blend sample (Figs. 5.1a–5.1b). For dedoped PEDOT:PSS, lower conductivity is measured as expected. Field effect transistor measurements reveal a significant drop in conductivity between the neat and 20 % blend samples from around 3875 µS cm^{-1} to 420 µS cm^{-1} (Fig. 5.1d). The dedoping-induced change in conductivity is strongly correlated to the optical absorption. The main dedoping effect occurs between 4.5 % and 20 % NaOH, leading to a significant drop in the bipolaron absorption, accompanied by almost an order of magnitude drop in conductivity. An

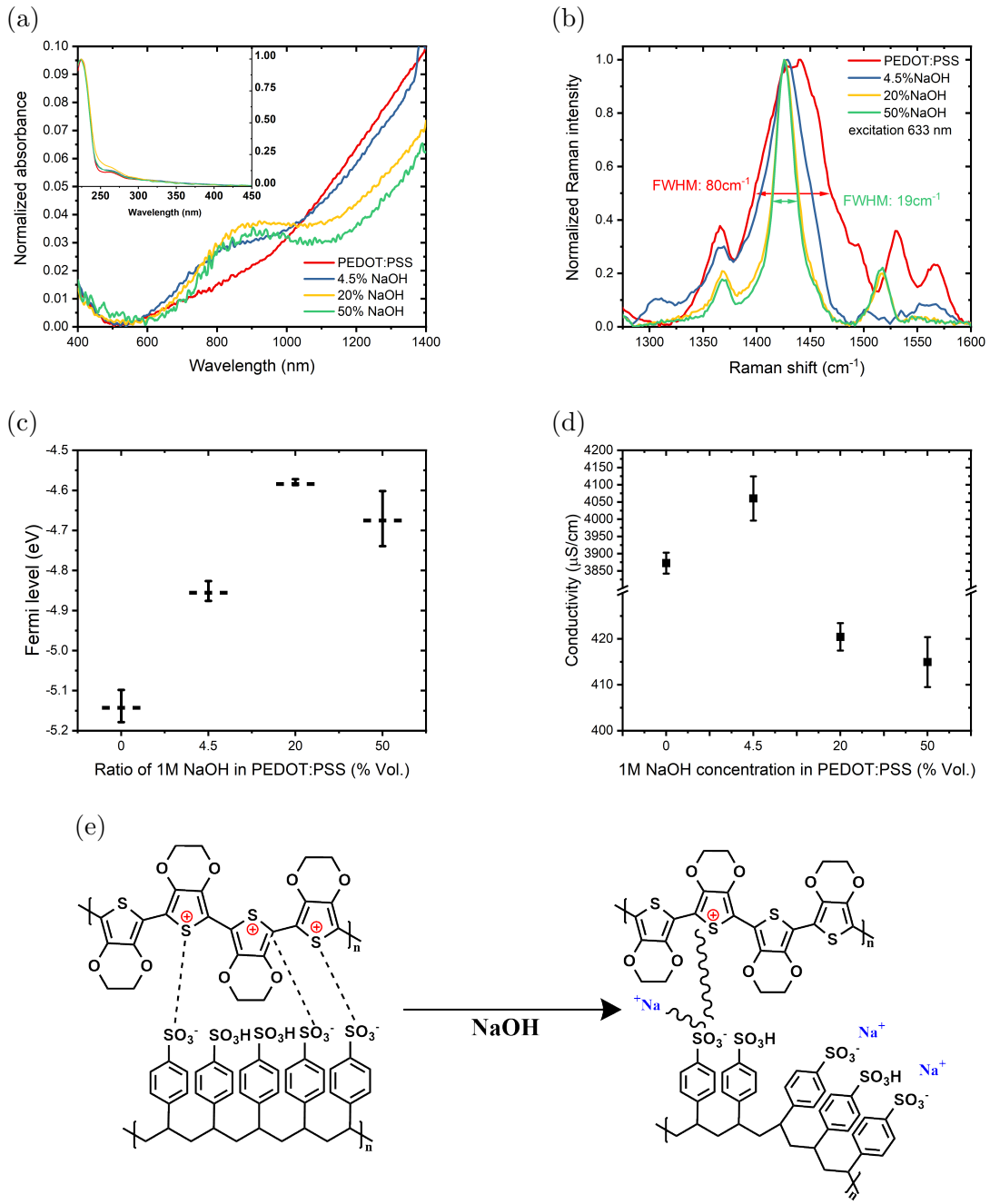


Figure 5.1: Optical and electrical properties of neat and dedoped PEDOT:PSS with 4.5, 20, and 50 % volume fractions of 1 M NaOH. (a) UV-vis spectra normalized at 220 nm with the inset of full spectra, (b) Raman spectra with 633 nm laser excitation, (c) Fermi level (measured by Kelvin probe), (d) conductivity, and (e) proposed dedoping hypothesis (the dash/wiggly lines indicate a strong/weak ionic interactions).

increase of NaOH from 20 % to 50 % does not produce any further changes in either absorption or conductivity, which is consistent with no significant changes in the Raman spectrum and the work function. Interestingly, however, the 4.5 % blend shows a slightly higher conductivity compared to the neat sample, which suggests a potential contribution of the ionic current from sodium ions introduced by the NaOH solution. Though the exact dedoping mechanism of

PEDOT:PSS dedoping by NaOH is unclear, a proposed hypothesis is illustrated in Fig. 5.1e. In this hypothesis, the hydroxide ions deprotonate the acidic sulfonates and thus reduce the interactions between polarons on PEDOT and the sulfonate functional groups on PSS. A slightly increased surface roughness is seen in Figs. 5.2a–5.2c, but the overall surface morphology is maintained. These data show the possibility of fine-tuning the energetics of PEDOT:PSS by blending with NaOH solution, enabling further study of the influence of this on perovskite solar cells.

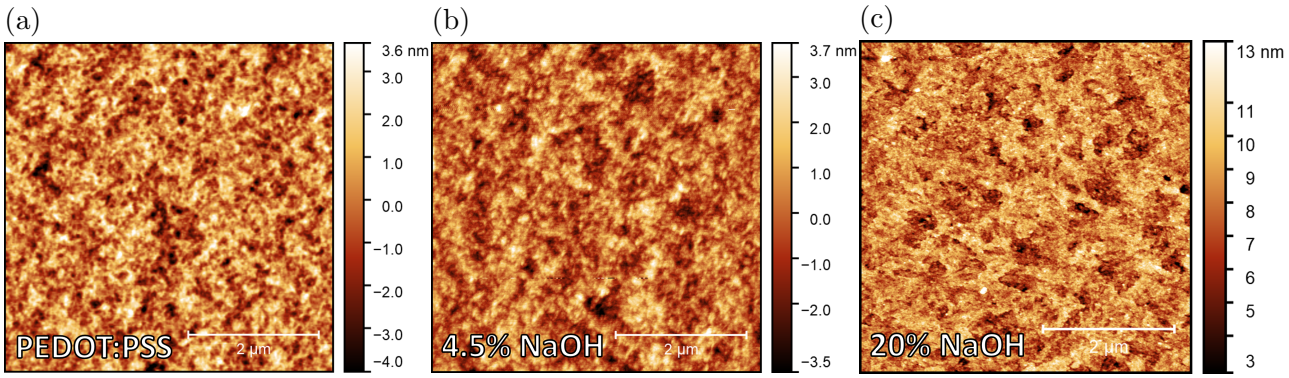


Figure 5.2: AFM image of PEDOT:PSS with different NaOH blend ratio in vol%.

5.3 Characterizations of Dedoped PEDOT:PSS HTL in Perovskite Devices

To unveil the impact of dedoped PEDOT:PSS HTL on recombination losses and device characteristics, we apply neat, 4.5 % and 20 % blends in a p-i-n perovskite solar cell architecture: ITO/PEDOT:PSS/methylammonium lead iodide (MAPI)/phenyl-C61-butyric acid methyl ester (PCBM)/2,9-dimethyl-4,7diphenyl-1,10-phenanthroline (BCP)/Ag, as shown in Fig. 5.3a. From the neat to 20 % blend, the short-circuit current density (J_{SC}) and V_{OC} decrease simultaneously and, as a result, the overall device PCE decreases. However, we notice an improvement in the FF, originating mostly from a reduced shunt resistance as can be seen by the much shallower slope close to J_{SC} (Fig. 5.3a). This indicates that the dedoped PEDOT:PSS HTL has better electron blocking capability, which is consistent with the widened band gap (E_g) shown in the absorption spectra (Fig. 5.1a). Here, the highly doped PEDOT:PSS shows mainly a bipolaron absorption band (<1400 nm), and upon dedoping, this

absorption band shifts to high energy (∼800 nm) due to more polarons, leading to a larger E_g in the dedoped PEDOT:PSS.

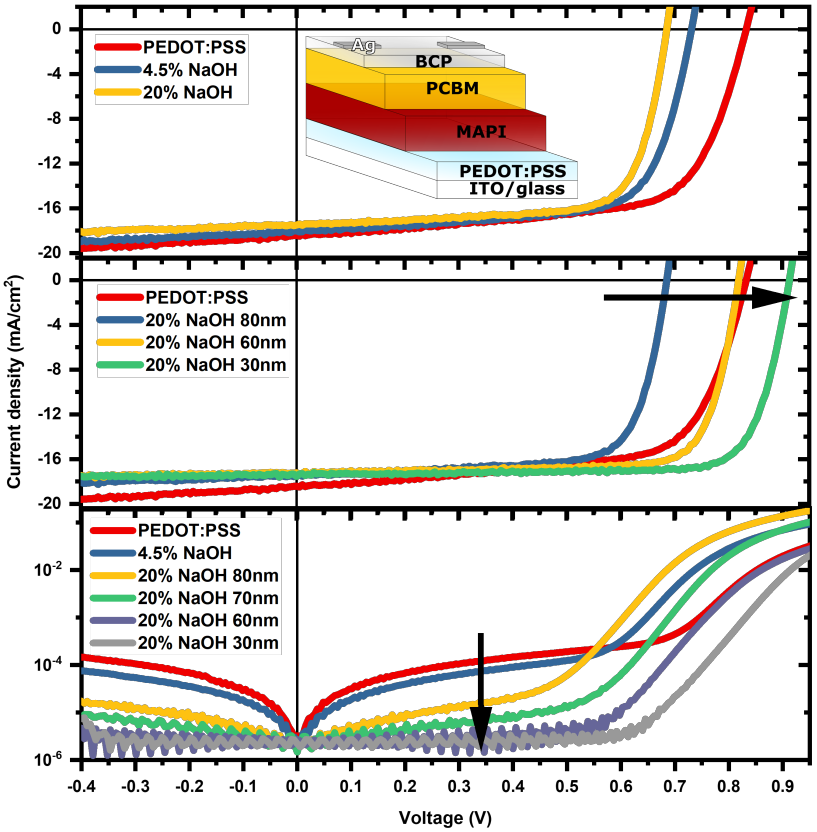


Figure 5.3: NaOH-dedoped device structure and reverse current density-voltage scans. (a) Reverse current density-voltage scans of NaOH-dedoped PEDOT:PSS devices, (b) reverse current density-voltage scans of the 20 % NaOH-dedoped PEDOT:PSS solar cells with different transport layer thicknesses, and (c) dark current density-voltage scans of all NaOH-dedoped PEDOT:PSS devices.

Dedoping, nonetheless, decreases the conductivity of PEDOT:PSS, which can slow down charge transport/extraction. Therefore, optimization of the HTL thickness is crucial to maintain efficient charge transport/extraction and, at the same time, utilize the benefits of reduced recombination and better charge selectivity. Herein, we control the HTL thickness by diluting the 20 % blend PEDOT:PSS with deionized water to obtain a range of thickness from 80 ± 10 nm (no dilution) to 30 ± 10 nm (4 times dilution). Further dilution was attempted but failed to provide good coverage over the ITO substrates. Kelvin probe measurements confirm that the doping level is maintained under dilution (Fig. 5.4) with E_F maintained at -4.58 ± 0.03 eV across different levels of dilution.

With the optimized thickness, the device performance sharply increased as shown in

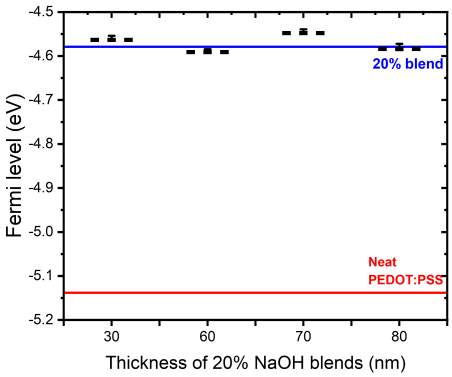


Figure 5.4: Fermi level of different thickness 20 vol% NaOH dedoped PEDOT:PSS.

Fig. 5.3b with an average V_{OC} of 0.92 V and PCE of 12.7 %. This is a 10 % improvement for V_{OC} and 25 % for PCE compared to the optimized neat PEDOT:PSS devices. The superior charge blocking ability can also be seen in the dark current-voltage scans (Fig. 5.3c). Dark current in the shunt region (<0.2 V) is significantly reduced by dedoping, and the dark currents at 0.4 V (before turn-on) have been sharply reduced from 1.47×10^{-3} mA cm^{-2} (neat) to 3.05×10^{-5} mA cm^{-2} (20 % blend, 30 nm). Note that the dark current density around 3×10^{-5} mA cm^{-2} is corresponding to the instrument sensitivity in the current (0.1 nA), so a plateau appears for the thin dedoped PEDOT:PSS devices. This indicates a significant increase in shunt resistance and a trend toward more-ideal diode behavior. Noticeably, the turn-on voltage is coherent with the V_{OC} trend, which decreases with increased dedoping of thick PEDOT:PSS layer and increases by reducing the thickness of dedoped PEDOT:PSS layer.

The statistics of V_{OC}, J_{SC}, shunt resistance, PCE, and FF are shown in Fig. 5.5. The average V_{OC}, as mentioned above, decreases from 0.83 V to 0.69 V through dedoping due to the recombination of the accumulated charges at the interface and significantly improves to 0.92 V with a thinner HTL. Although thickness affects the charge extraction, dedoped PEDOT:PSS already improves the average FF from 0.67 to 0.74 without thickness optimization. Since their thickness is not optimized here, the improvement is mainly coming from the better charge blocking ability. With thickness optimization, the full potential of dedoping is utilized, and the average FF reaches 0.8 with our best devices. Surprisingly, the deviation of FF over different devices is reduced with dedoping. We believe this is due to a change in the wettability of the PEDOT:PSS surface, which results in better perovskite crystallization and higher consistency,

as demonstrated by the AFM images in Figs. 5.6a–5.6c. Despite the huge drop in conductivity from dedoping (Fig. 5.1d), only a small drop in the J_{SC} values is observed when dedoped PEDOT:PSS is incorporated into devices (Fig. 5.5d). As the dedoped PEDOT:PSS thickness is reduced, the J_{SC} improves slightly, consistent with the improvements in shunt resistance. Combining the improvement in FF and V_{OC} , the overall PCE increased from 10.2 % for the neat PEDOT:PSS devices to 12.7 % for the optimized 30 nm 20 % NaOH-dedoped devices.

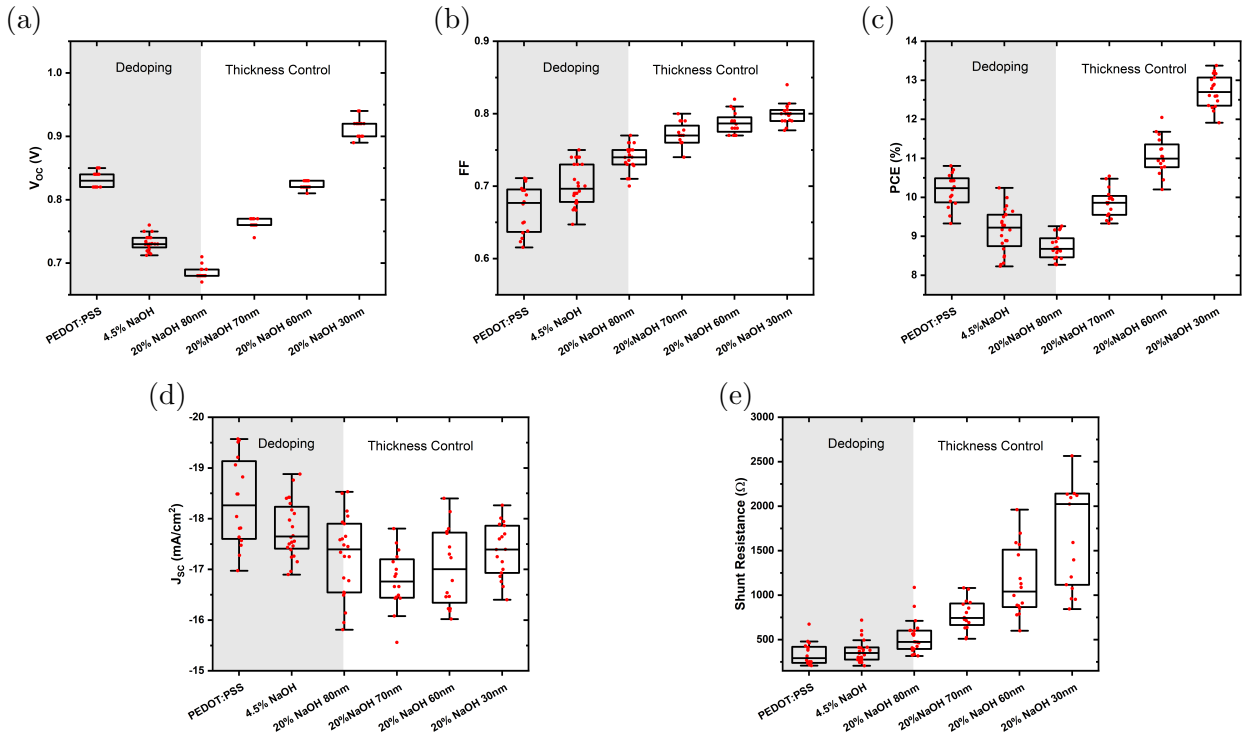


Figure 5.5: Box plots of (a) open-circuit voltage (V_{OC}), (b) fill factor (FF), (c) power conversion efficiency (PCE), (d) short-circuit current density (J_{SC}) and (e) shunt resistance of NaOH-dedoped devices.

5.4 Reduced Interfacial Recombination Loss in Perovskite Solar Cells

To confirm the origin of the performance improvement, we investigate the optoelectronic properties of half cells with a structure of ITO/HTL/MAPI (Fig. 5.7). First, the intensity of photoluminescence (PL) of the MAPI layer is significantly enhanced when deposited on top of the dedoped PEDOT:PSS HTL layer and further increased when applying a thinner HTL layer. The higher magnitude of PL at open circuit (i.e.,no external connections) has been shown

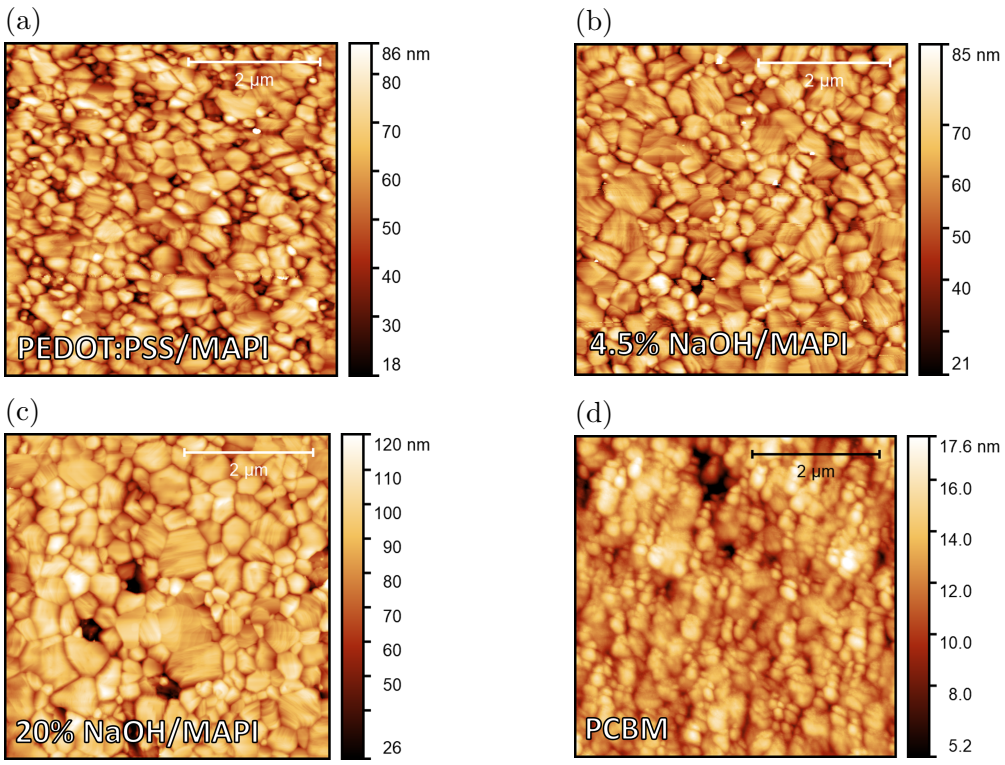


Figure 5.6: MAPI or PCBM on top of PEDOT:PSS with different NaOH blend ratio in vol%.

to indicate the strength of surface recombination loss.[18,19] Since the half cells are not grounded, free charges generated by photoexcitation will remain in the system; thus, more nonradiative recombination of free charge carriers results in lower PL intensity. Notably, only a small PL shift (∼3 nm) occurs among different doping levels as seen in the inset of Fig. 5.7a, which is attributed to the small compositional differences across the MAPI films. We have shown that a small but similar amount of tail states is found among the perovskite layers on top of different dedoped PEDOT:PSS (Fig. 5.7d). It indicates that even though tiny compositional difference may exist, the overall perovskite quality across samples is comparable, and the difference is negligible. Further evidence for reduced recombination losses can be seen from the transient PL probed at 780 nm (Fig. 5.7b). The dedoped PEDOT:PSS samples show a slightly longer charge carrier lifetime even without thickness optimization, which is linked to reduced recombination loss at the interface. Nonetheless, the reduced recombination for thick PEDOT:PSS devices was not seen as an increase in V_{OC}, due to the losses caused by its lower conductivity (Fig. 5.3a). By decreasing the thickness of dedoped PEDOT:PSS, the reduced interfacial recombination loss is fully revealed and gives a nearly single exponential PL decay. This indicates that the radiative recombination dominates the system at optimal thickness. For comparison, we also measured the optical behaviors in full cells (Fig. 5.8). With the top PCBM layer, the same trends in

PL intensity and decay are observed; however, the charges generated by photoexcitation are fully extracted from perovskite layer, so a lower PL intensity and faster PL decay are observed, demonstrating a higher efficiency of charge extraction in the full device. The characteristic behavior from both PL intensity and dynamics suggests a reduction in nonradiative surface recombination with thin, dedoped PEDOT:PSS HTL.

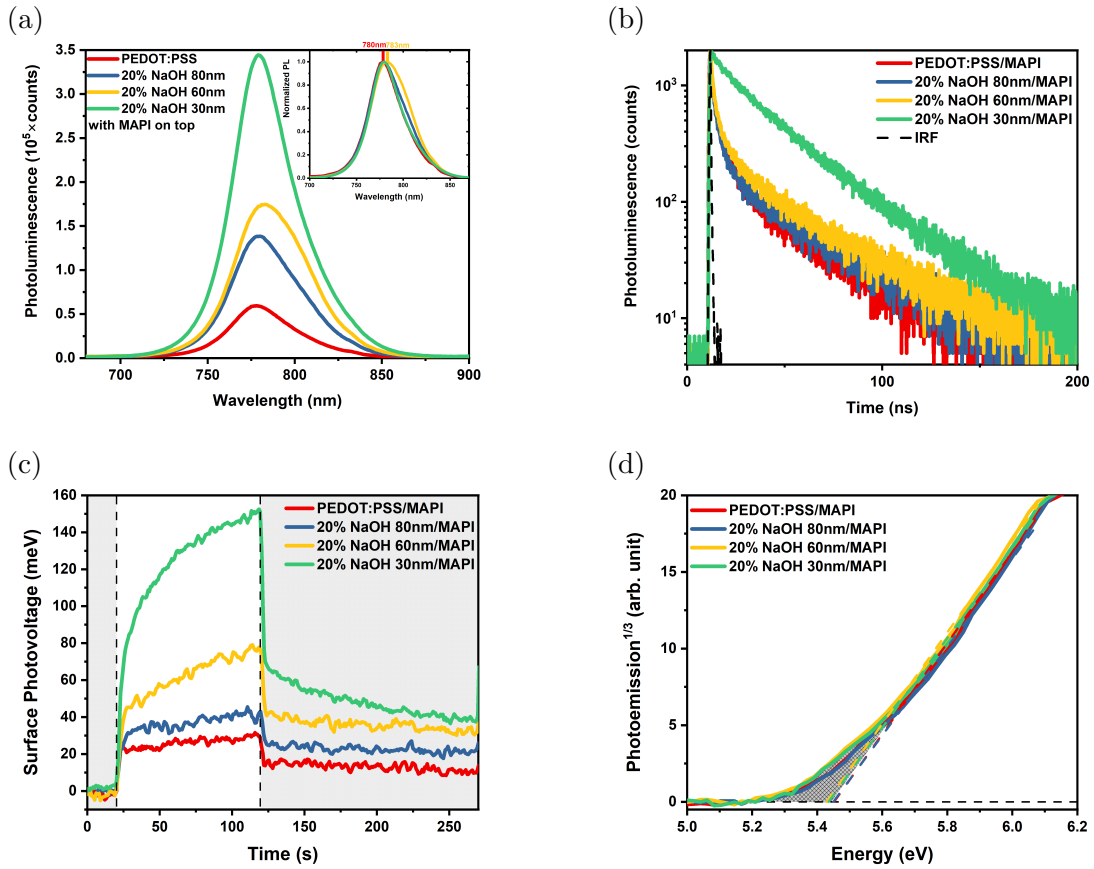


Figure 5.7: Thickness-dependent optical and optoelectronic measurements of NaOH-dedoped PEDOT:PSS HTL with MAPI on top. (a) Photoluminescence (PL) with an inset of normalized PL and (b) transient PL decay of MAPI probed at 780 nm (with a 405 nm excitation wavelength). (c) Surface photovoltage signals generated by 0.2 sun white light illumination. Dashed vertical lines indicate the transitions between light off (gray) and light on (white). (d) Ambient photoemission spectra of MAPI on top of doped and dedoped PEDOT:PSS HTL with different thicknesses.

To directly detect the differences in surface recombination between the doped and dedoped HTL, surface photovoltage (SPV) with MAPI on top was measured (Fig. 5.7c).[10,20] SPV measures the change of surface potential under illumination, which is related to the remaining charge density on the top surface and any ionic rearrangement within the perovskite. Since the samples are only grounded on the HTL side, the holes are fully extracted, while the electrons remain in the MAPI layer building up a surface voltage difference analogous to open-circuit

conditions. The SPV signal is slightly larger with the 80 nm dedoped sample compared to the neat PEDOT:PSS, indicating a higher density of electrons accumulating in the MAPI layer. With thicker dedoped PEDOT:PSS devices, the advantage of dedoping is not clear in the device current-voltage curves due to the decreased conductivity opposing the increased selectivity and reduced recombination. However, when the thickness of dedoped PEDOT:PSS layer is reduced, a significantly larger SPV signal (130 meV) is observed. The same results were seen in full cells using the optimized thickness of dedoped PEDOT:PSS producing the highest SPV signal (80 meV) (Fig. 5.8c). It is interesting to notice that the optimized dedoped PEDOT:PSS shows the largest but slowest SPV increase during illumination. This might indicate that with a larger amount of free charges in the perovskite layer, the strong electric field induced by the optimized HTL causes more ionic movement, resulting in slow turn-on in the SPV transient. As soon as illumination is off, there is a significant drop in SPV (<50 % within the subsecond time scale), followed by a slow decay at longer time scale (<100 s). The main cause of this slow decay is not clearly understood at the moment, although any charge trapping induced by the photoactive layer (e.g. grain boundaries) cannot be ruled out, as found in organic bulk heterojunction blends (a large number of domains formed by donor and/or acceptor molecules) compared to bilayers (no domains formed).[21] In the thicker dedoped PEDOT:PSS devices, the low conductivity of the HTL severely limits charge transport/extraction. With thickness optimization, this limitation on charge transport/extraction is less of an issue, and the SPV demonstrates that there is reduced recombination and improved charge selectivity at the HTL/MAPI interface.

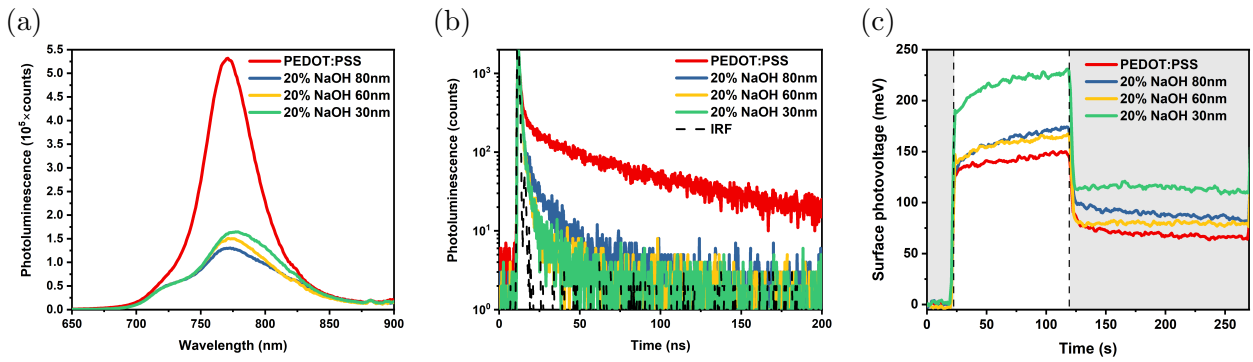


Figure 5.8: Thickness-dependent optical and optoelectronic measurements of NaOH de-doped PEDOT:PSS with MAPI and PCBM on top. (a) Photoluminescence (PL) and (b) transient PL decay with 405 nm excitation. (c) Surface photovoltage generated by 0.2 sun white light illumination. Dashed vertical lines indicate the transitions between light off (gray) and light on (white).

In order to further confirm the changes are solely coming from a different doping level of the PEDOT:PSS layer, ambient photoemission spectroscopy (APS) measurements were performed for MAPI on top of different HTLs (Figs. 5.7d and 5.9). The APS spectra of MAPI on top of all doped and dedoped HTLs show very similar signal intensity and extrapolated valence band edges (indicated by the dash line) as well as equal intraband tail states (indicated by the shaded area). In previous studies, the APS areas below the band edge were shown to be directly related to the trap states and defects in perovskites.[22–24] Therefore, the same amount of tail states measured on all HTLs suggests that the physical and electronic composition of MAPI is unaffected by the different underlayer HTLs. Despite the similar amount of traps in the MAPI layer, atomic force microscopy (AFM) shows a significantly larger MAPI grain size when it is formed on top of dedoped PEDOT:PSS (Figs. 5.6a–5.6c). This is related to changes in PEDOT:PSS wettability due to NaOH quenching the sulfonate groups on the PSS units. With sodium quenching off the sulfonate group, the hydrophilicity of the polymer increases, which is beneficial to perovskite crystallization. This makes the perovskite layer fabrication more consistent, shown by reduced FF deviation between dedoped devices (Fig. 5.5).

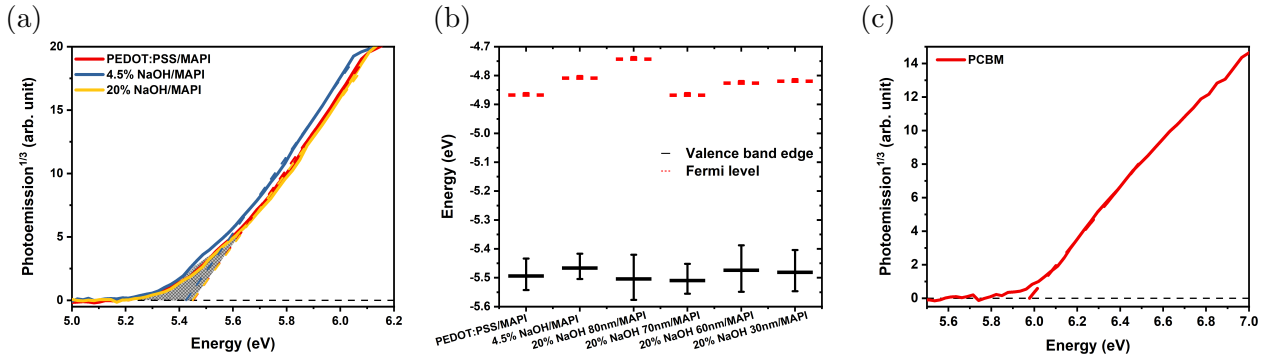


Figure 5.9: Energetics of MAPI and PCBM. (a) Ambient photoemission spectra of MAPI, and (b) valence band edge and Fermi levels of MAPI on top of neat, 4.5 vol% and 20 vol% NaOH blend PEDOT:PSS. (c) Ambient photoemission spectrum of PCBM on top of MAPI.

5.5 Conclusion

To illustrate the exceptionally low recombination loss mechanism revealed by the SPV measurements, a band alignment diagram is shown in Fig. 5.10. At dark equilibrium, at the interface of PEDOT:PSS and MAPI there is downward band-bending in the MAPI (toward the surface) due to the shallower E_F of MAPI compared to PEDOT:PSS. The highly

doped PEDOT:PSS has its E_F close to the HOMO level with a large density of pre-existing holes, which, under illumination, charge carriers are driven in opposite directions due to this interfacial band-bending. As charges accumulate at the PEDOT:PSS/MAPI interface, the band-bending is reduced toward open circuit. As this situation is reached, the excess holes in the PEDOT layer drive strong interfacial recombination, reducing the amount of electrons in the MAPI layer. Additionally, the highly doped PEDOT:PSS is less selective with a smaller E_g and has more metallic character, which both contribute to interfacial recombination. These effects result in lower SPV and reduced V_{OC} in full devices. On the contrary, dedoped PEDOT:PSS has its E_F matching or slightly shallower than MAPI, resulting in a small, effectively negligible upward band-bending. This band-bending and the lower conductivity of dedoped HTL require a thinner transport layer for optimal hole extraction. With the optimized thickness, dedoped PEDOT:PSS benefits from the enhanced selectivity and reduced interfacial charge carrier recombination allowing for an increased density of electrons in the perovskite photoactive layer at the open-circuit condition. This is reflected in a sharp increase of recorded SPV signal and an increased V_{OC} and PCE of solar cells based on the thin, dedoped PEDOT:PSS HTL.

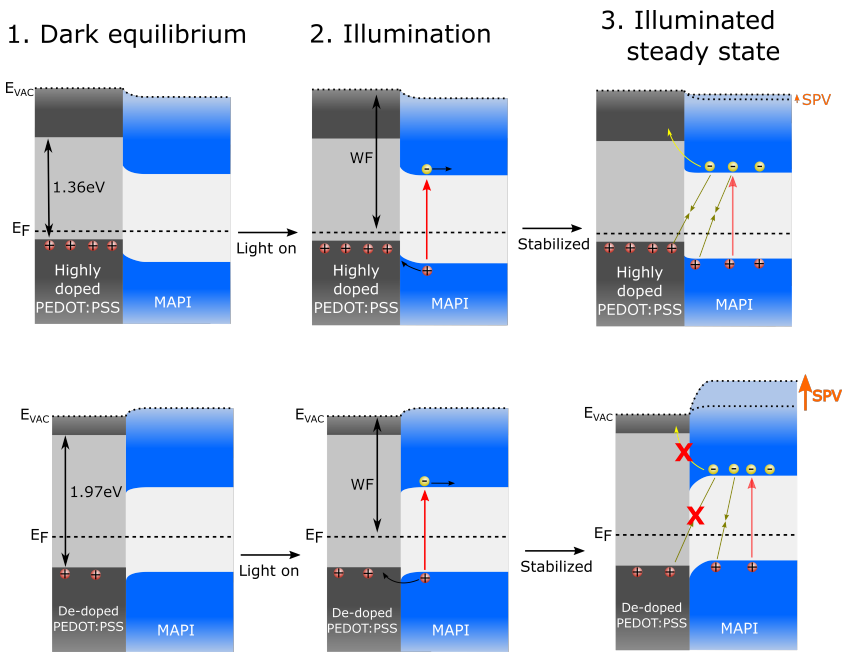


Figure 5.10: Schematic diagrams of surface photovoltage for neat and dedoped PEDOT:PSS with MAPI on top in three different stages. The Fermi level (E_F) and local vacuum level (E_{vac}) are indicated by dashed and dotted lines, respectively. The red arrows indicate charge generation, and the olive-green arrows indicate recombination. Measured SPV signals are shown by the orange arrow in the steady state stage. (Note that the confined interfacial band-bending in MAPI is drawn in a larger scale for visual clarity.)

In summary, this work demonstrates the correlation between the PEDOT:PSS doping level and interfacial recombination loss, providing a strategy to utilize less-doped HTLs in PSCs by thickness control. This approach should be applied to other HTL materials to confirm the generality of this strategy. Additionally, the higher performance from dedoping reveals another route to commercialize PSCs based on PEDOT:PSS HTL with its low cost and wide availability.

5.6 Experimental Methods

For basic experimental methods, refer to Chapter 3. Only project specific methods are listed in this section.

Device/Sample Fabrication

Poly(3,4-ethylenedioxythiophene) polystyrenesulfonate (PEDOT:PSS, Clevios AI4083 Heraeus) was dedoped by 1 M sodium hydroxide solution by 4.5 %, 20 % or 50 %, and the well-mixed 20 % blend solutions were then further diluted to 3:1, 1:1, and 1:3 volume ratios with deionized water. PEDOT:PSS solutions were then spin-coated at 2500 rpm for 1 min, followed by 10 min of annealing at 135 °C. Methylammonium lead iodide (MAPI) solutions (1.5 M) were prepared with lead iodide (Sigma-Aldrich, 99 %) and methylammonium iodide (Sigma-Aldrich, 98 %) and dissolved in a mix solution of dimethylformamide (DMF)/dimethyl sulfoxide (DMSO) (9:1.1,%v/v). The MAPI layer was deposited by spin-coating at 4000 rpm and with 400 µL of diethyl ether dripped at 7 s. The samples were then annealed at 80 °C for 1 min and at 100 °C for 30 min. The electron transport layers were prepared by spin-coating [6,6]-phenylC61-butyric acid methyl ester (PCBM 98 %, Ossila) from 23 mg mL^{-1} of chlorobenzene solution at 2000 rpm. Bathocuproine (BCP, Ossila) solution (0.05 mg mL^{-1}) was then spin-coated at 4000 rpm for 20 s to form a protective layer on top of PCBM.

References

[1]Y.-C. Chin, M. Daboczi, C. Henderson, J. Luke, and J.-S. Kim, "Suppressing PEDOT:PSS Doping-Induced Interfacial Recombination Loss in Perovskite Solar Cells", ACS Energy Letters **7**, 560–568 (2022).

[2]F. M. Rombach, S. A. Haque, and T. J. Macdonald, "Lessons learned from spiro-OMeTAD and PTAA in perovskite solar cells", Energy & Environmental Science **14**, 5161–5190 (2021).

[3]T. H. Schloemer, J. A. Christians, J. M. Luther, and A. Sellinger, "Doping strategies for small molecule organic hole-transport materials: impacts on perovskite solar cell performance and stability", Chemical Science **10**, 1904–1935 (2019).

[4]Y. Wu, J. Wang, X. Qiu, R. Yang, H. Lou, X. Bao, and Y. Li, "Highly Efficient Inverted Perovskite Solar Cells with Sulfonated Lignin Doped PEDOT as Hole Extract Layer", ACS Applied Materials and Interfaces **8**, 12377–12383 (2016).

[5]D. Liu, Y. Li, J. Yuan, Q. Hong, G. Shi, D. Yuan, J. Wei, C. Huang, J. Tang, and M. K. Fung, "Improved performance of inverted planar perovskite solar cells with F4-TCNQ doped PEDOT:PSS hole transport layers", Journal of Materials Chemistry A **5**, 5701–5708 (2017).

[6]Q. Wang, C. C. Chueh, M. Eslamian, and A. K. Jen, "Modulation of PEDOT:PSS pH for efficient inverted perovskite solar cells with reduced potential loss and enhanced stability", ACS Applied Materials and Interfaces **8**, 32068–32076 (2016).

[7]T. Du, W. Xu, M. Daboczi, J. Kim, S. Xu, C.-T. Lin, H. Kang, K. Lee, M. J. Heeney, J.-S. Kim, J. R. Durrant, and M. A. McLachlan, "P-Doping of organic hole transport layers in p–i–n perovskite solar cells: correlating open-circuit voltage and photoluminescence quenching", Journal of Materials Chemistry A **7**, 18971–18979 (2019).

[8]K. M. Reza, S. Mabrouk, and Q. Qiao, "A Review on Tailoring PEDOT:PSS Layer for Improved Performance of Perovskite Solar Cells", Proceedings of the Nature Research Society **2**, 02004 (2018).

[9]M. Neophytou, J. Griffiths, J. Fraser, M. Kirkus, H. Chen, C. B. Nielsen, and I. McCulloch, "High mobility, hole transport materials for highly efficient PEDOT:PSS replacement in inverted perovskite solar cells", Journal of Materials Chemistry C **5**, 4940–4945 (2017).

[10]M. Daboczi, I. Hamilton, S. Xu, J. Luke, S. Limbu, J. Lee, M. A. McLachlan, K. Lee, J. R. Durrant, I. D. Baikie, and J. S. Kim, "Origin of Open-Circuit Voltage Losses in Perovskite Solar Cells Investigated by Surface Photovoltage Measurement", ACS Applied Materials and Interfaces **11**, 46808–46817 (2019).

[11]J. Huang, K.-X. Wang, J.-J. Chang, Y.-Y. Jiang, Q.-S. Xiao, and Y. Li, "Improving the efficiency and stability of inverted perovskite solar cells with dopamine-copolymerized PEDOT:PSS as a hole extraction layer", Journal of Materials Chemistry A **5**, 13817–13822 (2017).

[12]T. C. Tsai, H. C. Chang, C. H. Chen, Y. C. Huang, and W. T. Whang, "A facile dedoping approach for effectively tuning thermoelectricity and acidity of PEDOT:PSS films", Organic Electronics **15**, 641–645 (2014).

[13]S. Sakamoto, M. Okumura, Z. Zhao, and Y. Furukawa, "Raman spectral changes of PEDOT-PSS in polymer light-emitting diodes upon operation", Chemical Physics Letters **412**, 395–398 (2005).

[14]S. Garreau, J. L. Duvail, and G. Louarn, "Spectroelectrochemical studies of poly(3,4-ethylenedioxythiophene) in aqueous medium", Synthetic Metals **125**, 325–329 (2001).

[15]M. M. De Kok, M. Buechel, S. I. Vulto, P. Van De Weyer, E. A. Meulenkamp, S. H. De Winter, A. J. Mank, H. J. Vorstenbosch, C. H. Weijtens, and V. Van Elsbergen, "Modification of PEDOT:PSS as hole injection layer in polymer LEDs", Physica Status Solidi (A) Applied Research **201**, 1342–1359 (2004).

[16]F. C. Tang, J. Chang, F. C. Wu, H. L. Cheng, S. L. C. Hsu, J. S. Chen, and W. Y. Chou, "Alignment of poly(3,4-ethylenedioxythiophene) polymer chains in photovoltaic cells by ultraviolet irradiation", Journal of Materials Chemistry **22**, 22409–22417 (2012).

[17]E. Tan, A.-M. Pappa, C. Pitsalidis, J. Nightingale, S. Wood, F. A. Castro, R. M. Owens, and J.-S. Kim, "A highly sensitive molecular structural probe applied to in situ biosensing of metabolites using PEDOT:PSS", Biotechnology and Bioengineering **117**, 291–299 (2020).

[18]P. Caprioglio, C. M. Wolff, O. J. Sandberg, A. Armin, B. Rech, S. Albrecht, D. Neher, and M. Stolterfoht, "On the Origin of the Ideality Factor in Perovskite Solar Cells", Advanced Energy Materials **10**, 2000502 (2020).

[19]P. Caprioglio, M. Stolterfoht, C. M. Wolff, T. Unold, B. Rech, S. Albrecht, and D. Neher, "On the Relation between the Open-Circuit Voltage and Quasi-Fermi Level Splitting in Efficient Perovskite Solar Cells", Advanced Energy Materials **9**, 1901631 (2019).

[20]M. Daboczi, J. Kim, J. Lee, H. Kang, I. Hamilton, C. T. Lin, S. D. Dimitrov, M. A. McLachlan, K. Lee, J. R. Durrant, and J. S. Kim, "Towards Efficient Integrated Perovskite/Organic Bulk Heterojunction Solar Cells: Interfacial Energetic Requirement to Reduce Charge Carrier Recombination Losses", Advanced Functional Materials **30**, 2001482 (2020).

[21]S. Y. Park, C. Labanti, J. Luke, Y.-C. Chin, and J.-S. Kim, "Organic Bilayer Photovoltaics for Efficient Indoor Light Harvesting", Advanced Energy Materials **12**, 2103237 (2022).

[22]J. Wu, J. Lee, Y.-C. Chin, H. Yao, H. Cha, J. Luke, J. Hou, J. S. Kim, and J. R. Durrant, "Exceptionally low charge trapping enables highly efficient organic bulk heterojunction solar cells", Energy and Environmental Science **13**, 2422–2430 (2020).

[23]S. Lee, D. B. Kim, I. Hamilton, M. Daboczi, Y. S. Nam, B. R. Lee, B. Zhao, C. H. Jang, R. H. Friend, J. S. Kim, and M. H. Song, "Control of Interface Defects for Efficient and Stable Quasi-2D Perovskite Light-Emitting Diodes Using Nickel Oxide Hole Injection Layer", Advanced Science **5**, 1801350 (2018).

[24]C. Labanti, M. J. Sung, J. Luke, S. Kwon, R. Kumar, J. Hong, J. Kim, A. A. Bakulin, S.-K. Kwon, Y.-H. Kim, and J.-S. Kim, "Selenium-Substituted Non-Fullerene Acceptors: A Route to Superior Operational Stability for Organic Bulk Heterojunction Solar Cells", ACS Nano **15**, 7700–7712 (2021).

Chapter 6

Perovskite Photovoltaic Materials – Reduced Recombination Loss and Spiro-OMeTAD Dopant Leakage by Phenethylammonium-Based Low-Dimensional Perovskite Passivation

In recent years, Ruddlesden-Popper phase perovskites (2D perovskite) have been applied in perovskite solar cells (PSCs) as either an interfacial or bulk passivation layer to reduce the trap-assisted charge recombination losses and extending device lifetime. Although most of the studies attribute the advancement to trap state passivation as well as high stability originating from high formation energy, the role of 2D perovskite in PSCs, particularly its dimensionality and interfacial relationship to the hole transport layer (HTL), such as Spiro-OMeTAD, is still unclear. Herein, the dimensionality of 2D perovskite as an interfacial passivation layer is investigated by tuning the passivating solution concentration. A faster surface photovoltage (SPV) signal in the passivated samples indicates the reduction in the trap states and ionic movement. However, the ionic contribution is recovered by quasi-2D

perovskite causing a slowing down SPV signal. Also, quasi-2D perovskite contributes to a faster transient photoluminescence (PL) decay indicating that quasi-2D perovskite is acting as recombination sites. Therefore, the device performance peaks in passivation with pure 2D perovskite with higher $V_{OC}$and fill factor. Apart from trap reduction, 2D perovskite also acts as a dopant blocking layer maintaining the doping level of the Spiro-OMeTAD on top while further contributing to higher device performance by reducing the energetic disorder in 3D perovskite.

6.1 Introduction

The presence of interfacial trap states is one of the critical issues for perovskite solar cells (PSCs) as they reduce open-circuit voltage (V_{OC}) and thus reduce the power conversion efficiency (PCE).[1,2] A commonly used method to reduce the interfacial trap states is by passivating the perovskite/charge transport layer with bulky organic cations which converts part of the perovskites into Ruddlesden-Popper perovskite (noted as 2D perovskite).[3–5] This approach is advantageous because it reduces the surface recombination loss and potentially increases device stability.[6,7] Despite the success in improving the device performance, the role of different dimensional 2D perovskites on the interface is still remain unclear. As the energetics of 2D perovskites deepen with lower n number, the interfacial energetic alignment would be altered dramatically. In addition, introducing a new 2D perovskite interlayer between charge transport layers and perovskite layers will result in a different perovskite/transport layer relationship, such as dopant diffusion. Therefore, a systematic investigation on the impact of dimensionality and the interfacial chemistry between perovskite and charge transport layer is crucial to complete the understanding of the role of passivation in PSCs.

In this chapter, the role of phenethylammonium-based 2D perovskite is investigated. By tuning the passivation concentration, different dimensional 2D perovskite heterostructures are fabricated with or without top Spiro-OMeTAD hole transport layer (HTL). The details of the energetic alignment, surface photovoltage (SPV) and alternating surface photovoltage (ASPV) are measured to show the impact of either pure $n = 1$ 2D perovskite or quasi-2D perovskite in n-i-p PSCs. The results highlight the importance of pure 2D perovskite with an improved V_{OC} as well as PCE, and reveal the dopant blocking ability of 2D perovskite on the interface which

may play an important role in device stability.

6.2 Surface Passivation Induced Energetic Shifts in Perovskite

To explore the benefit of 2D perovskite passivation, perovskite with a mixed of both cation and anion ($Cs_{0.03}FA_{0.82}MA_{0.15}PbBr_{0.44}I_{2.56}$, noted as 3D perovskite) is fabricated since it was shown to have higher PCE and longer stability than methylammonium lead iodide in Chapter 5, and then passivated with $5\,mg\,mL^{-1}$, $10\,mg\,mL^{-1}$ and $15\,mg\,mL^{-1}$ of phenethylammonium iodide (PEAI) solutions (noted as PEAI 5, PEAI 10, PEAI 15).[8] Their ambient photoemission spectroscopy (APS) spectra and the derived density of state (DOS) are shown in Fig. 6.1a. According to the literature, the PEAI passivated surface was reported with a shallower valence band edge (VBE) than the 3D perovskite.[4,9] Therefore, it was commonly applied to assist hole extraction by located between the 3D perovskite and the hole extraction layer.[10–12] However, the 3D here shows a shallower VBE than the PEAI passivated samples which leads to a hole extraction barrier instead of a beneficial energy gap. It would result in charge accumulation on the interface and thus reduce the device performance with higher recombination loss. Turning to the impact of the concentration, it is interesting that the VBE is getting shallower from 5.80 eV to 5.76 eV with higher PEAI concentration which suggests a gradual reappearing of the 3D perovskite presence. This concurs with the DOS distribution where PEAI 10 and PEAI 15 have a slightly larger amount of DOS around 5.4 eV to 5.6 eV. Turning to the Fermi level (E_F), the PEAI passivation shifts it shallower, and this trend continues as the PEAI concentration gets higher. Since 3D perovskite has a more p-type nature, a shallow-shifting E_F indicates a more intrinsic perovskite which may be related to the surface defect removal. In summary, the energetic diagram of PEAI passivation is shown in Fig. 6.1b.

To confirm the condition of the 2D perovskite formed by PEAI passivation, photoluminescence (PL) measurements are carried out (Fig. 6.1c). Firstly, a prominent PL peak at 510 nm indicates the existence of the $n = 1$ 2D perovskite (pure 2D perovskite) in all the passivated samples.[13] This peak becomes larger with more concentrated PEAI solution which is coherent with the idea that higher concentration will convert more 3D perovskite into 2D perovskite. It is

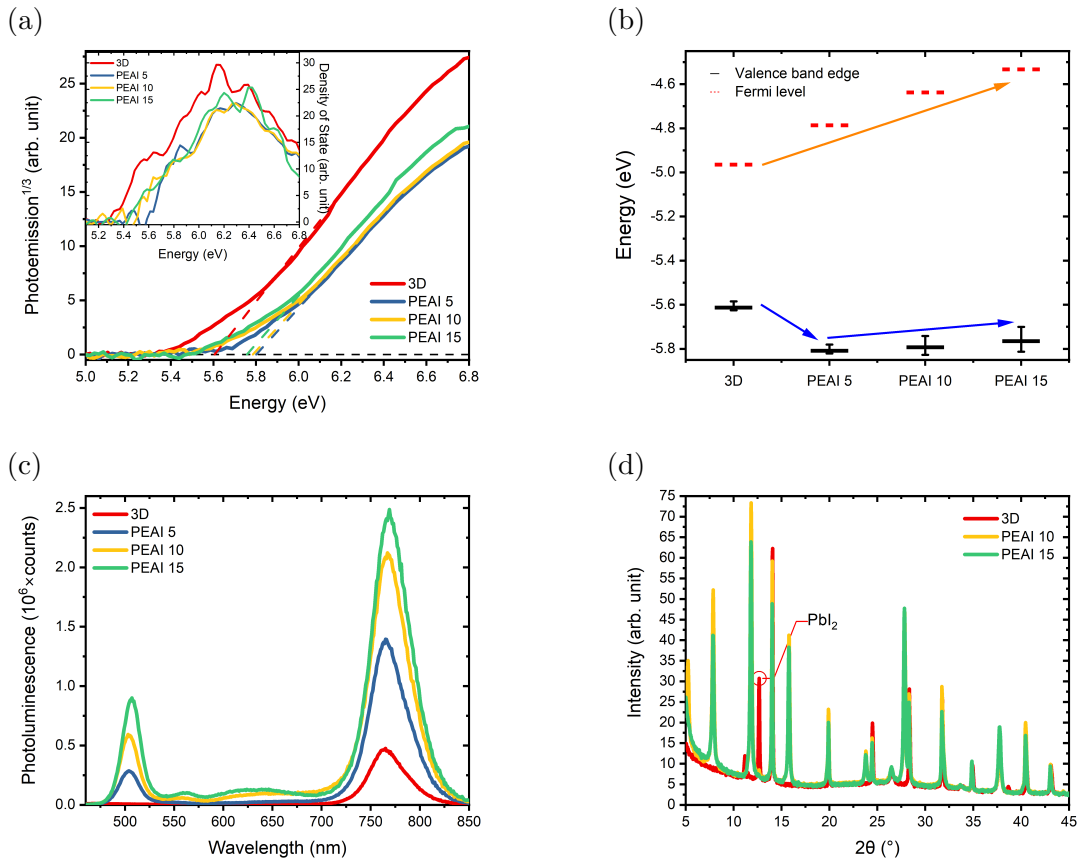


Figure 6.1: The effect of phenethylammonium iodide (PEAI) passivation on $Cs_{0.03}FA_{0.82}MA_{0.15}PbBr_{0.44}I_{2.56}$ (3D) with different concentrations. (a) The ambient photoemission spectroscopy (APS) spectra with the inset of the density of state (DOS), (b) the energetic diagram, (c) the photoluminescence spectra and (d) the X-ray diffraction (XRD) spectra of 3D, 5 mg mL^{-1}, 10 mg mL^{-1} and 15 mg mL^{-1} PEAI passivated 3D (denoted as PEAI 5, PEAI 10, PEAI 15 respectively). (The XRD spectrum of PEAI 5 was not measured successfully.)

interesting that there is a weak but broad PL band between 525 nm to 700 nm for PEAI 10 and PEAI 15. This longer wavelength PL is originated from the $n > 1$ 2D perovskite (quasi-2D perovskite).[14,15] Since 2D perovskite exhibits a strong quantum confinement effect, smaller n number would lead to stronger exciton binding energy, and thus higher PL energy. The formation of quasi-2D perovskite in PEAI 10 and PEAI 15 explains the regain of 3D perovskite DOS and the slight shallow shifting on the VBE. Despite the formation of different types of 2D perovskite, all the passivations successfully reduce the surface defect states as shown by the X-ray diffraction (XRD) spectra in Fig. 6.1d (Note that PEAI 5 was not measured successfully). The excess PbI_2 peak which is related to the dangling bonds or perovskite crystal defects is completely diminished, leaving only the perovskite peaks. This correlates well with the increasing 3D perovskite PL peak at 760 nm since the non-radiative recombination by

the defect states is significantly reduced compensating the less amount of 3D perovskite after passivation. The XRD also shows the existence of the pure 2D perovskite at 5.2° as reported in the literature.[16] Overall, the PEAI passivation reduces the defect states as expected, and by controlling the concentration of PEAI solution, different types of 2D perovskite can be fabricated providing the freedom to tune the energetics.

To understand the changes by the PEAI passivation, the two possible pure 2D perovskites, namely PEA_2PbI_4 and PEA_2PbBr_4, are fabricated and studied. Since the 3D perovskite has both iodide and bromide ions, it would be relevant to identify the dominating 2D perovskite inside the film. As shown in Fig. 6.2a, the VBEs of these two 2D perovskites are largely different from each other with 5.78 eV for PEA_2PbI_4 and 5.99 eV for PEA_2PbBr_4. The deeper VBE of PEA_2PbBr_4 indicates that its presence is relatively low, which is not surprising as there are more iodide ions in the 3D perovskite as well as the passivation solution (PEAI(aq)). The DOS of PEA_2PbI_4 is also resembling that of PEAI 5 with an onset at 5.5 eV and peaks around 6.2 eV while the bromide case has a relatively low and deep DOS distribution. Interestingly, both 2D perovskites have similar E_F at 5.0 eV which is deeper than the passivated samples (Fig. 6.2b). Therefore, the shallower E_F in Fig. 6.1b should be related to the passivated 3D perovskite, which is less p-type, instead of the thin 2D layers on top. The topography of both 2D perovskites (Figs. 6.2d and 6.2e) are relatively smooth, but the coverage is poor in PEA_2PbBr_4 where there are significant ripple patterns. This may be the cause of the low APS response, but it does not influence the fitted VBE level.

To further verify the existence of the PEA_2PbI_4 in the passivated samples, PL measurements are carried out for the PEA_2PbI_4 sample (Fig. 6.2c). A clean PL spectrum with a very narrow peak centering at 525 nm is recorded. Despite the small discrepancy (525 nm in the neat film vs. 510 nm in the passivated film), which might be due to the re-absorption by the 3D perovskite, the PL measurement should be originated from the PEA_2PbI_4 on the passivated surface. According to the literature, the PL spectrum of PEA_2PbBr_4 should be around 410 nm which unfortunately is beyond the instrument limit.[17] Nonetheless, the increasing PL intensity at 510 nm with higher passivation concentration still confirms the increasing amount of PEA_2PbI_4.

Turning to the impact on surface topography, the atomic force microscopy (AFM) images are shown in Fig. 6.3. As the starting point for the PEAI passivation, the 3D perovskite exhibits

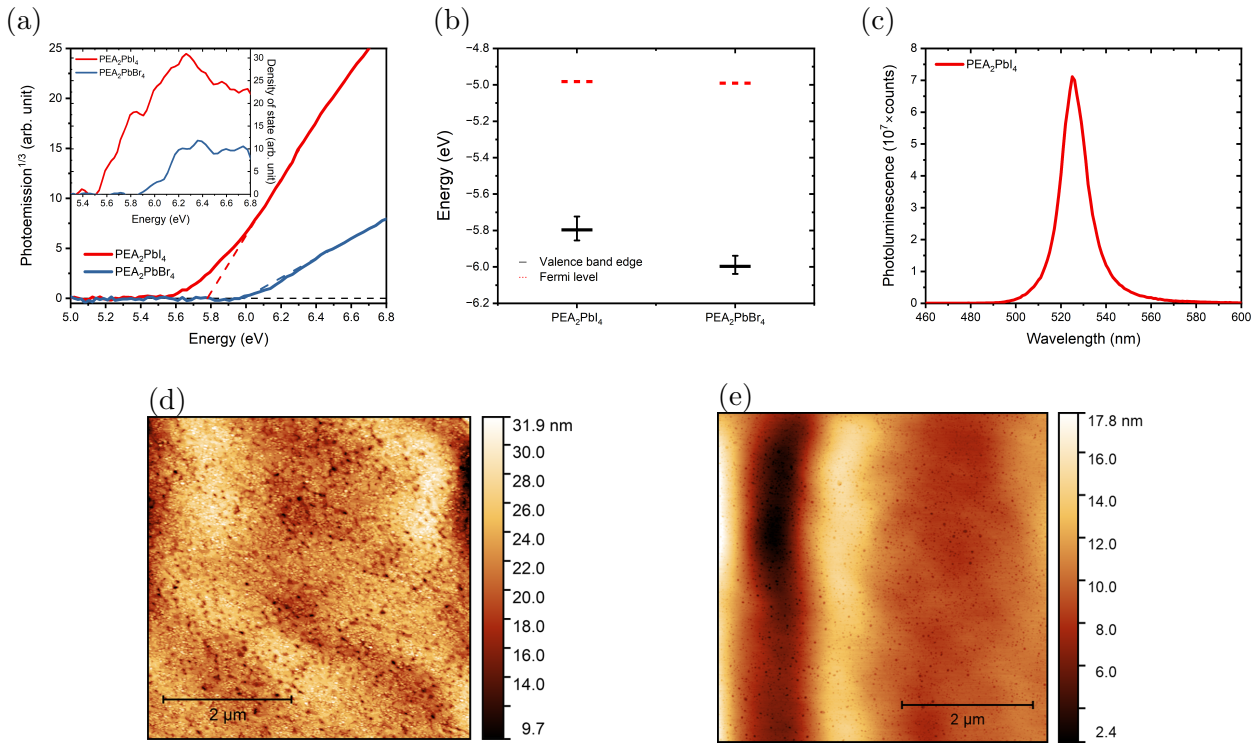


Figure 6.2: Energetics, photoluminescence (PL) and surface topography of PEA_2PbI_4 and/or PEA_2PbBr_4. (a) The APS spectra with their DOS as inset and (b) the energetic diagram. (c) The PL of PEA_2PbI_4. (the PL of PEA_2PbBr_4 is not measured due to instrument limit) The atomic force microscopy (AFM) images of (d) PEA_2PbI_4 and (e) PEA_2PbBr_4.

a vivid surface topography composed of pillar shape crystals with some small pinholes. Despite the continuous energetic shift, their surface topography significantly depends on the PEAI concentration. When passivated with the lowest concentration, the surface maintains similar pinhole nature as in the 3D sample. The passivation also smooths out the grain boundaries, and thus leaving a less separated but more agglomerated crystal structure. Different from the PEAI 5 sample, PEAI 10 starts to exhibit excessive agglomeration which may be related to the excess PEAI residuals. This feature is even more evidence in the PEAI 15 sample where the pinholes are starting to be filled by the excess PEAI. This is shown by the pinhole area coverage (Fig. 6.3e) where the pinhole area percentage is significantly dropped in PEAI 15.

To identify the impact of passivation on charge dynamics, surface photovoltage (SPV) is carried out (Fig. 6.4a). The SPV signal of the 3D perovskite on TiO_2 has a typical perovskite character with a biphasic turn-on.[18,19] The first sharp turn-on is correlated to the fast charge generation and separation while the following slow saturation towards steady state is more related to the charge redistribution and its coherent ionic movement. Surprisingly, the SPV signal of the PEAI 5 has a much smaller saturation value and a nearly negligible slow turn-on

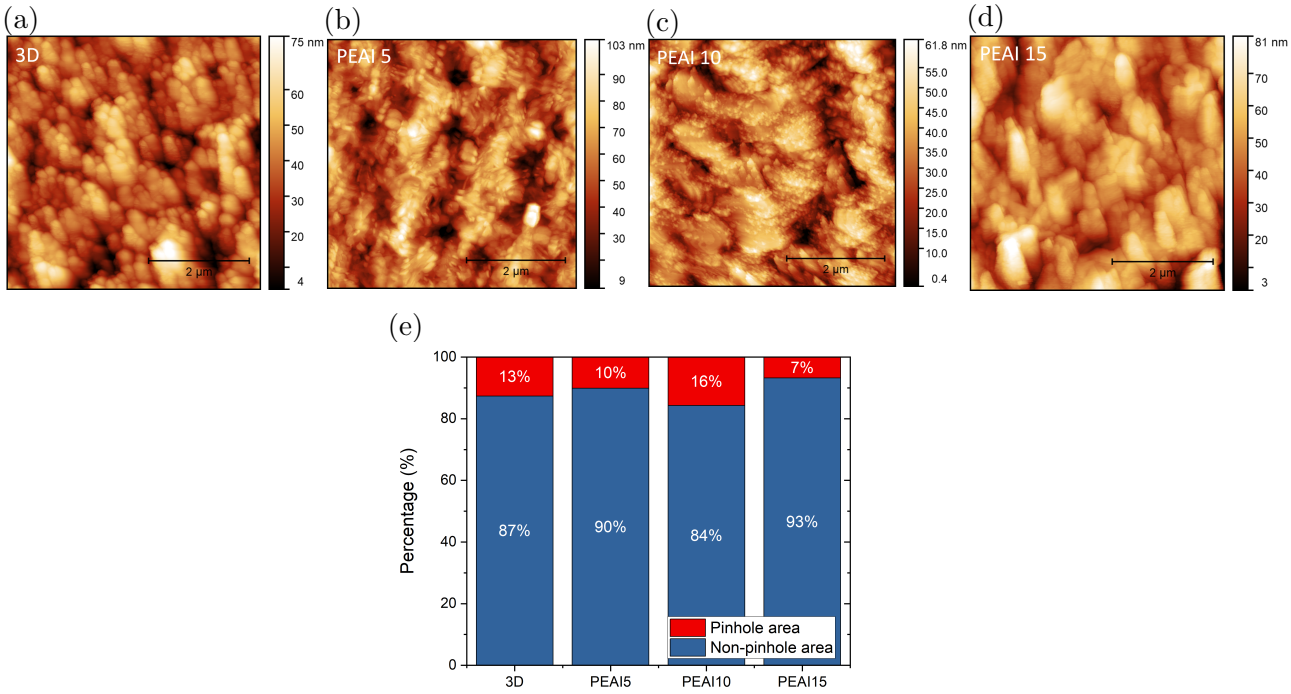


Figure 6.3: Atomic force microscopy images of (a) 3D perovskite, (b) PEAI 5, (c) PEAI 10 and (d) PEAI 15 with (e) their pinhole (<30 % of maximum height) coverage.

phase comparing to the 3D perovskite. For the smaller saturation value, it is caused by the blocking effect from the top passivation layer which has a deeper VBE, and thus prohibits holes moving to the top surface. Besides, the shallower E_F of the 2D layer would result in an interfacial band bending which pushes holes away from the interface. For the negligible second phase, the passivation reduces the ionic movement by removing the defect states and prohibiting ion redistribution particularly on the interface. These phenomena are weakened once quasi-2D perovskite is involved such as in PEAI 10 and PEAI 15. Despite removing the PbI_2, the quasi-2D perovskite reintroduces the potential defect states with the 3D structure sandwiched between the bulky cations. These defect states would promote the ionic movement leading to the reappearing of slow turn-on phase. Furthermore, these scattered quasi-2D perovskite grains provide places to store the holes with slightly shallower VBE as they are fused within pure 2D perovskite layer. As a result, the SPV signals are increasing with higher concentration passivation. To elucidate the mechanism, a schematic diagram is drawn in Fig. 6.4c accordingly.

The normalized transient photoluminescence (PL) is also measured with a 405 nm excitation laser in order to show the impact on decay dynamics (Fig. 6.4b). Here, the probe is set at 760 nm focusing on the radiative emission in the 3D perovskite layer. Similar to the SPV

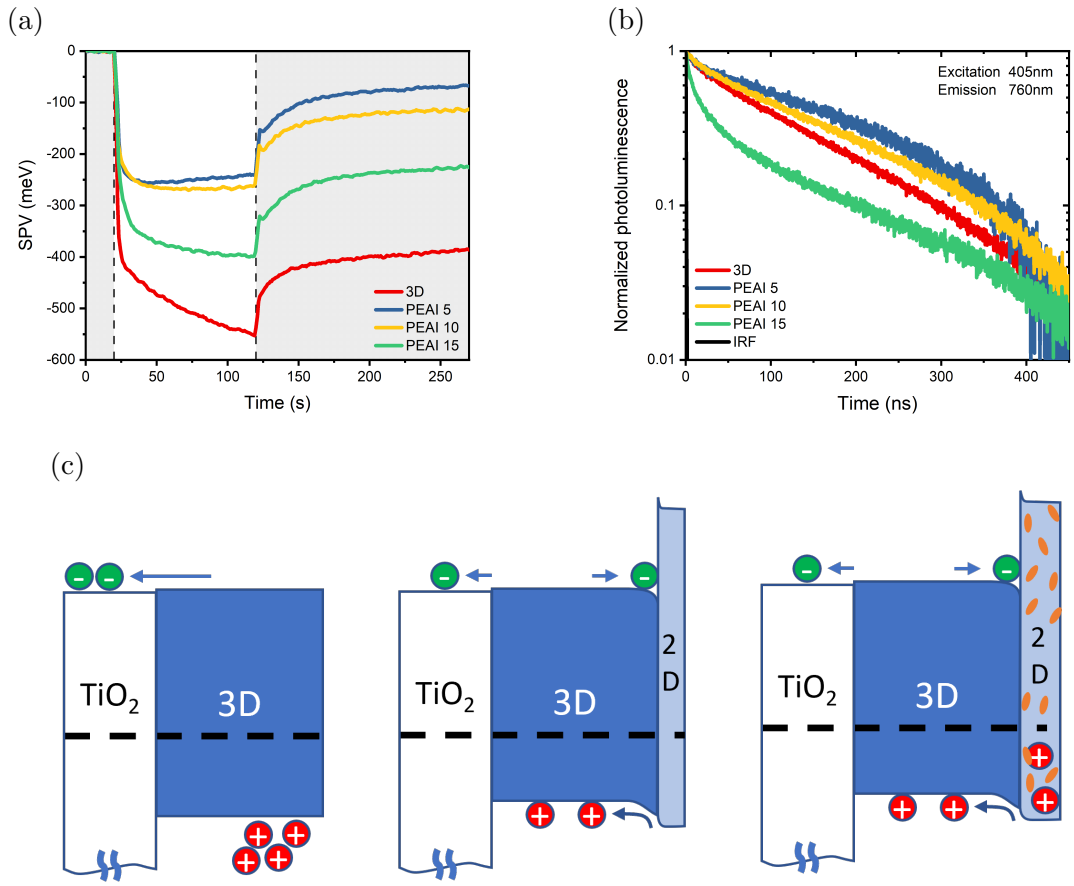


Figure 6.4: Charge dynamics of PEAI passivated 3D perovskite on top of TiO_2. (a) Surface photovoltage (SPV) signals of all samples under 0.2 sun white light illumination. Dashed vertical lines indicate the transitions between light off (gray) and light on (white). (b) Normalized transient photoluminescence probed at 3D perovskite (760 nm) with laser excitation at 405 nm. (c) Schematic diagram of charge dynamics for 3D case (left), PEAI 5 (middle) and the PEAI 10/15 (right) with electron extraction through the underneath TiO_2 (white). The orange spots inside 2D perovskite (the right panel) are the grains of quasi-2D perovskite.

observation, surface passivation successfully reduces the recombination rate by restraining free charges accessing the top surface, and therefore leading to a longer charge carrier lifetime in PEAI 5 than in 3D case. However, this benefit is gradually covered in PEAI 10 or completely overcome in PEAI 15 by the quasi-2D perovskite. The quasi-2D perovskite allows the free holes to re-access the top surface and to recombine on the air interface. Also, high concentration of PEAI significantly changes the grain structure deeper which would also introduce to some deeper defect states that is undesirable for charge carrier lifetime. To summarize, both SPV and transient PL measurements show that having thin pure 2D perovskite on the surface successfully reduces the PbI_2 remains and improves the surface recombination loss. However, the VBE of PEAI based 2D perovskite is not matching with the 3D perovskite for hole extraction which may inhibit the extraction process.

6.3 Reduced Recombination and Improved Charge Extraction with Low-Dimensional Passivation Layer

To further examine the impact of 2D perovskite within a full device structure, Spiro-OMeTAD (Spiro), a typical hole transport layer (HTL), on top of 3D, PEAI 5, PEAI 10 and PEAI 15 are fabricated. The energetics of the Spiro layer on top of the passivated perovskite is shown in Fig. 6.5. Despite using the same solution and deposition method, the HOMO levels of the Spiro are changed by 0.1 eV (Fig. 6.5a). Although this change is not dramatic, it is in confidence to be related to the surface passivation on the perovskite layer as the HOMO levels are consistent among the passivated samples. In addition, the DOS distribution has shown a horizontal shift which implies that the cause could be originated from the doping level or the electric field. Turning to their E_F (Fig. 6.5b), the figure shows that it is much shallower (4.6 eV) in the non-passivated case than in the passivated cases ($\sim$4.9 eV). This dramatic change indicates a change of the doping condition where the Spiro on top of the passivated samples is much more p-doped. Since the Spiro here serves as a hole transport layer, the stronger p-doping would benefit charge extraction by providing a higher charge mobility. In the literature, Habisreutinger et al. shows that 4-tert butylpyridine (4TBP) originally blended in the Spiro solution would diffuse into and p-dope the top contact of perovskite layer.[20] The consistent Spiro energetic in the passivated samples implies that the 2D perovskite in between 3D perovskite and Spiro prohibits such phenomenon to occur and maintain the same doping level of the Spiro. Further investigation on this dopant diffusion will be discussed in Section 6.4. This dopant blocking character, to the best of my knowledge, is not yet reported, and it should be one of the crucial point to understand the benefits of passivation in device performance.

Following the energetic findings of both perovskite and Spiro, the device character statistics of PEAI passivated are shown in Fig. 6.6. For the open-circuit voltage (V_{OC}), PEAI passivated devices show an improvement from 1.055 V to 1.083 V (Fig. 6.6a), consistent with the literature.[21,22] The higher V_{OC} reflects the significantly reduced surface defect states which is commonly associated with lower surface recombination loss and higher quasi-Fermi level splitting. However, the complicate energetic landscape, especially the extraction barrier from the 2D perovskite, means a non-trivial competition between recombination and extraction

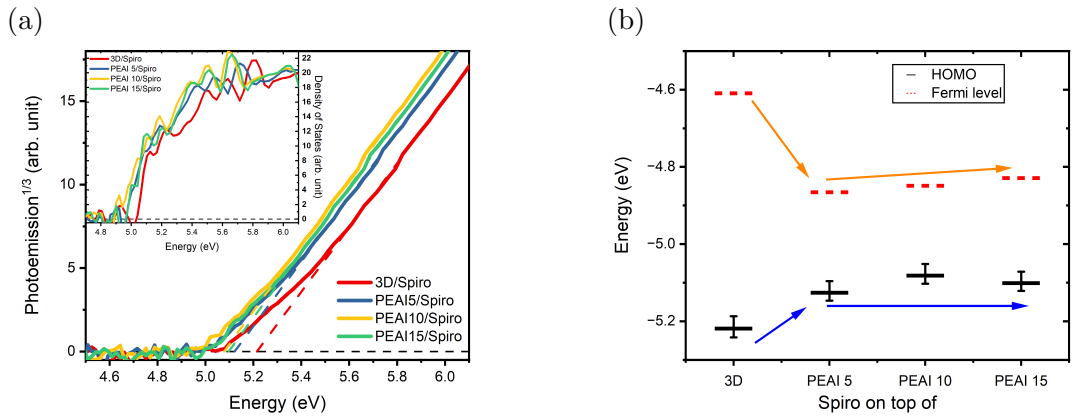


Figure 6.5: (a) The ambient photoemission spectroscopy (APS) spectra with the DOS inset and (b) the energetic diagram of Spiro-OMeTAD (Spiro) on top of 3D, PEAI 5, PEAI 10 and PEAI 15.

which will be discussed later.

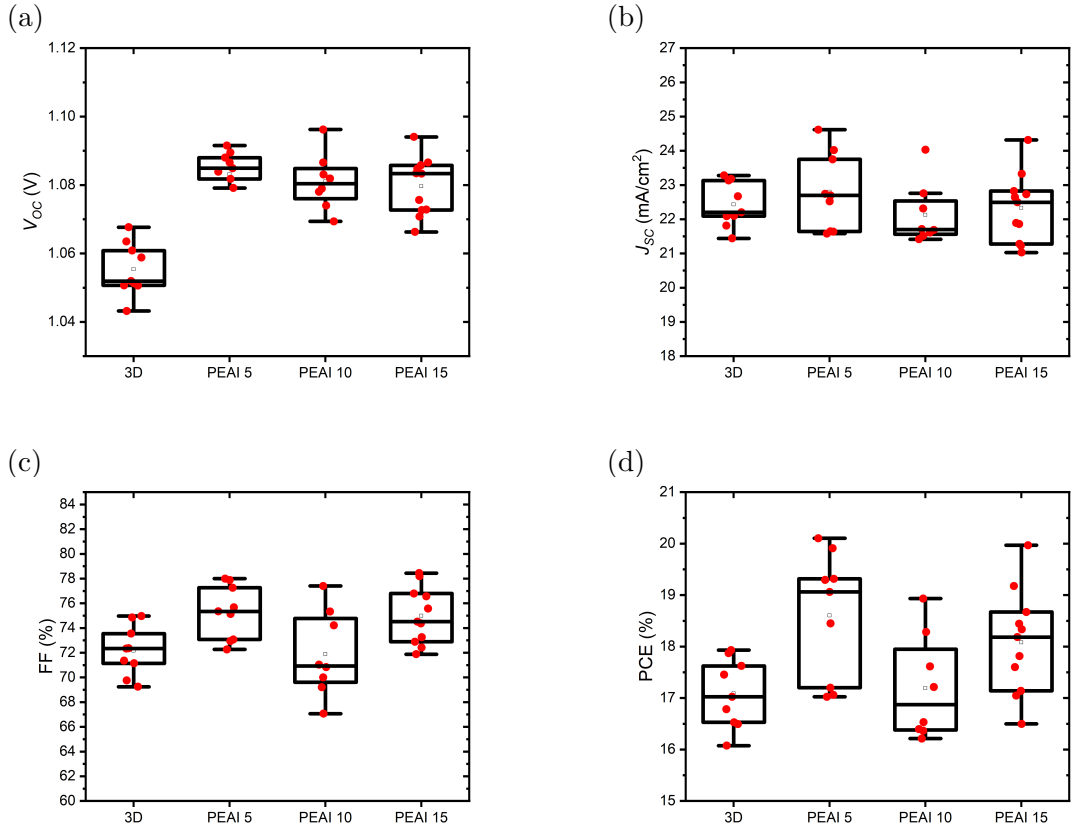


Figure 6.6: The (a) open-circuit voltage (V_{OC}), (b) short-circuit current (J_{SC}), (c) fill factor (FF) and (d) power conversion efficiency (PCE) statistics of PEAI passivated devices.

Different from the V_{OC}, the short-circuit current (J_{SC}) is surprisingly stable across all the passivated samples (Fig. 6.6b). By intuition, PEAI passivation should transform some of the existing 3D perovskite into 2D perovskite which has strong exciton binding energy. Thus, the

J_{SC} should decrease with less amount of effective photoactive layer, namely the 3D perovskite. To unveil this, the absorbance measurements are carried out (Fig. 6.7). Despite having different amount of PEAI, all the samples have nearly the same absorbance across 600 nm to 900 nm indicating that the surface passivation does not negatively contributing to the absorption. For the fill factor (FF), surface passivation seems not to have a clear advantage with most of the samples centered around 72 % (Fig. 6.3c). Note that PEAI 10 has a slightly wider distribution due to the uneven topography. Combining all these factors, the power conversion efficiency (PCE) of PEAI 5 is slightly higher (18.60 %) than the 3D reference (17.09 %), mainly by the higher V_{OC}. On the contrary, the quasi-2D perovskite seems not to benefit PCE with the wider FF distribution for PEAI 10 and wider V_{OC} distribution for PEAI 15.

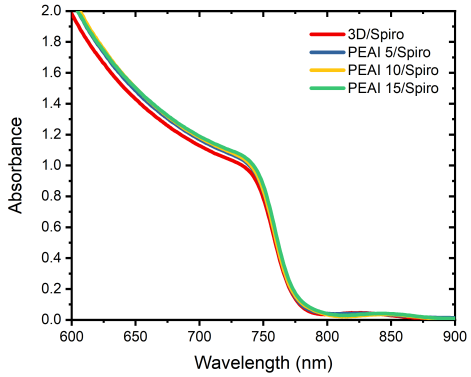


Figure 6.7: The absorbance of PEAI passivated perovskite solar cells.

In order to understand the trend of V_{OC} under surface passivation, photoluminescence (PL), transient PL, surface photovoltage (SPV) and alternating surface photovoltage (ASPV) measurements are carried out. Since the passivated devices have the Spiro layer on top, the PL measurement is done from the back side (ITO side) to avoid the Spiro re-absorption. The PL of the 3D perovskite device shows a significant broadening from 600 nm to 750 nm (Fig. 6.8a), indicating a higher level of disorder. Since this broadening does not exist in the case without Spiro layer (Fig. 6.1c), it is possible to be related to the dopant diffusion or penetration from the Spiro layer. This also explains the narrow PL in PEAI 5, where the 2D perovskite seems to be able to block the dopant diffusion. For PEAI 10 and PEAI 15, the quasi-2D perovkite would also contribute to the broad emission since the energy relaxation may happen as the measurement is carried out from the ITO side. Turning to the dynamics of the 3D perovskite PL, the passivated samples are all showing a much faster decay than the 3D reference, demonstrating a much faster

charge extraction and separation (Fig. 6.8b). As shown in the Spiro energetics, the Spiro on top of the passivated perovskite has a much stronger p-doping which would benefits the charge extraction by the faster charge mobility. Also, the E_F of the Spiro is getting deeper leading to an upward band bending which is preferential for hole extraction. Therefore, despite having the energy barrier from the 2D perovskite, PEAI surface passivation still able to provide efficient extraction and higher V_{OC}.

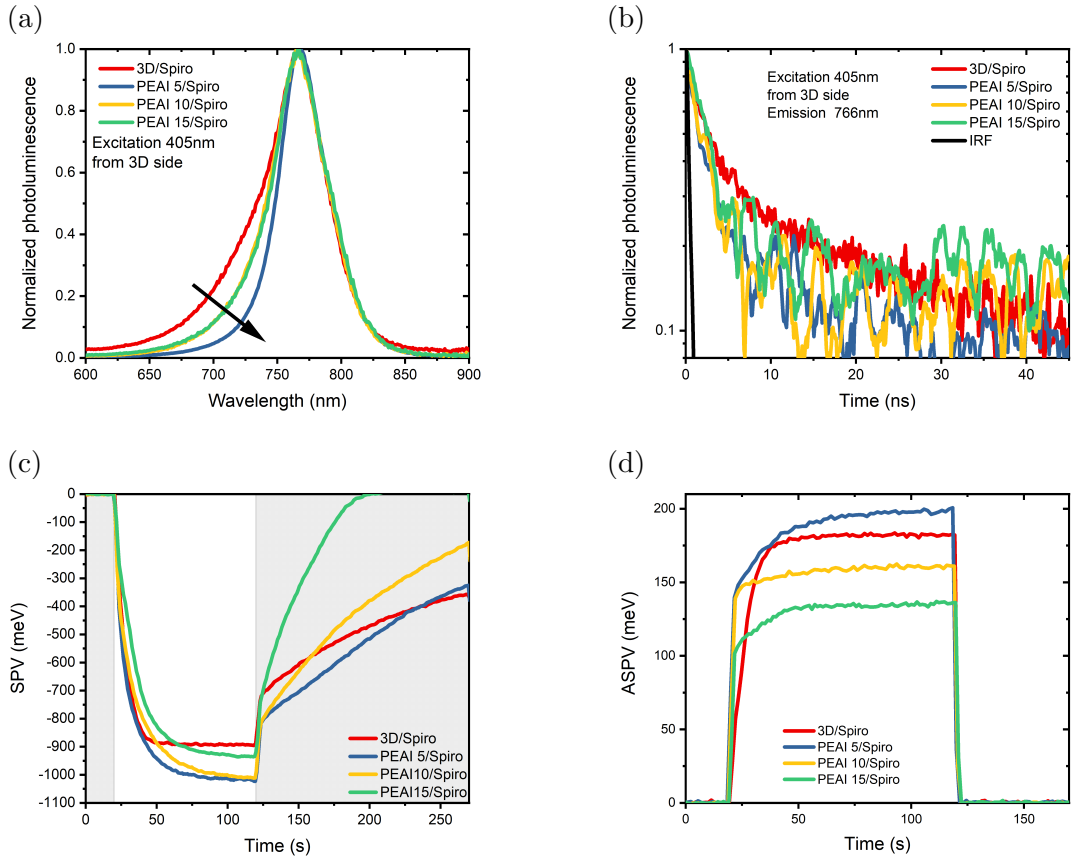


Figure 6.8: (a) The photoluminescence (PL), (b) transient PL, (c) surface photovoltage (SPV), (d) 300 Hz alternating surface photovoltage (ASPV) measurements of PEAI passivated perovskite with Spiro-OMeTAD (Spiro) on top. Note that the negative SPV signal indicates a positive surface potential while the APS signal is by definition the absolute change of the surface potential.

The PL measurements are not able to distinguish the subtle difference between PEAI 5 and the other two passivated devices which have quasi-2D perovskite. Since quasi-2D perovskite would have similar ionic movement similar to the 3D perovskite, it is relevant to compare the SPV and ASPV measurements to dissociate the ionic contributions to the V_{OC}. As shown in Fig. 6.8c, the SPV signals of all the passivated devices are slightly more negative than the 3D reference indicating a larger positive electric field build up on the surface under illumination.

This is coherent with the literature where the SPV signal shows strong correlation to the device V_{OC}.[18,23] However, the SPV signals of the passivated devices have a clear trend of slower turn-on when passivated with higher PEAI concentration. This slow turn-on phase should be related to the slow ionic movement created by the quasi-2D perovskite. In contrary to the SPV measurement, the ASPV signals of the passivated devices are not higher than the reference, except for the PEAI 5 (Fig. 6.8d). Since the ASPV is measured under high frequency (∼300 Hz), the ASPV measurement is able to screen out some of the slow ionic signal leaving only the electric potential of free charge carriers. Therefore, the reverse relationship in SPV and ASPV measurements demonstrates that PEAI 10 and PEAI 15 devices have a slightly lower free charge contribution in their V_{OC} which is compensated by the ionic contribution. PEAI 5, on the contrary, has both higher SPV and ASPV signal than the 3D reference showing the benefit of having only the thin pure 2D perovskite. To summarize the findings, a schematic diagram of charge extraction is drawn in Fig. 6.9.

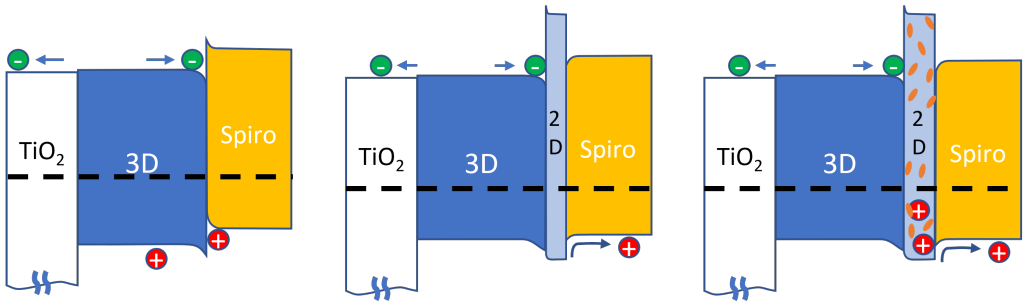


Figure 6.9: Schematic diagram for 3D case (left), PEAI 5 (middle) and the others (right) with electron extraction through the underneath TiO_2 (white) and hole extraction through the top Spiro (yellow). The orange spots inside 2D perovskite (the right panel) are the grains of quasi-2D perovskite

6.4 Suppressed Dopant Leakage by Surface Passivation with Low-Dimensional Perovskite

As pointed out in Section 6.3, the energetic shift of the Spiro on top of passivated perovskite is one of the key factors determining device performance. Although it was claimed to be due to dopant leakage or diffusion from the Spiro layer into perovskite, the origin of this energetic shift, especially how it correlates to 2D perovskite, is not clear. A comprehensive energetic measurements of different blends are carried out to examine the effect of each type

of perovskite ions (Fig. 6.10). In Figs. 6.10a and 6.10b, the Spiro solution is deposited as neat on top of glass substrate or blended with perovskite solution before deposition. The APS spectra of the neat Spiro has the HOMO level at 5.1 eV similar to the Spiro on the passivated perovskite while the perovskite blended Spiro resembles the Spiro on 3D perovskite. This shows that the passivated perovskite is able to maintain the same doping level of Spiro while protecting it from the influence of 3D perovskite. To show the phenomenon solely depends on 2D perovskite regardless of the anion, Spiro deposited on top of phenethylammonium bromide (PEABr) passivated perovskite is also measured, and it shows the same energetic as in the PEAI case. Interestingly, the converted DOS distributions show a horizontal shift on the energy spectra with the major DOS peak position shift from 5.7 eV to 5.9 eV. This indicates the change is coming from a change in the doping level instead of its amorphous packing structure.[24] Combining the E_F information (Fig. 6.10b), the samples are clearly separated into two groups as shown in Section 6.3, the highly p-doped group with Spiro on passivated perovskite and neat Spiro and the more intrinsic group with Spiro on or blended with 3D perovskite.

Since either 3D or 2D perovskite has multiple types of ions which may diffuse into the Spiro layer, Spiro blended with PbI_2 or PEAI is also measured in order to identify the cause of the energetic shift (Figs. 6.10c and 6.10d). Here, the PEAI blended Spiro sample shows exactly the same HOMO level at 5.1 eV and the same DOS distribution as neat Spiro. Also, its E_F and doping level fall in the same range. This demonstrates that the Spiro layer is inert to PEA^+ ion which explains the stable energetics regardless of the passivation concentration. In the other hand, the PbI_2 blended Spiro has the same unchanged energetics as the neat Spiro as well. As shown in Fig. 6.1d, the excess PbI_2 is the most abundant salt that may influence the Spiro layer. The stable HOMO level and E_F prove that the change of doping level is most likely related to dopant diffusing into the 3D perovskite crystal. Although dopant leaked from the transport layer was already reported in the literature, they mainly focused on its impact in perovskite layer.[20,25,26] Here, the measurements show that this leaking process significantly alters the Spiro energetic which ultimately influence the device performance. Moreover, it indicates that low dimensional perovskite interlayers may reduce this phenomenon, and thus benefit the device performance or stability.

Although the energetic results suggest the mechanism behind the doping level shift is dopant

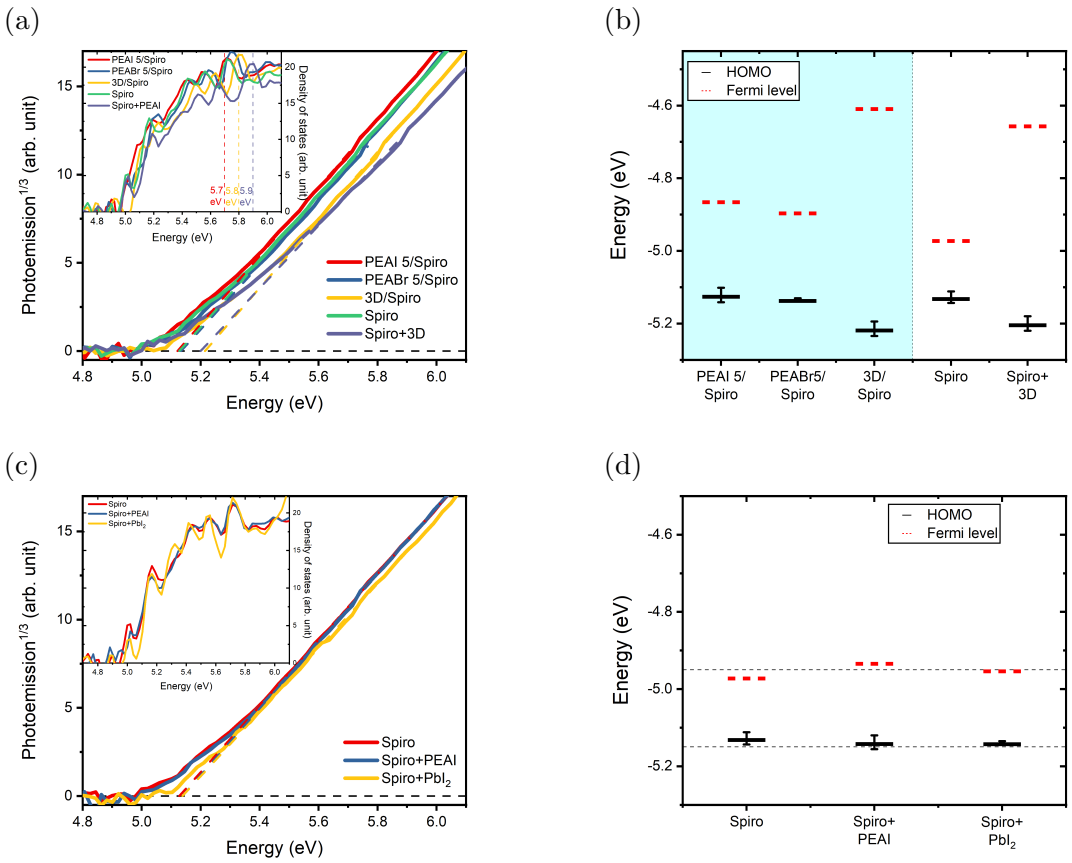


Figure 6.10: Energetics of Spiro-OMeTAD (Spiro) blended with (white background) or on top of (cyano background) different materials. (a), (c) The ambient photoemission spectroscopy (APS) spectra with a density of states inset and (b), (d) the energetic diagrams. Spiro is blended with or on top of (a) – (b) 3D or passivated perovskite and (c) – (d) PEAI, PbI_2 salts.

leaking, more optical evidence would be able to strengthen the hypothesis. The normalized Raman spectra of each Spiro samples are shown in Fig. 6.11a. Surprisingly, unlike other organic semiconductors, the Raman spectra are the same regardless of the doping level. A further density functional theory (DFT) simulation is carried out, showing the highly overlapped Raman peaks between the neutral state and the positive polaronic state (Fig. 6.11b). This indicates that Raman spectroscopy is insensitive to the doping induced peak changes which may be related the fully delocalized HOMO and HOMO-1 of Spiro-OMeTAD.[27]

A similar result happens in the normalized absorbance spectra where the spectra are nearly the same among neat Spiro and its PbI_2 or 3D blends (Fig. 6.11c). Beware that here the samples are prepared without having the perovskite layer in order to avoid the strong absorption covering the Spiro features. Nonetheless, a slightly blue-shifted absorbance from 525 nm to 600 nm is noticed in the 3D blended sample which might be related to the more neutral Spiro content within the blend. In contrast, the PL intensity of 3D blended Spiro shows a significant drop

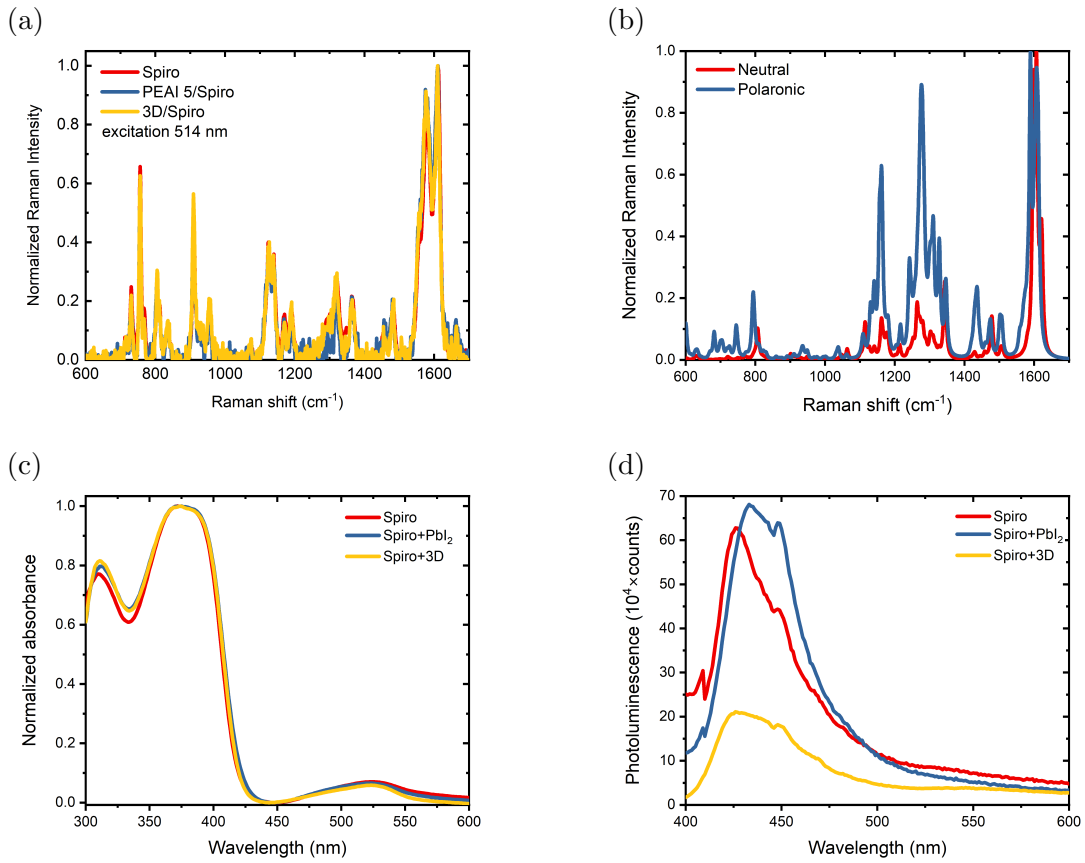


Figure 6.11: Optical characterizations of Spiro-OMeTAD (Spiro) in different doping conditions. (a) Normalized Raman spectra of neat Spiro, PEAI5/Spiro and 3D/Spiro. (b) The density functional theory (DFT) simulated Raman spectra of Spiro in neutral or positive polaronic state. (c) The normalized absorbance and (d) the photoluminescence spectra of neat Spiro and Spiro blended with PbI_2 or 3D perovskite.

compared to the other two samples (Fig. 6.11d). This can be related to a reduced amount of doped Spiro content, and therefore leading to the slightly lowered absorbance. Apart from the intensity, there is a significant change in the relative intensity when involving perovskite or lead ions. This may be related to the Pb_2^+ induced dopant aggregation, but it should not be related to the energetic shift.[28]

Apart from the energetic shift, the dopant leakage will also affect the morphology. As shown in Fig. 6.12, the Spiro on 3D perovskite has about doubled amount of pinholes than PEAI 5 and PEABr 5. This may be due to the leakage of 4TBP which was reported to be related to the morphology and uniformity of doped Spiro.[29–31] However, pinhole reduction does not occur in PEAI 10 or PEAI 15 which may be related to the formation of quasi-2D perovskite. Also, 4TBP is not a doping agent but rather dedoping agent.[30] Therefore, further investigation and evidence on the distribution and types of dopants are necessary to unveil the complex chemical

behind the phenomenon.

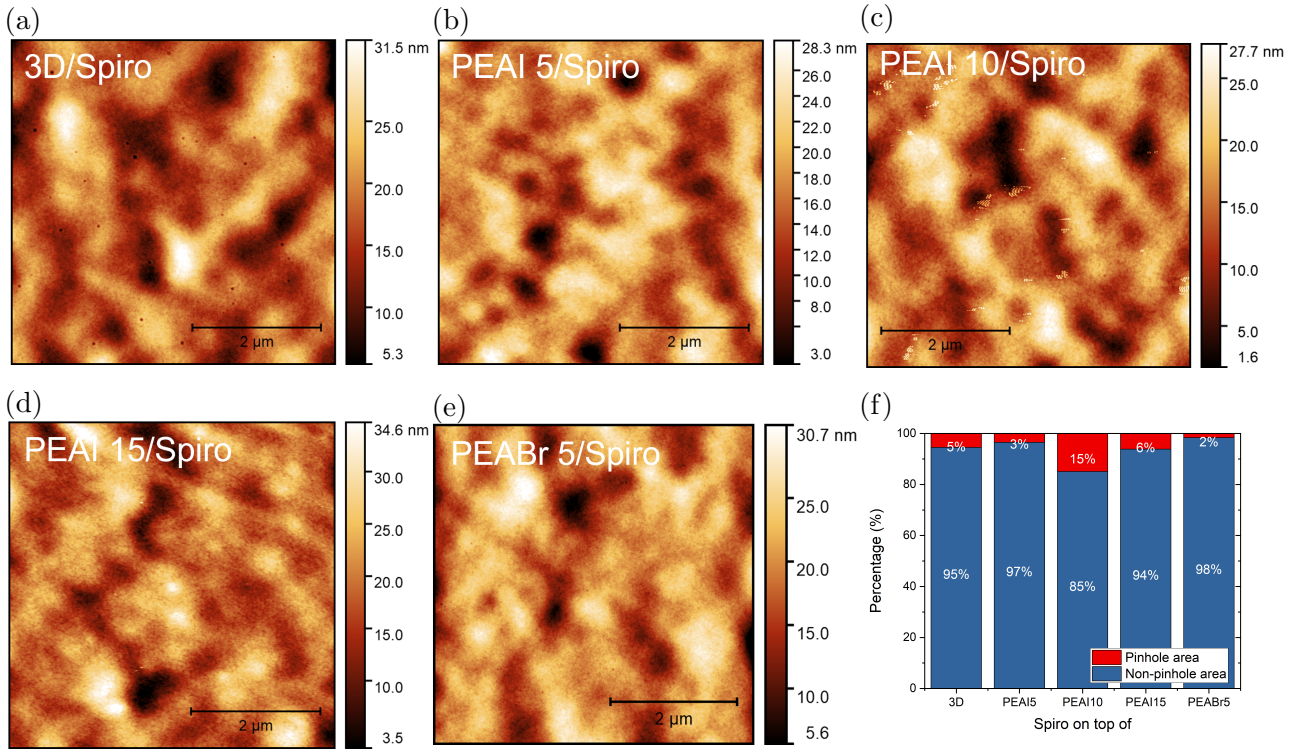


Figure 6.12: Atmoic force microscopy (AFM) images of Spiro-OMeTAD on (a) 3D, (b) PEAI 5, (c) PEAI 10, (d) PEAI 15, (e) PEABr 5 and (f) their pinhole (<30 % of maximum height) coverage.

6.5 Conclusion

In summary, the energetics of different n number 2D perovskite and its impact on the perovskite/Spiro interface is investigated by tuning the PEAI concentration. High concentration PEAI solution not only provides a much deeper passivation depth but also contributes to the formation of quasi-2D perovskite. Although the PEAI passivation manages to remove the PbI_2 defect states of the 3D perovskite, the VBE of the 2D perovskite is slightly deeper than the 3D perovskite leading to an extraction barrier. As a result, the passivated perovskite shows a weaker SPV response by inhibiting the holes transported to the surface and reducing the ionic contribution from the defect states. A regain on the slow ionic movement and the accessible surface states reappear in the high concentration group as the formation of quasi-2D perovskite reintroduce similar properties of the 3D perovskite. The results reveal the mechanism of the SPV response of perovskite while suggesting that having thin and pure $n = 1$ 2D perovskite should be necessary and sufficient for improving the device performance.

Apart from the impact on perovskite layer, surface passivation also influence the doping level and the energetics of the Spiro on top. Through blending series of perovskite related salts in Spiro, it is shown that the energetic shift in Spiro is unrelated to the ions of the perovskite, but rather the dopants leak into the 3D perovskite. Thus, by passivating the 3D perovskite surface, the 2D perovskite blocks the dopants from diffusing out and preserves the highly p-doped Spiro on top. This also improves the surface coverage by reducing the pinhole area. Unfortunately, the inert Raman nature of neutral and polaron Spiro makes it not possible to identify the change of dopant contents. Further investigation on the chemical matrix of the Spiro layer as well as the dopant distribution would be crucial for explaining long term impact on device performance.

6.6 Experimental Methods

Sample/Device Fabrication

For mix cation and anion perovskite or $Cs_{0.03}FA_{0.82}MA_{0.15}PbBr_{0.44}I_{2.56}$ (3D perovskite), two solutions (solution1 and solution2) were prepared and mixed as solution1:solution2 = 95:5 before use. Solution1 was composed of 1.5 M of formamidinium iodide (Greatcell Solar, >99.99 %), 1.5 M of lead iodide (Tokyo Chemical Industry, 99 %), 0.265 M of methylammonium bromide(Greatcell Solar, >99.99 %) and 0.265 M of lead bromide (Sigma-Aldrich, ≥98 %) in a mix solution of dimethylformamide (DMF)/dimethyl sulfoxide (DMSO) (4:1,%v/v). Solution2 was composed of 1.15 M of lead iodide (Sigma-Aldrich, 99 %) and cesium iodide (Sigma-Aldrich, 99.9 %) in a mix solution of DMF/DMSO (78:22,%v/v). The thin films of 3D perovskite were then deposited by spin-coating at 1000 rpm for 10 s and continuously at 4000 rpm for 30 s. At 5 s before the end, 110 µL of chlorobenzene was carefully dripped by micropipette at the center of the substrate. The samples were then annealed at 100 °C for 1 h. For the PEAI or PEABr passivation, the samples were spun at 4000 rpm with a dynamic dripping of 5 mg mL^{-1}, 10 mg mL^{-1} and 15 mg mL^{-1} PEAI or PEABr isopropanol solution at 5 s before the end.

For the electron transport layer (ETL), two solutions (ETL1 and ETL2) were prepared and mixed before use. ETL1 was composed of 1 mL of isopropanol (Sigma-Aldrich, anhydrous

99.5 %) and 13.83 µL of 2 M HCL(aq). ETL2 was composed of 1 mL of isopropanol and 145 µL of titanium isopropoxide (Sigma-Aldrich, 97 %). Then, ETL1 was added into ETL2 slowly with vigorous stirring. The compact TiO_2 layer was deposited at 2000 rpm for 30 s, and followed by 10 min annealing at 150 °C. After cooling down, samples were annealed in 500 °C for 30 min.

For the hole transport layer, 73 mg of Spiro-OMeTAD (Lumtech, 99 %) was dissolved in 1 mL of chlorobenzene first, and then adding 28.8 µL of 4TBP (Sigma-Aldrich, 98 %), 17.5 µL of LiTFSI (ACROS, 99 %) acetonitrile solution (520 mg mL^{-1}) and 29 µL of FK209 (Sigma-Aldrich, 98 %) acetonitrile solution (300 mg mL^{-1}) consecutively. The solution was always prepared no more than 24 h before use to prevent degradation or forming clusters. In Spiro blend study, Spiro solution was further blended with 1 % (v/v) of perovskite solution, PEAI isopropanol solution (5 mg mL^{-1}) or PbI_2 DMF solution (5 mg mL^{-1}).

References

[1]M. Stolterfoht, C. M. Wolff, J. A. Márquez, S. Zhang, C. J. Hages, D. Rothhardt, S. Albrecht, P. L. Burn, P. Meredith, T. Unold, and D. Neher, "Visualization and suppression of interfacial recombination for high-efficiency large-area pin perovskite solar cells", Nature Energy **3**, 847–854 (2018).

[2]C. M. Wolff, P. Caprioglio, M. Stolterfoht, and D. Neher, "Nonradiative Recombination in Perovskite Solar Cells: The Role of Interfaces", Advanced Materials **31**, 1902762 (2019).

[3]C. T. Lin, J. Lee, J. Kim, T. J. Macdonald, J. Ngiam, B. Xu, M. Daboczi, W. Xu, S. Pont, B. Park, H. Kang, J. S. Kim, D. J. Payne, K. Lee, J. R. Durrant, and M. A. McLachlan, "Origin of Open-Circuit Voltage Enhancements in Planar Perovskite Solar Cells Induced by Addition of Bulky Organic Cations", Advanced Functional Materials **30**, 1906763 (2020).

[4]S. Heo, G. Seo, K. T. Cho, Y. Lee, S. Paek, S. Kim, M. Seol, S. H. Kim, D.-J. Yun, K. Kim, J. Park, J. Lee, L. Lechner, T. Rodgers, J. W. Chung, J.-S. Kim, D. Lee, S.-H. Choi, and M. K. Nazeeruddin, "Dimensionally Engineered Perovskite Heterostructure for Photovoltaic and Optoelectronic Applications", Advanced Energy Materials **9**, 1902470 (2019).

[5]S. Gharibzadeh, P. Fassl, I. M. Hossain, P. Rohrbeck, M. Frericks, M. Schmidt, T. Duong, M. R. Khan, T. Abzieher, B. A. Nejand, F. Schackmar, O. Almora, T. Feeney, R. Singh, D. Fuchs, U. Lemmer, J. P. Hofmann, S. A. L. Weber, and U. W. Paetzold, "Two birds with one stone: dual grain-boundary and interface passivation enables >22% efficient inverted methylammonium-free perovskite solar cells", Energy & Environmental Science **14**, 5875–5893 (2021).

[6]S. Gharibzadeh, B. Abdollahi Nejand, M. Jakoby, T. Abzieher, D. Hauschild, S. Moghadamzadeh, J. A. Schwenzer, P. Brenner, R. Schmager, A. A. Haghighirad, L. Weinhardt, U. Lemmer, B. S. Richards, I. A. Howard, and U. W. Paetzold, "Record Open-Circuit Voltage Wide-Bandgap Perovskite Solar Cells Utilizing 2D/3D Perovskite Heterostructure", Advanced Energy Materials **9**, 1803699 (2019).

[7]C. Shen, Y. Wu, S. Zhang, T. Wu, H. Tian, W.-H. Zhu, and L. Han, "Stabilizing Formamidinium Lead Iodide Perovskite by Sulfonyl-Functionalized Phenethylammonium Salt via Crystallization Control and Surface Passivation", Solar RRL **4**, 2000069 (2020).

[8]M. Saliba, T. Matsui, J. Y. Seo, K. Domanski, J. P. Correa-Baena, M. K. Nazeeruddin, S. M. Zakeeruddin, W. Tress, A. Abate, A. Hagfeldt, and M. Grätzel, "Cesium-containing triple cation perovskite solar cells: Improved stability, reproducibility and high efficiency", Energy and Environmental Science **9**, 1989–1997 (2016).

[9]T. Zhu, D. Zheng, J. Liu, L. Coolen, and T. Pauporté, "PEAI-Based Interfacial Layer for High-Efficiency and Stable Solar Cells Based on a MACl-Mediated Grown FA0.94MA0.06PbI3 Perovskite", ACS Applied Materials & Interfaces **12**, 37197–37207 (2020).

[10]K. T. Cho, G. Grancini, Y. Lee, E. Oveisi, J. Ryu, O. Almora, M. Tschumi, P. A. Schouwink, G. Seo, S. Heo, J. Park, J. Jang, S. Paek, G. Garcia-Belmonte, and M. K. Nazeeruddin, "Selective growth of layered perovskites for stable and efficient photovoltaics", Energy and Environmental Science **11**, 952–959 (2018).

[11]Q. Jiang, Y. Zhao, X. Zhang, X. Yang, Y. Chen, Z. Chu, Q. Ye, X. Li, Z. Yin, and J. You, "Surface passivation of perovskite film for efficient solar cells", Nature Photonics **13**, 460–466 (2019).

[12]M. Lee, E. Choi, A. M. Soufiani, J. Lim, M. Kim, D. Chen, M. A. Green, J. Seidel, S. Lim, J. Kim, X. Dai, R. Lee-Chin, B. Zheng, Z. Hameiri, J. Park, X. Hao, and J. S. Yun, "Enhanced Hole-Carrier Selectivity in Wide Bandgap Halide Perovskite Photovoltaic Devices for Indoor Internet of Things Applications", Advanced Functional Materials **31**, 2008908 (2021).

[13]K. Lee, J. Kim, H. Yu, J. Woo Lee, C.-M. Yoon, S. Keun Kim, and J. Jang, "A highly stable and efficient carbon electrode-based perovskite solar cell achieved via interfacial growth of 2D PEA_2PbI_4 perovskite", Journal of Materials Chemistry A **6**, 24560–24568 (2018).

[14]W. Fu, H. Liu, X. Shi, L. Zuo, X. Li, and A. K. Jen, "Tailoring the Functionality of Organic Spacer Cations for Efficient and Stable Quasi-2D Perovskite Solar Cells", Advanced Functional Materials **29**, 1900221 (2019).

[15]S. Zeng, S. Shi, S. Wang, and Y. Xiao, "Mixed-ligand engineering of quasi-2D perovskites for efficient sky-blue light-emitting diodes", Journal of Materials Chemistry C **8**, 1319–1325 (2020).

[16]K. Liang, D. B. Mitzi, and M. T. Prikas, "Synthesis and Characterization of Organic-Inorganic Perovskite Thin Films Prepared Using a Versatile Two-Step Dipping Technique", Chemistry of Materials **10**, 403–411 (1998).

[17]B. Guo, C. Luo, C. Yan, B. Sun, W. Li, and W. Yang, "Understanding Excitonic Behavior in Light Absorption and Recombination Process", The Journal of Physical Chemistry C **124**, 26076–26082 (2020).

[18]M. Daboczi, I. Hamilton, S. Xu, J. Luke, S. Limbu, J. Lee, M. A. McLachlan, K. Lee, J. R. Durrant, I. D. Baikie, and J. S. Kim, "Origin of Open-Circuit Voltage Losses in Perovskite Solar Cells Investigated by Surface Photovoltage Measurement", ACS Applied Materials and Interfaces **11**, 46808–46817 (2019).

[19]Y.-C. Chin, M. Daboczi, C. Henderson, J. Luke, and J.-S. Kim, "Suppressing PEDOT:PSS Doping-Induced Interfacial Recombination Loss in Perovskite Solar Cells", ACS Energy Letters **7**, 560–568 (2022).

[20]S. N. Habisreutinger, N. K. Noel, H. J. Snaith, and R. J. Nicholas, "Investigating the Role of 4-Tert Butylpyridine in Perovskite Solar Cells", Advanced Energy Materials **7**, 1601079 (2017).

[21]X. Bu, R. J. E. Westbrook, L. Lanzetta, D. Ding, T. Chotchuangchutchaval, N. Aristidou, and S. A. Haque, "Surface Passivation of Perovskite Films via Iodide Salt Coatings for Enhanced Stability of Organic Lead Halide Perovskite Solar Cells", Solar RRL **3**, 1800282 (2019).

[22]S. Rahmany and L. Etgar, "Two-dimensional or passivation treatment: the effect of hexylammonium post deposition treatment on 3D halide perovskite-based solar cells", Materials Advances **2**, 2617–2625 (2021).

[23]S. Y. Park, C. Labanti, J. Luke, Y.-C. Chin, and J.-S. Kim, "Organic Bilayer Photovoltaics for Efficient Indoor Light Harvesting", Advanced Energy Materials **12**, 2103237 (2022).

[24]F. M. Rombach, S. A. Haque, and T. J. Macdonald, "Lessons learned from spiro-OMeTAD and PTAA in perovskite solar cells", Energy & Environmental Science **14**, 5161–5190 (2021).

[25]J. A. Dawson, A. J. Naylor, C. Eames, M. Roberts, W. Zhang, H. J. Snaith, P. G. Bruce, and M. S. Islam, "Mechanisms of Lithium Intercalation and Conversion Processes in Organic–Inorganic Halide Perovskites", ACS Energy Letters **2**, 1818–1824 (2017).

[26]W. Li, H. Dong, L. Wang, N. Li, X. Guo, J. Li, and Y. Qiu, "Montmorillonite as bifunctional buffer layer material for hybrid perovskite solar cells with protection from corrosion and retarding recombination", Journal of Materials Chemistry A **2**, 13587–13592 (2014).

[27]Y. Li, H. Li, C. Zhong, G. Sini, and J.-L. Brédas, "Characterization of intrinsic hole transport in single-crystal spiro-OMeTAD", npj Flexible Electronics **1**, 1–8 (2017).

[28]Y. Liu, Y. Hu, X. Zhang, P. Zeng, F. Li, B. Wang, Q. Yang, and M. Liu, "Inhibited aggregation of lithium salt in spiro-OMeTAD toward highly efficient perovskite solar cells", Nano Energy **70**, 104483 (2020).

[29]E. J. Juarez-Perez, M. R. Leyden, S. Wang, L. K. Ono, Z. Hawash, and Y. Qi, "Role of the Dopants on the Morphological and Transport Properties of Spiro-MeOTAD Hole Transport Layer", Chemistry of Materials **28**, 5702–5709 (2016).

[30]F. Lamberti, T. Gatti, E. Cescon, R. Sorrentino, A. Rizzo, E. Menna, G. Meneghesso, M. Meneghetti, A. Petrozza, and L. Franco, "Evidence of Spiro-OMeTAD De-doping by tert-Butylpyridine Additive in Hole-Transporting Layers for Perovskite Solar Cells", Chem **5**, 1806–1817 (2019).

[31]S. Wang, M. Sina, P. Parikh, T. Uekert, B. Shahbazian, A. Devaraj, and Y. S. Meng, "Role of 4-tert-Butylpyridine as a Hole Transport Layer Morphological Controller in Perovskite Solar Cells", Nano Letters **16**, 5594–5600 (2016).

Chapter 7

Conclusion and Future Work

7.1 Conclusion

In this thesis, the importance of understanding as well as manipulating the energetics in both perovskite and organic semiconductors (OSCs) are underlined in order to provide design rules to both perovskite solar cells (PSCs) and organic photovoltaics (OPVs). The chemical structures, packing structures, defect origins and interfacial band bending are mainly studied by theoretical simulations, surface photovoltage (SPV) and ambient photoemission spectroscopy (APS) with advanced data characterization in density of state (DOS). Here, the major conclusions of each chapter are illustrated. For more detailed conclusions, please refer to the conclusion section in each chapter.

In Chapter 4, the energetics of various photovoltaic OSCs are investigated in order to correlate both chemical structures and packing structures to the electron distributions, including tail states and highest occupied molecular orbital (HOMO) energy levels. Firstly, in Section 4.2, Y6 is found to exhibit the smallest amount of tail states among other high performance non-fullerene acceptors (NFAs), IDTBR series and ITIC, leading to less V_{OC} loss in device performance. From density functional theory (DFT) simulations, the conformational rigidity is pinpointed to the alkyl side chain, which locks the dihedral rotation of the accepting end group and improves the photostability.

Turn to the impact of packing structures in neat films (Section 4.3), evaporated standing and lying sexithiophene (α-6T) has shown a significant energetic shift (0.4 eV) due to their static electrostatic field. This energy difference is preserved in the mixed α-6T which is revealed by

its DOS distribution, a superposition of both lying and standing structures. As a result, the energy offset between different packing structure enables charge separation and contributes to an external quantum efficiency (EQE) ∼50 %. In Section 4.4, the concept of orientation dependent energetic shift is extended to solution-processed Y6. The Y6 CB is found to have a more mixed structure, and thus has a 0.2 eV deeper HOMO level than Y6 CF. Also, the mixed structure of Y6 CB also shows an efficient charge generation in SPV measurments. In PM6/Y6 bilayer devices, the orientation dependent energetic shift dominates the device performance as the CB device has a smaller V_{OC} due to the deeper HOMO and LUMO levels in Y6. By DFT simulation, the electrostatic effect is found to be related to the quadrupole moment perpendicular to the π-π stacking direction (Q_π), and it is shown to play an important role in the polymeric donor HOMO level shift in bulk heterojunction as well.

In the last section (Section 4.5), two polymer:fullerene acceptor blends are investigated to understand the DOS distribution under blending. The DOS distribution of PDTSiTTz gradually regain features from flat even distribution to clear features across the energy spectra. In comparison, PCPDTBT blends have a stable DOS distribution with or without fullerene acceptors. Moreover, the DOS distributions of PDTSiTTz:fullerene blends are identical to the PCPDTBT. Since the two polymer shares the same donor moiety, the same DOS features indicate a more localized MO on the donor moiety in PDTSiTTz blends while a more inter-chain character for neat PDTSiTTz upon blending. This provides a better understanding to the unusual non-Langevin recombination nature in PDTsiTTz and its correlation in DOS distribution.

In Chapter 5, the relationship between doping level and non-radiative recombination loss in PSCs is investigated In previous study, the doping level of the hole transport layer (HTL) in PSCs was correlated to the non-radiative recombination loss and V_{OC} loss.[1] However, a systematic tuning on the same HTL still remains unclear. Thus, a systematic dedoping in PEDOT:PSS is applied in inverted PSCs to unveil the doping induced recombination loss. Firstly, the originally highly doped PEDOT:PSS is dedoped by the basic NaOH(aq) solution, and the dedoping is confirmed by both Raman and absorption spectroscopy.[2] With thickness optimization, the dedoped PEDOT:PSS shows a much higher fill factor (FF), V_{OC} and power conversion efficiency (PCE). The higher FF is due to the improved charge

blocking capability from the shallower lowest unoccupied molecular orbital (LUMO). By transient photoluminescence (PL) and SPV measurements, the high V_{OC} is attributed to reduced non-radiative recombination leading to a longer PL decay and larger SPV signal. This work demonstrates the correlation between the doping level in PEDOT:PSS and interfacial recombination loss, providing a strategy to utilize less-doped HTLs in PSCs.

In Chapter 6, the impact of different dimensional Ruddlesden-Popper phase perovskite (2D perovskite) on the perovskite/HTL interface is investigated. By tuning the concentration of the passivation solution, the n number of phenethylammonium (PEA)-based 2D perovskite is tuned from mixed large n number (high concentration) to purely $n = 1$ (low concentration). The passivation manages to remove the isolated PbI_2 surface trap states in all cases coherent with the literature.[3,4] Also, a noticeable deeper VBE is found in the pure 2D passivated perovskite which results in a hole extraction barrier on the interface. Therefore, a weaker SPV response is recorded with the 2D passivated samples as the deeper VBE from 2D perovskite inhibits holes redistributing to the surface while reducing the defect related ionic contribution. In quasi-2D perovskite samples, the slow ionic contribution reappears as it shares a similar defect nature in the 3D perovskite. This is further confirmed by the faster transient PL decay showing the disadvantages of having high concentration passivation and quasi-2D perovskite. By implementing 2D perovskite into conventional PSCs, the surface passivation benefits the V_{OC} by reducing the recombination loss on the interface. However, the devices with quasi-2D perovskite does not gain a further improvement but rather a much wide spread statistic due to the rough surface morphology and the reappeared 3D characters. The results emphasize the benefit of having thin and pure 2D perovskite passivation as it inhibits trap related recombination loss, ionic movement as well as protecting the underneath 3D perovskite. Also, the study unveils the mechanism of the perovskite SPV response with a clear separation between charge related SPV signal and ionic contributions.

In addition to the 2D-to-3D relationship, surface passivation also influences dopant diffusion from Spiro-OMeTAD to 3D perovskite. In 2D passivated samples, the doping level of Spiro-OMeTAD maintains a much stronger p-doped condition compared to the one on top of 3D perovskite. By blending different perovskite components, PbI_2 or PEAI, the HOMO level of the Spiro-OMeTAD remains the same ruling out the possibility of perovskite related

ions. Furthermore, the DOS distributions show a clear horizontal shift on the energy spectra indicating the origin is dopant leakage into 3D perovskite. The results show the dopant blocking ability in 2D perovskite which may play an important role in device stability and dopant related degradation issues.

7.2 Future Work

Based on the results, there are some suggested future work that would extend the understanding and deepen the impact in real photovoltaic applications.

For orientation dependent energetics in Chapter 4, it is interesting to propose a much stronger Q_π molecular design by involving some of the key moieties such as cyano side groups and stronger donor-acceptor character in the A-D-A'-D-A system. Also, since Q_π has a C_2 rotational symmetry, it would be easier to be modulated in a linear molecular structure. It would be relevant to design strong Q_π linear NFAs in comparison to Y6. In either case, the stronger Q_π may benefit the device performance with a much lower V_{OC} loss and efficient charge separation process.

For solution-processed Y6 study (Section 4.4), mixed and face-on oriented structures are achieved without a pure edge-on oriented sample. By further solvent engineering, such as blending chloroform and chlorobenzene, the degree of mixing or pure edge-on Y6 may be controlled to achieve better matching with other existing polymeric donors for performance enhancement.

For α-6T study, the orientation controlled homojunction devices have shown an exceptional EQE implying the advantage of orientation controlled homojunction photodectors. A combined theoretical and experimental study based on other sublimable OSCs may provide a new approach to the architecture of organic photodetector field.

In Chapter 5, the success in improving PCE with cheap PEDOT:PSS makes it a good candidate to be commercialized. However, the results are still based on lab-scaled devices which require tedious fabrication process, namely spin-coating, and are usually in small active area. An investigation applying different preparation techniques, such as bar-coating or ink-jet printing, will realize the feasibility in larger area closer to commercial solar cells. Moreover, the improved charge blocking ability in dedoped PEDOT:PSS has shown a significantly reduced

dark current. As dark current plays an important role in signal-to-noise ratio of photodetectors, this makes the strategy of dedoping HTL also applicable in perovskite-based photodetectors.[5] A facile dedoped PEDOT:PSS based perovskite photodetector may be interesting to be explored.

In Chapter 6, the dopant blocking character of 2D perovskite is novel and has a potential in improving device stability. Firstly, a detailed dopant mapping in these devices would be meaningful to understand the mechanism behind and what types of dopants are affected here. Also, it can shed light in dopant redistribution and degradation under device operation. In addition, other types of 2D cations may be explored to examine the critical chemical structure contributing to the blocking character. Last but not the least, a comparison in device stability with continuous light exposure can prove this potential stability improvement.

As a large portion of this thesis are based on the newly found DOS conversion relationship with APS spectra (Section 3.4.3), a thorough theoretical derivation should be done and push further to generalized the understanding of photoemission mechanism in ambient environment. As part of the derivation is already provided in Section 3.4.3 and Fowler's publication, the theory should be only few steps of approximation further.[6] Also, a cross comparison between the DOS from APS and ultraviolet photoexcitation (UPS) would be important to demonstrate the reliability as UPS is still considered to be the most accurate DOS measurement. Lastly, the fitting algorithm of simulated molecular orbital energy to DOS in the software (Appendix C) can be further generalized to investigate wider range of materials and opening up to wider applications.

References

[1]T. Du, W. Xu, M. Daboczi, J. Kim, S. Xu, C.-T. Lin, H. Kang, K. Lee, M. J. Heeney, J.-S. Kim, J. R. Durrant, and M. A. McLachlan, "P-Doping of organic hole transport layers in p–i–n perovskite solar cells: correlating open-circuit voltage and photoluminescence quenching", Journal of Materials Chemistry A **7**, 18971–18979 (2019).

[2]T. C. Tsai, H. C. Chang, C. H. Chen, Y. C. Huang, and W. T. Whang, "A facile dedoping approach for effectively tuning thermoelectricity and acidity of PEDOT:PSS films", Organic Electronics **15**, 641–645 (2014).

[3]C. T. Lin, J. Lee, J. Kim, T. J. Macdonald, J. Ngiam, B. Xu, M. Daboczi, W. Xu, S. Pont, B. Park, H. Kang, J. S. Kim, D. J. Payne, K. Lee, J. R. Durrant, and M. A. McLachlan, "Origin of Open-Circuit Voltage Enhancements in Planar Perovskite Solar Cells Induced by Addition of Bulky Organic Cations", Advanced Functional Materials **30**, 1906763 (2020).

[4]M. Stolterfoht, C. M. Wolff, J. A. Márquez, S. Zhang, C. J. Hages, D. Rothhardt, S. Albrecht, P. L. Burn, P. Meredith, T. Unold, and D. Neher, "Visualization and suppression of interfacial recombination for high-efficiency large-area pin perovskite solar cells", Nature Energy **3**, 847–854 (2018).

[5]W. Tian, H. Zhou, and L. Li, "Hybrid Organic–Inorganic Perovskite Photodetectors", Small **13**, 1702107 (2017).

[6]R. H. Fowler, "The analysis of photoelectric sensitivity curves for clean metals at various temperatures", Physical Review **38**, 45–56 (1931).

Appendix A

List of Publications

1. **Chin, Y.-C.**; Daboczi, M.; Henderson, C.; Luke, J.; Kim, J.-S. Suppressing PEDOT:PSS Doping-Induced Interfacial Recombination Loss in Perovskite Solar Cells. ACS Energy Lett. 2022, 560–568. https://doi.org/10.1021/acsenergylett.1c02577.

2. Wu, J.; Lee, J.; **Chin, Y.-C.**; Yao, H.; Cha, H.; Luke, J.; Hou, J.; Kim, J. S.; Durrant, J. R. Exceptionally Low Charge Trapping Enables Highly Efficient Organic Bulk Heterojunction Solar Cells. Energy and Environmental Science 2020, 13 (8), 2422–2430. https://doi.org/10.1039/d0ee01338b.

3. Luke, J.; Yang, E. J.; **Chin, Y.-C.**; Che, Y.; Winkler, L.; Whatling, D.; Labanti, C.; Park, S. Y.; Kim, J.-S. Strong Intermolecular Interactions Induced by High Quadrupole Moments Enable Excellent Photostability of Non-Fullerene Acceptors for Organic Photovoltaics. Advanced Energy Materials 2022, 12 (30), 2201267. https://doi.org/10.1002/aenm.202201267.

4. Dong, Y.; Nikolis, V. C.; Talnack, F.; **Chin, Y.-C.**; Benduhn, J.; Londi, G.; Kublitski, J.; Zheng, X.; Mannsfeld, S. C. B.; Spoltore, D.; Muccioli, L.; Li, J.; Blase, X.; Beljonne, D.; Kim, J. S.; Bakulin, A. A.; D'Avino, G.; Durrant, J. R.; Vandewal, K. Orientation Dependent Molecular Electrostatics Drives Efficient Charge Generation in Homojunction Organic Solar Cells. Nature Communications 2020, 11 (1), 4617. https://doi.org/10.1038/s41467-020-18439-z.

5. Park, S. Y.; Labanti, C.; Luke, J.; **Chin, Y.-C.**; Kim, J.-S. Organic Bilayer Photovoltaics for Efficient Indoor Light Harvesting. Advanced Energy Materials 2103237, 2103237. https://doi.org/10.1002/aenm.202103237.

6. Cui, J.; Daboczi, M.; Regue, M.; **Chin, Y.-C.**; Pagano, K.; Zhang, J.; Isaacs, M. A.; Kerherve, G.; Mornto, A.; West, J.; Gimenez, S.; Kim, J.; Eslava, S. 2D Bismuthene as a Functional Interlayer between $BiVO_4$ and NiFeOOH for Enhanced Oxygen-Evolution Photoanodes. Adv Funct Materials 2022, 2207136. https://doi.org/10.1002/adfm.202207136.

7. Daboczi, M.; Ratnasingham, S. R.; Mohan, L.; Pu, C.; Hamilton, I.; **Chin, Y.-C.**; McLachlan, M. A.; Kim, J.-S. Optimal Interfacial Band Bending Achieved by Fine Energy Level Tuning in Mixed-Halide Perovskite Solar Cells. ACS Energy Lett. 2021, 6 (11), 3970–3981. https://doi.org/10.1021/acsenergylett.1c02044.

8. Jiang, Z.; Du, T.; Lin, C.-T.; Macdonald, T. J.; Chen, J.; **Chin, Y.-C.**; Xu, W.; Ding, B.; Kim, J.-S.; Durrant, J. R.; Heeney, M.; McLachlan, M. A. Deciphering the Role of

Hole Transport Layer HOMO Level on the Open Circuit Voltage of Perovskite Solar Cells. Advanced Materials Interfaces 2022, 2201737. https://doi.org/10.1002/admi.202201737.

9. Hart, L. J. F.; Grüne, J.; Liu, W.; Lau, T.; Luke, J.; **Chin, Y.-C.**; Jiang, X.; Zhang, H.; Sowood, D. J. C.; Unson, D. M. L.; Kim, J.-S.; Lu, X.; Zou, Y.; Gao, F.; Sperlich, A.; Dyakonov, V.; Yuan, J.; Gillett, A. J. Triplet-Triplet Annihilation Reduces Non-Radiative Voltage Losses in Organic Solar Cells. arXiv January 30, 2023. https://doi.org/10.48550/arXiv.2301.02112.

10. Marin-Beloqui, J.; Zhang, G.; Guo, J.; Shaikh, J.; Wohrer, T.; Hosseini, S. M.; Sun, B.; Shipp, J.; Auty, A. J.; Chekulaev, D.; Ye, J.; **Chin, Y.-C.**; Sullivan, M. B.; Mozer, A. J.; Kim, J.-S.; Shoaee, S.; Clarke, T. M. Insight into the Origin of Trapping in Polymer/Fullerene Blends with a Systematic Alteration of the Fullerene to Higher Adducts. J. Phys. Chem. C 2022, 126 (5), 2708–2719. https://doi.org/10.1021/acs.jpcc.1c10378.

Appendix B

Molecular Abbreviations

Table B.1: Molecular abbreviations and full names repeatedly used

Abbreviation(s)	Full name
4TBP	4-tert butylpyridine
BPhen	bathophenanthroline
BTP-4Cl (Y7)	2,2′-((2Z,2′Z)-((12,13-bis(2-ethylhexyl)-3,9-diundecyl-12,13-dihydro-[1,2,5]thiadiazolo[3,4-e]thieno[2″,3″:4′,5′]thieno[2′,3′:4,5]pyrrolo[3,2-g]thieno[2′,3′:4,5]thieno[3,2-b]indole-2,10-diyl)bis(methanylylidene))bis(5,6-dichloro-3-oxo-2,3-dihydro-1H-indene-2,1-diylidene))dimalononitrile
BTP-4F (Y6)	2,2′-((2Z,2′Z)-((12,13-bis(2-ethylhexyl)-3,9-diundecyl-12,13-dihydro-[1,2,5]thiadiazolo[3,4-e]thieno[2″,3″:4′,5′]thieno[2′,3′:4,5]pyrrolo[3,2-g]thieno[2′,3′:4,5]thieno[3,2-b]indole-2,10-diyl)bis(methanylylidene))bis(5,6-difluoro-3-oxo-2,3-dihydro-1H-indene-2,1-diylidene))dimalononitrile
C545T (Coumarin 545T)	10-(2-benzothiazolyl)-2,3,6,7-tetrahydro-1,1,7,7-tetramethyl-1H,5H,11H-(1)benzopyropyrano(6,7-8-i,j)quinolizin-11-one
DBzA	6-methyl-2-(4-(9-(4-(6-methylbenzo[d]thiazol-2-yl)phenyl)anthracen-10-yl)phenyl)benzo[d]thiazole
DMF	dimethylformamide
DMSO	dimethyl sulfoxide
EH-IDTBR	5,5′-[[4,4,9,9-tetrakis(2-ethylhexyl)-4,9-dihydro-s-indaceno[1,2-b:5,6-b′]dithiophene-2,7-diyl]bis(2,1,3-benzothiadiazole-7,4-diylmethylidyne)]bis[3-ethyl-2-thioxo-4-thiazolidinone]
F4TCNQ	2,3,5,6-tetrafluoro-7,7,8,8-tetracyanoquinodimethane
FK209	tris(2-(1H-pyrazol-1-yl)-4-tert-butylpyridine)cobalt(III) tri[bis(trifluoromethane)sulfonimide]
ICMA	1′,4′-dihydro-naphtho[2′,3′:1,2][5,6]fullerene-C60
ICBA	1′,1″,4′,4″-tetrahydro-di[1,4]methanonaphthaleno[1,2:2′,3′,56,60:2″,3″][5,6]fullerene-C60

continued on next page

Table B.1: (continued)

Abbreviation(s)	Full name
ICTA	1′,1″,1‴,4′,4″,4‴-hexahydro-tri[1,4]methanonaphthaleno[1,2:2′,3′,30,31:2″,3″,56,60:2‴,3‴][5,6]fullerene-C60
ITIC	3,9-bis(2-methylene-(3-(1,1-dicyanomethylene)-indanone))-5,5,11,11-tetrakis(4-hexylphenyl)-dithieno[2,3-d:2′,3′-d′]-s-indaceno[1,2-b:5,6-b′]dithiophene
LiTFSi	lithium bis(trifluoromethanesulfonyl)imide
O-IDTBR	(5Z,5′Z)-5,5′-((7,7′-(4,4,9,9-tetraoctyl-4,9-dihydro-s-indaceno[1,2-b:5,6-b′]dithiophene-2,7-diyl)bis(benzo[c][1,2,5]thiadiazole-7,4-diyl))bis(methanylylidene))bis(3-ethyl-2-thioxothiazolidin-4-one)
PBDB-T (PBDTBDD, PCE12)	poly[(2,6-(4,8-bis(5-(2-ethylhexyl)thiophen-2-yl)-benzo[1,2-b:4,5-b′]dithiophene))-alt-(5,5-(1′,3′-di-2-thienyl-5′,7′-bis(2-ethylhexyl)benzo[1′,2′-c:4′,5′-c′]dithiophene-4,8-dione)]
PBDB-T-2F (PM6)	poly[(2,6-(4,8-bis(5-(2-ethylhexyl-3-fluoro)thiophen-2-yl)-benzo[1,2-b:4,5-b′]dithiophene))-alt-(5,5-(1′,3′-di-2-thienyl-5′,7′-bis(2-ethylhexyl)benzo[1′,2′-c:4′,5′-c′]dithiophene-4,8-dione)]
PBDTTT-EFT (PBDTT-FTTE, PTB7-Th, PCE10)	poly[4,8-bis(5-(2-ethylhexyl)thiophen-2-yl)benzo[1,2-b;4,5-b′]dithiophene-2,6-diyl-alt-(4-(2-ethylhexyl)-3-fluorothieno[3,4-b]thiophene-)-2-carboxylate-2-6-diyl)]
PCBM	[6,6]-phenyl-C61-butyric acid methyl ester
PDTSiTTz	poly[(4,4′-bis(2-ethylhexyl)dithieno[3,2-b:2′,3′-d]silole)-2,6-diyl-alt-(2,5-bis 3-tetradecylthiophen-2-yl thiazolo 5,4-d thiazole)-2,5diyl]
PEABr	phenethylammonium bromide
PEAI	phenethylammonium iodide
PEDOT:PSS	poly(3,4-ethylenedioxythiophene) polystyrene sulfonate
PffBT4T-2OD (PCE11)	poly[(5,6-difluoro-2,1,3-benzothiadiazol-4,7-diyl)-alt-(3,3‴-di(2-octyldodecyl)-2,2′;5′,2″;5″,2‴-quaterthiophen-5,5‴-diyl)]
Rubrene	5,6,11,12-tetraphenyltetracene
Si-PCPDTBT	poly[(4,4-bis(2-ethylhexyl)-dithieno[3,2-b:2′,3′-d]silole)-2,6-diyl-alt-(2,1,3-benzothiadiazole)-4,7-diyl]
Spiro (Spiro-OMeTAD)	2,2′,7,7′-tetrakis[N,N-di(4-methoxyphenyl)amino]-9,9′-spirobifluorene
TBPe	2,5,8,11-tetra-tert-butylperylene
TCTA	4,4′,4”-tris(carbazol-9-yl)triphenylamine
TPBA	9,9′,10,10′-tetraphenyl-2 ,2′-bianthracene
TPBI	2,2′,2-(1,3,5-benzinetriyl)-tris(1-phenyl-1H-benzimidazole)

continued on next page

Table B.1: (continued)

Abbreviation(s)	Full name
Y11	2,2′-((2Z,2′Z)-((12,13-bis(2-ethylhexyl)-3,9-diundecyl-12,13-dihydro-2-(2-ethylhexyl)-[1,2,3]triazole[3,4-e]thieno[2″,3″:4′,5′]thieno-[2′,3′:4,5]pyrrolo[3,2-g]thieno[2′,3′:4,5]thieno-[3,2-b]indole-2,10-diyl)bis(methanylylidene))bis-(5,6-difloro-3-oxo-2,3-dihydro-1H-indene-2,1-diylidene))dimalononitrile
α-6T	α-sexithiophene

Appendix C

Python code of APS module

This latest Python code used for APS data processing is copied as below. The code is also available on https://github.com/joe6302413/APS under MIT license.

```
# -*- coding: utf-8 -*-
"""
Created on Mon Nov  9 16:30:53 2020
The module is for measurements done by APS04.
It includes a function for general csv saving in origin format.
The class APS is for handling APS signals, cube(sqr)-root v.s.
   energy.
The APS class has multiple methods for different physical
   quantities including HOMO level fit.
The DWF class handles all variations of CPD measurements.
Calibrate class takes into APS and DWF object for calibrating
   factor building.
Build DWF related measurements based on root class of DWF such as
    SPV.
Note:
    1.
Last editing time: 12/11/2020
@author: Yi-Chun Chin   joe6302413@gmail.com
"""
#%% define and libraries
import matplotlib.pyplot as plt, csv
import numpy as np
from scipy.optimize import curve_fit, shgo
from scipy import integrate
from os.path import split,join,exists
from scipy.signal import savgol_filter
from scipy.special import erf
from typing import List,Tuple
import tkinter as tk
from tkinter.filedialog import asksaveasfilename
__version__='1.2'
def save_csv_for_origin(data:Tuple[List[List[float]]],location:
   str,
                        filename:str=None,datanames:List[List[str
                           ]]=None,
                        header:List[List[str]]=None) -> None:
    '''
    save data sets to csv format for origin.
    data=([x1,x2,...],[y1,y2,...],...) where each element is a
       list of array
    location string is the location for output file
    string filename will be used as output into filename.csv
    datanames=[[yname1,zname1,...],[yname2,zname2]] names should
       be for each individual data sets
    header=[[longname X, longname Y,...],[unit X, unit Y,...]]
    '''
    path_name=join(location,str(filename)+'.csv')
    if exists(path_name):
        root=tk.Tk()
```

```
        filename=asksaveasfilename(title=f'rename save file name
           for {filename}',
                                   initialdir=location,filetypes
                                      =[('csv','.csv')],
                                   defaultextension='.csv',
                                      initialfile=filename)
        if filename=='':
            raise Exception('saving process cancelled due to
               overwriting.')
        path_name=join(location,str(filename))
        root.destroy()
    data_dim=len(data)
    assert [len(i) for i in data][1:]==[len(i) for i in data
       ][:-1], \
        'number of data mismatch'
    assert len(header[0])==data_dim, 'header mismatch data
       dimension'
    numberofdata=len(data[0])
    data=[j for i in zip(*data) for j in i]
    maxlength=max(len(i) for i in data)
    data=np.transpose([np.append(i,['']*(maxlength-len(i))) for i
        in data])
    if datanames==None:
        datanames=[[f'data{i}' for i in range(numberofdata) for j
            in range(data_dim)]]
    else:
        datanames=[[j for i in datanames for j in (['']+i+['']*(
           data_dim-1-len(i)))]]
    if header==None:
        header=datanames+[['']*numberofdata*data_dim]
    else:
        header=[i*numberofdata for i in header]
    with open(path_name,'w',newline='') as f:
        writer=csv.writer(f)
        writer.writerows(header)
        writer.writerows(datanames)
        writer.writerows(data)
def find_overlap(x,y):
    '''
    Given 2D x=[x1,x2,...] and 2D y=[y1,y2,...] of each array xn
       or yn is a
    positive monotonic numpy array.
    Output x' and y' for which x' is a numpy array of the common
       x
    And y' is a 2D list such that y'=[y1',y2',...] with numpy
       array yn'
    contains the value of yn with resspect to xn'
    '''
    x_min=np.max([i[0] for i in x])
    x_max=np.min([i[-1] for i in x])
    for i in range(len(x)):
        min_index=next(l for l,k in enumerate(x[i]) if k==x_min)
        max_index=next(l for l,k in enumerate(x[i]) if k==x_max)
        y[i]=y[i][min_index:max_index+1]
    x=x[-1][min_index:max_index+1]
    return x,y
def inv_gradient(x,g,y0=0):
    '''
    An inverse function of numpy.gradient.
    g=np.gradient(y,x) == y=inv_gradient(x,g,y0=y[0])
    Output numpy array y
    '''
    length=len(g)
    if length!=len(x):
        raise Exception('length of x and gradient should have
           match length')
    xdiff=np.diff(x)
```

```
    xdiff2=xdiff[:-1]+xdiff[1:]
    y=np.array([y0,g[0]*xdiff[0]+y0])
    s=g[0]
    for i in range(1,length-2):
        s=(g[i]-s*xdiff[i]/xdiff2[i-1])*xdiff2[i-1]/xdiff[i-1]
        y=np.append(y,y[i]+s*xdiff[i])
    y=np.append(y,y[-1]+g[-1]*xdiff[-1])
    return y
class APS:
    def __init__(self,energy,pes_raw,sqrt=False,Name='no_name'):
        self.energy=np.array(energy)
        self._pes_raw=np.array(pes_raw)
        self.name=Name
        self._DOS=self.DOS_raw
        self._sqrt=bool(sqrt)
    @property
    def sqrt(self):
        return self._sqrt
    @property
    def status(self):
        return {'sqrt': self.sqrt,'baseline':self.baseline if \
                        hasattr(self,'_baseline') else False,
                        'cutoff': self._has_cutoff,
                        'analyzed':self._is_analyzed,
                        'DOS smoothed': self._is_DOS_smoothed}
    @property
    def _is_analyzed(self):
        return True if hasattr(self,'homo') else False
    @property
    def _is_DOS_smoothed(self):
        return True if (self._DOS!=self.DOS_raw).any() else False
    @property
    def _has_cutoff(self):
        return True if hasattr(self,'_cutoff_index') else False
    @property
    def pes_raw(self):
        '''
        Calling for the original input pes.
        '''
        return self._pes_raw
    @property
    def pes(self):
        '''
        Calling the pes-baseline if possible. Otherwise, return
           pes_raw
        '''
        try:
            return self.pes_raw-self._baseline
        except AttributeError:
            return self.pes_raw
    @property
    def pes_base(self):
        '''
        Calling for pes-baseline. It will do automatic baseline
           fitting if
        baseline doesn't exit.
        '''
        return self.pes_raw-self.baseline
    @property
    def DOS_raw(self):
        return np.gradient(self.pes,self.energy)
    @property
    def DOS(self):
        return self._DOS
    @property
    def cutoff_energy(self):
```

```
    try:
        return self._cutoff_energy
    except AttributeError:
        print(f'Automatic find cutoff for {self.name}')
        self.find_cutoff()
        return self._cutoff_energy
@property
def cutoff_index(self):
    try:
        return self._cutoff_index
    except AttributeError:
        print(f'Automatic find cutoff for {self.name}')
        self.find_cutoff()
        return self._cutoff_index
@property
def baseline(self):
    try:
        return self._baseline
    except AttributeError:
        print(f'Automatic find baseline between (1,5) for {
           self.name}')
        self.find_baseline(plot=False)
        return self._baseline
def __repr__(self):
    return self.name
def __str__(self):
    summary=f'Name:\t{self.name}\n'
    summary+='\n'.join([f'{i}:\t{j}' for i,j in self.status.
       items()])+'\n'
    if self._is_analyzed:
        summary+=f'HOMO(eV):\t{self.homo:.2f}\u00b1'\
            f'{self.std_homo:.4f} eV\n'
    return summary
def pick_range(self):
    plt.figure()
    self.DOSplot()
    _=plt.title('Pick the range for fitting (min&max)')
    [self.xmin,self.xmax]=np.array(plt.ginput(2))[:,0]
    plt.close()
    if self.xmax<self.xmin:
        self.xmax,self.xmin=self.xmin,self.xmax
    minindex=next(p for p,q in enumerate(self.energy) if q>
       self.xmin)
    maxindex=next(p for p,q in enumerate(self.energy) if q>
       self.xmax)
    return minindex,maxindex
# def read_gaussian_MO(self,MOenergy):
#     self.MOenergy=MOenergy
def find_baseline(self,baseline_bounds=(1,5),plot=True):
    baseline_res=shgo(lambda x: -APS.mofun(x,0.3,self.pes_raw
       ),
                      [baseline_bounds],iters=2)
    if baseline_res.x in baseline_bounds:
        raise ValueError(f'Found baseline is on the boundary
           ({baseline_res.x[0]}). '\
                         'Please rerun with better
                            baseline_bounds.')
    self._baseline=baseline_res.x[0]
    if plot==True:
        plt.figure()
        self.plot()
def find_cutoff(self):
    try:
        index=next(len(self.pes_base)-i for i,j in enumerate(
           self.pes_base
                                                            [::-1])
```

```
                                                                    if
                                                                    j
                                                                    <0)
        except:
            raise ValueError('Baseline was not correct. Please
               redo '\
                             'find_baseline.')
        self._cutoff_index,self._cutoff_energy=index,self.energy[
           index]
    def plot(self):
        plt.grid(True,which='both',axis='x')
        fig=plt.plot(self.energy,self.pes,label=self.name)
        plt.axhline(y=0, color='k',ls='--')
        if self._is_analyzed:
            plt.plot([self.homo,self.energy[self.lin_stop_index
               ]],
                     [0,np.polyval(self.lin_par,self.energy[
                         self.lin_stop_index])],'--',c=fig[0].
                            _color)
        # if hasattr(self,'fit_par') and hasattr(self,'APSfit'):
        #     plt.plot(self.energy,self.APSfit,label=
        #              f'fit: c={self.fit_par[0]:.4f}, shift={
           self.fit_par[1]:.4f}'\
        #                  f', scale={self.fit_par[2]:.1f}')
        plt.legend()
        plt.xlabel('Energy (eV)')
        if not self.sqrt:
            plt.ylabel('Photoemission$^{1/3}$  (arb. unit)')
        else:
            plt.ylabel('Photoemission$^{1/2}$  (arb.unit)')
        plt.autoscale(enable=True,axis='both',tight=True)
        plt.gca().set_ylim(bottom=-0.5)
    def DOSsmooth(self,*args,scale=4.122623,y0=0.1,plot=False,**
       kwargs):
        shift=0.053547 #this value is derived from empirical
           measurements
        cutoff=self.cutoff_energy+shift
        self._DOS=self.DOS_raw*self.erfsmooth(self.energy,scale,
           cutoff,y0)
        self._DOS=savgol_filter(self._DOS,*args,**kwargs)
        if plot:
            plt.figure(f'{self.name} DOS smooth')
            self.DOSplot()
            # index=self.cutoff_index-5
            _=plt.plot(self.energy,self.DOS_raw,'o-',
                       label='no smooth',mfc='none')
            plt.legend()
    def DOSplot(self):
        plt.grid(True,which='both',axis='x')
        # index=self.cutoff_index-5
        _=plt.plot(self.energy,self.DOS,'*-',label=self.name,
                   mfc='none')
        plt.axhline(y=0, color='k',ls='--')
        plt.autoscale(enable=True,axis='both',tight=True)
        plt.gca().set_ylim(bottom=-0.5)
        plt.legend()
        plt.xlabel('Energy (eV)')
        plt.ylabel('DOS (arb. unit)')
    def analyze(self, fit_lower_bound=0.5,fit_upper_bound=np.inf,
       points=7,
                plot=True):
        if points<=2:
```

```
            raise Exception('Linear fit must contain more than 2
               points to be'\
            'meaningful.')
        try:
            start=len(self.energy)-next(i for i,j in enumerate(
                self.pes_base[::-1]) if j<fit_lower_bound)-1
        except StopIteration:
            print('fit_lower_bound is lower than the lowest PES.
               Use'\
                  f' the beginning as fit_lower_bound for {self.
                     name}.')
            start=0
        stop=len(self.energy)-next(i for i,j in enumerate(
            self.pes_base[::-1]) if j<fit_upper_bound)
        self.std_homo=np.inf
        for i,j in [[i,j] for i in range(start,stop) for j in
                     range(i+points,stop)]:
            x,y=self.energy[i:j],self.pes_base[i:j]
            fit=np.polyfit(x,y,1)
            x_intcp=-fit[1]/fit[0]
            sig_square=((np.polyval(fit,x)-y)**2).sum()/(j-i-2)
            X=np.concatenate(([x-x_intcp],[np.repeat(-fit[0],j-i)
               ]),0)
            [[_,_],[_,var_homo]]=np.linalg.inv(X.dot(X.T))*
               sig_square
            std_homo=var_homo**0.5
            if std_homo<self.std_homo:
                self.lin_start_index,self.lin_stop_index=i,j
                self.lin_par,self.std_homo=fit,std_homo
                self.homo=x_intcp
        if self.std_homo==np.inf:
            plt.figure()
            self.plot(f"{self.name} fitting fail!!!")
            raise Exception("Fitting fail!!! Rechoose fitting
               condition.")
        if plot:
            fig=plt.figure(f'{self.name} APS plot')
            ax=fig.gca()
            self.plot()
            plt.title(self.name)
            plt.text(.5, .95, f'HOMO={self.homo:.2f}\u00b1 '\
                     f'{self.std_homo:.4f} eV'
                     , style='italic',
                     bbox={'facecolor': 'yellow', 'alpha': 0.5},
                     horizontalalignment='center',
                        verticalalignment='center',
                     transform=ax.transAxes)
            ax.legend().remove()
        if self.lin_stop_index-self.lin_start_index==points:
            print(self.name+' is using the minimum number of
               points\t')
    def DOSfit(self,p0):
        minindex,maxindex=self.pick_range()
        fit,_=curve_fit(lambda x,scale,c,center: scale*APS.
           gaussian(x,c,center),
                        self.energy[minindex:maxindex],
                        self.DOS[minindex:maxindex],p0)
        plt.figure()
        plt.plot(self.energy[minindex:maxindex],
                 fit[0]*APS.gaussian(self.energy[minindex:
                    maxindex],
                                     *fit[1:3]),label='fit')
        self.DOSplot()
```

```
def MOfit(self,p0=[2,0.12,0.2],bounds=([0.01,0.1,-0.5],[1e2
   ,0.3,0.5]),
          repick=True):
    self.p0=p0
    self.bounds=bounds
    if repick:
        minindex,maxindex=self.pick_range()
        self.MOfit_range=(self.energy[minindex],self.energy[
           maxindex])
    else:
        assert hasattr(self,'MOfit_range'), 'No previous
           fitting range!'
        minindex,maxindex=self.MOfit_range
    if not hasattr(self, 'MOenergy'):
        MOenergy=np.array(input("Input MOs from Gaussian:\n")
           .split(),
                          'float')
        self.MOenergy=np.abs(MOenergy)
    else:
        temp=input("Use previous MO input?\n")
    if temp in ('yes','y','Yes','Y','True','true'):
        pass
    elif temp in ('no','n','No','N','False','false'):
        MOenergy=np.array(input("Input MOs from Gaussian:\n")
           .split(),
                          'float')
        self.MOenergy=np.abs(MOenergy)
    else:
        raise ValueError('Input yes or no for Using previous
           MO input.\n')
    x=self.energy[minindex:maxindex]
    y=self.DOS[minindex:maxindex]
    self.MOfit_par,_ = curve_fit(lambda x,scale,c,shift:
       scale*self.mofun(x,c,self.MOenergy+shift),x,y,p0=p0,
       bounds=bounds,absolute_sigma=True,ftol=1e-12)
    plt.figure()
    self.DOSplot()
    MOfit=self.MOfit_par[0]*self.mofun(self.energy,self.
       MOfit_par[1],
                                       self.MOenergy+self.
                                          MOfit_par[-1])
    plt.plot(self.energy,MOfit,label=
             'fit: scale=%2.1f, c=%1.4f, shift=%1.4f'
             %tuple(self.MOfit_par))
    x=np.arange(*self.MOfit_range,1e-3)
    plt.plot(x,self.mofun(x,0.02,self.MOenergy+self.MOfit_par
       [-1])
             *self.MOfit_par[0])
    plt.legend()
    plt.title('FitAPS')
    print('scale=%1.4f, broaden facter=%1.4f, shift=%2.1f' %
       tuple(self.MOfit_par))
@classmethod
def import_from_files(cls,filenames,sqrt=False,trunc=-4):
    '''
    This classmethod is used to import APS files from
       KPtechnology output.
    The software can do all the fitting parts but not able to
        handle the turn-on threshold because the threshold
       data is the IP of KPtechnology.
    '''
    data=[]
    sqrt=np.resize(sqrt,len(filenames))
    # index of saved column from raw data. 2 is energy and 7
       is cuberoot.
```

```
        #6 is square-root.
        for file,sqrt_type in zip(filenames,sqrt):
            with open(file,'r',newline='') as f:
                lf=list(csv.reader(f))[1:]
                for i,j in enumerate(lf):
                    try:
                        if not 'WF' in j[0] and float(j[3])<1e4:
                            pass
                        else:
                            stopindex=i
                            break
                    except:
                        print(j)
                        raise ValueError(f'{file} does not have
                           the right'\
                                                ' format from APS04
                                                 ')
                save_index=[2,6] if sqrt_type else [2,7]
                temp=np.array([[float(j[save_index[0]]),
                                float(j[save_index[1]])]
                               for i,j in enumerate(lf)
                               if i < stopindex])
            data.append(cls(temp[:,0],temp[:,1],sqrt_type,split(
               file)[1][:trunc]))
        return data
    @classmethod
    def from_DOS(cls,energy,DOS,sqrt,Name='no_name'):
        pes_raw=inv_gradient(energy,DOS)
        APS_obj=cls(energy,pes_raw,sqrt,Name)
        APS_obj.find_baseline((-1,1),plot=False)
        return APS_obj
    @staticmethod
    def group_sqrt(data):
        sqrt_list=(i.sqrt for i in data)
        if not all(sqrt_list) and any(sqrt_list):
            raise Exception('data has not uniform sqrt type.')
        else:
            return data[0].sqrt
    @staticmethod
    def lc_DOS(data,coeff,cov,Name='linear_combination'):
        '''
        linear combine the DOS of each data element with coeff.
        ----
        data=[data1,data2,...] where each element is an APS
           object
        coeff is a list or tuple of n-element [coeff1,coeff2,...]
        cov is a list or tuple of the covariant of the
           coefficients
        fmt has option 'd' (data) or 'o' (object).
        d will output (energy,DOS) and o will output APS_object
        Name for the output APS object.
        '''
        assert len(data)==len(coeff), 'Dimension mismatch'
        sqrt=APS.group_sqrt(data)
        energy,DOS=[i.energy for i in data],[i.DOS for i in data]
        energy,DOS=find_overlap(energy,DOS)
        DOS=np.dot(coeff,DOS)
        APS_obj=APS.APS_from_DOS(energy,DOS,sqrt,Name)
        APS_obj.lc_source=[i.name for i in data]
        APS_obj.lc_coeff,APS_obj.lc_cov=coeff,cov
        return APS_obj
    @staticmethod
    def lc_DOSfit(source,target,constrain=True):
        '''
        Linear combine multiple DOS from source to fit the DOS of
            target.
```

```
        source is a list of APS objects [APS1,APS2,...] to fit
           APS obj target.
        '''
        cutoff_energy=[i.cutoff_energy for i in source]
        index=cutoff_energy.index(min(cutoff_energy))
        energy=[j.energy if i!=index else j.energy[j.cutoff_index
           :] for i,j
                in enumerate([*source,target])]
        DOS=[j.DOS if i!=index else j.DOS[j.cutoff_index:] for i,
           j in
             enumerate([*source,target])]
        energy,DOS=find_overlap(energy,DOS)
        input_DOS=DOS[:-1]
        fit_DOS=DOS[-1]
        if constrain==1:
            fit,cov=curve_fit(lambda x,*c: np.dot((*c,1-sum(c)),x
               ),input_DOS,
                              fit_DOS,p0=[1/len(input_DOS)]*(len(
                                 input_DOS)-1),
                              absolute_sigma=True,bounds=(0,np.inf))
            cov=np.diag(cov)
            return np.array([*fit,1-sum(fit)]),cov
        else:
            fit,cov=curve_fit(lambda x,*c: np.dot(c,x),input_DOS,
                              fit_DOS,p0=[1/len(input_DOS)]*len(
                                 input_DOS),
                              absolute_sigma=True,bounds=(0,np.inf))
            cov=np.diag(cov)
            return fit,cov
    @staticmethod
    def save_all(data,location,filename=''):
        APS.save_aps_all(data,location,filename=filename)
        APS.save_DOS_csv(data,location,filename=f'{filename}_DOS
           ')
    @staticmethod
    def save_aps_all(data,location,filename=''):
        APS.save_aps_csv(data,location,filename=f'{filename}_APS
           ')
        APS.save_aps_fit_csv(data,location,
                             filename=f'{filename}
                                _APS_linear_regression')
        APS.save_homo_error_csv(data,location,filename=f'{
           filename}_APS_HOMO')
    @staticmethod
    def save_aps_csv(data,location,filename='APS'):
        datanames=[[i.name] for i in data]
        origin_header=[['Energy','Photoemission\\+(1/3)'],['eV','
           arb. unit']] if \
        all([i.sqrt==False for i in data]) else [['Energy','
           Photoemission\\+(1/2)'],['eV','arb. unit']]
        x,y=[i.energy for i in data],[i.pes for i in data]
        save_csv_for_origin((x,y),location,filename,datanames,
           origin_header)
    @staticmethod
    def save_aps_fit_csv(data,location,filename='
       APS_linear_regression'):
        assert all(i._is_analyzed for i in data), 'Input not yet
           analyzed'
        origin_header=[['Energy','Photoemission\\+(1/3)'],['eV','
           arb. unit']] if all([i.sqrt==False for i in data])
           else [['Energy','Photoemission\\+(1/2)'],['eV','arb.
           unit']]
        datanames=[[i.name] for i in data]
```

```
        x=[np.array([i.homo,i.energy[i.lin_stop_index]]) for i in
            data]
        y=[np.array([0,np.polyval(i.lin_par,i.energy[i.
           lin_stop_index])]) for i in data]
        save_csv_for_origin((x,y),location,filename,datanames,
           origin_header)
    @staticmethod
    def save_homo_error_csv(data,location,filename='APS_HOMO'):
        assert all(i._is_analyzed for i in data), 'Input not yet
           analyze'
        origin_header=[['Material','Energy','HOMO std'],[None,'eV
           ','eV']]
        datanames=[['HOMO']]
        x=[[i.name for i in data]]
        y=[[-i.homo for i in data]]
        z=[[i.std_homo for i in data]]
        save_csv_for_origin((x,y,z),location,filename,datanames,
           origin_header)
    @staticmethod
    def save_DOS_csv(data,location,filename='DOS'):
        origin_header=[['Energy','DOS'],['eV','arb. unit']]
        datanames=[[i.name] for i in data]
        x,y=[i.energy for i in data],[i.DOS for i in data]
        save_csv_for_origin((x,y),location,filename,datanames,
           origin_header)
    @staticmethod
    def gaussian(x,c,center):
        return np.exp(-(x-center)**2/2/c**2)/c/(2*np.pi)**0.5
    @staticmethod
    def mofun(x,c,MOenergy):
        return np.sum([APS.gaussian(x,c,i) for i in MOenergy],
           axis=0)
    @staticmethod
    def mo2dosfun(x,scale,c,MOenergy):
        return scale*APS.mofun(x,c,MOenergy)
    @staticmethod
    def apsfun(x,c,scale,MOenergy):
        return np.cumsum([scale*integrate.quad(APS.mofun,x[i-1],x
           [i],args=(c,MOenergy))[0] if i!=0 else 0 for i in
           range(len(x))])
    @staticmethod
    def erfsmooth(x:np.array,scale:float,cutoff:float,y0:float)->
       np.array:
        if y0<0:
            raise ValueError('y_scale must be larger than 0.')
        return erf((x-cutoff)*scale)*(1-y0)/2+(1+y0)/2
class dwf:
    allowed_kwargs=[]
    _calibrated=False
    def __init__(self,time,CPDdata,name='no_name',**kwargs):
        self.time=np.array(time)
        self.CPDdata=np.array(CPDdata)
        self.name=name
        self.data_type,self.data_unit='CPD','meV'
        try:
            self.__dict__.update((i,kwargs[i]) for i in self.
               allowed_kwargs)
        except KeyError:
            raise Exception('expect key words '+','.join(self.
               allowed_kwargs)
                            + ' missing')
    @property
    def status(self):
        return {'calibrated':self._is_calibrated,
                'statistics':self._has_statistics}
```

```
@property
def _is_calibrated(self):
    return self._calibrated
@property
def _has_statistics(self):
    return True if hasattr(self,'average_CPD') else False
def __repr__(self):
    return self.name
def __str__(self):
    summary='Name:\t'+self.name+'\n'
    summary+='\n'.join([f'{i}:\t{j}' for i,j in self.status.
       items()])+'\n'
    if self._has_statistics==True:
        summary+=f'Statistic region:\tlast {self.length}'\
            f's\naverage:\t{self.average_CPD:.3f}\u00b1{self.
               std_CPD:.3f}eV\n'
    return summary
def plot(self):
    plt.plot(self.time,self.CPDdata,label=self.name)
    plt.grid(True,which='both',axis='both')
    plt.ylabel(f'{self.data_type} ({self.data_unit})')
    plt.legend()
    plt.xlabel('Time(s)')
    plt.autoscale(enable=True,axis='both',tight=True)
def dwf_stat(self,length=200):
    try:
        start=next(i-1 for i,j in enumerate(self.time) if
                   j>self.time[-1]-length)
    except StopIteration:
        raise ValueError('average length is larger than data
           length')
    self.average_CPD=np.average(self.CPDdata[start:])
    self.std_CPD=np.std(self.CPDdata[start:])
    self.length=length
@classmethod
def import_from_files(cls,filenames,trunc=-4,**kwargs):
    data=[]
    for file in filenames:
        with open(file,'r',newline='') as f:
            reader=csv.reader(f)
            first_row=next(reader)
            time_ind=first_row.index('Time(Secs)')
            wf_ind=first_row.index('WF (mV)')
            for i,j in enumerate(reader):
                if len(j)==1:
                    stopindex=i
                    break
            f.seek(0)
            acceptlines=range(1,stopindex)
            temp=np.array([[float(j[time_ind]),
                            float(j[wf_ind])]
                           for i,j in enumerate(reader)
                           if i in acceptlines])
        data.append(cls(temp[:,0],temp[:,1],split(file)[1][:
           trunc],**kwargs))
    return data
@staticmethod
def save_csv(data,location,filename='DWF'):
    assert all([data[i].__class__==data[i+1].__class__ for i
       in range(len(data)-1)]), 'Data are not the same class
       objects'
    origin_header=[['Time',data[0].data_type],['s',data[0].
       data_unit]]
    datanames=[[i.name] for i in data]
    x=[i.time for i in data]
```

```
        y=[i.CPDdata for i in data]
        save_csv_for_origin((x,y),location,filename,datanames,
           origin_header)
    @staticmethod
    def save_dwf_stat_csv(data,location,filename='DWF_stat'):
        assert all([data[i].__class__==data[i+1].__class__ for i
           in range(len(data)-1)]), 'Data are not the same class
           objects'
        if not all([i._has_statistics for i in data]):
            print('Use last 200sec data for statistic analysis')
            _=[i.dwf_stat() for i in data]
        origin_header=[['Material','Energy',data[0].data_type+'
           std'],[None,data[0].data_unit,data[0].data_unit]]
        datanames=[[data[0].data_type]]
        x=[[i.name for i in data]]
        y=[[i.average_CPD for i in data]]
        z=[[i.std_CPD for i in data]]
        save_csv_for_origin((x,y,z),location,filename,datanames,
           origin_header)
class calibrate:
    def __init__(self,ref_APS,ref_dwf):
        if not ref_APS._is_analyzed:
            raise Exception('Analyze ref. APS first by ref_APS.
               analyze()')
        if not ref_dwf._has_statistics:
            raise Exception('Find average CPD by ref_dwf.dwf_stat
               ()')
        self.tip_dwf=-ref_APS.homo+ref_dwf.average_CPD/1000
        self.name=f'{ref_APS}\n{ref_dwf}'
    def __repr__(self):
        return self.name
    def __str__(self):
        return self.name
    def cal(self,data:list)->List[dwf]:
        assert all([i.__class__.__name__=='dwf' for i in data]),\
            'Calibrate only applicable to CPD measurements'
        for i in data:
            i.CPDdata=-i.CPDdata/1000+self.tip_dwf
            i.data_type,i.data_unit='Fermi level','eV'
            i._calibrated=True
            i.ref_dwf=self.tip_dwf
class spv(dwf):
    allowed_kwargs=['timemap']
    def __init__(self,time,CPDdata,name='no_name',**kwargs):
        super().__init__(time,CPDdata,name=name,**kwargs)
        self.timeline=np.cumsum(self.timemap)
        self.timeline_index=[next(j-1 for j,k in enumerate(self.
           time) if k>i)
                             for i in self.timeline[:-1]]
        self.timeline_index.insert(0,0)
        self.timeline_index.append(len(self.time)-1)
        self.data_type,self.data_unit='raw SPV','meV'
    @property
    def status(self):
        return {'background calibrated':self.bg_calibrated,
                'normalized':self.is_normalized}
    @property
    def bg_calibrated(self):
        return True if hasattr(self,'bg_cpd') else False
    @property
    def is_normalized(self):
        return True if hasattr(self,'norm_spv') else False
    def __str__(self):
        summary='Name:\t'+self.name+'\n'
```

```
        summary+='\n'.join([i+':\t'+str(j) for i,j in self.status
            .items()])+'\n'
        summary+='timemap:'+str(self.timemap)+'\n'
        return summary
    def cal_background(self,plot=False):
        self.bg_cpd=np.average(self.CPDdata[0:self.timeline_index
            [1]])
        self.CPDdata=self.CPDdata-self.bg_cpd
        self.data_type='SPV'
        if plot:
            plt.figure()
            self.plot()
    def normalize(self,timezone=1,plot=False):
        if not self.bg_calibrated:
            self.cal_background()
        self.norm_zone=timezone
        scale_fac=max(abs(self.CPDdata[self.timeline_index[
            timezone]:self.timeline_index[timezone+1]]))
        self.norm_spv=self.CPDdata/scale_fac
        if plot:
            plt.figure()
            self.norm_plot()
    def plot(self):
        super().plot()
        self.plot_highlight()
    def norm_plot(self):
        if not self.is_normalized:
            raise Exception(f'{self.name} is not noramlized yet')
        plt.grid(True,which='both',axis='both')
        plt.plot(self.time,self.norm_spv,label=self.name)
        plt.ylabel('normalized SPV')
        plt.legend()
        plt.xlabel('Time(s)')
        plt.autoscale(enable=True,axis='both',tight=True)
        self.plot_highlight()
    def plot_highlight(self):
        for i in range(len(self.timeline)//2):
            plt.axvspan(self.timeline[2*i],self.timeline[2*i+1],
                color='yellow',alpha=0.5)
    @staticmethod
    def save_norm_spv_csv(data,location,filename='Normalized_SPV
        '):
        assert all([data[i].__class__==data[i+1].__class__ for i
            in range(len(data)-1)]), 'Data are not the same class
            objects'
        if not all([i.is_normalized for i in data]):
            print('Use first light on for normalization')
            _=[i.normalize() for i in data]
        origin_header=[['Time','Normalized SPV'],['s','']]
        datanames=[[i.name] for i in data]
        x=[i.time for i in data]
        y=[i.norm_spv for i in data]
        save_csv_for_origin((x,y),location,filename,datanames,
            origin_header)
```

Appendix D

Visualization of Quadrupole Moment and Multipole Expansion

Quadrupole moment is the second order of multipole expansion, a mathematical series used to describe spherical coordinates. Since many physical force fields, such as electric, magnetic and gravitational fields, have spherical symmetry, multipole expansion has been widely applied in order to approximate these systems. The multipole expansion can be described as

$$f(\theta,\phi) = \sum_{l=0}^{\infty} \sum_{m=-l}^{l} C_l^m Y_l^m(\theta,\phi), \tag{D.1}$$

where Y_l^m are the spherical harmonic functions, C_l^m are the constant coefficients, and θ is the polar angle and ϕ is the azimuthal angle in spherical coordinate system. This expansion forms a complete and orthogonal basis sets to describe a spherical system. In fact, it is part of the solution to Laplace's equation, which is the Schrodinger equation for a hydrogen atom. Therefore, multipole expansion can be visualized and analogous to atomic orbitals. Y_0^0 is known as charge monopole, which can be analogous to the s orbital, while Y_1^1, Y_1^0 and Y_1^{-1} are known as charge dipoles, similar to p_x, p_y and p_z orbitals. For $l = 2$ or quadrupole, there will be five unique terms, $Y_2^{\{2,1,0,-1,-2\}}$, analogous to the five d orbitals. Among them, the d_{z^2} is the most directly related to the Q_{zz} which has been highlighted throughout Chapter 4. Thus, Q_{zz} or Q_π can be visualized or conceptualized as positive charges spreading over the z direction while the negative charges forming a circular rim over the xy plane or vice versa. This type of charge distribution coincides with planar conjugated molecules as the conjugated π bonds and the side chains forming a similar charge distribution.